

https://dspace.org/

Broadband beam shaping

Perumal, Leerin Michaela

2024-03
University of the Witwatersrand, Johannesburg
https://hdl.handle.net/10539/45214
Perumal, Leerin Michaela. (2024). Broadband beam shaping. [Master's dissertation, University of the Witwatersrand, Johannesburg]. WIReDSpace. https://hdl.handle.net/10539/45214

Downloaded from a DSpace repository. https://dspace.org/

UNIVERSITY OF THE WITWATERSRAND

MASTER'S THESIS

Broadband beam shaping

Author:
Leerin Michaela Perumal

Supervisors:
Prof. Andrew Forbes
Dr. Angela Dudley



WITS
UNIVERSITY

A thesis submitted in fulfillment of the requirements
for the degree of Master of Science

in the

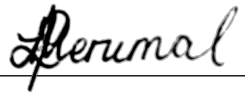
Structured Light Laboratory
School of Physics

March 8, 2024

Declaration of Authorship

I, Leerin Michaela Perumal, declare that this thesis titled, "Broadband beam shaping" and the work presented in it are my own. I confirm that:

- This work was done wholly or mainly while in candidature for a research degree at this University.
- Where any part of this thesis has previously been submitted for a degree or any other qualification at this University or any other institution, this has been clearly stated.
- Where I have consulted the published work of others, this is always clearly attributed.
- Where I have quoted from the work of others, the source is always given. With the exception of such quotations, this thesis is entirely my own work.
- I have acknowledged all main sources of help.
- Where the thesis is based on work done by myself jointly with others, I have made clear exactly what was done by others and what I have contributed myself.

Signed: 

Date: March 8, 2024

"Our deepest fear is not that we are inadequate. Our deepest fear is that we are powerful beyond measure. It is our light, not our darkness that most frightens us. We ask ourselves who am I to be brilliant, gorgeous, talented and fabulous? Actually, who are you not to be? You are a child of God."

Marianne Williamson

UNIVERSITY OF THE WITWATERSRAND

Abstract

Master of Science

Broadband beam shaping

by Leerin Michaela Perumal

Laser beam shaping is a venerable topic that enjoyed an explosion in activity in the late 1990s with the advent of diffractive optics for arbitrary control of coherent fields. Today, the topic is experiencing a resurgence, fueled in part by the emerging power of tailoring light in all its degrees of freedom, so-called structured light, and in part by the versatility of modern day fabrication and implementation tools. Since its development, structured light has become a priceless tool in various applications such as telecommunication, imaging and microscopy, industrial manufacturing, quantum computing, optical trapping and medical treatments, to name a few. With recent advancements in these various applications, broadband beam shaping (creating structured light with many wavelengths) has become topical as it offers an additional degree of freedom for one to manipulate. In this thesis we look at how to generate broadband light using both digital and physical beam shaping optics. In so doing we provide a method to introduce broadband beam shaping into various applications that may benefit from either the compact size of a physical optic or the dynamic ability of a digital.

Acknowledgements

To my supervisor, **Prof. Andrew Forbes**, thank you for taking a chance on me and believing in my potential, even when I didn't believe in myself. Your constant support, guidance, and teachings have impacted me in more ways than can be expressed, and I shall forever be grateful. These past two years have been the most difficult for my family and I, and I wouldn't be where I am today without you. Thank you for introducing me to the world of optics and igniting my love for research. I look forward to continuing this journey with you and hopefully making an impact in the world.

To **Dr. Garry Morrison** *(De Beers)*, from the day we met until now, your constant encouragement, kindness, and insight have been a pillar of strength for me throughout this journey. You always saw the best in me and made me believe I could do the impossible, and I shall never forget that. I would like to thank both you and De Beers for the funding and entrusting me with this once-in-a-lifetime opportunity. I hope it will continue to be a foundation for great discoveries.

To **Dr. Angela Dudley**, you have always been someone that I could rely on in every possible way. The countless laughs and chats we have shared will forever be engraved in my heart, so thank you for always being more than a co-supervisor to me.

To **Prof. Jan Korvink** *(Karlsruhe Institute of Technology)*, although our paths crossed quite late in my master's journey, I am so grateful that it did. Before we even met, you invested both your time and finances in our collaboration. Not many would do that, hence I believe that you saw much potential in me, this project, and our collaboration. I am truly grateful for the kindness and support you have shown me. Thank you for opening the doors of IMT to me and exposing me to the most amazing ideas and ongoing research. I cannot wait to continue this journey with you.

To my seniors: **Chané, Isaac, Keshaan, Bereneice**, and **Lehloa**. All I can say is 'wow.' You all have been such a source of inspiration to me. More than that—thank you for the wisdom, guidance, love, and support you have given me. There were so many days when I wanted to give up, but your encouragement and guidance showed me how to take the next steps and gave me the strength to take them.

To my Structured Light Lab family: **Light, Neelan, Mwezi, Sachleen, Ané, Ashley, Bertus, Wagner, Paola**, and all the new masters and honours students. Thank you for bringing me so much joy, especially when life was so hard. The countless memories (especially at the PIG) are tattooed on my heart. Thank you for inspiring and encouraging me throughout this journey. I look forward to the next few years with you.

To **Pedro** and **Cade**, we made it! What a rollercoaster this has been. You've seen and been with me through it all—the highs and lows—and I thank God for blessing me with you two. I wouldn't have made it without you. Thank you for never believing me when I said I was backing out. Here's to another one, and many more to come.

To my colleagues at IMT, Karlsruhe Institute of Technology: **Stefan, Celine, Arndt**,

and **Razia** from De Beers, thank you for being so kind and welcoming during my visits. You all have taught me so much in such a short period of time, and I look forward to continuing the collaboration.

To my **family, friends**, and **educators**, I am what I am because of you. Thank you for the love, support, and guidance you have given me throughout the years.

To my **parents** and **brother**, everything I have done has always been for you. Thank you for teaching me the value of life and the importance of doing things with excellence. It is because of your prayers, teachings, and love that I have become who I am. Mum and Dad, I am forever grateful to you for giving me the opportunities in life that were never afforded to you, even when it came at a high expense. I promise that I will never take it for granted, and I hope to always make you proud.

Finally, to my Lord and saviour—**Jesus Christ**, it is by your grace alone that I am here. Thank you for making Jeremiah 29:11 a reality for me. May everything always be for your glory.

List of Publications

Journal Papers

1. **Perumal, L.**. and Forbes, A., 2023. Broadband structured light using digital micro-mirror devices (DMDs): a tutorial.
   Journal of Optics, 25(7), pp.4003 (*selected as Editor's pick*)

2. Forbes, A. and **Perumal, L.**, 2023. Twisted light gets a splash of colour.
   Nature Nanotechnology, 18(3), pp.221-222.

Presentations

1. Dudley, A. **Perumal, L.** and Forbes, A., 2023.
   Manipulating broadband light with a digital micromirror device.
   SPIE Optics and Photonics (San Diego, USA).

2. **Perumal, L.** and Forbes, A., 2023.
   Shaping a kaleidoscope of colours.
   67th Annual Conference of the South African Institute of Physics (Richard's Bay, South Africa).

3. **Perumal, L.** and Forbes, A., 2023.
   Digitally shaping a spectrum of light.
   9th Siegman International School on Lasers (Dublin, Ireland).

4. **Perumal, L.** and Forbes, A., 2023.
   Twisting broadband light using a digital micromirror device.
   67th Annual African Laser Conference (Stellenbosch, South Africa)
   (Awarded Wirsam prize for best MSc oral).

5. **Perumal, L.** and Forbes, A., 2022.
   Broadband beam shaping using a digital micromirror device.
   66th Annual Conference of the South African Institute of Physics (online).

Contents

Declaration of Authorship iii

Abstract vii

Acknowledgements ix

Publications xi

List of Figures xviii

List of Tables xix

List of Abbreviations xxi

1 Introduction 1
- 1.1 The theory of beam shaping . . . 3
  - 1.1.1 Beam types . . . 4
  - 1.1.2 Beam shaping techniques . . . 8
- 1.2 Thesis outline . . . 12

2 Experimental tools for broadband beam shaping 15
- 2.1 Broadband source: argon-ion laser . . . 15
  - 2.1.1 Laser properties . . . 15
- 2.2 Lenses . . . 22
- 2.3 Beam shaping elements . . . 28
  - 2.3.1 Physical optics . . . 29
  - 2.3.2 Digital beam shaping optics . . . 33
    - Spatial light modulators (SLMs) . . . 34
    - Digital micro-mirror devices (DMDs) . . . 37
  - 2.3.3 Considering wavelength-dependence . . . 39

3 Broadband beam shaping using a digital micro-mirror device 43
- 3.1 DMD structure and operating principles . . . 43
- 3.2 Computer generated holograms for DMDs . . . 45
  - 3.2.1 Theory . . . 46
  - 3.2.2 Writing the hologram to the DMD . . . 49
- 3.3 Setting up the DMD . . . 51
  - 3.3.1 Mounting . . . 51
  - 3.3.2 Connecting the DMD . . . 51
  - 3.3.3 Optical setup before the DMD . . . 53
  - 3.3.4 Optical considerations . . . 54
- 3.4 Monochromatic beam shaping . . . 57
  - 3.4.1 Creating flat-top beams . . . 58
  - 3.4.2 Creating LG beams . . . 60

3.5 Broadband beam shaping . . . 63
3.5.1 Wavelength independent beam shaping . . . 64
3.5.2 Experimental compensation of dispersion . . . 66

4 3-D printing optics for broadband beam shaping 73
4.1 The Quantum-X Nanoscribe . . . 73
4.1.1 How it works . . . 73
4.1.2 Structure . . . 75
4.1.3 The general printing process . . . 76
4.1.4 Calibration . . . 86
4.2 Fabrication of beam shaping optics . . . 87
4.2.1 Hologram encoding scheme . . . 87
4.2.2 Design considerations . . . 91
4.2.3 Printing the optics . . . 93
4.2.4 Analysis . . . 95
4.3 Optical testing . . . 103
4.3.1 Mounting and aligning the sample . . . 103
4.3.2 Experimental setup . . . 103
4.3.3 Experimental results . . . 105

5 Conclusion and prospectives 113
5.1 Conclusion . . . 113
5.2 Future work . . . 114

A Supplementary information on the calibration of a Spatial Light Modulator (SLM) 117

Bibliography 121

List of Figures

1.1 The general beam shaping problem and system. . . . 4
1.2 The simulated intensity profiles of HG beams with indices (n) and (m). 5
1.3 The intensity profile of a simulated LG beams for various azimuthal (l) and radial (p) indices. . . . 6
1.4 The intensity profile of a simulated vortex beams for various azimuthal (l) indices. . . . 7
1.5 Examples of intensity and cross-sectional profiles of flat-tops ($N = 2$, 4, 10 and 50) that were generated using the Super-Gaussian approximation 8
1.6 Beam shaping techniques: a) complex-amplitude modulation which is a one-step, lossy process; b) one-step, lossless phase-only modulation that is imperfect; c) two-step lossless phase-only modulation that is perfect. . . . 10

2.1 A depiction of the general broadband beam shaping problem from a experimental point-of-view. . . . 16
2.2 Determining the beam profile of each discrete wavelength and the multiline emitted of the argon-ion laser. . . . 18
2.3 Determining the beam waist size, w_0 per wavelength for each emitted beam from the argon-ion laser. . . . 19
2.4 Determining the relative (absolute) off-axis shift in the $x-$direction per wavelength for each emitted beam from the argon-ion laser. . . . 21
2.5 The different lens arrangements used in experimental setups. . . . 23
2.6 Conventional versus achromatic lenses. . . . 24
2.7 The Sellmeier equation depicting the relationship between the refractive index and wavelength of the incident beam for NBK-7 glass. . . . 25
2.8 Determining the focal length of an achromatic lens experimentally. . . . 27
2.9 How light is refracted when it passes through an interface, and how the shape of the surface/interface can be used to refract light to create a desired intensity distribution pattern. . . . 29
2.10 An example of a refractive lens- spiral phase plates (SPPs). . . . 30
2.11 Diffraction explained using Huygens; wave principle. . . . 31
2.12 Young's famous double slit experiment. . . . 32
2.13 How the binary slits can be arranged to focus light, i.e., create a Fresnel zone plate. . . . 32
2.14 The structure and operating principle of a spatial light modulator (SLM). 35
2.15 How grayscale holograms are used to cause a re-orientating of the liquid-crystals and thus induce a desired phase shift. . . . 36
2.16 Comparison of experimentally generated HG modes when the SLM was un-calibrated and calibrated to the wavelength of the incident light. . . . 37
2.17 A comparison of the structures of a) deformable mirrors and b) digital micro-mirror devices (DMDs). . . . 38

2.18 Image showing that a broadband beam of light is dispersed by a DMD even when it is un-powered. . . . 39
2.19 A plot depicting the effect on the intensity of the structured beam (in the +1st diffraction order) when a phase element is designed for wavelength λ_0 but one operates at wavelength λ. . . . 40

3.1 The structure of the DMD. . . . 44
3.2 The different layouts of their micro-mirror arrays in the DMD screen. . . . 45
3.3 The three possible states of the DMD micro-mirrors: *on*, *parked* and *off*. 46
3.4 Computer generated hologram for creating a vortex beam by a complex amplitude function on a DMD. . . . 49
3.5 How binary holograms act as a means to control each micro-mirror in the DMD's screen. . . . 50
3.6 The effects of incorrect scaling/mapping between the hologram and DMD pixels results in a distortion of the generated mode. . . . 51
3.7 The recommended way to mount the DMD. . . . 52
3.8 The driver unit of a DLP3000 DMD with labels highlighting the key components needed to connect to the DMD. . . . 53
3.9 A common optical setup before the DMD. . . . 54
3.10 Rough aligning the DMD. . . . 54
3.11 The grating encoded in the DMD hologram diffracts the incident beam and a telescope can be used to recombine the beams to single point again. . . . 55
3.12 An encoded converging lens can be used to determine the +1st diffraction order. . . . 56
3.13 Experimental images depicting the effect misalignment and aberrations have on a structured vortex ($l = 5$) beam. . . . 57
3.14 An illustration depicting how to generate a flat-top beam using an encoded DMD hologram as the beam shaping element. . . . 59
3.15 The simulated results of converting an incident Gaussian through phase-only modulation to an output flat-top beam. . . . 59
3.16 The experimental process and setup of making a flat-top beam. . . . 60
3.17 Experimental results of a created flat-top (λ = 514 nm) . . . 61
3.18 An illustration depicting how to generate an LG beam using an encoded DMD hologram as the beam shaping element. . . . 61
3.19 The simulated results of converting an incident Gaussian through complex-amplitude modulation to an output LG_0^3 beam using a hologram that would be encoded on a DMD. . . . 62
3.20 The experimental setup to generate an LG beam using monochromatic incident light (λ = 514 nm). . . . 63
3.21 Experimental results of a created LG_0^3 (λ= 514 nm). . . . 63
3.22 How to simulated multi-wavelength LG_0^3 modes, all created with a hologram designed for $\lambda_0 = 488$ nm. . . . 64
3.23 Experimental setup and process to generate flat-top beams for various wavelengths. . . . 65
3.24 Experimental results of flat-top beams that have been generated for various wavelengths. . . . 66
3.25 Experimental optical tools and techniques to compensate for the dispersion of the broadband beam. . . . 68

3.26 An experimental method for structuring a broadband beam using a DMD and a single lens so that it has the correct intensity at a single plane only. . . . 69
3.27 Experimental setup for demonstrating single-plane recombination where LG_0^3 modes were created for mutliple wavelengths. . . . 70
3.28 Experimental results demonstrating single-plane recombination. a) The intensity profiles of each structured LG_0^3 per wavelength, as well as the single-plane broadband beam with the simulated case shown as inserts; b) the cross-sectional comparison of each structured LG_0^3 mode per wavelength with the broadband beam; c) a cross-sectional comparison of the experimentally generated broadband beam and the simulated case (shown as insert), which correlate to each other by a factor of 95.3%. . . . 71
3.29 Experimental results demonstrating broadband beam shaping and single-plane recombination for various LG modes with varying azimuthal (l) and radial (p) indices for a) 457 nm; b) 488 nm; c) 514 nm; d) Multiline. Inserts depict the simulated case for each mode. . . . 72

4.1 The process of 2 photon absorption for lithography. . . . 74
4.2 The process of how polymerisation occurs in two-photon lithography 74
4.3 Relationship between different laser intensities, voxel sizes and eventually different sizes and heights of the polymer that is printed. Image taken from [130, 132] . . . 75
4.4 The structure of the Quantum-X Nanoscribe. . . . 77
4.5 A summary of the general 3D-printing process. . . . 78
4.6 The two methods for partitioning a model into printable sections. a) hatching; b) slicing . . . 79
4.7 The objective lenses that can be used in the Quantum-X. . . . 81
4.8 Substrates used for 3D-printing. . . . 82
4.9 Adding resin to the chosen substrate. . . . 82
4.10 Preparing the 3D-printer and setting the parameters for printing. . . . 83
4.11 Solvents used in the developement of the printed sample. . . . 83
4.12 Diagrams of the plasma sputtering high vacuum metallising (PSHVM) spin coating machine and the physical vapour deposition (PVD) process which are needed to metallise a sample. . . . 85
4.13 The thickness of the sputtered material (Au or Ag) versus time for various applied currents (30 mA or 45 mA), when the chamber is maintained at a pressure of 0.05 mbar and the inert gas used is Ar. Results provided were courtesy of IMT, KIT. . . . 86
4.14 A summary of the calibration process of the Quantum-X Nanoscribe. . . 88
4.15 Generated calibration curves for the Quantum-X. . . . 89
4.16 Examples of how to generate holograms, that when printed, generate modes through phase-only and complex-amplitude modulation for a) vortex ($l = 1$) and b) HG_2^1. . . . 92
4.17 Refractive indices for various wavelengths for different printing resins when in solid state at 20° C . . . 94
4.18 A summary of the printing process to make the desired beam shaping optics. . . . 95

4.19 A comparison of the holograms that were previously generated for a vortex ($l = 3$) and HG_2^1 mode (left), and the microscopic images of the respective printed optics. Images of the printed optic were taken both the darkfield (middle) and brightfield (right). In all cases the scale is 500 μm. 97
4.20 Determining the dimensions of the printed optic which was designed to produce a vortex ($l = 1$) mode. 98
4.21 Analysing a vortex ($l = 1$) printed optic using a laser microscope (LM) to determine the thickness, and spacing between structures. 100
4.22 A visual depiction of the effect of undissolved resin on the surface of the optic. Resin deposits disfigure and distort the surface of the optic in a random manner. The scale bar for the first image is 20 μm, while the scale bar for the second and third are 10 μm. 101
4.23 SEM images used to determine the true printing resolution of the Quantum-X when a $\times 63$ objective lens is used and thus the surface roughness of the sample. Results show that the surface roughness is measured to be 231 nm,i.e., the volume "pixel" size for the $\times 63$ objective lens is 200 nm. 102
4.24 The ideal manner to mount the 3D- printed sample. 104
4.25 The effect of misalignment of the sample to the produced mode causes the mode to appear astigmatised. 104
4.26 The experimental setup used to optically test the beam shaping ability of the 3-D printed optics (sample). 106
4.27 The experimental results for a printed optic that generates a vortex ($l = 1$) mode through phase-only modulation. The results are shown for various incident wavelengths. 107
4.28 Experimental results for a 3D- printed optic that generates an HG_1^2 mode through complex-amplitude modulation. Results are shown for various incident wavelengths 109
4.29 Broadband beam shaping can be achieved for various modes with 3-D printed optics. Here we showcase additional examples in the following columns: a) vortex ($l = 3$), b) LG_1^2 and c) HG_1^1. 110

5.1 A microscopic image of a printed converging lens designed to focus x-rays (λ_0 = 0.52 nm). 115

A.1 Experimental setup of the calibration procedure for an SLM. 118
A.2 The effect of how holograms are used to orientate the liquid crystals in the SLM screen, induce a phase shift and thus shift the interference pattern during the calibration process. 119
A.3 Interference pattern shifts a) before and b) after the SLM was calibrated. 119
A.4 Comparison of the reference (black) vs measured phase shift before and after calibration. 120

List of Tables

2.1 Derived minimum beam sizes , w_0 per wavelength for the argon-ion laser. . . . 17
2.2 Angle of deviation, θ (relative to λ = 488 nm) per wavelength for each emitted beam from the argon-ion laser. . . . 20
2.3 The refractive index and focal length of a conventional lens (f = 199.3 mm for λ_0 = 488 nm). . . . 26
2.4 The experimental values of the beam size before the lens, w and beam size at the beam waist w_0' and effective focal length of an achromatic lens (f = 200 mm) per wavelength. . . . 28
2.5 A summary (for discrete wavelengths) of the expected intensity of the structured beam (in the +1st diffraction order) when a phase element is designed for wavelength λ_0 but one operates at wavelength λ 41

3.1 Summary of the important properties for 3 common DMD models. . . . 44

4.1 A list of the possible objective lenses that can be inserted into the Quantum-X Nanoscribe, with their respective field of views and the type of resin they require [130, 133]. . . . 80
4.2 A list of printing resins (when in solid state) and their refractive indices for various wavelengths at 20°C. Experimental results provided by Nanoscribe[133]. . . . 93
4.3 A summary of the printing parameters and their chosen/set values. These values were used for printing of any and all beam shaping optics in this chapter. . . . 96
4.4 Measured beam sizes per wavelength of HG_1^2 modes produced by a 3-D printed optic 108

List of Abbreviations

2PP	Two-photon polymerisation
Ag	Silver
Ar	Argon
Au	Gold
BG	Bessel-Gaussian
CAM	Complex-amplitude modulation
CCD	Charged coupled device
CGH	Computer generated hologram
DLP	Digital light processing
DoF	Degree of freedom
DMD	Digital micro-mirror device
FOV	Field of view
HG	Hermite-Gaussian
HUD	Head-up display
LC	Liquid crystal
LCoS-SLM	Liquid-crystal on silicon spatial light modulator
LG	Laguerre-Gaussian
LM	Laser microscope
MEMS	Micoelectromechanical systems
NIR	Near-infrared
OAM	Orbital angular momentum
PGMEA	Propylene glycol methyl ether acetate
PSHV	Plasma sputtering high vacuum
PVD	Physical vapour deposition
RMSE	Root mean square error
SEM	Scanning electron microscope
SG	Super-Gaussian
SLM	Spatial light modulator
SPP	Spiral phase plate
STL	Stereolithography
UCNP	Up-conversion nanoparticle

Chapter 1

Introduction

From the ancient mirrors adorning Egyptian tombs to the intricate glass prisms unveiling the vivid spectrum of sunlight, humanity's enduring fascination with light transcends the annals of history. Yet, beneath this captivation lies a profound quest to not only scrutinise but also wield light for diverse objectives. The inception of beam shaping can arguably be traced back to 213-211 BC, credited to Archimedes. Employing polished metal pieces akin to mirrors, he redirected and concentrated sunlight onto adversary ships [1–3]. Fast-forwarding to the 1700s, the groundbreaking Fresnel lens emerged. Crafted by the French physicist Augustine-Jean Fresnel, it was initially designed to focus incoherent light for lighthouses and became instrumental in guiding ships along coastlines [2, 4].

Although the chronicles of beam shaping extend far into history, its true resurgence occurred in recent decades [5–8], coinciding with the emergence of microelectronics. Improved lithography processes not only facilitated the production of smaller, faster computer chips but also inaugurated a new era in beam shaping.

The advent of microelectronics enabled the numerical calculation of novel optical elements using computers. Simultaneously, lithographic fabrication techniques, honed for computer chip manufacturing, seamlessly transitioned into creating optical elements with small feature sizes. This catalysed innovations in the field, notably the establishment and experimental validation of 'lossless beam shaping' by Frieden in 1965 [9]. Frieden's system, comprising two optical elements, transformed an incident Gaussian beam into one with a uniform intensity distribution, correcting any phase distortions caused by light redistribution.

The true revolution, however, awaited the invention of the laser [10], paving the way for contemporary beam shaping. Leveraging diffractive elements and computer-generated optics, this era birthed 'structured light' [11, 12] —unique optical states crafted by tailoring light's various degrees of freedom (DoFs). While the manipulation of all DoFs is conceivable, current research primarily revolves around spatial control of light's amplitude, phase, and polarisation. Notable examples of structured light modes include Bessel-Gaussian (BG), airy, vortex, flat-top, Laguerre-Gaussian (LG), and Hermite-Gaussian (HG) beams [13].

Structured light can be meticulously fashioned either within the laser cavity [14], generating shaped light directly from the source, or externally [15], employing sophisticated beam shaping tools. A plethora of physical tools has been employed for beam shaping, ranging from refractive [16] and free-form optics [17] to geometric phase liquid crystals [18–20] and metasurface elements [21–23]. However, modern

approaches embrace computer-generated holograms (CGHs) and digital modulating devices, such as liquid crystal spatial light modulators (SLMs) [24–26] and digital micro-mirror devices (DMDs) [27, 28].

Since its inception in the late 1990s, structured light has sparked a transformative revolution across diverse sectors, becoming a cornerstone in commercial, industrial, and scientific applications [29]. One striking example of structured light's impact is its profound contribution to microscopy [30–35]. This revolutionary technique involves generating a meticulously designed pattern of light with predetermined characteristics. When applied to specimens with variations in thickness, surface profile, or refractive index, a phase-shift is imparted in the structured light pattern. Areas with minimal phase variation retain the original pattern, while regions experiencing significant phase changes manifest observable distortions. Through careful analysis of these distortions, intricate details about the specimen emerge, surpassing the capabilities of traditional microscopy. Structured light has elevated microscopy by enhancing surface profiling, enabling 3-D imaging, facilitating phase-contrast imaging, and empowering advanced techniques like super-resolution imaging.

In the realm of optical communications [36–39], structured light finds utility as an innovative information carrier. This is done by modulating the phase, amplitude, or polarisation of light and assigning specific patterns or regions within the pattern to represent distinct symbols or data bits. At the receiving end, the encoded light is decoded to reconstruct the transmitted data. For example, a *circle* could represent the letter *A*, while a *square* could represent the letter *B*. By transmitting the following sequence of beams, *circle-square-square-circle*, across a link this can be interpreted by the receiver as *'ABBA'*. The potential data encoding capacity is theoretically boundless, limited only by the multitude of unique structured light patterns that can be generated. This approach offers a substantial bandwidth advantage, and its resilience in turbulent [40, 41] environments and complex media [42] renders it indispensable in free-space and underwater communication systems.

Structured light's versatility extends across various applications, including laser drilling, nanopatterning, laser annealing, and photopolymerisation in manufacturing processes [43–46]. Its influence has permeated medical procedures, such as surgery [47, 48], skin treatments [49, 50], and hair removal [51, 52]. Additionally, structured light plays a vital role in the pharmaceutical and chemical industries, aiding in the identification and isolation of optically active compounds [53]. Within the research sector, the application of structured light transcends disciplinary boundaries, serving pivotal roles in diverse fields such as quantum communication [54, 55] and optical trapping [56–59]. The enduring impact of structured light continues to unfold, propelling innovation across a multitude of scientific and industrial domains.

In the wake of recent advancements across diverse fields, the spotlight has increasingly shifted towards the potential of broadband structured light, owing to its additional advantages [60–67]. To unravel the rationale behind this shift, let us consider the distinct advantages that broadband light offers in comparison to its narrowband counterparts.

In microscopy, as an example, broadband light enhances resolution and contrast in imaging because different wavelengths of light interact with specimens in unique ways. This interaction reveals hidden details about the structure of the specimen.

In microscopy, optimal wavelengths are often needed for samples, but with a broadband source, one can easily switch between wavelengths without making any changes to the setup. This flexibility not only simplifies the process but also makes it cost-efficient. In optical communication the wavelength of light is considered an additional DoF to manipulate and carry information. For example, a *red circle* could represent the letter *A*, while the same circle with a different colour, such as a *blue circle*, could represent the letter *B*, leaving the 'square' shape free to be used as an additional means to carry information. Therefore, by using a broadband source, one is able to increase the bandwidth [68]. Considering the advantages that structured light and broadband light independently offer to these applications, it should be clear why focus has been placed on developing tools and techniques to generate and detect broadband structured light.

Yet, the creation of broadband structured light poses a formidable challenge, given that conventional beam shaping tools are typically tailored for specific wavelengths or, at best, a very limited range. When light of a different wavelength is incident on these optics it is imparted with the incorrect phase and incorrectly modulated. If multiple wavelengths of light are simultaneously incident on the optic one will also observe dispersion of the broadband beam. Hence, when shaping broadband light there are two main challenges: (1) to impart the correct phase and thus modulate all wavelengths in the same manner; (2) overcome the dispersion. Although this has proven to be a challenging task, recent breakthroughs showcase researchers successfully generating broadband structured light. This achievement is made possible by utilising tools and techniques that compensate for any manifestations arising from wavelength-dependence within the setup. For example, according to the work independently presented by Spangenberg *et al.* [65] and Cheng *et al.* [64], when a blazed grating is used, despite the incident beam's wavelength, the +1st order will always have the correct phase, i.e., a broadband beam will be correctly modulated across its entire spectrum at the cost of efficiency. The dispersion caused by the grating can then be compensated for with the use of additional optics, such as a grating, prism or lens. This innovative approach thus enables a singular setup to seamlessly accommodate multiple wavelengths, rendering it not only versatile and cost-effective but also the foundation for novel and exhilarating advancements in the field.

The task is now to choose between physical and digital broadband beam shaping tools. The answer hinges on specific requirements dictated by the intended application. In some cases, the compact, affordable, and user-friendly nature of physical optics is advantageous, particularly in applications like microscopy and industrial manufacturing. Conversely, fast, dynamic generation of multiple broadband structured modes, as demanded by communication systems, may favour the use of digital tools despite their bulkiness. This thesis showcases the capability of both physical optics and digital modulating devices in shaping broadband light. While the subsequent chapters delve into the practical demonstration of this concept, the remainder of this chapter explores structured light and the underlying beam shaping theory employed in its creation.

1.1 The theory of beam shaping

Whether one desires to shape incident light that is incoherent or coherent, monochromatic or broadband, the general concept can be summarised as follows: to transform

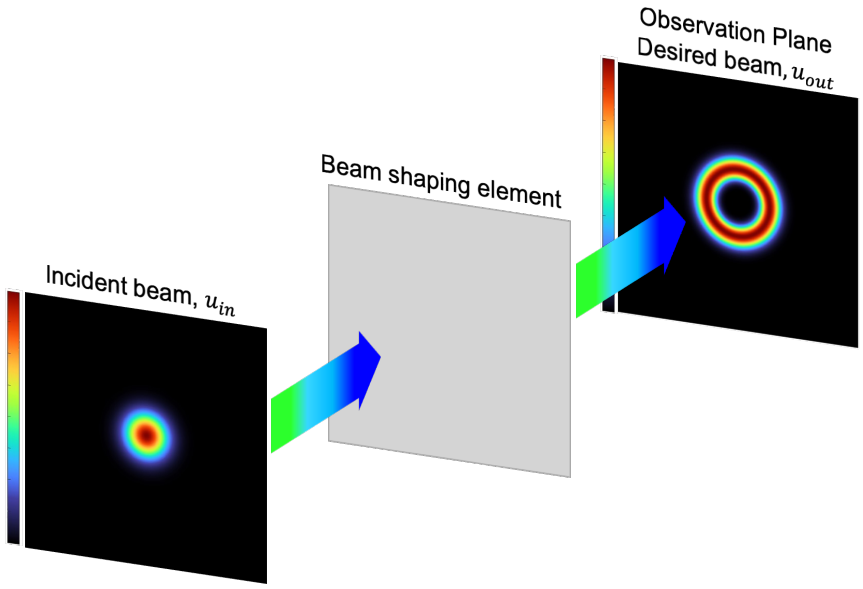


FIGURE 1.1: The general beam shaping system. The source emits an initial beam, u_{in} which is incident on a beam shaping element. The beam shaping element modulates the beam, and at some observation plane located a distance away, the desired output beam, u_{out} is viewed.

an incident beam of light into a desired structured mode at an observation plane, a beam shaping element is needed as depicted in Figure 1.1. When creating structured light from a coherent incident beam, the beam shaping element is designed to manipulate the incident beam's various DoFs, such as its amplitude and phase, in a spatially controlled manner. To successfully shape light one is then left with the task to: (1) determine the transmission function which mathematically describes *how* the beam shaping element should operate, and (2) determine *what* is needed to practically implement it. The remainder of this chapter addresses the first part and establishes a general method to determine *how* the beam shaping element, and system as a whole, should operate, while subsequent chapters focus on *what* is required for its implementation.

1.1.1 Beam types

To establish *how* the beam shaping element should operate, it is essential to first define the structured light pattern, u_{out} intended for generation in the observation plane. Light can be precisely tailored into a multitude of structured patterns, each possessing distinctive properties. While the structured light 'menu' offers a plethora of possibilities, this thesis specifically focuses on four beam types: Hermite-Gaussian (HG), Laguerre-Gaussian (LG), vortex, and flat-top beams [13].

Hermite-Gaussian modes. HG modes are a subset of symmetric solutions of the paraxial wave equation in Cartesian coordinates (x, y, z), and are expressed as

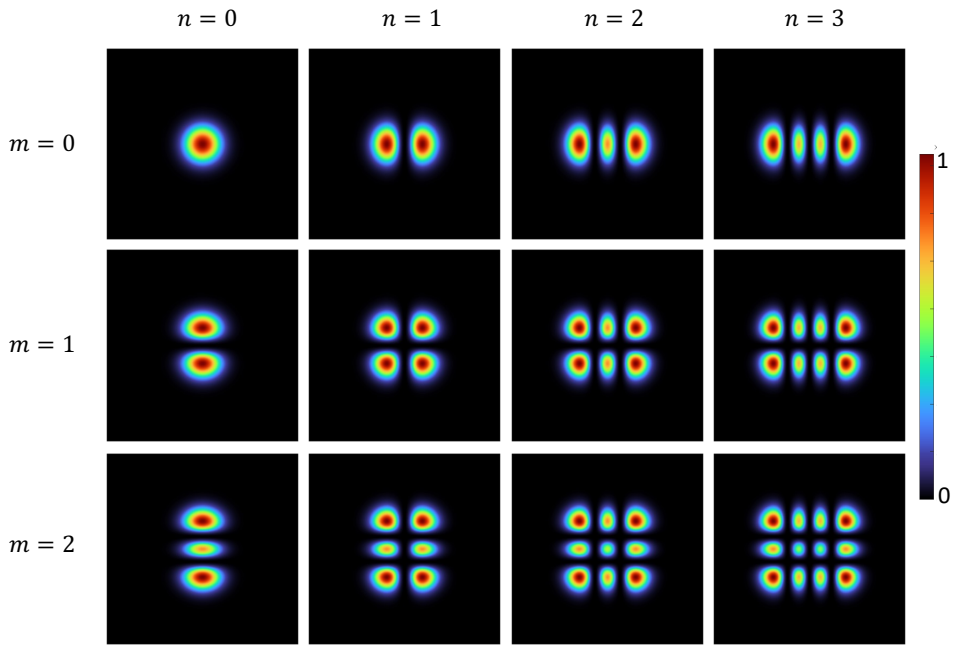


FIGURE 1.2: The simulated intensity profiles of HG beams with indices (n) and (m).

$$\begin{aligned}\mathrm{HG}_n^m(x,y,z) &= \sqrt{\frac{2^{(1-n-m)}}{w(z)^2\pi n!m!}}H_n\left(\frac{\sqrt{x}}{w(z)}\right)\\ &\times H_m\left(\frac{\sqrt{y}}{w(z)}\right)\exp\left[-\left(\frac{r}{w(z)}\right)^2\right]\\ &\times \exp[i(n+m+1)\eta(z)]\exp\left(-\frac{ikr^2}{2R(z)}\right)\exp(-ikz)\end{aligned} \tag{1.1}$$

where n and m are the indices in the x, y directions respectively, $r = \sqrt{x^2+y^2}$ and H_n, H_m are the generalised Hermite polynomials. Examples of the intensity profiles of simulated HG modes for various n, m indices are shown in Figure 1.2.

Laguerre-Gaussian modes. LGs are a subset of symmetric solutions of the paraxial wave equation in cylindrical coordinates (ρ, ϕ, z), and are expressed as

$$\begin{aligned}\mathrm{LG}_p^l(r,\phi,z) &= \sqrt{\frac{2p!}{\pi w^2(z)(p+|l|)!}}L_p^{|l|}\left(\frac{2r^2}{w^2(z)}\right)\\ &\times\left(\frac{\sqrt{2}r}{w(z)}\right)^{|l|}\exp\left[-\left(\frac{r}{w(z)}\right)^2\right]\\ &\times\exp\left[i(2p+|l|+1)\eta(z)\right]\exp\left(-\frac{ikr^2}{2R(z)}\right)\exp(il\phi)\exp(-ikz),\end{aligned} \tag{1.2}$$

where p and l are the radial and azimuthal indices, respectively and $L_p^{|l|}$ is the generalised Laguerre polynomial. Examples of the intensity profiles of simulated LG modes for various l, p indices are shown in Figure 1.3.

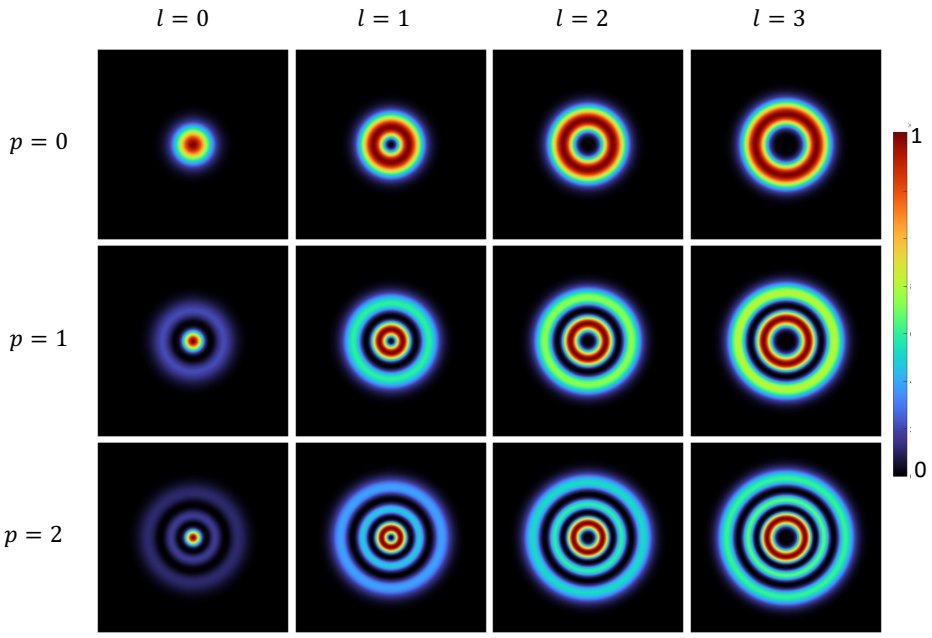


FIGURE 1.3: The intensity profile of a simulated LG beams for various azimuthal (l) and radial (p) indices.

For both HGs and LGs the functional arguments take the form

$$\begin{aligned} w(z) &= w_0\sqrt{1+\frac{z^2}{z_R^2}}, \\ R(z) &= z\left(1+\frac{z_R^2}{z^2}\right), \\ \eta(z) &= \arctan\left(\frac{z}{z_R}\right), \end{aligned}$$

and

$$z_R = \frac{\pi w_0^2}{\lambda},$$

where w_0 is the Gaussian (fundamental mode) radius at its waist plane ($z = 0$) and λ is the wavelength of the light. The functional modes are commonly defined as follows: $w(z)$ is the beam radius; $R(z)$ is the radius of curvature; η is the Guoy phase and z_R is the Rayleigh range.

For both HGs and LGs, these complex modes reduce to the special case of the Gaussian beam when their indices $n = m = 0$ and $p = l = 0$. In this case

$$\mathrm{G}(r,z) = \sqrt{\frac{1}{\pi w^2(z)}}\exp\left(-\frac{r^2}{w^2(z)}\right)\exp\left(i\eta(z)\right)\exp\left(-\frac{ikr^2}{2R(z)}\right)\exp(-ikz). \quad (1.3)$$

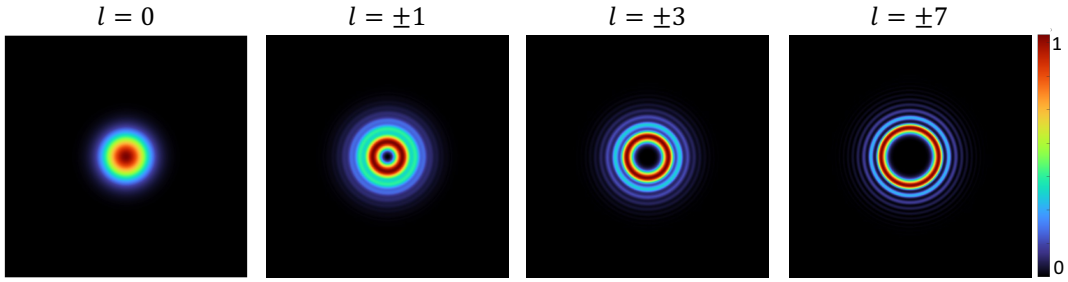


FIGURE 1.4: The intensity profile of a simulated vortex beams for various azimuthal (l) indices.

HG and LG modes are both examples of beams that are considered propagation invariant. This implies that although their beam size may change with propagation they retain their original structure, even when focused through a lens.

Vortex beams. Vortex beams [69, 70] are commonly used to define modes of light that carry orbital angular momentum (OAM) and are identified by the azimuthal phase term $\exp(il\phi)$, where the topological charge, l defines the helicity of the phase, for $l \times 2\pi$ phase twists about the azimuth and $l\hbar$ of OAM per photon. Because the azimuthal phase is undefined at the origin of the axis, this leads to an intensity null in the centre. While the value of l is related to the amount of twists about the axis in the wavefront per unit wavelength, the sign $\pm$ indicates if this twisting is done in an anti/clockwise direction, hence $l \in [-\infty, \infty]$. These modes are therefore referred to as "twisted" light.

In the waist plane, a vortex beam is defined as [71]:

$$\text{Vortex}(r, \phi) = G(r, 0) \exp(il\phi) \tag{1.4}$$

where $G(r, 0) = \exp -(\frac{r}{w(0)})^2$ is a Gaussian envelope (from Equation 1.3, where $z = 0$), r is the radial coordinate, w_0 is the Gaussian beam waist and the term $\exp(-il\phi)$ is an azimuthal phase variation where l is some non-zero integer. If one considers the intensity profile of a vortex beam there will be undesirable rings around the central beam. These higher order radial modes can be removed by manipulating both the phase and amplitude of the incident beam [71], as in the case of LGs. Examples of the intensity profiles of various simulated vortex modes for various l indices are shown in Figure 1.4.

Flat-top beams. Consider the profile of a Gaussian beam. It has a peak intensity towards the centre of the beam, which smoothly decays as one moves towards the edges of the beam. In contrast to this are flat-top beams [9, 72–74] with a uniform intensity distribution over most of the beam and a steep gradient towards its edges. The flat-top beam can therefore be viewed as a Gaussian beam whose top half has been "cut off". Although the profile of an ideal flat-top beam is simple its generation is not as it needs an infinite spatial frequency spectrum. In fact, only approximations to the ideal flat-top can be practically realised. There are several approximations which exist: flattened Gaussian, Fermi-Dirac and super Lorentzian and super-Gaussian. Each approximation is distinguished in the way that uniquely defines its intensity normalisation constant. The super-Gaussian approximation as an example, is defined as

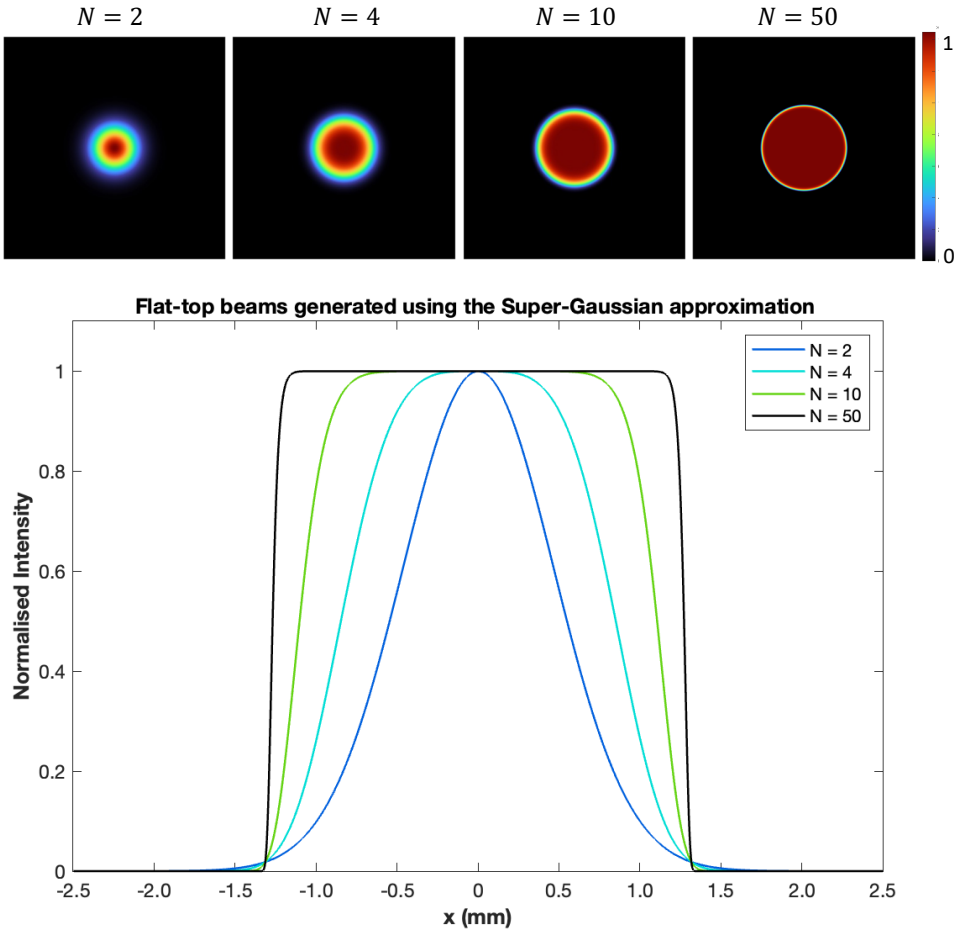


FIGURE 1.5: Examples of intensity and cross-sectional profiles of flat-tops (N = 2, 4, 10 and 50) that were generated using the Super-Gaussian approximation

$$\mathrm{SG}_N(r) = \sqrt{\frac{4^{\frac{1}{N}} N}{2\pi w^2 \Gamma\left(\frac{2}{N}\right)}} \exp\left[-\left(\frac{r}{w}\right)^N\right], \tag{1.5}$$

where Γ is the Gamma function and w is a radial size parameter. The Super-Gaussian order, N, determines both the flatness of the peak and the steepness of the edges, reducing to a Gaussian beam when $N = 2$ and becoming an ideal flat-top beam at large N. These beams are not propagation invariant as they do not have a simple analytical expression that includes z. This implies that they only have the desired flat-top profile in a single plane. Examples of intensity and cross-sectional profiles of flat-tops (N = 2, 4, 10 and 50), that were generated using the Super-Gaussian approximation, are shown in Figure 1.5.

1.1.2 Beam shaping techniques

Now that we have defined the types of beams we would like to generate in the observation plane, assuming that either a Gaussian beam or plane wave will be the incident beam, we have all the information we need to determine the properties of the beam shaping element needed in the system. To do this let us first look at *how*

the beam shaping system could operate.

It is often not fully appreciated that, in principle, lossless and ideal beam shaping can be done with just two phase-only optical elements separated by some distance [75–77]. If instead the shaping is done in a single step then the output is imperfect and/or lossy. One can appreciate this point by considering the simple telescope to resize an optical field: two appropriate lenses (phase-only beam shaping elements) can execute this ideally and in-principle losslessly, while a single lens will correctly resize the beam but at the expense of the phase at the output plane so that the "shaping" is imperfect. Another example is the creation of OAM vortex beams: single step transformations using an azimuthal phase element results in the correct "vortex" phase but leaves the amplitude as a free DoF where many radial modes are excited with low power content in the desired ring of light [71, 78]. This can be overcome and perfect reshaping achieved in one step, but then the process is lossy, requiring amplitude control, as has been done for the creation of radial mode controlled vortex beams [79]. A similar scenario is seen in another common beam shaping problem, the conversion of a Gaussian beam to a flat-top beam subsequently implemented by a variety of means [80–84].

This point is illustrated in Figure 1.6. In Figure 1.6 (a) a vortex beam is created in a single step with the correct amplitude and phase, but in a lossy approach using complex amplitude modulation on a single optical element. If a phase-only single element is used, as in Figure 1.6 (b), then only one DoF can be controlled. Here it is the amplitude structure of a flat-top beam, with the phase left as a free variable. It requires a second phase-only element to correct this unwanted phase, as shown in Figure 1.6 (c). Now the set-up has two phase-only elements separated by some distance, but can in principle execute the desired transformation both ideally and losslessly.

So in general, the beam shaping system can operate in one- or two-step manner. In the case of one-step beam shaping, it can be ideal but lossy if both amplitude and phase are controlled, while two-step beam shaping can be both ideal and lossless with just two phase-only elements. In the context of this thesis the term "lossless" has to be quantified. In practice beam shaping elements cannot be entirely lossless but this is not an issue of the design but rather its implementation. The term is used in the sense that the *design* is lossy or lossless.

Now that we have established *how* the beam shaping system could operate, the task left for us is to determine the transmission function which mathematically describes *how* the beam shaping element should operate.

There are two options available. In Method 1, we apply complex amplitude modulation (CAM), that is, we alter both the amplitude and phase of the incoming beam to tailor it to the desired output, which can be done in a single step with loss. If the incoming beam is $u_{in} = A_{in}\exp(i\varphi_{in})$ and the output beam is $u_{out} = A_{out}\exp(i\varphi_{out})$ then the transmittance function is

$$t = \frac{u_{out}}{u_{in}} = \frac{A_{out}}{A_{in}}\exp(\varphi_{out} - \varphi_{in}), \tag{1.6}$$

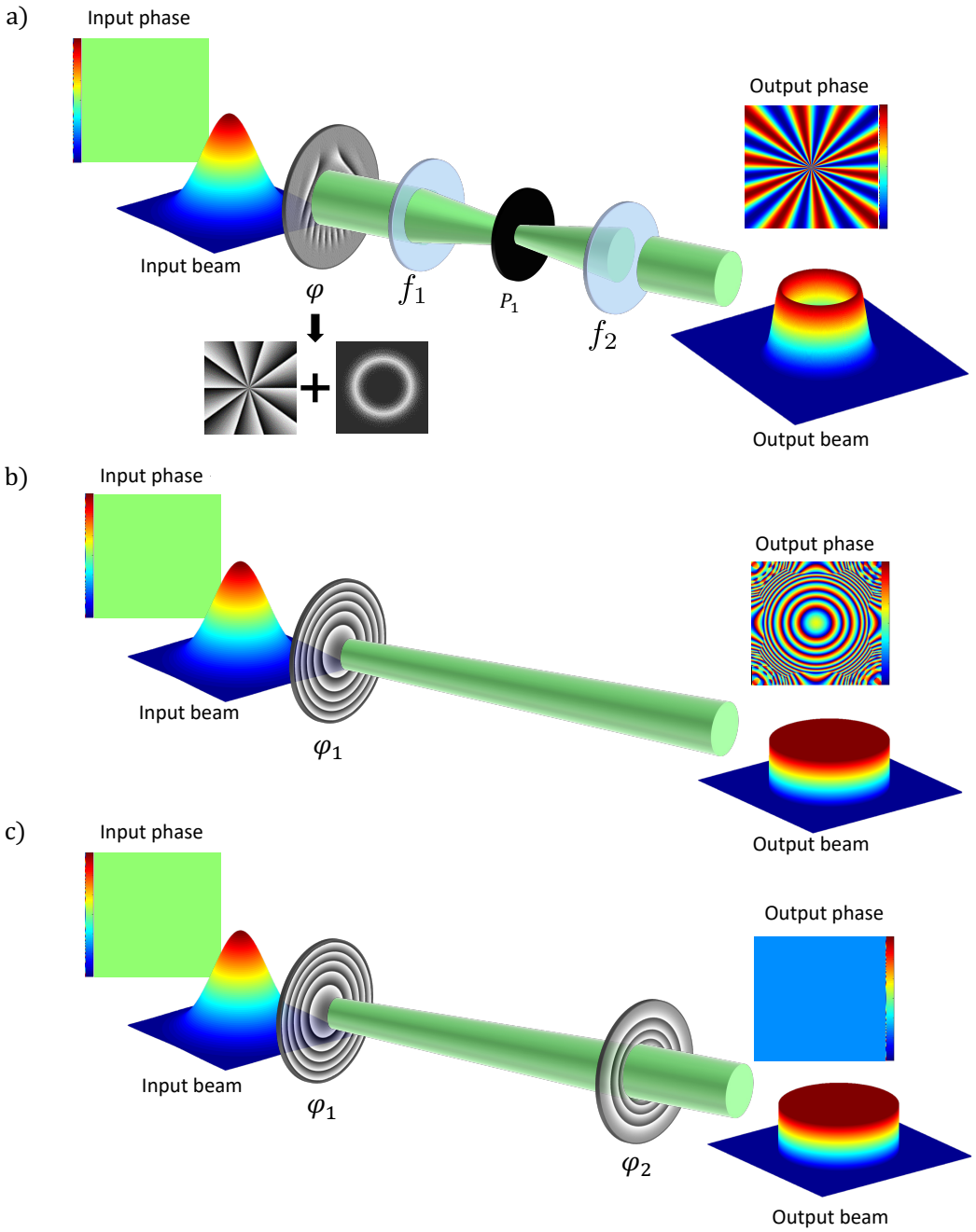


FIGURE 1.6: (a) A Gaussian beam is modulated in amplitude and phase in one step by a complex amplitude hologram (ϕ) to create a vortex beam, (b) a single phase only hologram (ϕ_1) converts a Gaussian beam to a flat-top beam in amplitude but without phase control, and (c) a second phase-only hologram (ϕ_2) can correct the phase to make a two-step ideal and lossless process. Adapted from [14, 85]

with the requirement that the amplitude is normalised such that light is only removed and not created. In many instances it is convenient to have the incident beam be a plane wave so that $u_{in} = 1$ and the beam shaping element is identical to the amplitude and phase of the desired output beam.

In Method 2, two elements are used, both in principle phase-only, so that the execution can be lossless, in principle. The first element redistributes the energy to shape

the desired amplitude, leaving the phase as a free variable, and the second element corrects for the phase. The two elements are separated by some distance to allow the energy redistribution, which is usually a focal distance from a lens incorporated into the first element (the far-field being the farthest that one could propagate).

To derive the phase of the first element, ϕ we need to find a mapping function from the input beam to the output beam that moves energy from a specific spatial region of the input beam to a specific spatial region of the output beam while conserving energy. It is the calculation of this mapping function, α, which lies at the heart of the method. This has been outlined for the arbitrary creation of structured light [86, 87], and here we summarise the key steps. If the input beam is passed through an element with phase ϕ and a lens, and both the input and output beam are energy normalised to 1, then at the focal plane of the lens we have

$$P(X) \propto \int_{-\infty}^{\infty} A_{in}(x) e^{i\phi(x)} e^{-i\frac{2\pi}{\lambda f}Xx} dx. \tag{1.7}$$

Recall that $\alpha(x) \rightarrow X$ since it maps co-ordinates (and energy) from the input to the output plane, so that

$$P(\alpha(x)) \propto \int_{-\infty}^{\infty} A_{in}(x) e^{i\phi(x)} e^{-i\frac{2\pi}{\lambda f}\alpha(x)x} dx. \tag{1.8}$$

By setting $\phi(x) = \frac{2\pi}{\lambda f}\Phi(x)$ and $\gamma = \frac{2\pi}{\lambda f}$ we have that

$$P(\alpha(x)) \propto \int_{-\infty}^{\infty} A_{in}(x) e^{i\gamma[\Phi(x)-\alpha(x)x]} dx. \tag{1.9}$$

Equation 1.9 can be evaluated by the method of stationary phase as

$$P(\alpha(x)) \propto A_{in}(x) e^{i\gamma[\Phi(x)-\alpha(x)x]} e^{i\frac{\pi}{4}} \frac{\sqrt{2\pi}}{\sqrt{\gamma\Phi(x)''}} \tag{1.10}$$

with

$$\frac{d}{dx}\left[\Phi(x) - \alpha(x)x\right] = 0. \tag{1.11}$$

If we have devised ϕ correctly then we have that $|P|^2 \propto |A_{out}(X)|^2$ and so

$$|A_{in}(x)|^2 \frac{2\pi}{\phi''} = |A_{out}(X)|^2 \tag{1.12}$$

$$\frac{|A_{in}(x)|^2}{|A_{out}(\alpha(x))|^2} = \phi''. \tag{1.13}$$

Which can be reduced to solving for $\alpha(x)$ (in 1-dimensional Cartesian coordinates) as

$$\frac{d\alpha(x)}{dx} = \frac{|A_{in}(x)|^2}{|A_{out}(\alpha(x))|^2}. \tag{1.14}$$

This equation describes how energy can be mapped from the input profile to the output profile in a manner consistent with the conservation of energy. The phase $\phi(x)$ can then be easily calculated from the expression for α. The phase is

$$\phi(x) = \gamma \int_0^x \alpha(s) ds. \tag{1.15}$$

Once the first phase element has been designed there are two viable approaches to designing the second phase element: in some approximations (short focal lengths and smooth beams) the second phase element can be well approximated as the complex conjugate of the first shaping element, otherwise the phase of the output beam from the system can be calculated and the second element given an appropriate correction. For example, if the input field is now mapped to an output of $A_{out}\exp(i\theta)$ rather than $A_{out}\exp(i\varphi_{out})$, then the second phase correcting element requires a phase of $\varphi_{out} - \theta$.

What remains is to consider the effects of broadband shaping. Imagine that the desired transmittance function is $t(x) = A(x)\exp(i\varphi(x))$ and that added to this is a blazed grating of the form $\exp(i2\pi x/\lambda_x)$, where λ_x is the grating period in the $x-$direction. One can show that the effect of designing the phase element for wavelength λ_0 but actually operating at wavelength λ is to alter the action of the transmission function to [65]

$$\hat{t}(x) = \sum_{m=-\infty}^{\infty} \mathrm{sinc}[\pi(m - \frac{\lambda}{\lambda_0})]A(x)\exp(im[\varphi(x) + 2\pi x/\lambda_x]). \tag{1.16}$$

We see that in the first diffraction order, $m = 1$, we have the desired field but modulated in amplitude by a constant factor $\zeta = \mathrm{sinc}[\pi(1 - \lambda/\lambda_0)]$. When $\lambda = \lambda_0$ we find that $\zeta = 1$, as expected, decreasing as the difference in wavelength increases. What this means is that the operation of the element will remain intact and wavelength independent except for a decrease in efficiency as the design wavelength is altered. There is however one downside. The angle at which light is diffracted is still wavelength dependent, following the familiar rule for periodic structures of $m\lambda = \lambda_x \sin\theta_m$, where θ_m is the angle of the m-th order. A consequence is that the desired light will be created for all wavelengths, but they will appear to emerge at different angles, thus at different positions in the far-field. This dispersion effect has to be corrected in the experiment by using a compensating element such as a grating or prism [64].

Now that we have established a general method to determine the transmission function of the broadband beam shaping element, i.e., *how* the beam shaping element should operate, the task is now left to determine *what* optical components are needed to implement the beam shaping. This will be the focus for the remainder of the thesis.

1.2 Thesis outline

The focus of this work was to create a system that could shape multiple wavelengths of light either discretely or simultaneously and thus generate broadband structured light, specifically HGs, LGs, vortices and or flat-tops. To do this, the task was broken up into 3 objectives: (1) determine how the broadband beam shaping system (the beam shaping technique) and element should operate, i.e., determine the transmission function. Then, create a broadband beam shaping system that uses (2) a digital or (3) a physical beam shaping element to demonstrate the generation of broadband

structured light through the implementation of the beam shaping techniques discussed.

In Chapter 1 we considered *how* beam shaping systems could operate through CAM and phase-only modulation, and then established general expressions to determine the transmission function of the necessary broadband beam shaping element. With the basis set, the task is now to demonstrate broadband beam shaping using the beam shaping techniques and physical and digital tools.

In Chapter 2 we consider the experimental tools and techniques needed to practically implement broadband beam shaping. The chapter begins by first characterising the broadband laser source as well as lenses, which are instrumental in any optical experiment. The chapter then continues with a discussion and introduction of physical beam shaping optics (refractive and diffractive) and digital beam shaping devices, such as the SLM and DMD. With the foundation laid, all that is left to do is showcase the practical demonstration of broadband beam shaping.

In Chapter 3 we look at using DMDs for broadband beam shaping. We begin by introducing and discussing the operational mechanisms of the DMD. Since the DMD is an amplitude-only device, the chapter continues by first establishing how to create holograms, when encoded on the DMD, are capable of CAM despite the binary manner of the DMD. The chapter then continues with demonstrating how to setup and shape monochromatic light through phase-only and CAM modulation, resulting in flat-top and LG beams for each case respectively. This concept is then extended to broadband beam shaping. Although there are dispersion effects, solutions are investigated for both the phase-only and CAM cases to compensate this.

In Chapter 4 the objective is to showcase the practical demonstration of broadband beam shaping with a physical optic. To do this, we resort to 3-D printing as a fabrication method. Due to the properties of the printing material, the printed optic is only able to impart phase changes into an incident beam. Therefore we could use the same encoding technique to create CGHs (usually intended for the SLM) which serve as a design for the optic. The chapter begins therefore with a brief summary of the encoding scheme, followed by a discussion of how the optics were fabricated. Next, an analysis is done to determine the quality of the printed optics. Finally the chapter concludes with a demonstration of how the optics can be used to shape broadband light through phase-only modulation and CAM and thus generate vortex and HG modes, respectively.

Chapter 5 then offers a conclusion and glance of future work that this could be applicable for.

Chapter 2

Experimental tools for broadband beam shaping

To experimentally do broadband beam shaping the general problem mentioned in Chapter 1 and shown in Figure 1.1 is now altered, as seen in Figure 2.1: a source (labelled 1) emits a broadband beam which is expanded and collimated or imaged using two lenses (labelled 2). The incident beam, u_{in} is then shaped by some beam shaping element (labelled 3), which can be physical or a computer generated hologram (CGH) that is displayed on a digital device. The structured beam is then Fourier transformed using a single lens (labelled 4) or imaged using two lenses (labelled 5). In the observation plane the output beam, u_{out} will have the desired structure and properties.

In this thesis we use or mention the following experimental tools: the argon-ion laser which serves as the broadband source (labelled 1), achromatic and conventional lenses (labelled 2, 4 and 5) and beam shaping devices (labelled 3) which include liquid crystal on silicon spatial light modulators (LCoS-SLMs) and digital micro-mirror devices (DMDs). The focus of this chapter is therefore to introduce and discuss the operating mechanism of these experimental tools.

2.1 Broadband source: argon-ion laser

The first experimental tool needed to shape broadband light is a coherent broadband source (labelled 1 in Figure 2.1). In this thesis we use a Stellar-Pro-L Select 300 argon-ion laser that was manufactured by Laser Physics [88]. This particular laser emits the following discrete wavelengths which can be independently selected as needed: 457 nm, 488 nm, 514 nm as well as a multiline - a single beam which is comprised of all three discrete wavelengths.

2.1.1 Laser properties

Before using laser as the broadband source in our beam shaping system, we must ensure that we know all its properties, namely: (1) the beam profile, (2) size and (3) angles of propagation for each emitted wavelength and the multiline.

Beam profile. The first property of the laser we will consider is the beam profile. It is important to know the beam profile of the incident beam (in this case the beam emitted by the laser) in any beam shaping system so that one can correctly modulate it to generate the desired structured mode at some observation plane. Based on the information provided by the manufacturer, the emitted beam should have a Gaussian

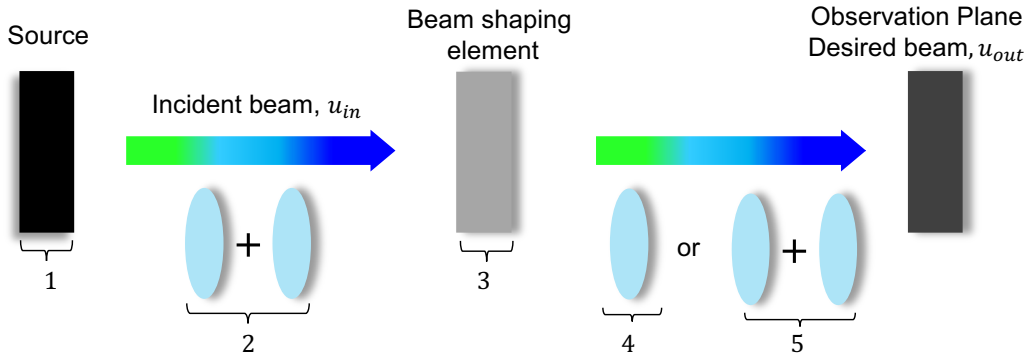


FIGURE 2.1: A depiction of the general broadband beam shaping problem from a experimental point-of-view. A source (labelled 1) emits a broadband beam which is expanded and collimated or imaged using two lenses (labelled 2). The incident beam, u_{in} is then shaped by some beam shaping element (labelled 3), which can be physical or a computer generated hologram (CGH) that is displayed on a digital device. The structured beam is then Fourier transformed using a single lens (labelled 4) or imaged using two lenses (labelled 5). In the observation plane the output beam, u_{out} will have the desired structure and properties.

profile [88]. However, due to misalignments or other imperfections within the laser cavity that arise from degradation with time, the emitted beam may be distorted, hence it is important to check the purity of the emitted beam for each wavelength.

To determine this we used the experimental setup seen in Figure 2.2 a) which consisted of two mirrors m_1, m_2 (to redirect and align the beam) and a charged coupled device (CCD) camera that was fixed at some arbitrary distance z = 0.725 m after the laser. The setup was aligned for λ = 488 nm, and this alignment was maintained throughout the experiment even when a different incident wavelength was selected. Images of the beams for each discrete wavelength and the multiline were captured. An example of the captured colour images are shown in Figure 2.2 b).

Using the captured image we determined the beam profile by taking a horizontal cross-section at some z plane of and plotting it as seen in Figure 2.2 c) for λ = 488 nm. To test the purity of the emitted beam, i.e., its likeliness to a Gaussian mode, we fit the experimental data to a Gaussian curve

$$I = I_0 \exp\left(\frac{-2(x - x_0)^2}{w(z)^2}\right), \tag{2.1}$$

where I is the intensity, $w(z)$ is the beam size at $1/e^2$ ($\approx$ 13.5%) of the maximum intensity (as seen in Figure 2.2 c)), x_0 is the distance the beam was shifted off-axis in the x- direction, I_0 is the peak intensity at the centre of the beam where $I_0 = 2P/\pi w(z)^2$ and P is the power of the incident beam. Across each of the various wavelengths, the Gaussian curve fit the experimental data with an average R^2 value of 0.999 and a root-mean-square error (RMSE) of 0.009. The closer the R^2 value is to 1, and the RMSE value is to 0, the better the fitted curve represents the experimental data and predicts future values. Hence, the fitted Gaussian curves have an excellent correlation to the experimental data and thus confirms that across the various wavelengths the laser does in fact emit highly pure Gaussian beams.

TABLE 2.1: Derived minimum beam sizes , w_0 per wavelength for the argon-ion laser.

Wavelength	w_0 **(mm)** $\pm$ **0.054 mm**
457 nm	0.408
488 nm	0.448
514 nm	0.425
Multiline	0.421

Now that we know the emitted beams are Gaussian we can use the fitting parameters to determine the properties of the emitted beams such as the beam size, $w(z)$ and off-axis shift, x_0 at various observation planes after the laser.

Beam size. Although we have an experimental method to determine the beam size at the observation plane, it would be tedious to do this every time we needed to know the beam size of a certain wavelength. Hence, we need a general expression that can output the desired beam size given the propagation distance, z from the laser and incident wavelength λ. This can be determined using the following expression

$$w(z) = w_0\sqrt{1+\left(\frac{z\lambda}{\pi w_0^2}\right)^2}, \tag{2.2}$$

where $w(z)$ is the beam size at some observation plane located a distance z away, λ is the wavelength of the incident beam and w_0 is the beam size at the beam waist (z =0) which we will assume is located at the opening of the laser. The only issue with using this equation is that w_0 is unknown for each wavelength. Hence, if we determine this parameter, we have a general expression per wavelength that allows us to know the beam size at any distance after the laser (assuming free space propagation).

To determine w_0 we use the setup seen in Figure 2.3 a). This is the exact setup used before in Figure 2.2 a). However the CCD camera is now mounted on a rail so that it can be moved to various observation planes after the laser while still maintaining the alignment (which was done using to λ = 488 nm). Using the same procedure as before, we can take the horizontal cross-section of each beam's intensity profile, fit it to a Gaussian curve and use the fitting parameters to obtain the beam sizes of each wavelength at various propagation distances.

Using the obtained information, one can plot the beam size versus propagation distance as seen in Figure 2.3 b). The experimental data was fitted against Equation 2.2 where w_0 was considered an unknown parameter. For the multiline, however, λ was considered an unknown parameter. On average the fitted curves matched the experimental data with an R^2 value = 0.951 and RMSE = 0.012, indicating a good correlation. Therefore, using the fitting parameters we could determine w_0 for each beam. The results are summarised in Table 2.1. The average $w_{0,ave}$ = 0.426 $\pm$ 0.054 mm matches the expected value $w_{0,ave}$ = 0.375 mm provided by the manufacturer. By substituting these values into Equation 2.2, one now has a general expression for each emitted beam that will output the beam size at any propagation distance from the laser.

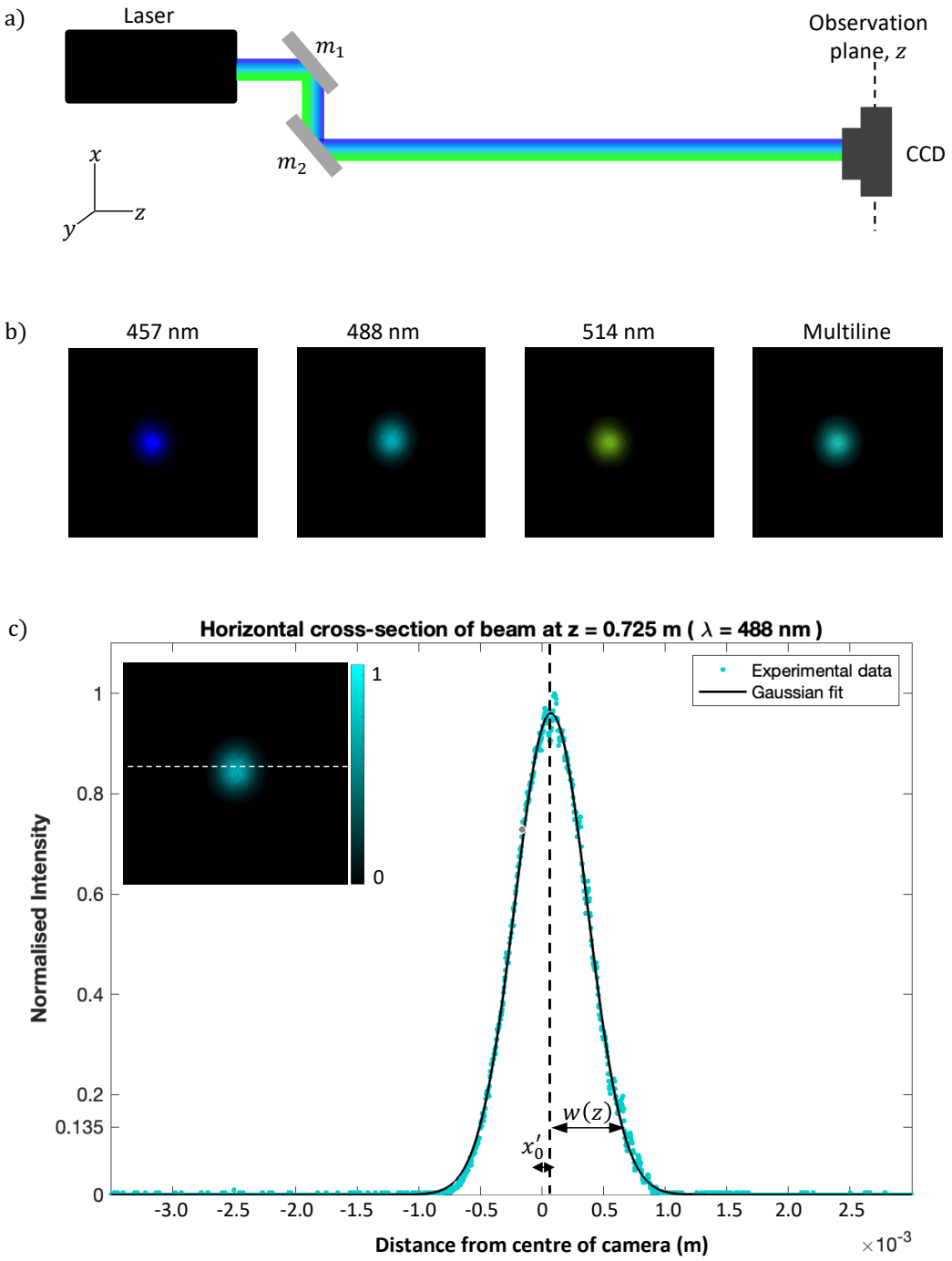


FIGURE 2.2: The process to determine the beam profile of each discrete wavelength and the multiline emitted of the argon-ion laser. a) The experimental setup consists of the source, mirrors m_1 and m_2 which are used for alignment, and a charged coupled device (CCD) camera which is placed at some observation plane located a distance z away from the source. The setup was aligned using λ = 488 nm. b) Colour images of the beams for each discrete wavelength and the multiline when the CCD camera was fixed at $z = 0.725$ m. c) A horizontal cross-section of the beam's intensity profile (insert) along the dashed line is taken, normalised and plotted for λ = 488 nm. A Gaussian curve is then fit to the experimental data. The fitted curve fit the data with an R^2 value of 0.9984 and a root-mean-square error (RMSE) of 0.0096, which indicates a that the emitted beam has an excellent likeness to a Gaussian beam. This was repeated for the other discrete wavelengths and the multiline (not shown), and similar results were obtained.

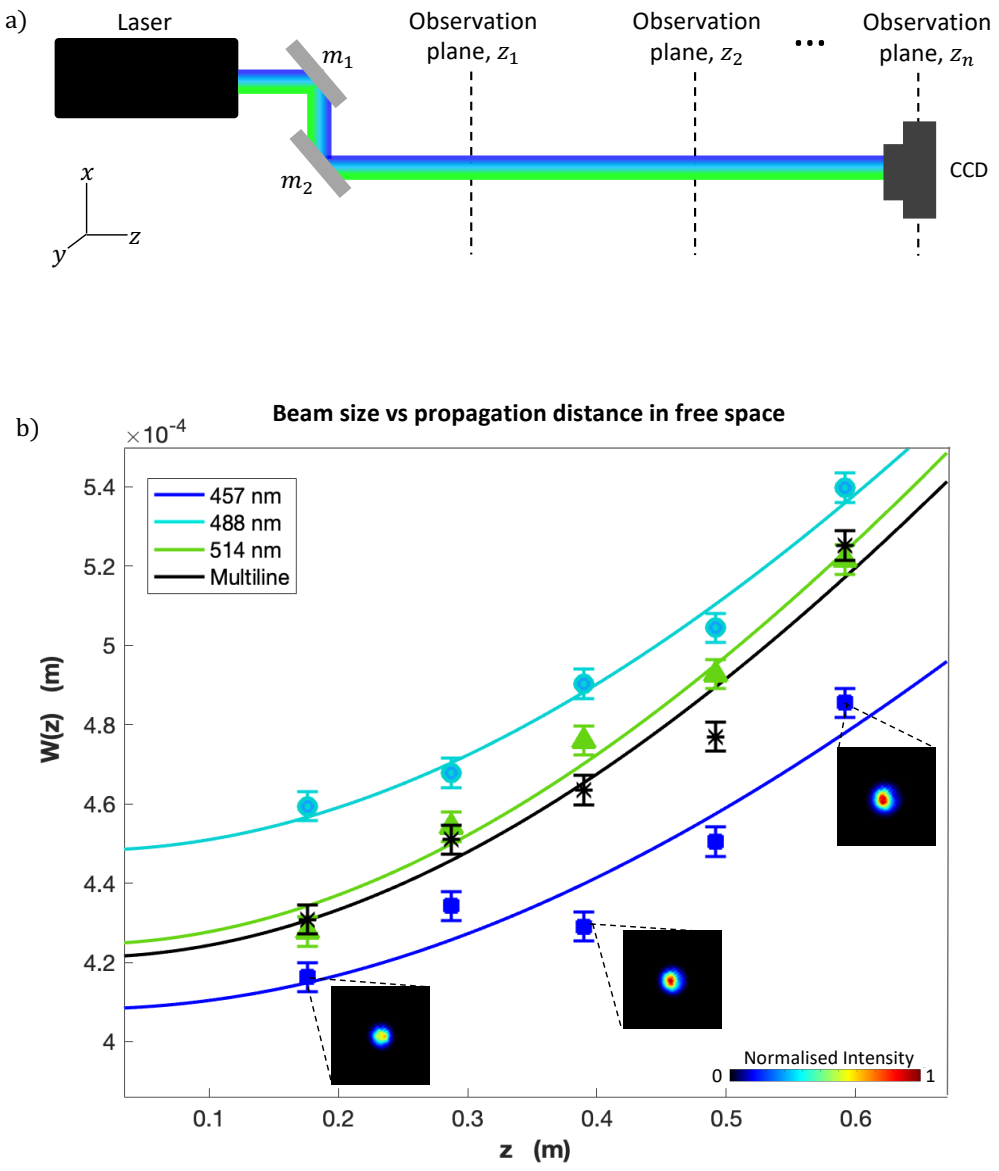


FIGURE 2.3: Determining the beam size at the beam waist, w_0 per wavelength. a) The setup is identical to that used before in Figure 2.2 however, the measurements are taken at multiple observation planes located a distance $z_1 \rightarrow z_n$ after the laser. Using the same Gaussian fitting procedure as before we can retrieve the beam size propagation distances per wavelength. Plotting the beam size, $w(z)$ against the respective propagation distance, z and fitting this data to Equation2.2, we end up with b). From the fitting parameters we can then determine w_0 for each wavelength. The inserts show the normalised intensity profiles for λ = 457 nm at selected propagation distances.

TABLE 2.2: Angle of deviation, θ (relative to λ = 488 nm) per wavelength for each emitted beam from the argon-ion laser.

Wavelength	θ **(mrad)** $\pm$ **0.001 mrad**
457 nm	0.371
488 nm	-
514 nm	0.377
Multilline	0.317

Beam shift and angle of propagation. The next property of the laser to consider is the angle that the emitted beams (per wavelength) propagate with respect to each other. Ideally the beams should travel co-linearly, but if this is not true it will have an effect on the alignment, for example, and must be taken into account.

To determine the beam shift we used the same setup as depicted in Figure 2.3 a), aligned the setup using the reference wavelength (λ_0 = 488 nm) and repeated the same process of capturing images of the emitted beam (per wavelength) at different propagation distances. By plotting the horizontal cross-section of the intensity image and fitting it to a Gaussian curve we can obtain the beam's off-axis shift, x_0 relative to centre of the camera (in the $x-$direction) at various propagation distances after the laser. This process was repeated for each wavelength.

Figures 2.4 a), b) depicts the (absolute) off-axis shift relative to the centre of the camera for the reference beam and non-reference beam, respectively. If the setup was aligned with a high accuracy the centre of the reference beam would align perfectly with the centre of the camera. However, due to a slight misalignment the reference beam did not lie perfectly on the camera's central axis. This was taken into account by calculating the relative beam shift, $\Delta x = x_0 - x_0'$, where x_0' is the off-axis shift for λ_0 (refer to Figure 2.2 c)). Plotting the absolute relative beam shift, $|\Delta x|$ versus the propagation distance for each wavelength resulted in Figure 2.4 b). Because we expect the beam shift and propagation distance to have a linear relationship the data was fitted to a linear curve. On average the fitted curves had an R^2 value = 0.966 and RMSE 0.009, indicating a good match to the data.

Using the fitting parameters we could thus determine the angle, θ that each wavelength diverges from λ = 488 nm. This can be determined using the following expression: $\theta = \arctan(x_0/z)$, where x_0 and z are the beam shift and propagation distance, respectively. However because $\theta \approx 0$, $\theta \approx (x_0/z) = m$, where m is the gradient of the linear curve. The results are summarised in Table 2.2, where the average divergence θ_{ave} = 0.356 mrad $\pm$ 0.001 mrad. Considering that most CCD cameras have a resolution of $\approx 1000 \times 1000$ and a pixel size ≈ 3.6 μm, this implies that for every meter the beams propagate they will be shifted by ≈ 10 pixels. Not taking into account the beam size, if we keep the total propagation distance from the source to the observation plane in our system under 50 m, we will be able to observe the beam even if the system was not aligned for that wavelength.

Now that we know the important parameters of the system in free space, let us consider what happens when we add optics into the system.

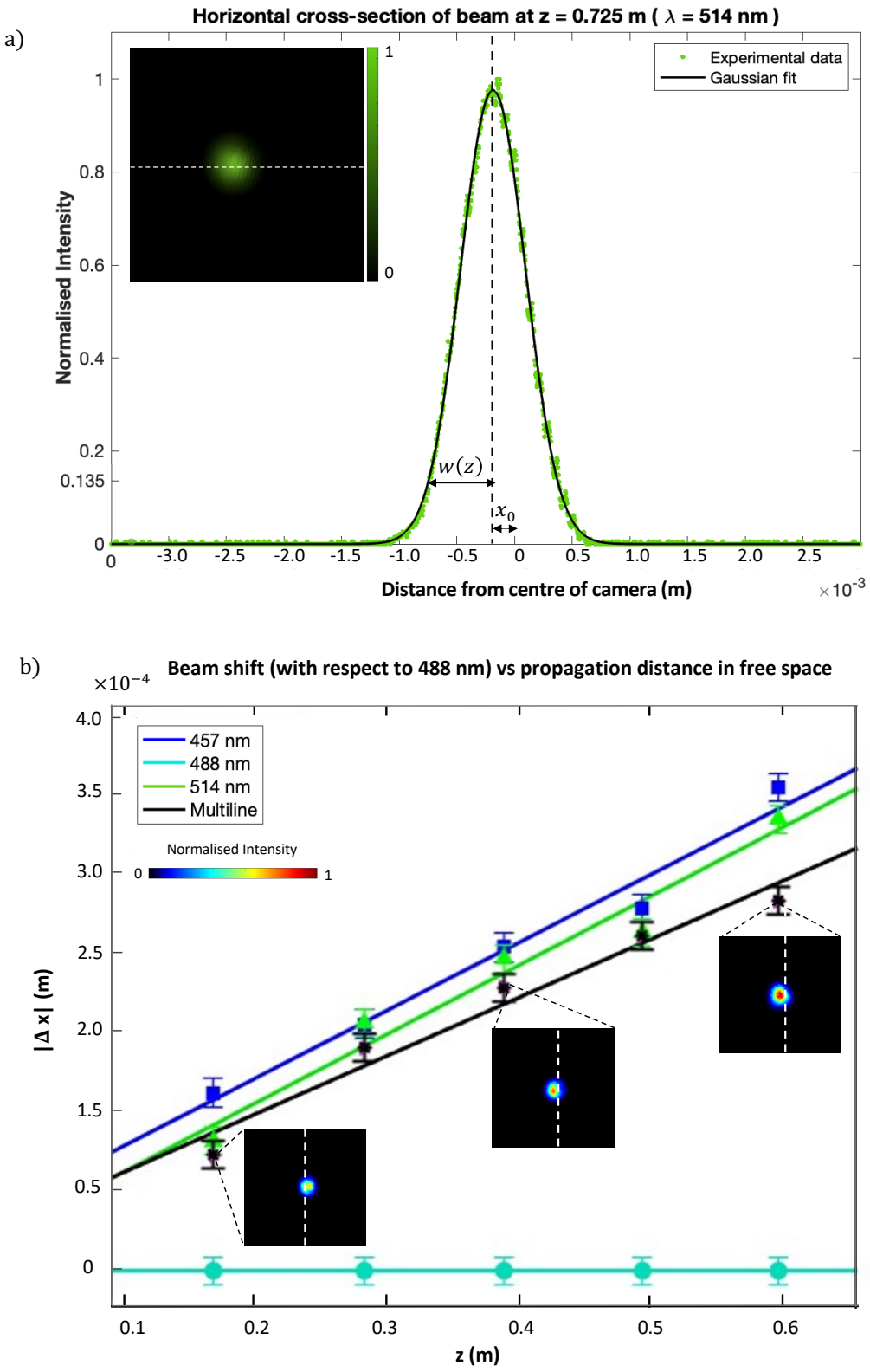


FIGURE 2.4: Determining the relative off-axis shift in the $x-$direction per wavelength. Using the same procedure as before, a) we can plot the cross section of the beam, fit it to a Gaussian curve and determine the off-axis shift, x_0 in the $x-$ direction with respect to the camera's axis. We then calculate the absolute off-axis shift relative to the reference beam λ = 488 nm. If we plot $|\Delta x|$ against the propagation distance z, and fitting it to a linear curve the result is the following diagram. The inserts show normalised intensity profiles of the multiline beam at selected propagation distances with the dashed line indicating the camera's vertical axis.

2.2 Lenses

The first optic we will add to the setup are lenses. Consider Figure 2.1. Lenses are used before the beam shaping element to image or expand-and-collimate the incident beam (labelled 2), or they are used after the beam shaping element to Fourier transform or image the outgoing beam (labelled 4 and 5, respectively).

To image the initial beam the lenses are arranged so that they are separated by a distance equal to the sum of their focal lengths as seen in Figure 2.5 a). In this way they form a $4f$-telescopic system that relays the beam at the initial plane to the image plane. The beam in the image plane will have the same phase as the beam in the initial plane, except it will be magnified by a factor $M = (-f_2/f_1)$ where f_1, f_2 are the focal lengths of lenses l_1 and l_2, respectively. A $4f$-imaging system can also be created using a single lens as seen in Figure 2.5 b). In this case the phase of the initial beam is not relayed, and the beam cannot be magnified. Hence this configuration must be used with caution.

When the beam shaping system requires a large incident beam with a uniform intensity distribution and phase, as in the case of complex-amplitude modulation, an expansion-collimation system is added prior to the beam shaping system. The system is comprised of two lenses separated by a distance equal to the sum of their focal lengths, where the beam is magnified by $M = (-f_2/f_1)$ where f_1, f_2 are the focal lengths of lenses l_1 and l_2, respectively. To expand the incident beam, the first lens must have a shorter focal length than the second lens. The first lens focuses the beam, while the second collimates the beam as seen in Figure 2.5 c).

Now that we know the different ways we could arrange the lenses in an experimental setup, let us look at the different types of lenses we could use, namely conventional and achromatic lenses.

Conventional lenses. In this thesis, we will refer to 'conventional lenses' which are plano-convex refractive lenses made of N-BK7 glass. Lenses can have various coatings which filter certain wavelengths of light. However, we will use uncoated lenses from ThorLabs which are designed for λ_0 = 587.6 nm and can be used for wavelengths within the 350 nm - 2000 nm range [89].

The focal length of a conventional lens can be calculated as follows:

$$\frac{1}{f} = (n-1)\left(\frac{1}{R_1} - \frac{1}{R_2}\right), \tag{2.3}$$

where f is the focal length, R_1 and R_2 are the radius of curvature of the first and second surfaces of the lens and n is the refractive index. For plano-convex lenses the second surface of the lens is flat. Equation 2.3 is thus simplified to

$$f = \left(\frac{R_1}{n-1}\right). \tag{2.4}$$

The refractive index is given as $n = c/\lambda v$ where c is the speed of light, λ is the wavelength and v is the frequency of the incident light. Because the refractive index is wavelength dependent conventional lenses will focus the beam at a different plane depending on the incident beam's wavelength i.e., it has a different focal length, as

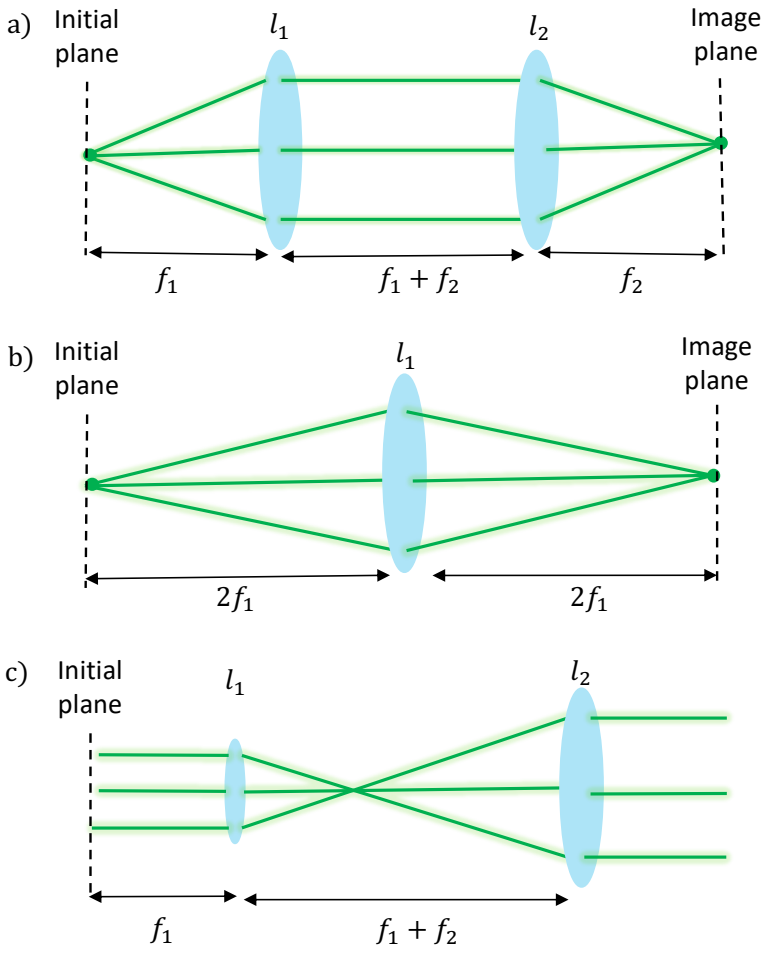


FIGURE 2.5: The different lens arrangements. a) Two lenses, l_1 (f_1) and l_2 (f_2) are separated by a distance equal to $f_1 + f_2$. Together they form an imaging system that relays the beam in the initial plane to the image plane. The phase is maintained and the beam size is magnified by a factor $M = f_2/f_1$. b) A single lens l_1 (f_1) forms an imaging system by relaying the beam located $2f$ before the lens, to the image plane $2f$ after the lens. The beam size is maintained but the phase is not. c) Two lenses l_1 (f_1) and l_2 (f_2), where $f_1 < f_2$, expand and collimate the incident beam when they are placed a distance $f_1 + f_2$ apart.

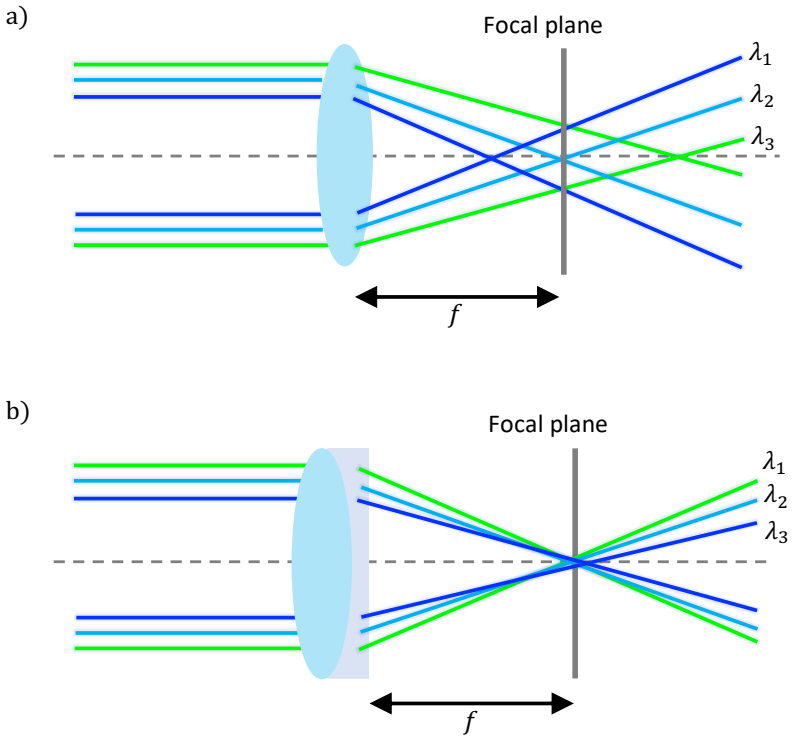


FIGURE 2.6: How lenses focus light depending on their wavelength ($\lambda_1 < \lambda_2, \lambda_3$). a) Conventional lenses focus the design wavelength, λ_2 at the focal plane. b) Achromatic lenses focuses all the wavelengths at the focal plane.

illustrated in Figure 2.6 a). This is commonly referred to as chromatic aberration and usually leads to leads to a distortion of an incident broadband beam.

To use Equation 2.4 we must determine refractive index with respect to the wavelength of the incident beam. This is done using the Sellmeier equation, which is a mathematical formula used in optics to model how the refractive index of a material changes with the wavelength of light. The Sellmeier equation is often expressed in the form:

$$n^2(\lambda) = 1 + \frac{B_1\,\lambda^2}{\lambda^2 - C_1} + \frac{B_2\,\lambda^2}{\lambda^2 - C_2} + \frac{B_3\,\lambda^2}{\lambda^2 - C_3} \tag{2.5}$$

where n is the refractive index, λ is the wavelength of the incident light, B_1, B_2, B_3 are the coefficients related to the material's properties and C_1, C_2, C_3 are the coefficients related to the wavelengths of absorption. The coefficients are all experimentally determined and dependent on the material.

For NBK-7 glass the Sellmeire equation becomes [89]:

$$n^2(\lambda) = 1 + \frac{1.03961212\,\lambda^2}{\lambda^2 - 0.00600069867} + \frac{0.231792344\,\lambda^2}{\lambda^2 - 0.0200179144} + \frac{1.01046945\,\lambda^2}{\lambda^2 - 103.560653}, \tag{2.6}$$

and can be visualised as seen in Figure 2.7. From Equation 2.6, the refractive indices of the lens for the various wavelengths are summarised in Table 2.3. As an example, consider a ThorLabs lens with f = 199.3 mm (λ = 488 nm) and R_1 = 103.3 mm. The focal length for the various beams emitted by the argon-ion laser can be determined

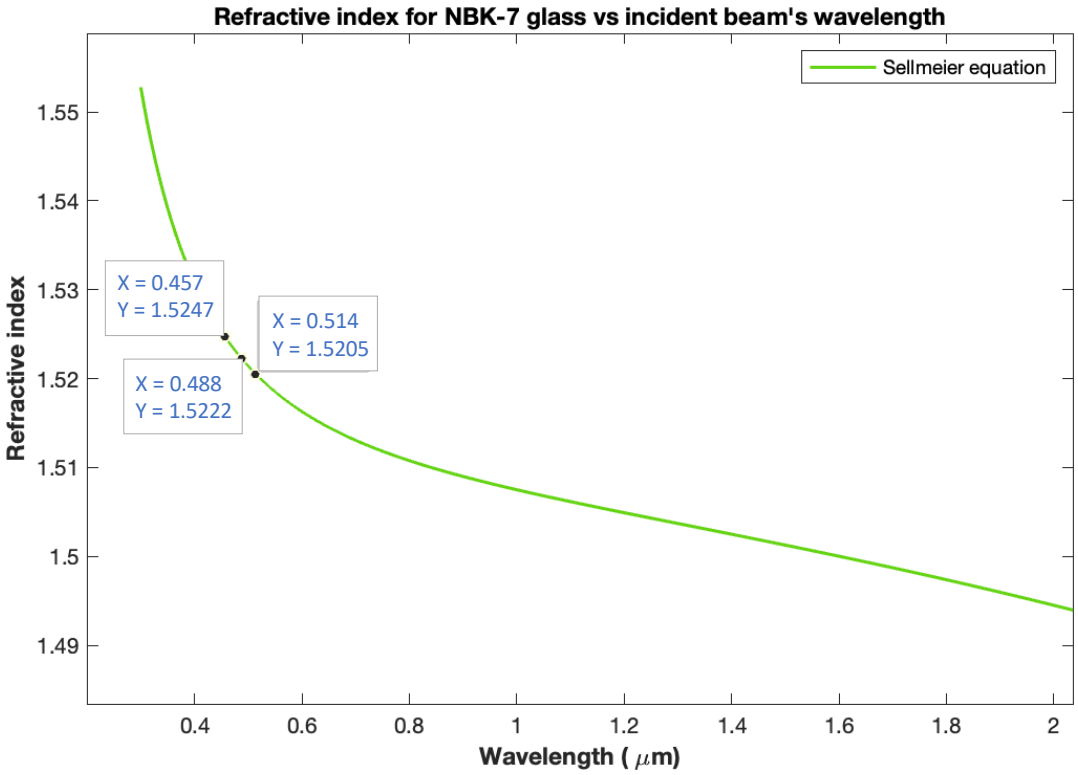


FIGURE 2.7: The Sellmeier equation depicting the relationship between the refractive index and wavelength of the incident beam for NBK-7 glass.

by substituting the respective refractive indices into Equation 2.4. The results are summarised in Table 2.3. The multiline consists of multiple discrete wavelengths. Every discrete wavelength in the multiline will be focused at different planes, hence the multiline will have multiple focal lengths.

Achromatic lenses. To limit the effects of chromatic aberration achromatic lenses were invented, and are typically designed to focus two wavelengths (typically red and blue) or three wavelengths (typically red, green and blue) to a single plane, as seen in Figure 2.6 b). Achromatic lenses will also focus wavelengths that lie within the range of the design wavelengths to the same focal plane. Achromatic lenses, are made of two individual lenses that are usually cemented together. One lens is made from flint glass and has a concave shape. It is therefore highly dispersive. The other lens is made of crown glass, has a convex shape and is less dispersive. When mounted together, the dispersion of the one is counterbalanced by the other. However, they are designed in such a way that the positive focusing power is not completely cancelled out, and ultimately the achromatic lens will act as a weak positive lens that can focus multiple wavelengths. The achromatic lenses used in this thesis [90] were designed for λ_0 = 486.1 nm (blue), 587.6 nm (green) and 656.3 nm (red), and can be used for any wavelength within the range of 400 - 700 nm.

Because the achromatic lens is made of two different materials, we cannot use Equation 2.4 to calculate the focal length of the lens in the same manner that we did for the conventional lens. We must therefore experimentally determine the focal length of the lens, i.e., the effective focal length. Assuming that the incident beam is Gaussian and does not rapidly diverge (has a divergence angle, $\Theta < 1$ rad), the effective

TABLE 2.3: The refractive index and focal length of a conventional lens (f = 199.3 mm for λ_0 = 488 nm).

Wavelength (nm)	**Refractive index**	**Focal length (m)**	**Effective focal length (m) ± 0.001 m**
457	1.5247	0.1969	0.205
488	1.5222	0.1978	0.208
514	1.5205	0.1985	0.211
Multiline	-	0.1981	0.195

focal length can be determined using the following formula

$$f = \frac{w\, w_0' \, \pi}{\lambda} \tag{2.7}$$

where λ is the wavelength of the incident beam, w is the size of the incident Gaussian beam and w_0' is the size of the beam at the beam waist after the lens as shown in Figure 2.8 a). For Equation 2.7 to be valid: (1) $\lambda << w$ for the paraxial approximation to hold, (2) $w_0' < w$. According to the manufacturer the emitted beams have Θ = 0.95 mrad and we have confirmed that the beams have a Gaussian profile [88]. Therefore without collimating the emitted beam we can use Equation 2.7 to determine the focal length of the lens.

However, to use Equation 2.7 we must know: (1) the incident beam's size at the plane of the lens, w and (2) the beam size at the beam waist after the lens, w_0'. We can determine w by Equation 2.2 and substituting in the propagation distance z = 500 mm and the determined minimum beam size w_0 values. As expected, the beam size varied by a negligible amount, and thus has the same values as w_0 - confirming that our 'collimated beam approximation' is valid. However, w_0' is unknown. This can be determined experimentally by measuring the beam size at various planes after the lens. Then, using Equation 2.2 we can determine w_0'.

The experimental setup was built as seen in Figure 2.8 b). Here, the setup is similar to that used in Figure 2.2 with the addition of an achromatic lens, l_1 with a focal length of f = 200 mm. The setup was aligned using λ = 488 nm. The CCD camera was placed at a certain distance, z_1 after the lens and a picture of the beam for each wavelength was captured. This was then repeated at various distances from the lens. Experimental images for λ = 488 nm are shown as inserts in Figure 2.8 c). Using the same procedure as before, we could determine the beam size for each wavelength at each observation plane. Plotting the beam size against the propagation distance and fitting it to Equation 2.2 resulted in the plot seen in Figure 2.8 c) and allowed us to determine w_0'. By substituting these values into Equation 2.7, we were able to determine the focal lengths per wavelength for an achromatic lens where the design focal length, f = 200 mm. To calculate the focal length of the multiline we required the value of the wavelength. So, we assumed that all the beams would be emitted at an equal intensity and thus approximated the wavelength of the multiline as the average of all the wavelengths, λ_{av} = 498 mm. The results are summarised in Table 2.4. For comparison the same experimental procedure was repeated for a conventional lens with a design focal length, f = 199.3 mm. The results are summarised in Table 2.4.

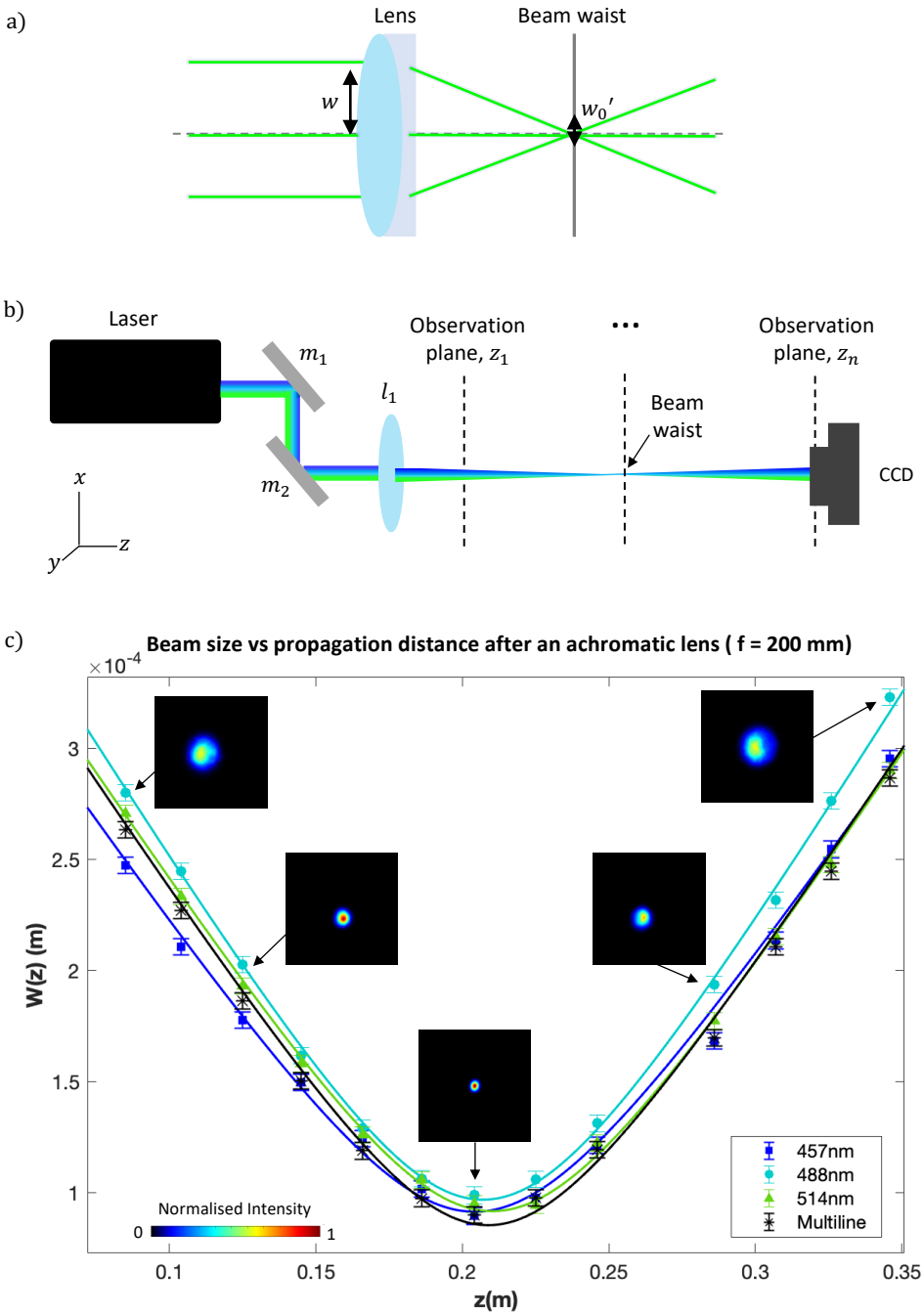


FIGURE 2.8: Determining the focal length of an achromatic lens experimentally. a) To calculate the focal length we must first determine the beam size of the incident Gaussian, w and the beam size at the beam waist after the lens, w_0'. To determine w_0' the experimental setup consisted of a source that is redirected by two mirrors m_1, m_2 through a lens. A CCD camera took images of the beam at various observation planes after the lens, l_1 (f = 200 mm). First an achromatic lens was used, then the process was repeated with a conventional lens. b) A plot of the beam size with respect to the propagation distance after the lens and fitting the data to Equation 2.2 allows one to determine the minimum beam size, w_0' and thus the focal length. Although the plot shown here is for only the achromatic lens, a similar plot was obtained for the conventional lens. Experimental images of the beam (λ= 488 nm) at various planes are shown as inserts.

TABLE 2.4: The experimental values of the beam size before the lens, w and beam size at the beam waist w_0' and effective focal length of an achromatic lens (f = 200 mm) per wavelength.

Wavelength (nm)	w **(mm)** $\pm$ **0.5 mm**	w_0' **(mm)** $\pm$ **0.5 mm**	**Effective focal length (m)** $\pm$ **0.001 m**
457	0.408	0.786	0.223
488	0.448	0.765	0.224
514	0.425	0.856	0.225
Multiline	0.421	0.806	0.217

Consider the results from Tables 2.3 and 2.4 for both the conventional and achromatic lenses, respectively. If we only consider the results of the discrete wavelengths, we see that in both cases the general trend is as follows: as the wavelength increases so does the focal length. For the conventional lens we notice that the shift in the focal length is between 2 - 3 mm. If we account for the experimental error which arises from the measurement of the distance, z when determining the beam sizes, the shift in the focal length is quite small and may even be considered negligible in some applications. For the achromatic lens the focal length shift is approximately 1 mm — the same value as the associated experimental error. This implies that indeed the achromatic lens does focus the various wavelengths to the same focal plane and is more suitable for broadband beam shaping. Now let us consider the results for the multiline. It is clear that in both cases the obtained results do not follow the general trend and are in fact an outlier. We can consider the values of the beam size to be reliable as the method used to determine it produced good results when used for the discrete wavelengths. This implies that the error must lie in the way we determined the focal length, in particular the approximation used where we assumed that all discrete wavelengths that make-up the multiline have equal intensities and the multiline's wavelength is the average of all the discrete wavelengths. Based on the results, the true value of the multiline's wavelength must be smaller than the average value to match the general trend. To truly characterise the multiline, one should measure the intensity of each discrete wavelength. This will give the weighting/contribution of each discrete wavelength to the multiline. One can then confirm the value of the wavelength of the multiline by using a spectrometer.

2.3 Beam shaping elements

Consider Figure 2.1 again. The next fundamental piece of the beam shaping system that we need is a beam shaping element that satisfies the transmission function (labelled 3). These beam shaping elements can be physical optics or computer generated holograms (CGHs) that are encoded on a digital device such as spatial light modulators (SLM) or digital micro-mirror-device (DMD). In this section we will briefly introduce physical beam shaping optics and digital modulating devices. An in-depth discussion and demonstration on how to generate CGHs and fabricate physical optics for broadband beam shaping will be provided in subsequent chapters.

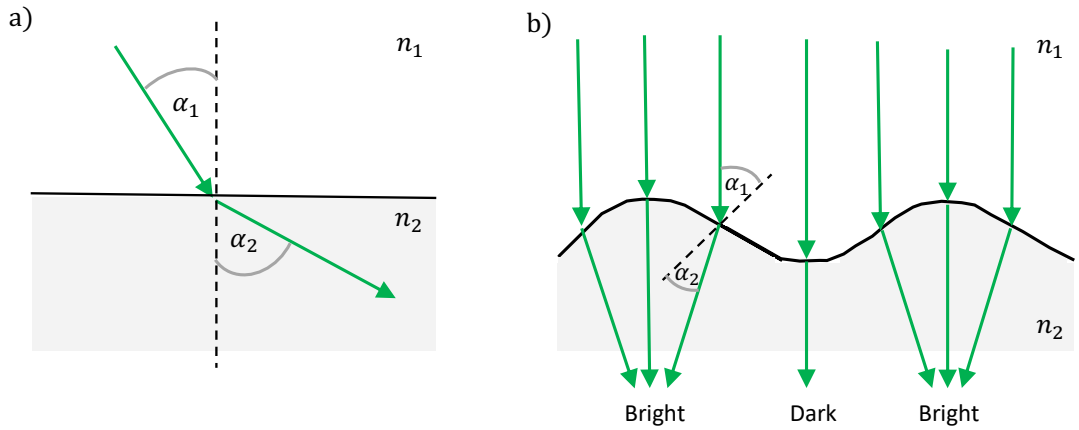


FIGURE 2.9: The refraction of light. a) A ray of light travels from a medium with a refractive index n_1 into a medium with a refractive index n_2 where $n_1 < n_2$. The incident beam initially travels at an angle α_1 with respect to the normal of the surface (shown with a black dashed line), but at the interface it is refracted and now travels at an angle α_2 with respect to the normal. b) The surface is designed to refract the incident light rays in such a way that at certain positions at the observation plane there will be a high density of rays and the interference pattern will be bright, while at other positions there will be scarcity of rays and the interference pattern will appear dark.

2.3.1 Physical optics

The earliest demonstrations of beam shaping relied on physical optics with surfaces that were designed to manipulate an incident beam's phase and amplitude in a manner that they interfered to produced a desired pattern/structure of light at an arbitrary observation plane [9]. In general, beam shaping optics can be classified as refractive or diffractive based on their structure and operating principles.

Refractive optics. As the name suggests, refractive optics manipulate light through the principle of refraction. Refraction is a phenomenon that occurs when light travels from one medium into another with a different refractive index. In this process, the speed of light changes and as a result the direction of the light wave is altered according to Snell's law:

$$n_1 \sin\alpha_1 = n_2 \sin\alpha_2 \tag{2.8}$$

where n_1 and n_2 are the refractive indices of the initial and subsequent medium, respectively, and α_1, α_2 are the angles of incidence and refraction, respectively, as seen in Figure 2.9. Exploiting this concept and relying on the principle of conservation of energy, refractive optics are designed using analytical methods to calculate a local mapping (deflection angle) for each point of the incident beam so that desired interference pattern (structured beam) is created in the observation plane. For example, consider the Figure 2.9 b). The surface is designed to refract the incident light rays in such a way that at certain positions at the observation plane there will be a high density of rays and the interference pattern will be bright, while at other positions there will be scarcity of rays and the interference pattern will appear dark.

Traditionally refractive optics were used to shape collimated incident beams, however with recent advancements it became possible to shape Gaussian beams using

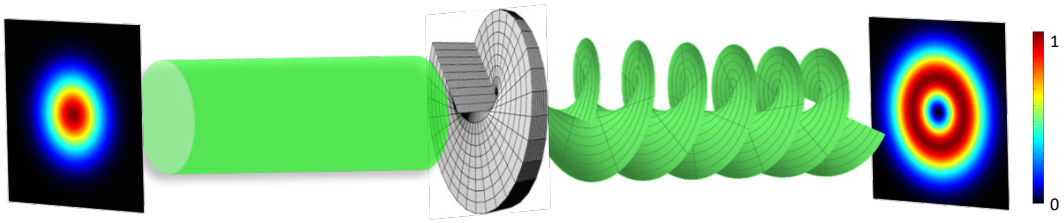


FIGURE 2.10: An example of a refractive lens- spiral phase plates (SPPs). SPPs converts incident light such with a flat wavefront into modes that carry orbital angular momentum (OAM) and have a helical wavefront. The inserts are the intensity profiles of the incident Gaussian beam and resultant vortex beam.

free-form optics [17]. In principle any desired structured mode can be realised using analytical methods, however the more complex the desired mode the greater the complexity of the surface structure. Hence, for refractive optics physical properties such as the thickness, surface curvature and refractive index will influence the optic's beam shaping ability [77, 91]. Fabrication of these optics requires an accuracy and a surface roughness in the nanometer range, to ensure that the beam is correctly refracted at each point along its surface [91]. To achieve such accuracy during manufacturing requires highly specialised methods such as diamond turning, which is expensive and thus not suitable for commercial use. The pros of refractive optics is that they can be used for multiple wavelengths so long as the refractive index doesn't vary greatly [61]. However, they are limited in design and cannot be used to achieve complex beam shapes. Refractive optics also tend to be quite bulky. Common examples of refractive optics include lenses or spiral phase plates (SPPs) which converts incident light into modes that carry orbital angular momentum (OAM) and have a helical wavefront, as seen in Figure 2.10 [58, 92, 93].

Diffractive optics. Diffractive optics rely on the wave nature of light to manipulate light through the principle of diffraction. Diffraction can be explained using Huygens wave principle: assume that the incident beam is a plane wave. Every point on the wavefront acts as a source of secondary wavelets that generate another plane wave. If a portion of the wavefront encounters some obstacle like a slit, the wavefront will be bent around the edges, as seen in Figure 2.11. Hence diffraction is typically described as the bending of light around obstacles.

Consider Young's famous double slit experiment, as seen in Figure 2.12. In this case, 2 slits were placed a distance d apart, causing the incident plane wave to be diffracted at two points. As the light from each point propagates, certain portions will destructively interfere (rays 1, 2) while others will constructively interfere (rays 3, 4). This result in the formation of an interference pattern at an observation plane some distance z away.

In principle if one knew how many slits to use and where to position them one could manipulate an incident beam so that it forms any desired interference pattern (structured mode) at an observation plane. For example, assume that you would like the incident beam to be focused at a point P some distance f away, i.e., all the transmitted light must constructively interfere at this single point. How can we arrange the slits to achieve this? Simply position the slits so that portions of light that are in phase and constructively interfere with each other are transmitted, while portions of light that are exactly out of phase and destructively interfere are blocked. In this

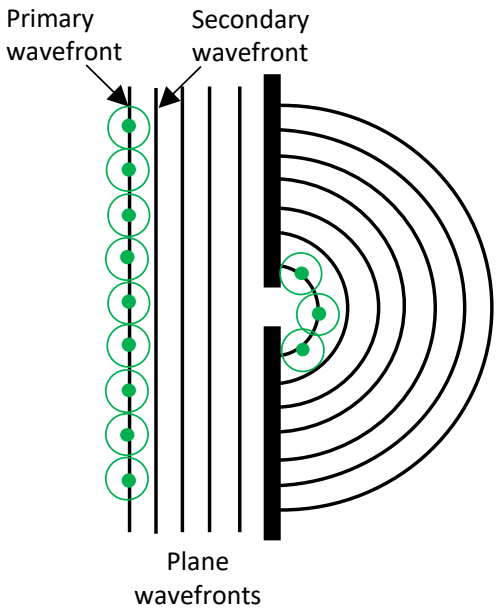


FIGURE 2.11: Diffraction can be explained using Huygens' wave principle: assume that the incident beam is a plane wave. Every point on the wavefront acts as a source of secondary wavelets that generate another plane wave. If a portion of the wavefront encounters some obstacle like a slit, the wavefront will be bent around the edges

way we have manipulated incident light in an amplitude-only manner by carving out the desired portions of light while discarding the rest, as seen in Figure 2.13 a). The result is a Fresnel zone plate (shown in Figure 2.13 b)) which has been used extensively in the past to focus various wavelengths of light such as x-rays [94–96].

It is clear to see why this process is considered quite lossy. So how could one improve the efficiency? The solution is this: instead of using material that would absorb the portions of light that are exactly out of phase, use a material that has a higher refractive index than the medium the incident beam is travelling in. This material will delay the incident beam and impart a phase shift. If the thickness of the material is meticulously chosen, the transmitted beam will now be in phase with the other portions of incident light. Hence this phase-only approach is considered more efficient as no light is lost during the process. In this case we have considered a binary case, but in reality there are portions of incident light that have phases which lie between these values and require material of different thickness.

Therefore, unlike refractive optics, diffractive optics have a surface that is composed of multiple structures that are small when compared to the incident beam's wavelength. When designing a diffractive optic the structures must arranged in such a manner that when an incident beam passes through them it will be diffracted and interfere in a way, that at some observation plane, one will observe a beam with the desired amplitude and phase. The height and spacing of the apertures are designed based on the incident beam's wavelength, hence the optic is wavelength-dependent and should be operated with the design wavelength for optimal beam shaping. Because the amplitude and phase to be imparted in the incident beam is dependent on the structures' positioning diffractive optics can be designed for complex/exotic beam shapes. Diffractive optics are also advantageous in systems that are limited

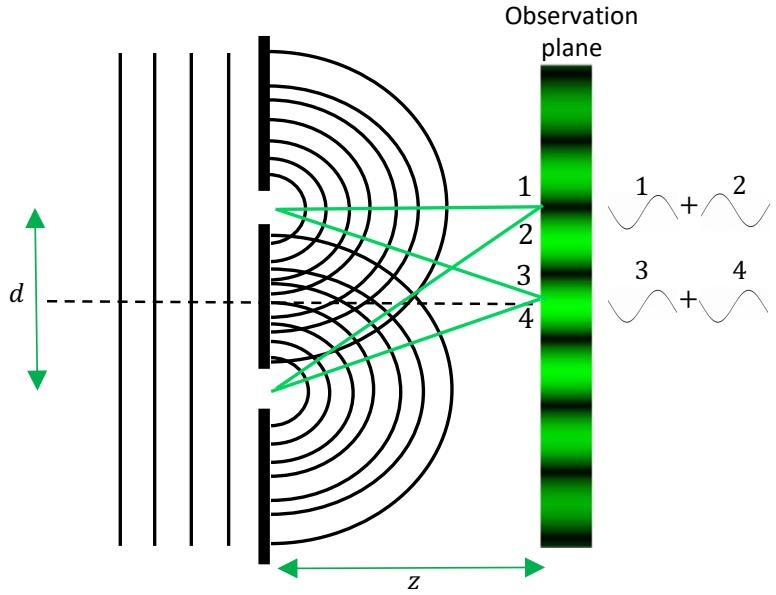


FIGURE 2.12: Young's famous double slit experiment. 2 slits are placed a distance d apart, causing the incident plane wave to be diffracted at two points. As the light from each point propagates, certain portions will destructively interfere (rays 1, 2) while others will constructively interfere (rays 3,4). This result in the formation of an interference pattern at an observation plane some distance z away.

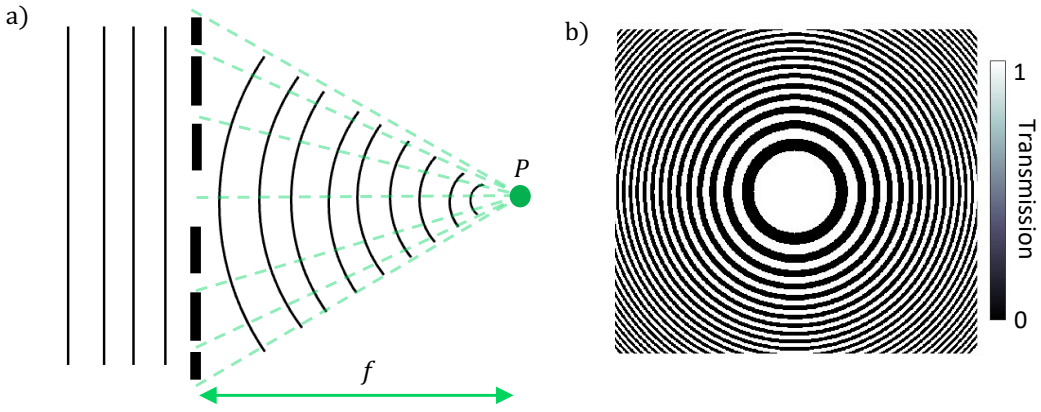


FIGURE 2.13: How the binary slits can be arranged to focus light, i.e., create a Fresnel zone plate. a) By arranging the slits in a selective manner, one can focus the incident light at a point P, located a distance f away. The slits are arranged to transmit light is in phase and constructively interfere, while blocking portions of light that are out of phase and destructively interfere. This is the underlying concept of a b) Fresnel zone plate.

in space as they are usually made of a single element, whereas multiple refractive optics are usually needed for beam shaping. Due to the extremely small sizes of the apertures, to fabricate a diffractive optic requires processes with high accuracy on the order of nanometers. For a while this was not easy to achieve, however with recent advances in etching and lithography methods (such as 3-D printing), now not only is it possible create such optics, but complex designs can be achieved, allowing for the possibility of complex structured beams to be generated. This will be discussed and demonstrated in Chapter 4. Some common examples of diffractive optics [97] include gratings, diffractive lenses [66] and metasurfaces [23].

To summarise the difference between refractive and diffractive optics (specifically focusing lenses) consider the following analogy: multiple athletes (portions of incident light) are lined up together at the beginning of a straight race track. The goal is for all the athletes to arrive at the finish line at the same time (be in phase and constructively interfere at the observation plane). However, some athletes are faster than others. To ensure that they all arrive at the same time we could do one of the following: (1) ensure that only athletes that run at the same speed are allowed to race (amplitude-only diffraction optics); (2) precisely add hurdles to the tracks of those who run faster, so that they are delayed and arrive at the same time as those much slower (phase-only diffraction optics); (3) reshape the race track itself (refractive optics).

Although there are limitations and difficulties when fabricating physical optics, once created they offer the advantage of being easy to use and integrate into systems (either pre-existing or not) due to their compact size. However, they are static and can only be used to generate a single mode. In certain applications such as microscopy or imaging the advantage of its compact size and easy integration outweigh the need for an optic that produces a variety of modes on hand. However, in other applications such as optical communication systems that require multiple structured modes, this is not the case. For such applications a dynamic system and different method of generating structured light is needed.

2.3.2 Digital beam shaping optics

It was for these reasons that researchers developed the modern art of beam shaping using computer generated holograms (CGHs) [98] which are encoded on digital modulating devices. These devices consist of an array of pixelated micro-structures (such as micro-mirrors or liquid crystals) that are responsive to some external stimulation such as an applied voltage. In this way the pixels can be individually controlled and the micro-structures within them re-orientated to impart a desired amplitude and or phase change to an incident beam. All that is needed is a manner to instruct each pixel as required. This is achieved through digital holograms, which have a one-to-one mapping with each pixel in the device. In this way the hologram serves as a set of instructions for each pixel, thus allowing for dynamic beam shaping to be achieved. In this section we will consider two types of digital modulating devices: (1) spatial light modulators (SLMs) , (2) digital micro-mirror devices (DMDs) that operate in a phase-only and amplitude-only manner, respectively.

Spatial light modulators (SLMs)

Liquid crystal on silicon spatial light modulators (LCoS-SLMs), commonly referred to as SLMs are digital devices that can be used to manipulate light in a phase-only manner [25]. SLMs are composed of two main parts: a pixelated display screen and a driver unit that controls the screen, as seen in Figure 2.14 a). An SLM screen typically has a resolution of 1920 $\times$ 1080 pixels, fill factor (ratio of the area of active pixels versus the entire screen area) >90% and a 8 μm pixel size. [99].

In an SLM, each pixel in the screen can be independently controlled and is composed of liquid-crystals (LCs), as seen in the insert of Figure 2.14 a). LCs are organic molecules that have an elongated oval shape and have a dipole nature, making them responsive to external stimuli such as an applied electric field. LCs are also birefringent, i.e., they refract light with different polarisations in a different way, as depicted in Figure 2.14 b). For example, assume a beam containing both horizontal and vertical polarisation states is incident on the LC. Within the LC there is an optical axis, and any light ray that has a polarisation state perpendicular to this optical axis (referred to as the "ordinary ray") will experience a fixed refractive index, n_o. A light ray that has polarisation perpendicular to the ordinary ray (referred to as the "extraordinary" ray) will experience a varying refractive index, n_e that is dependent on the orientation of the LCs as seen in Figure 2.14 c).

This is the underlying working principle of SLMs, as depicted in insert of Figure 2.14 a): apply a particular voltage, $V(p_x, p_y)$ (where p_x, p_y are the pixel coordinates) across electrodes to induce an electric field of a certain strength. Due to their dipole nature, the LCs sandwiched between the electrodes LCs will re-orientate themselves at an angle, $\theta(V(p_x, p_y))$ with respect to the axis for that particular pixel. This rotation in the LCs will result in a proportional change in the refractive index of the effective extraordinary ray, $n'_e(\theta(V(p_x, p_y)))$ [25]

$$\frac{1}{n_e'^2} = \left(\frac{\cos(\theta)}{n_e}\right)^2 + \left(\frac{\sin(\theta)}{n_o}\right)^2. \tag{2.9}$$

This variation in the refractive index introduces a path delay as the extra-orindary ray propagates through the LC, which leads to a phase change $\Delta\phi$, of the extraordinary ray which can be calculated as follows:

$$\Delta\phi = \frac{2\pi}{\lambda}\Delta n t, \tag{2.10}$$

where

$$\Delta n = n_e - n_o, \tag{2.11}$$

and λ is the wavelength of the incident light and t is the thickness of the LC. Hence, if the incident light is polarised in the direction of the extraordinary axis, by simply adjusting the voltage applied to each pixel one is able to alter the refractive index in such a way that a desired phase change is imparted to the incident beam. For this reason SLMs are referred to as phase modulating devices, and are typically able to impart a minimum phase change of 2π.

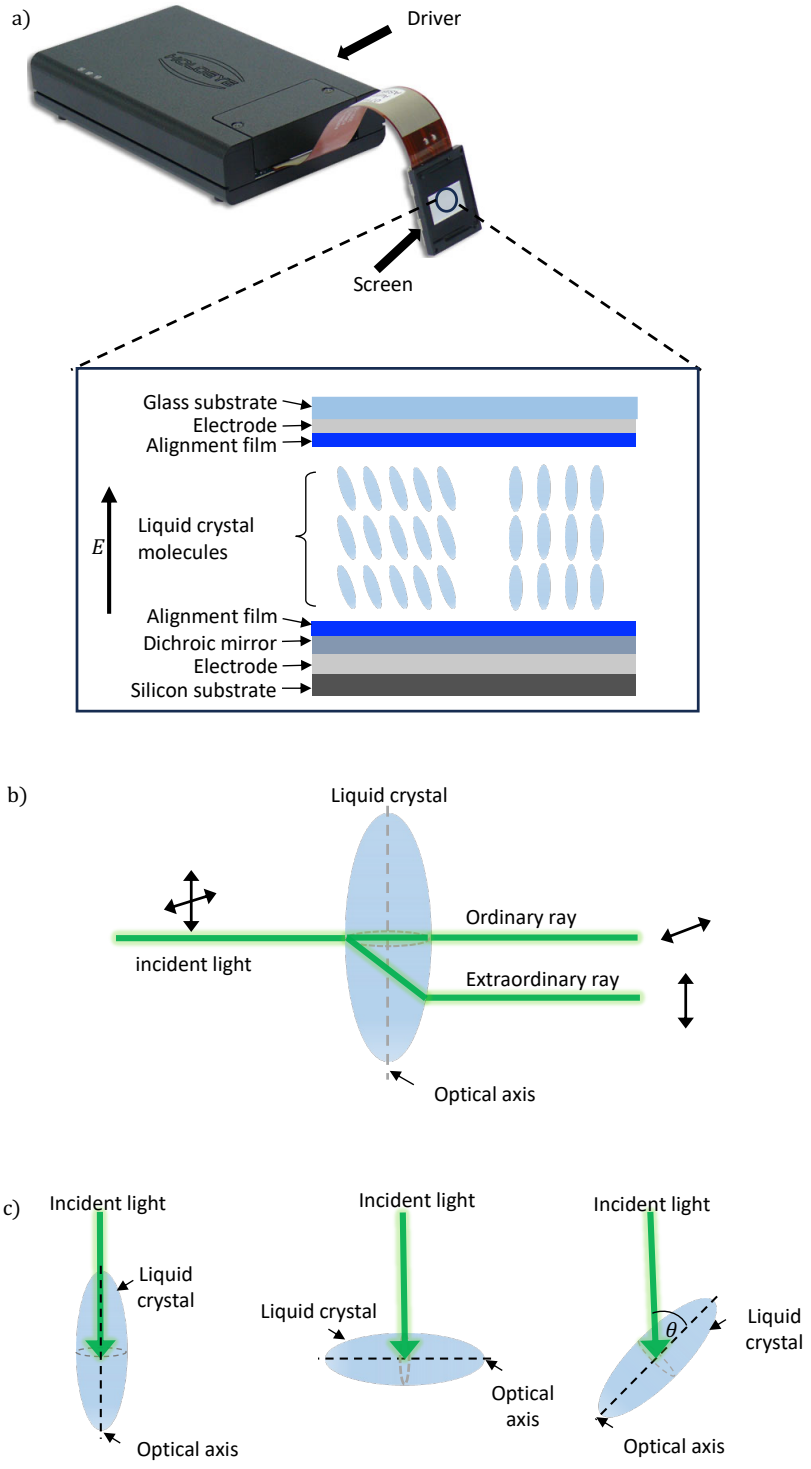


FIGURE 2.14: The structure and operating principle of a spatial light modulator (SLM). a) SLMs consist of a pixelated screen and driver unit that controls the screen. Each pixel in the screen is composed of liquid crystals (LCs) that are sandwiched between electrodes (insert). As a voltage is applied across the electrodes an electric field is induced. Due to the dipole nature of the LCs, they will be re-orientated causing a phase change between $[0, 2\pi]$. b) The Liquid crystals (LCs) in the SLM are birefringent. If an unpolarised beam of light is incident on a LC, the ordinary ray will experience a fixed refractive index, n_o. However, the extraordinary ray will experience a different refractive index n_e. c) Depending on the orientation of the LC, the incident light will experience a varying refractive index, n_e which a maximum when the optical axis is parallel to the incident beam (left), a minimum when it is perpendicular to the incident beam (middle), and some value between when it is orientated at an angle, θ (right).

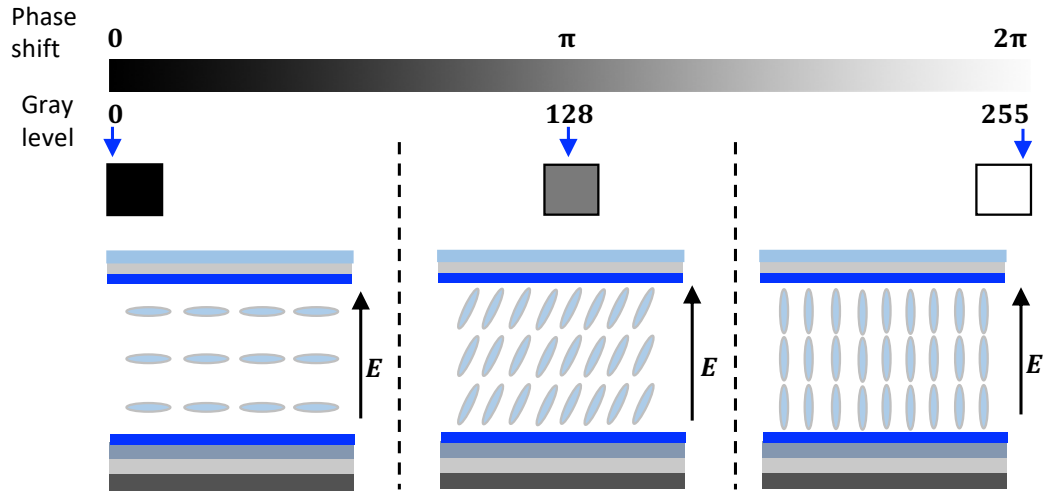


FIGURE 2.15: How grayscale holograms are used to cause a re-orientating of the liquid-crystals and thus induce a desired phase shift. SLMs are encoded with grayscale images called holograms (shown in the inserts) that have a one-to-one mapping with each pixel in the screen. In a well calibrated device, the grayscale value of the hologram is interpreted by the SLM driver as a particular voltage that must be applied to the pixel to induce an electric field of a certain strength, and thus a rotation of the LCs to a specific angle. Hence the incident light will be refracted in such a way that it will impart a phase shift ranging between $0 \rightarrow 2\pi$. Thus, there is a correlation between the encoded greylevel and the induced phase shift.

To impart the desired phase change in the incident beam, the SLM acts a secondary screen which displays an 8-bit grayscale image (preferably in .bmp format), referred to as a hologram, which is composed of 256 shades of grey ranging from black to white. The encoded hologram has a one-to-one mapping with each pixel in the SLM screen. Each grayscale value, L in the hologram is mapped by the driver to a particular voltage, $V(p_x, p_y)$ that should be applied to that specific pixel to rotate the LCs by an angle $\theta(V(p_x, p_y))$ to produce a phase shift, $\Delta\phi$ that lies between 0 (black) and 2π (white), as depicted in Figure 2.15. This implies that there are $2\pi/256$ possible phase increments that could be encoded per pixel in the screen and imparted to the incident beam.

To ensure an accurate mapping between the hologram's grayscale values and the induced phase shift, one must calibrate the SLM as outlined in Appendix A. Figure 2.16 shows a comparison of experimentally generated HG modes when the SLM was incorrectly and correctly calibrated to the wavelength of the incident light. Because the imparted phase shift, $\Delta\phi$ is wavelength dependent (hence the need for calibration), this implies that the mapping created during the calibration process is wavelength-dependent too. In other words, if the incident beam of light has a wavelength that differs from the calibration wavelength, the SLM should incorrectly modulate the incident beam, thus posing an issue in the case of broadband beam shaping. However, in recent work Spangenberg *et al.* [65] successfully showed that if a blazed grating is encoded on the SLM the mode in the +1st order will always have the desired structure and phase at the cost of efficiency loss. Any dispersion effects were then compensated for with the use of additional optics, in this case, a complementary digital grating.

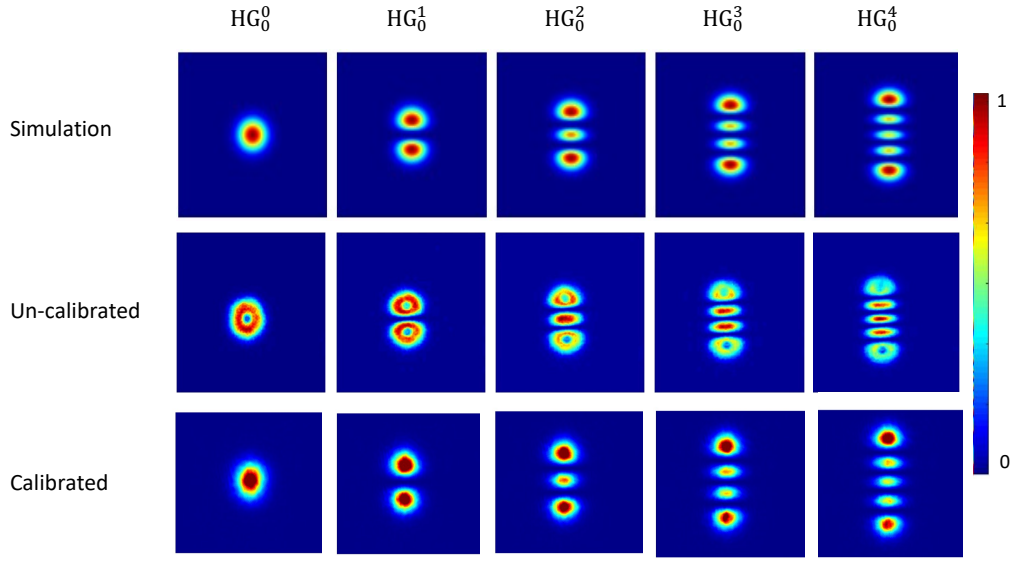


FIGURE 2.16: Comparison of experimentally generated HG modes when the SLM was un-calibrated and calibrated to the wavelength of the incident light.

Digital micro-mirror devices (DMDs)

Another common digital beam shaping device used in the optics community is a digital micro-mirror device (DMD). Since its invention in the late 1980s by Larry Hornbeck from Texas Instruments [100–103], DMDs have proven to be one of the most successful micro-electro-mechanical-systems (MEMS) available and has become a key component in all digital light processing (DLP) technologies.

DMDs were initially conceptualised as a deformable mirror [100]- an analogue device composed of a single mirror membrane that could be distorted in a pixel-like, spatially controlled manner using an applied voltage, as seen in Figure 2.17 a). In 1993 the focus was shifted from a single mirror membrane to an array of micro-mirrors that were mounted on torsion hinges and attached to electrodes that were connected to a computer chip. When a voltage was applied the electrostatic force caused the micro-mirror to be tilted in one of two directions [103, 104]. In this way each micro-mirror in the array could be independently controlled in a digital manner, as seen in Figure 2.17 b).

DMDs were originally designed with the purpose of replacing LCD technologies in personal televisions, and within a year of its commercialisation it became clear that DMDs could be used for high resolution projection technologies such as movie cinema projectors [105–107]. DMDs gained much popularity since for its ability to provide high-quality images with sharp details, vibrant colours, and high contrast ratios and have become an integral part in various display technologies such as smartphones [108], virtual and augmented reality systems [109], industrial large-scale display systems and even automotive head-up display (HUD) and headlight systems [110], to name a few.

In 2003 Dudley *et al.* highlighted emerging DMD applications [111] which ranged from projection to lithography. It was now clear that DMDs had the potential to extend far beyond its initial intended use. In fact, one of the earliest demonstrations of

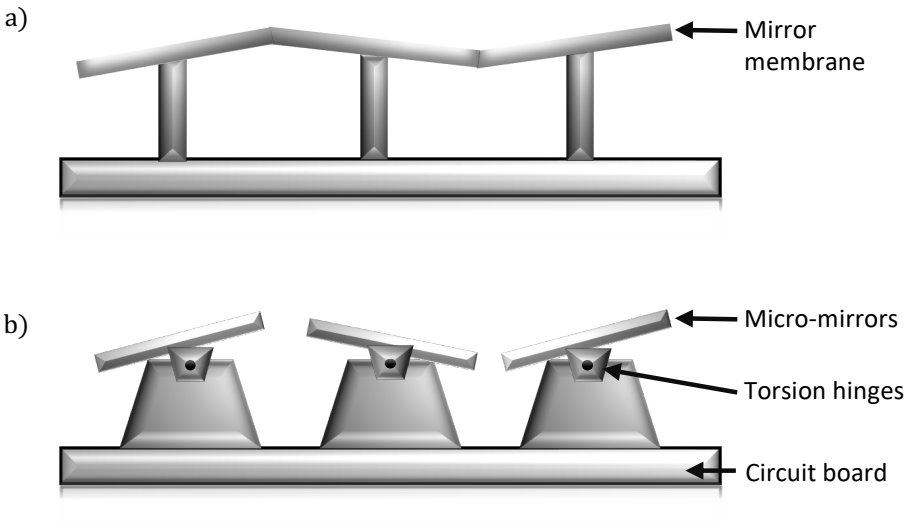


FIGURE 2.17: A comparison of the structures of a) deformable mirrors and b) digital micro-mirror devices (DMDs).

this was when DMDs were used to reconstruct a digital hologram.

The appealing characteristics of DMDs rendered them attractive for beam shaping applications. This led to the inaugural use of DMDs as a beam shaping tool. By 2010, DMDs were effectively utilised as spatial light modulators with laser sources, thus enabling the creation of unique intensity profiles like flat-tops [112, 113]. During the same period of time, advanced techniques to implement digital holography on DMDs were presented. A summary of three of the presented approaches is given as follows. In the first approach, the 'super-pixel' method [114] involved grouping multiple pixels together to form a larger pixel. The field in the observation plane is then the cumulative result of responses from all super-pixels. The second approach, presented by Wai-Hon Lee [115] involves the generation binary computer holograms while the third method is an iterative method for producing computer generated holograms by means of the Gerchberg-Saxton algorithm [112].

With the use of these various methods the role of DMDs as spatial light modulators became solidified and expanded the possibility of DMDs to generate structured light modes like LG, HG, Bessel and Airy beams [28]. With the advancement of beam shaping techniques it became possible to control more degrees of freedom during the creation of structured light. For example, DMDs have been used in the generation of vector vortex modes which are created by controlling the polarisation of OAM-carrying beams [116]. In recent work, DMDs have proven useful beyond just structured light generation. In fact, they have be used as a wavefront sensor to characterise an unknown optical field [117, 118], thus acting as an alternative to traditional wavefront sensing devices like the Shack-Hartmann [119, 120].

When compared to SLMs, DMDs relatively low cost, rapid refresh rate, and polarisation invariance make them a much more suitable tool for commercial applications which involve beam shaping. However, when it comes to broadband beam shaping although there has been some research done with SLMs the same cannot be said for DMDs. Why is this the case when the DMD has no wavelength dependency in its operating mechanism nor does it require any wavelength-dependent calibration?

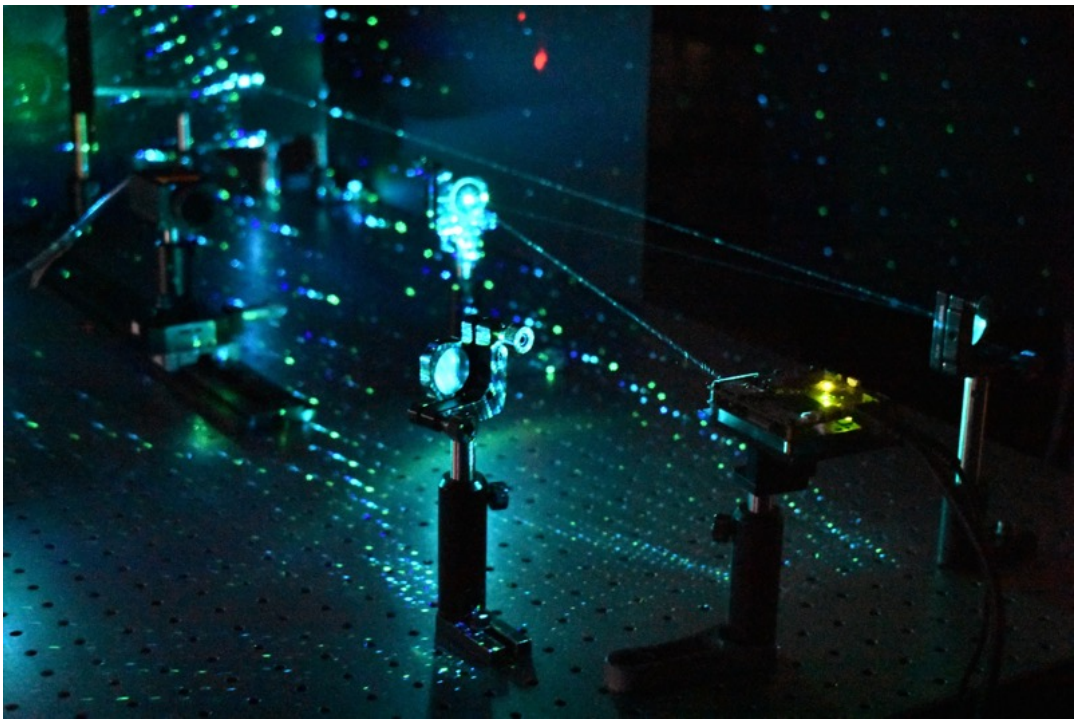


FIGURE 2.18: Image showing that a broadband beam of light is dispersed by a DMD even when it is un-powered.

Due to the spacing between the micro-mirrors DMDs will diffract and thus disperse any incident broadband beam, as seen in Figure 2.18. Considering that the DMD is extremely inefficient (maximum efficiency is 6.2% [27]) and additional optics coupled with precise alignment are needed, it is clear to see why DMDs are not usually considered. Nevertheless, with the invention of new applications DMDs are now being investigated as a potential tool for broadband shaping [64]. In Chapter 3 we will look at how to use DMDs for broadband beam shaping and how to compensate for the dispersion of the incident beam using a single lens.

However, before we do this, let us consider how to create broadband beam shaping elements and what the effects are.

2.3.3 Considering wavelength-dependence

Regardless of whether we opt to use a physical or digital beam shaping element, this general question remains - how can we design the beam shaping element so that it imparts the correct phase across various wavelengths? As discussed in Chapter 1, if a grating is added to the optic, in +1st order the beam will have the desired structure and phase regardless of the wavelength of the incident beam. The effect, however, of designing the phase element for wavelength λ_0 but actually operating at wavelength λ is to alter the action of the transmission function to Equation 1.16 [65] and thus change the intensity by a factor $I = |\zeta|^2$, where $\zeta = \text{sinc}[\pi(1 - \lambda_0/\lambda)]$.

Because we will be using argon-ion laser throughout this thesis we shall only consider what happens when $\lambda_0 \in \{457\text{ nm}, 488\text{ nm}, 514\text{ nm}\}$. Figure 2.19 depicts how the intensity of the beam changes for various incident wavelengths, λ. We see that

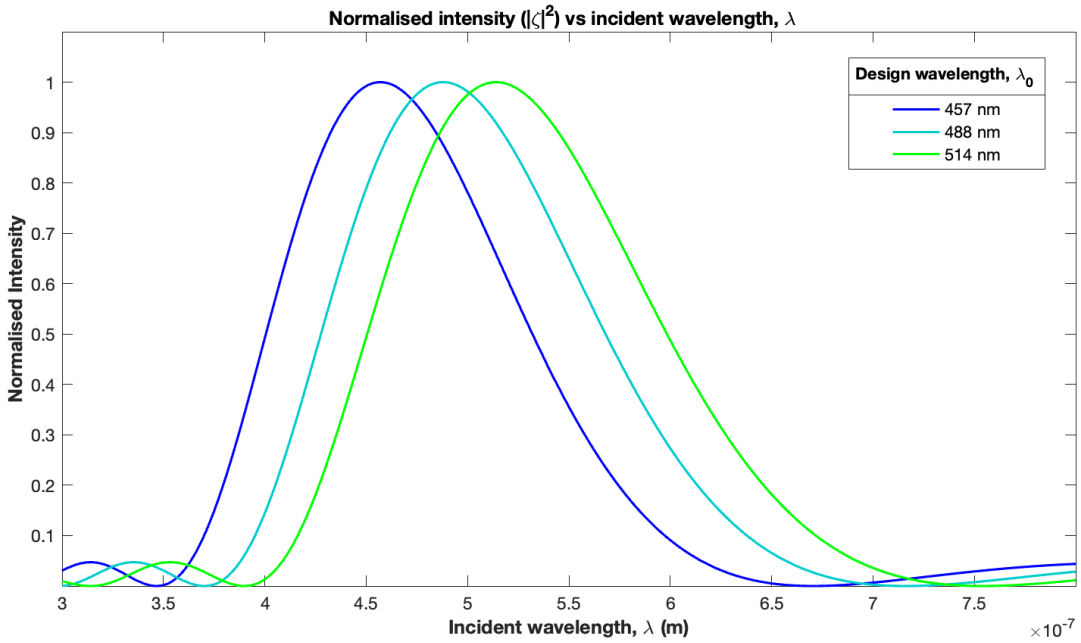


FIGURE 2.19: A plot depicting the effect on the intensity of the structured beam (in the +1st diffraction order) when a phase element is designed for wavelength λ_0 but one operates at wavelength λ.

when $\lambda_0 = \lambda$, $\zeta = 1$ and the beam has a maximum intensity, as expected. As the difference in wavelength increases, ζ decreases and so does the intensity of the beam. Since the laser emits discrete wavelengths of light, it is not necessary to consider a wide spectrum of light. The results applicable for our purposes can thus be summarised in Table 2.5 for $\lambda \in \{457$ nm, 488 nm, 514 nm.$\}$ Examining the results highlights the pivotal role of the chosen design wavelength, λ_0, in influencing the extent of efficiency loss across different incident wavelengths. Notably, when the design wavelength aligns with the central region of the incident wavelength spectrum, the efficiency loss is notably lower compared to when the design wavelength is closer to the extremes of the spectrum. Consequently, if efficiency is a priority, opting for a centrally positioned design wavelength is advisable. However, it's important to note that in this thesis, the design wavelength is arbitrarily chosen, deviating from this efficiency-centric recommendation.

To summarise, what this means is that the operation of the element will remain intact and wavelength independent except for a decrease in efficiency as the design wavelength is altered. There is however one downside. The angle at which light is diffracted is still wavelength dependent, following the familiar rule for periodic structures of $m\lambda = \lambda_x \sin\theta_m$, where θ_m is the angle of the m-th order. A consequence is that the desired light will be created for all wavelengths, but they will appear to emerge at different angles, thus at different positions in the far-field. This dispersion effect has to be corrected in the experiment by using a compensating element such as a grating or prism [64].

TABLE 2.5: A summary (for discrete wavelengths) of the expected intensity of the structured beam (in the +1st diffraction order) when a phase element is designed for wavelength λ_0 but one operates at wavelength λ

Design wavelength, λ_0	**Incident wavelength,** λ		
	457 nm	**488 nm**	**514 nm**
457 nm	1.0000	0.8592	0.5866
488 nm	0.8757	1.0000	0.9112
514 nm	0.6593	0.9196	1.0000

Chapter 3

Broadband beam shaping using a digital micro-mirror device

This chapter is based on the paper:

Leerin Perumal *and Andrew Forbes, "Broadband structured light using digital micro-mirror devices (DMDs): a tutorial." (2023) Journal of Optics, 25 (7), pp. 4003*

In this chapter we demonstrate how to shape multiple wavelengths of light using computer generated holograms (CGH) written to DMDs. The chapter begins with an overview on the structure and operating principles of the DMD followed by a discussion on how to setup and align the DMD in an optical system. Next we begin provide the basic theory behind generating binary holograms for the DMD that contain both the phase and amplitude information that we wish to impart into some incident beam. Using the generated holograms we then demonstrate how to shape monochromatic light, and by extension broadband light. We will also consider and discuss how to compensate for any manifestations, such as dispersion, that may arise due to any wavelength-dependence present in the system.

3.1 DMD structure and operating principles

Digital micro-mirror devices (DMDs) are amplitude-only digital devices that can be used for shaping light. DMDs consist of two main components: a micro-mirror array (the screen) and a set of electronics (the driver unit) that controls the mirrors, as depicted in Figure 3.1.

At present Texas Instruments is the sole manufacturer of all commercially available DMDs and they offer a variety of models with various properties and resolutions. In our lab, we have access to three models namely the *DLP3000* [121], *DLP6500* [122] and *DLP660* [123]. The important properties of each model are summarised in Table 3.1.

From Table 3.1, one can see that the number of micro-mirrors in the screen, i.e., the resolution, varies between different models. Another property that differs between DMDs models is the layout of the micro-mirror array within the screen. There are two distinct layouts: Cartesian and diamond, as seen in the Figure 3.2 a) and b), respectively. In a Cartesian layout the micro-mirrors (depicted as white squares) are arranged in a manner resembling a Cartesian grid, i.e., the mirrors' axes (depicted by green dashed lines with x, y) are aligned parallel to the axes of the base (depicted by black solid lines with x, y) the mirrors are attached to. In this layout, the

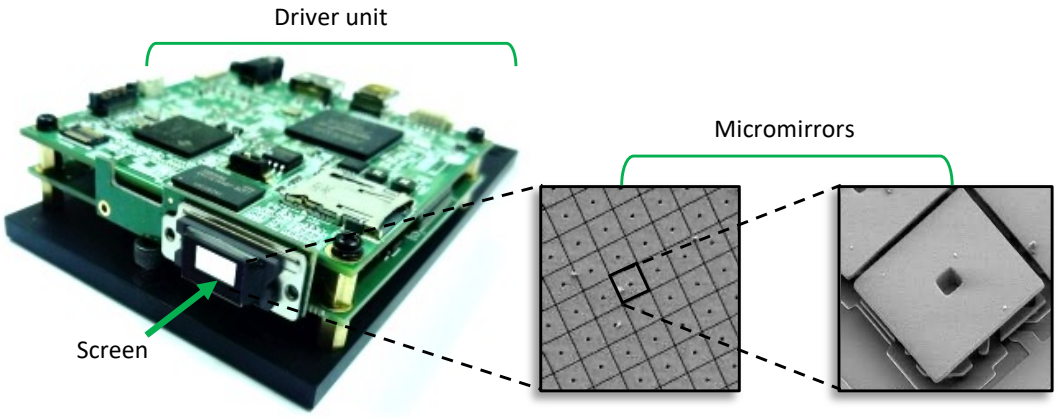


FIGURE 3.1: The DMD consists of two main components: the driver unit and screen (as labelled). The screen consists of a micro-mirror array composed of individual micro-mirrors (inserts). Panels 2 and 3, micrographs are courtesy of University of Rochester/URnano.

TABLE 3.1: Summary of the important properties for 3 common DMD models.[121–123]

Model	**Resolution** (number of pixels)	**Layout of micro-mirror array**	**Size of a micro-mirror** (μm)	**Tilt angle of micro-mirror** ($^\circ$)
DLP3000	608×684	Diamond	7.56	12
DLP6500	1920×1080	Cartesian	7.56	12
DLP660	3840×2160	Cartesian	5.4	17

micro-mirrors have a separation distance d between adjacent micro-mirrors' centres (depicted by green arrows with solid lines) that is equivalent in both the vertical and horizontal directions. In a diamond layout, however, the micro-mirrors are rotated at a 45°-angle relative to the base, making the square mirrors appear diamond-like. To optimise the packing of the micro-mirrors in a diamond layout, the mirrors are arranged so the separation distance in the vertical direction, $2d$, is twice the distance in the horizontal direction, d. The difference between the two layouts must be taken into account when encoding holograms onto different DMD models. In this thesis we used a *DLP3000* which has a diamond layout; the square micro-mirrors had a width and height of 7.6 μm and a separation distance, d = 10.8 μm between adjacent micro-mirrors.

Micro-mirrors are small, highly reflective aluminium squares that pivot about their diagonal and reflect the incident light. The movement of the micro-mirrors are made possible by the torsion hinges they are attached to. However, the spring tips restrict the micro-mirrors' possible rotation angles. These torsion hinges connect the micro-mirrors to electrodes which are further connected to circuit board. When a voltage is applied, an electric field is generated between the electrode and micro-mirror, and the electric force causes the micro-mirror to tilt in a particular direction along its diagonal. When a beam of light is incident on the tilted micro-mirror the beam will be directed in a +/- direction off axis. By convention the positive (+) state is referred to as *on* and the negative ($-$) state is referred to as *off*. Micro-mirrors in the *on* state direct light toward the desired direction and micro-mirrors in the *off* state direct light in the opposite direction. When powered and operational all micro-mirrors in the DMD must occupy one of the two states. However, when the DMD

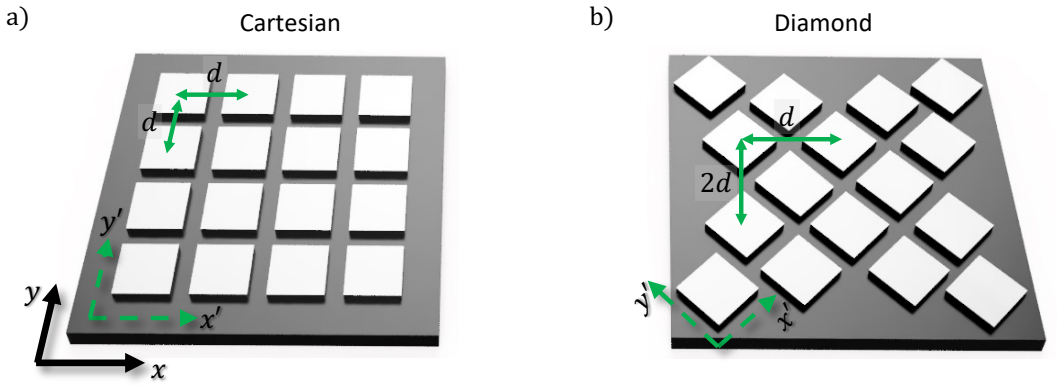


FIGURE 3.2: Based on the model, DMDs have different layouts of their micro-mirror arrays. In a) a Cartesian layout the micro-mirrors (depicted as white blocks) are arranged in a manner resembling a Cartesian grid where the micro-mirrors axes (depicted as dashed green arrows with x and y) are aligned to axes of the base (depicted as solid black arrows with x, y) that they are attached to. The separation distance between the micro-mirrors' centres in the x-direction, d is equivalent to the separation distance in the y-direction. In a b) diamond layout the micro-mirrors are rotated at a 45° angle relative to base. In this layout the square micro-mirrors appear 'diamond like'. To maximise the packing efficiency, the separation distance between the mirrors' centres in the vertical direction, $2d$ is twice the separation distance in the horizontal direction, d.

is non-operational no voltage is applied. Hence the micro-mirrors will experience no electric force and are in a *'parked'* state where they are neither *on* nor *off*. In the 'parked' state the micro-mirrors are roughly parallel to circuit board the mirrors are attached to. Figure 3.3 shows the possible orientations of the micro-mirrors. The angle that the micro-mirrors are tilted when in the *on* or *off* state is dependent on the DMD model, as shown in Table 3.1. In this thesis we used a *DLP3000*, hence when powered, the micro-mirrors will be tilted $\pm 12°$ relative to the normal of the circuit board/base of the screen.

3.2 Computer generated holograms for DMDs

When powered, the micro-mirrors in the DMD screen can only occupy one of two states (*on* or *off*) and will therefore reflect the incident beam towards the desired plane or away from it. Therefore, the DMD is considered a binary amplitude-only device. If we wish to use the DMD to manipulate both the phase and amplitude of an incident beam and thus generate some desired mode, we must be able to modulate the light in a spatially resolved manner. This implies that we require a way to independently control each micro-mirror in the DMD's screen. The solution lies in binary computer generated holograms.

Two questions then remain: (1) how does one calculate the desired amplitude and phase profiles, and (2) how does one convert that to a hologram which can be written to a simple binary amplitude device such as a DMD?

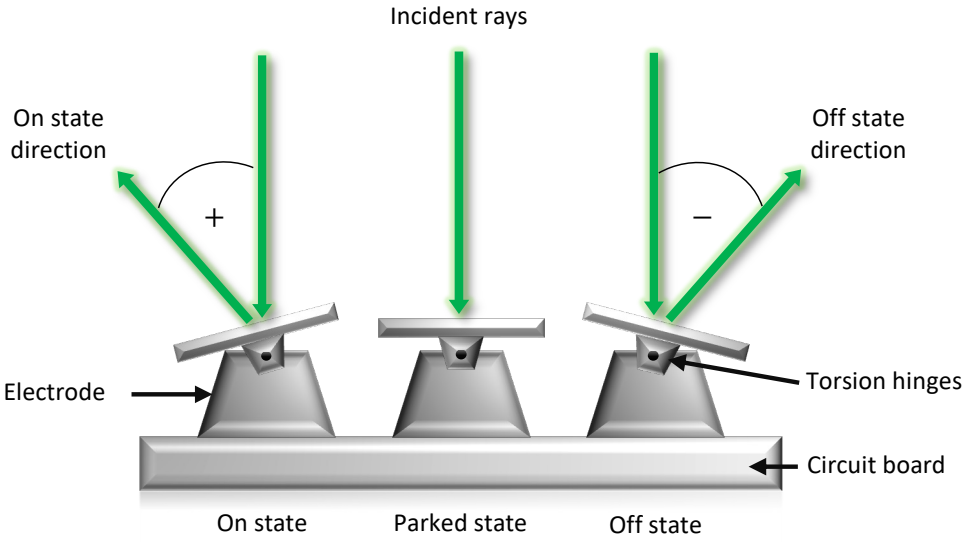


FIGURE 3.3: The three possible states of the DMD micro-mirrors: *on*, *parked* and *off*. When non-operational the micro-mirrors are in the 'parked' state. When operational the micro-mirrors will either be *on* or *off* and deflect the incident light in a +/- direction relative to normal incidence.

3.2.1 Theory

We shall address the second part first. Imagine that in general you may want to have a computer generated hologram that encodes both amplitude and phase, and write this onto the DMD. To create such a hologram, begin with assuming that we wish to create a complex field, given as: $U(x) = A(x)\exp(i\varphi(x))$, where $A(x)$ is the desired amplitude structure and $\varphi(x)$ is the desired phase. How can one write a complex amplitude and phase to a simple binary on/off device to create such a beam? Fortunately this problem was solved nearly half a century ago when sophisticated match filters for pattern recognition were required, but only rudimentary optical elements existed [115]. Although there have been other methods to generate binary holograms since then [114], here we consider the method outlined by Lee [115]. Both a conventional hologram and a computer generated hologram (CGH) are formed by the interference of a reference plane wave, $R\exp(-i2\pi x/\lambda_x)$ (where R is the amplitude and λ_x is the grating period in the x direction) with an object wave, $A(x)\exp(i\varphi(x))$. For a conventional hologram this is done physically and the CGH is done computationally. The hologram transmittance is proportional to

$$t(x) = R^2 + A^2(x) + 2RA(x)\cos[2\pi x/\lambda_x + \varphi(x)] \tag{3.1}$$

where the third term performs the object wave reconstruction. Unfortunately if only a simple binary on/off amplitude-only hologram is possible, then the binary version of the key reconstruction term becomes

$$\hat{t}(x) = \begin{cases} 1, & \text{for } \cos[2\pi x/\lambda_x + \varphi(x)] \geq 0 \\ 0, & \text{otherwise} \end{cases} \tag{3.2}$$

which mathematically can be executed by the function

$$\hat{t}(x) = \frac{1}{2} + \frac{1}{2}\text{sign}\left\{\cos[2\pi x/\lambda_x + \varphi(x)]\right\}, \tag{3.3}$$

returning 1 or 0 as the sign of the cosine function changes. We see that the amplitude information is lost (as there is no need to insert the $2RA(x)$ term) since this on/off oscillation is not amplitude dependent, so that the resulting train of on-off amplitude pulses only holds the desired phase information. To get around this one introduces a bias function for the clipping level, $\cos \pi q(x)$ instead of 0, which is equivalent to subtracting it from the original function, namely [115]

$$\hat{t}(x) = \begin{cases} 1, & \text{for } \cos[2\pi x/\lambda_x + \varphi(x)] - \cos[\pi q(x)] \geq 0 \\ 0, & \text{otherwise} \end{cases} \tag{3.4}$$

so that now the pulse train has leading and trailing edges in its pulses given by solutions to $2\pi x/\lambda_x + \varphi(x) = 2\pi m \pm \pi q(x)$. Now the challenge is to find the function $q(x)$. The Fourier series representation of this pulse train can be written as

$$T(x) = \sum_{m=-\infty}^{\infty} T_m \exp\left(i2\pi m \frac{x}{\lambda_x}\right), \tag{3.5}$$

with

$$T_m = \frac{\sin[\pi m q(x)]}{\pi m} \exp[im\varphi(x)]. \tag{3.6}$$

We see that the $m = 1$ term (T_1) has the desired phase, $\varphi(x)$, and an amplitude factor $\sin[\pi q(x)]/\pi$. Since we will normalise all amplitude to 1 anyway, if we simply set $A(x) = \sin[\pi q(x)]$ so that $\pi q(x) = \arcsin[A(x)]$ then we have our solution.

The DMD hologram then becomes

$$H_{\text{DMD}}(x,y) = \frac{1}{2} + \frac{1}{2}\text{sign}\left\{\cos[2\pi\left(\frac{x}{\lambda_x} + \frac{y}{\lambda_y}\right) + \varphi(x,y)] - \cos(\arcsin[A(x,y)])\right\}, \tag{3.7}$$

where now we have written it in two-dimensions (for a 2D pulse train). It is worth unpacking this function. The encoding can be understood as larger pulse widths in the pulse train leading to larger amplitudes being diffracted into the first order, while local shifts in the pulse position allow for propagation phase control through small path length differences. Note that the input to the pulse train is the desired amplitude and phase of the output beam, which is now formed in the near-field, at the plane of the DMD.

Up until now we have assumed that the DMD is completely efficient at producing modes with high purity. In reality, due to the gaps between the micro-mirrors, some unmodulated light is reflected toward the desired plane. This unmodulated light will mix with the modulated light and distort the desired beam. To overcome this the desired beam is separated from the undesired diffraction orders by virtue of the blazed grating (our reference wave), of the form $\exp(i2\pi(x/\lambda_x + y/\lambda_y))$ with grating periods λ_x and λ_y in the x and y directions, respectively. This alters the diffraction angle of the desired light relative to the zeroth-order by $\theta_x = \lambda/\lambda_x$ and $\theta_y = \lambda/\lambda_y$, and is referred to as an off-axis design. Because this requires propagation, it is common to use a telescope to map angles to position in the Fourier plane (located a focal length after the first lens in the system), separate out the desired beam, and then return to the image plane of the DMD (located at the focal plane of the second lens in the system) but now with only the desired field.

The $\frac{1}{2} + \frac{1}{2}\text{sign}(x, y)$ function binarises the output so that the function returns 1 for $(x, y) \geq 0$ or 0 (all else), ensuring the binary on/off input to the DMD as per Equation 3.4. The low efficiency of the DMD (< 6.4 % [27]) can be appreciated by noticing that only the T_1 component has the desired amplitude and phase, with the other terms T_2, T_3 and so on all carrying unwanted light.

One can further explore this function by re-framing the problem in terms of the pulse train itself. The one dimensional (1D) binary amplitude grating is a pulse train of the form

$$T(x) = \sum_{m=-\infty}^{\infty} \text{rect}\left(\frac{x - (m+p)\lambda_x}{w\lambda_x}\right), \tag{3.8}$$

where m represents each opening in the grating at the position p of width w, with period λ_x. Now we wish to relate these pulse train parameters to the amplitude and phase of the hologram. We can expand $T(x)$ into a Fourier series to find [27, 124]

$$T(x) = \sum_{m=-\infty}^{\infty} T_m \exp\left(i2\pi m\frac{x}{\lambda_x}\right), \tag{3.9}$$

and

$$T_m = \frac{\sin(\pi m w)}{\pi m}\exp(i2\pi m p). \tag{3.10}$$

We can see that the coefficients T_m dictate the amplitude and phase diffracted into the m-th order. If this binary amplitude grating represents the on/off states of the light, then for instance, T_1 is an amplitude and phase associated with the plane wave at angular frequency $2\pi/\lambda_x$, T_2 is an amplitude and phase associated with the plane wave angular frequency $4\pi/\lambda_x$, and so on. Using T_1 as an example, we see now that we can find solutions for the unknown p and w from

$$\frac{1}{\pi}A(x)\exp(i\varphi(x)) = T_1(x) = \frac{1}{\pi}\sin[\pi w(x)]\exp[i2\pi p(x)], \tag{3.11}$$

from which we immediately find that we need to make the pulse width w and position p spatially varying according to

$$w(x) = \frac{1}{\pi}\arcsin(A(x)) \tag{3.12}$$

$$p(x) = \frac{1}{2\pi}\varphi(x) \tag{3.13}$$

relating the train parameters to the desired beam parameters. We see that indeed the amplitude is now encoded into the width of each pulse, with the period holding the phase information. The solution is identical in 2D by replacing $(x) \rightarrow (x, y)$ in the arguments of all functions in the solutions i.e.,

$$w(x, y) = \frac{1}{\pi}\arcsin(A(x, y)), \tag{3.14}$$

$$p(x, y) = \frac{1}{2\pi}\varphi(x, y), \tag{3.15}$$

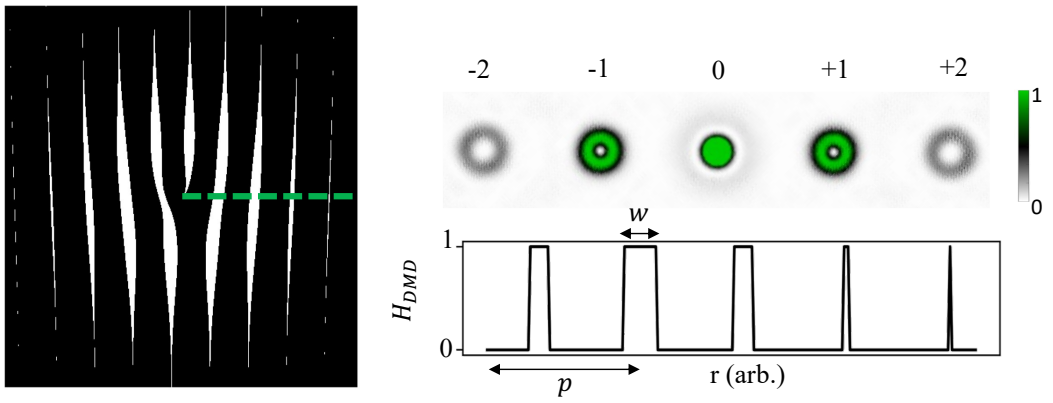


FIGURE 3.4: Computer generated hologram for creating a vortex beam by a complex amplitude function on a DMD. The main frames show the binary hologram with the inset depicting the simulated output in various diffraction orders. A cross-section of the hologram is shown along the dashed green line as an inset.

so that now we have a two-dimensional pulse train.

Figure 3.4 illustrates an example of a complex amplitude function written to a DMD (with desired transmittance $t \propto LG_0^1(r, \varphi, \theta)\exp(i2\pi x/\lambda x)$). The panels show the binary amplitude hologram and a cross-section along the dashed green line on the right. The simulated outcome of the diffraction orders is also shown. In all cases the desired beam is in the +1 order. The pulse train in Figure 3.4 now visualises the role of the functions p and w.In the rest of the chapter we will use specific examples of desired amplitudes and phases in order to make the treatment practical, and to do so we select from the common beam types previously mentioned in Chapter 1

3.2.2 Writing the hologram to the DMD

Implementing the computer generated holograms on a pixelated device such as a DMD entails the computation of a two dimensional matrix with dimensions that match the resolution of the device's screen. Each element in the matrix will have a one-to-one mapping to a particular pixel (micro-mirror) in the device and must therefore be scaled so that it is the size of the pixel. If matrix is generated with the incorrect resolution or pixel size this will lead to an incorrect mapping between and device. Since each micro-mirror can occupy one of two states when operational (the *on* or *off* states), the DMD is considered to be binary in nature, hence the matrix must be binary too, with each element having a value of 0 or 1. When this matrix is encoded on the DMD, the driver interprets a value of 0 as an instruction for that particular micro-mirror to occupy the *off* state, and a value of 1 for the micro-mirror to occupy the *on* state.

To visualise the matrix, we assign colours to each value and thus create a binary hologram. Because light is directed towards the desired plane when the micro-mirrors are in the *on* state, the matrix element or pixel is assigned the colour white in the hologram. However, because light is directed away from the desired plane when the micro-mirrors are in the *off* state the pixel is assigned the colour black. Figure 3.5 illustrates the relationship between the generated binary matrix, the hologram and the micro-mirrors' states, while the left panel in Figure 3.4 depicts an example of a

hologram (for an LG_0^1 mode) that would be directly written to the DMD.

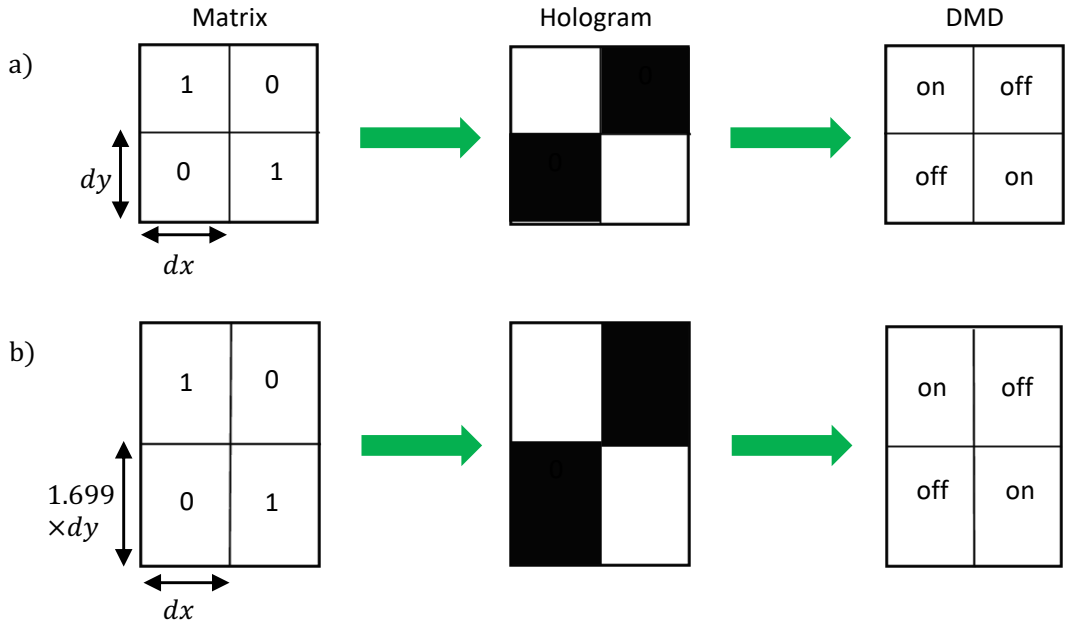


FIGURE 3.5: Holograms act as a means to control each micro-mirror in the DMD's screen. First a binary matrix with the same dimensions as the DMD's screen is generated. a) For DMDs with a Cartesian micro-mirror array layout, each matrix element has a vertical size equivalent to the micro-mirror's height dy and a horizontal size equivalent to the micro-mirror's width, dx. b) For a DMD with a diamond micro-mirror array layout, the orientation of the mirrors must be taken into account as mentioned by [27]. Hence each matrix element is up-scaled by a factor of 1.699 in the vertical direction relative to the micro-mirror's height dy, i.e., each element will have a vertical size of $1.699(dy)$. However, each matrix element will have a horizontal size equivalent to the width of the micro-mirror, dx. To visualise this matrix, each value is assigned a colour i.e., the colour black is assigned to elements with a value of 0 and white is assigned to the elements which have a value of 1. In this way a binary hologram is created, which can be encoded on the DMD. Because each element in the hologram has a one-to-one mapping with each micro-mirror in the DMD's screen, in essence the colour of the hologram element or pixel corresponds to the micro-mirror's state. Hence, when the element is coloured black it corresponds to the micro-mirror in the *off* state, and when it is coloured white it corresponds to the micro-mirror in the *on* state. In this way one can control the micro-mirrors in DMD.

The layout of the micro-mirror array must be taken into account when designing the geometry of the pixel array, otherwise an elliptical distortion of the beam may be observed. It was shown that for DMDs with a diamond layout, one simply needs to upscale the initial matrix's dimensions in the vertical direction to compensate for this incorrect mapping. This scaling factor was determined in an iterative manner until it converged to the ideal ratio of the vertical and horizontal pixel size of 1.6889. In other words when encoding the hologram matrix, the vertical dimension (or y co-ordinates) should be upscaled by a factor of 1.6889. When this is done, the hologram matrix will be correctly mapped and the beam will no longer appear elongated. Figure 3.5 a) shows an appropriate mapping for a Cartesian micro-mirror array, with Figure 3.5 b) showing an example for the diamond geometry, where the pixel size in the vertical direction is up-scaled by a factor of 1.699. The outcome experimentally

of using the incorrect or correct scaling is shown in Figure 3.6: in a) we see an elongated beam when no scaling is applied but the hologram is displayed on a diamond geometry device, with part b) showing the same hologram correctly scaled.

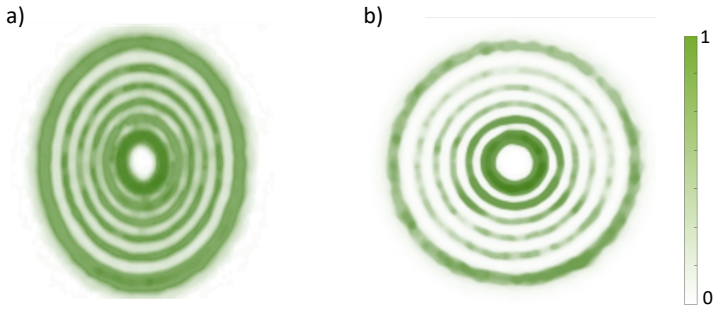


FIGURE 3.6: The scaling/mapping between the hologram and DMD pixels results affects the shape of the generated mode. a) Incorrect scaling of the hologram resulting in an elongated beam, and b) correct scaling of the hologram resulting in a symmetric beam [27].

3.3 Setting up the DMD

Before using a DMD for beam shaping, we must first ensure that it is correctly setup within an optical system. This section will focus on the experimental techniques used to ensure the efficient and optimal beam shaping.

3.3.1 Mounting

It is recommended that the DMD be mounted to a 3-axis translation stage as seen in Figure 3.7. This can easily be achieved by securing the base plate (labelled 2) of the DMD to a right-angle bracket (labelled 3) with a single screw (labelled 4). This bracket is then attached to translation stages. Using the screw gauges (labelled 5, 6 and 7) one can adjust the DMD's position in the x, y and z directions, respectively. The use of the translation stages make the alignment process easier. However, it is not necessary. Instead, one could rather secure the base plate directly to a post which is placed in a holder and fixed directly to the optical bench.

3.3.2 Connecting the DMD

To power a DMD one uses a power cable connected to a power brick. It is important to note that various models use different voltages, and so the appropriate power cable and brick must be used. The power cable is plugged into the port (labelled 1) in Figure 3.8. To switch the DMD on, one uses the button (labelled 2) in Figure 3.8.
One can connect and control the DMD using either a USB or an HDMI connection. When using a USB cable, it can be plugged into the port (labelled 3) in Figure 3.8. The DMD can then be controlled using software which can be downloaded from Texas Instrument's website. In principle the software allows for multiple DMDs and devices to be simultaneously connected and controlled by a PC. However, due to the poor optimisation of the software it is often unresponsive and prone to crashing. Therefore, connecting to the DMD in this manner is not recommended.

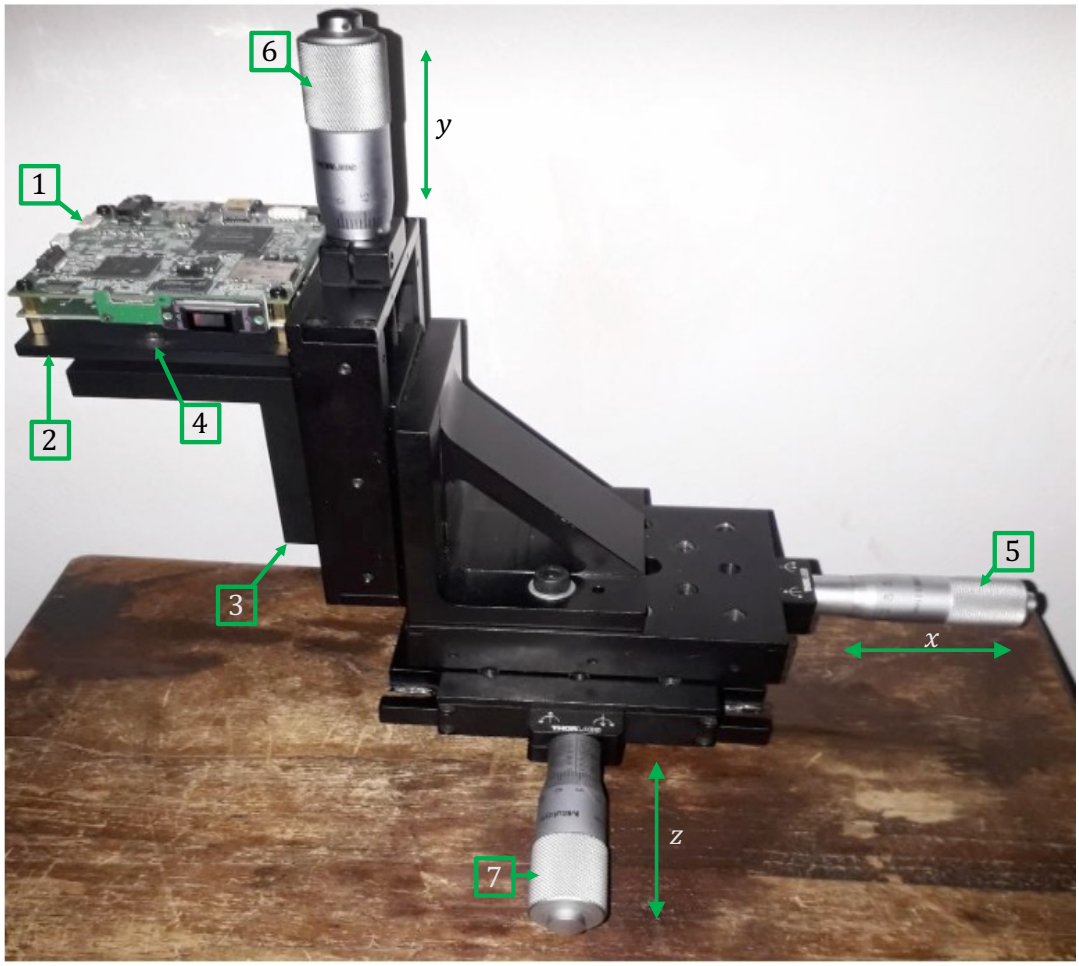


FIGURE 3.7: The recommended way to mount the DMD (labelled 1) is to secure the base plate (labelled 2) to a right-angled bracket (labelled 3) using a screw (labelled 4). By adjusting screws 5,6 and 7 one can reposition the DMD in the x, y and z directions, respectively.

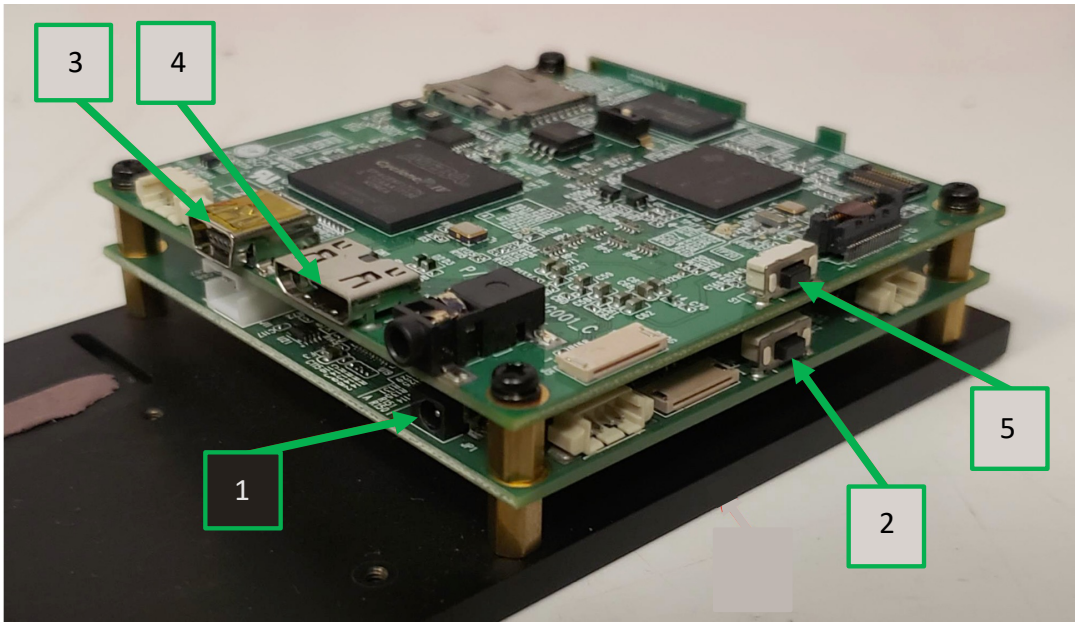


FIGURE 3.8: The driver unit of a DLP3000 DMD with labels highlighting the key components needed to connect to the DMD. (1) The power cable port; (2) The power button used to switch the DMD on; (3) USB port used to connect a PC to the DMD using a USB cable; (4) HDMI port to connect to the PC using an HDMI cable. This allows the DMD to act as a second screen to the PC; (5) Input source selection button used to choose the correct channel and screen for display.

Instead, one could connect to the DMD using an HDMI cable which can be inserted into the port (labelled 4) in Figure 3.8. This allows the DMD to act as a second screen to the PC. The DMD can now be controlled using Matlab. The benefit of this is that the hologram generation, displaying and capturing of a camera image can all be done using a single program and even automated. To ensure that the DMD is displaying the hologram it one must ensure that the correct input channel is selected. This can be done by continuously pressing the button (labelled 5)1 in Figure 3.8 until all inbuilt patterns have been cycled through and the HDMI input channel is selected, allowing for the hologram to be displayed.

3.3.3 Optical setup before the DMD

A common working configuration for a DMD, shown in Figure 3.9, is to use an expanded and collimated beam as the incident field. This ensures that the beam has a flat wavefront with a uniform intensity distribution. It is important to note that collimation is only necessary when doing amplitude-only and complex-amplitude modulation as it involves the 'carving' out of the incident light to form the desired shape. This is easily achieved with a suitable telescope prior to the DMD, as discussed in Chapter 2.

A collimated beam should have a constant beam size over a long propagation distance (more than a few metres). This can be verified in the lab by roughly measuring the beam size just after the telescope and comparing it to the size of the beam after it has propagated a distance > 3 m. If the beam sizes differ the separation distance between l_1 and l_2 must be adjusted until they do match.

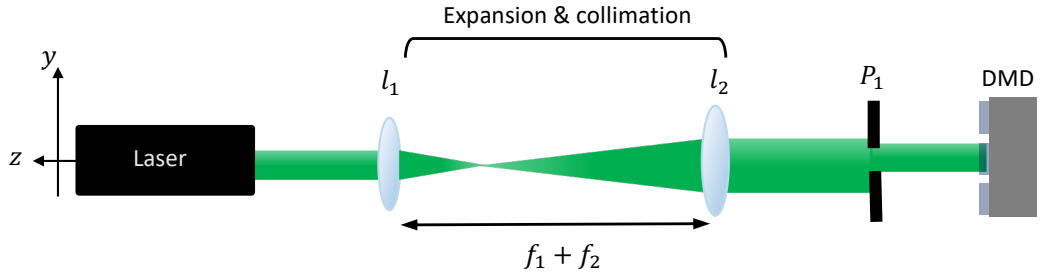


FIGURE 3.9: A common optical setup before the DMD includes a telescope comprised of two lenses l_1 and l_2 with focal lengths f_1 and f_2, respectively where $f_1 < f_2$. The lenses are separated by a distance equal to the sum of the focal lengths. An aperture P_1 is placed just before the DMD to control the size of the incident beam.

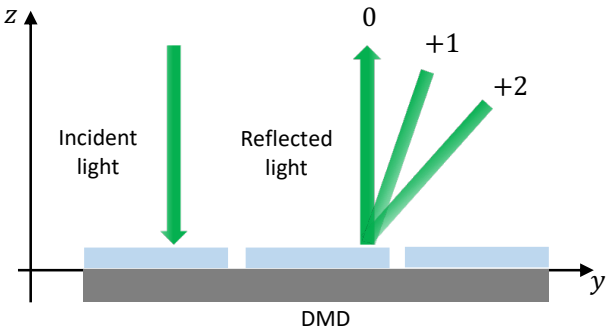


FIGURE 3.10: Due to the spacing between the micro-mirrors with the DMD screen, the incident beam will be diffracted into higher orders even though the DMD is not powered and the mirrors in the *parked* state. When setting up the DMD, the reflected and incident beams are then aligned through back reflection.

Once the incident beam has been successfully expanded and collimated an aperture, P_1 is added just before the DMD to control the beam size. By adjusting the aperture one can ensure that the beam fits comfortably on the DMD screen. It is important to note that the aperture should be kept fairly open to ensure that the beam is not diffracted.

3.3.4 Optical considerations

Rough alignment. To ensure that the DMD is correctly aligned we position the DMD until the incident beam sits roughly in the centre of the screen. Due to the spacing between the micro-mirrors, the incident beam will be diffracted even when the DMD is not powered and the micro-mirrors are in the *parked* state. Through the back reflection, the DMD is shifted until the reflected beam (0th order, which is usually the brightest spot) is aligned to the incident beam as seen in Figure 3.10. In this configuration the micro-mirrors are roughly perpendicular to the incident beam. However when the DMD is powered, mirrors in the *on* and *off* states will reflect light at $\pm 12^\circ$ relative to the normal incident beam.

Sorting diffraction orders. When a hologram is written on the DMD, due to the grating encoded in it, the light directed toward the desired plane will be separated into diffraction orders where the +1st order ($m = 1$) mode has the correct phase and

structure. To calculate the spatial position or angle of any of these orders, consider the diffraction grating equation

$$m\lambda = \lambda_x \sin\theta_m, \tag{3.16}$$

where m is the diffraction order number, θ_m is the diffraction angle for order m, λ is the incident wavelength and λ_x is the grating period (here shown for the x direction). This is illustrated in Figure 3.11, where a binary grating applied to the DMD, creates both $m = \pm 1$ orders as well as the unconverted $m = 0$ order, shown for a Gaussian input. The angles for each order determine the location of the spots in the Fourier plane, one focal length after a lens, and are given by $x_{\pm 1} = f\theta_{\pm 1} = \pm f\lambda/\lambda_x$, and similarly for the y off-set if there is a grating in y with a period λ_y. The physical separation of the beams allows one to select the desired order by a simple aperture. A second lens to form the image plane of the DMD recombines the light back to a single spot.

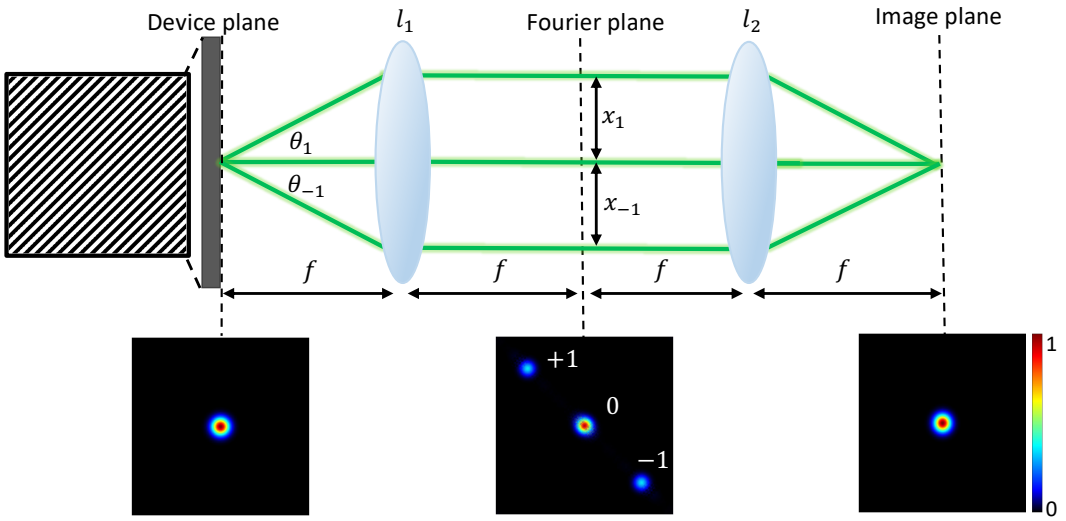


FIGURE 3.11: A Gaussian beam is incident on a binary grating displayed on a DMD, producing new diffraction orders of $m = \pm 1$. A Fourier transforming lens maps angles ($\theta_{\pm 1}$) to positions ($x_{\pm 1}$) in the Fourier plane, while a second lens reverses the process to return to the image plane of the DMD screen.

To ensure that there is no overlap between the orders, appropriate grating periods of λ_x and λ_y in the x and y directions, respectively, should be chosen. If the grating period is too low the orders will not be well separated, and if the grating frequency is too high ghost orders (a replica of the higher order modes) will appear. In both cases this will lead to an increase in background noise and/or a distortion of the mode.

Before aligning the output from the DMD, one needs to locate the +1st order diffracted beam. Against popular belief, the DMD does not act as a blazed grating [27]. Hence the +1st order beam is not necessarily the brightest one, making it difficult to distinguish from the other orders. This can be solved by programming a converging lens and a grating onto the DMD. To see how this works, consider the flow diagram shown in Figure 3.12. An incoming Gaussian beam is imparted with a lens and grating phase, resulting in it forming a converging beam in the +1st diffraction order

and a diverging beam in the -1st diffraction order (the 0th order is not influenced by the hologram phase). As shown in the right-hand panel, the $+1$st beam will be smallest near the focal plane of the programmed lens, and is therefore easy to locate. So long as the grating period is not change, the desired order will remain in the same position and can be selected with a judiciously sized and placed aperture.

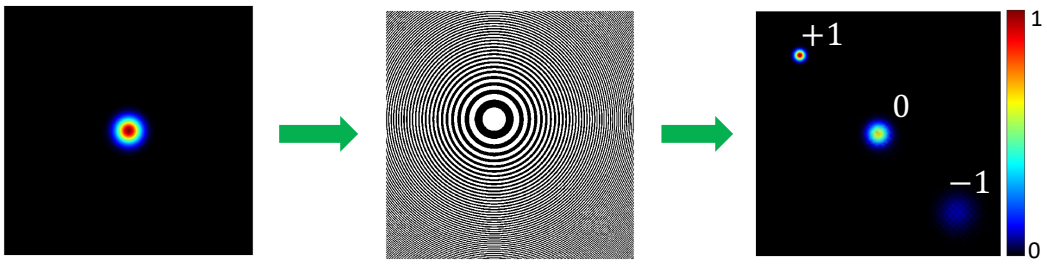


FIGURE 3.12: When a Gaussian beam is incident on a DMD encoded with a grating and converging lens, the output beam will diffract into orders that are converging, diverging or unaltered, shown here for $m = 0, \pm 1$. The desired +1st order will be the smallest in size compared to the other orders at a distance close to the programmed focal length, making it easy to identify and thus single out with an aperture.

Aberration correction. Aberrations are an inherent property of any optical element or system that arises from imperfections introduced during the manufacturing process and/or through wear-and-tear. Imperfections are not always noticeable and easy to locate, yet they can severely distort a structured beam. An example of this is shown in Figure 3.13 a) for a DMD that is both misaligned and aberrated. Correcting the alignment by following the steps already outlined results in a marginal improvement as shown in Figure 3.13 b), but the vortex splitting into many vortices is now clearly evident by the five central intensity nulls along a diagonal line. Correcting for the device aberrations produces the desired beam in Figure 3.13 c). This example illustrates why aberration correction is a vital step when using DMDs. A good way to describe the aberrations is to use the Zernike polynomials with weighting coefficients to describe the wavefront as

$$W_{\text{ab}}(x,y) = W_{\text{ref}}(x,y) - \sum_{j=0}^{N} C_j Z_j(x,y) \tag{3.17}$$

where C_j are the Zernike coefficients (units of waves) for the corresponding j_{th} Zernike polynomial $Z_j(x,y)$. A wavefront sensor can do this decomposition, but it is often more convenient to use the structured light itself as a probe. To this end, vortex modes with a low OAM value ($l = 1$) are extremely sensitive to any phase distortions. When observed in the Fourier plane these irregularities are converted to amplitude distortions, making it easier to identify: take another look at the vortex splitting in Figure 3.13 b). By adjusting the correcting phase until the beam is pristine, the aberrations in the entire path to the detector are corrected, including that of the DMD.

When doing aberration corrections a semi-empirical approach is the easiest to implement. Often, first-order astigmatism is the main contributor of aberrations to the system. Therefore, by encoding Zernike phase maps corresponding to first-order

astigmatism, or any other prominent aberration, and manually adjusting the weighting coefficients of these polynomials until the vortex mode appears 'perfect' in the Fourier plane, one can correct for much of the phase error. The weighting coefficients represent the root-mean-square (RMS) wavefront error attributed to the respective aberration and they are independent of the number of polynomials used in sequence [125]. In other words, coefficients of a term can be changed without it affecting other polynomial terms.

It is important to note that in some cases, DMDs have a prominent defocusing aberration associated with it. Unlike astigmatism or other aberrations, the defocusing aberration cannot be corrected for in a traditional manner. To correct for the defocusing of the DMD a converging lens must be encoded with a focal length that is exactly equal to the separation distance of the DMD and observation plane. The weighting coefficient of the defocus Zernike polynomial should then be adjusted until the mode is the smallest size.

Finally, to optimise the setup one must do a fine alignment to account for minute misalignments. This cannot be easily seen if the beam is quite distorted, hence aberration correction is usually done first. To do this the DMD is now encoded with a hologram consisting of a grating (the same frequencies as before) and a mode with a circular shape, for example a vortex $l = 5$ (in this case a high OAM value is preferable). The modulated +1st order beam should be singled out using an aperture. If the DMD is misaligned as seen in Figure 3.13 a), then as the aperture in the expansion and collimation system is closed so the intensity of the beam will be reduced. To correct for this misalignment the encoded hologram needs to be shifted in the $x - y$ plane until the beam appears perfect, as seen in Figure 3.13 c). This can be done by shifting the $x - y$ coordinates when creating the matrix for the hologram code. If the shift required is large, the DMD itself should be shifted slightly using the translation stages it is mounted on.

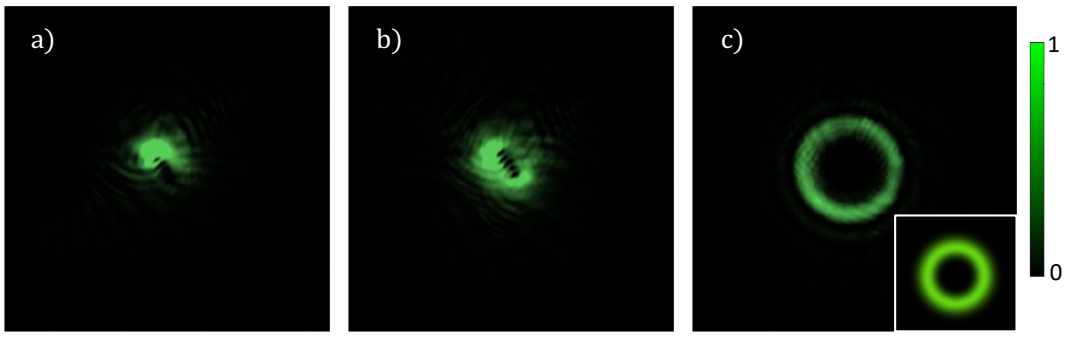


FIGURE 3.13: Experimental images depicting the effect misalignment and aberrations have on a structured vortex ($l = 5$) beam. a) Misaligned and aberrated, b) Aligned and aberrated, c) Aligned and corrected for aberrations. The simulated/ideal beam is shown as an insert.

3.4 Monochromatic beam shaping

As previously mentioned, one can shape light through phase-only or complex-amplitude modulation. In this section we explore how to use a DMD to shape monochromatic light (one wavelength) using both methods. To do this we select two examples: (1)

the creation of a flat-top beam from a Gaussian using a phase-only solution, and (2) the creation of a LG beam by complex amplitude modulation from an input plane wave.

3.4.1 Creating flat-top beams

In the first example, a Gaussian beam is incident on an element with desired the phase-only transmittance $t(r) = 1\exp[i\varphi(r)]$ followed by a lens with transmittance $t_{\text{lens}} = \exp\left[-ikr^2/(2f)\right]$, where f is the focal length of the lens. The desired flat-top beam is located at a distance f after the lens. To understand the role of the lens, consider the following: When performing phase-only modulation the beam shaping element, a DMD in this case, imparts a phase change to the incident coherent light that causes a redistribution of the Gaussian's intensity until it is uniform i.e., a flat-top. Although this phase change occurs at the DMD's plane, it is noticeable as an amplitude effect as the beam propagates. Hence, when performing phase-only modulation the beam should be observed in the far field where it will have the desired phase and structure of a flat-top. This process is illustrated in Figure 3.14. Using the theory in Chapter 1, one can solve this problem in integral form to find

$$\varphi(r) = \beta\frac{\sqrt{\pi}}{2}\int_0^{\frac{\sqrt{2}r}{w}}\sqrt{1-\exp(-\rho^2)}\mathrm{d}\rho. \tag{3.18}$$

where

$$\beta = \frac{2\sqrt{2\pi}w_0 w}{\lambda f}. \tag{3.19}$$

Here w_0 is the $1/e^2$ Gaussian radius and w is the flat-top beam size. When β is large (> 30) the solution is easy to implement, the flat-top will be of a high quality, and the geometric approximations are valid. In this one-step solution, the first shaping element converts the Gaussian into a flat-top beam while leaving the phase as a free parameter, implying that we would need a second shaping element, such as a lens, to correct the phase. We have not manually added a grating since this is already assumed in Equation 3.7. Thus the desired hologram to be encoded on the the DMD has the following form and can be visualised in the inset of Figure 3.14:

$$H_1(x,y) = \frac{1}{2} + \frac{1}{2}\text{sign}\left\{\cos[2\pi\left(\frac{x}{\lambda_x}\right) + 2\pi\left(\frac{y}{\lambda_y}\right) + \varphi(x,y)] - \cos(\arcsin[1])\right\}. \tag{3.20}$$

A simulation of the outcome is seen in Figure 3.15, where an incident Gaussian beam (left) is converted into an output flat-top beam (right).

To demonstrate this process experimentally, we use the system as seen in Figure 3.16 a). In this experiment a monochromatic beam (λ = 514 nm) was imaged onto the DMD using lenses l_1 (f = 100 mm), l_2 (f = 100 mm). Imaging the beam allows us to control the incident beam size, an important factor when generating flat-top beams. The DMD was encoded with a hologram depicted in Figure 3.16 b), consisting of the desired phase, a grating and aberration correction, before binarisation for the DMD. A lens (l_3 with a focal length f_3= 200 mm) and aperture were used to select the desired diffraction order, with the lens acting as a Fourier transforming element (as needed in this design approach). It would be ideal to place the aperture in the Fourier plane as the beams are smallest in size, making it possible to discard most of

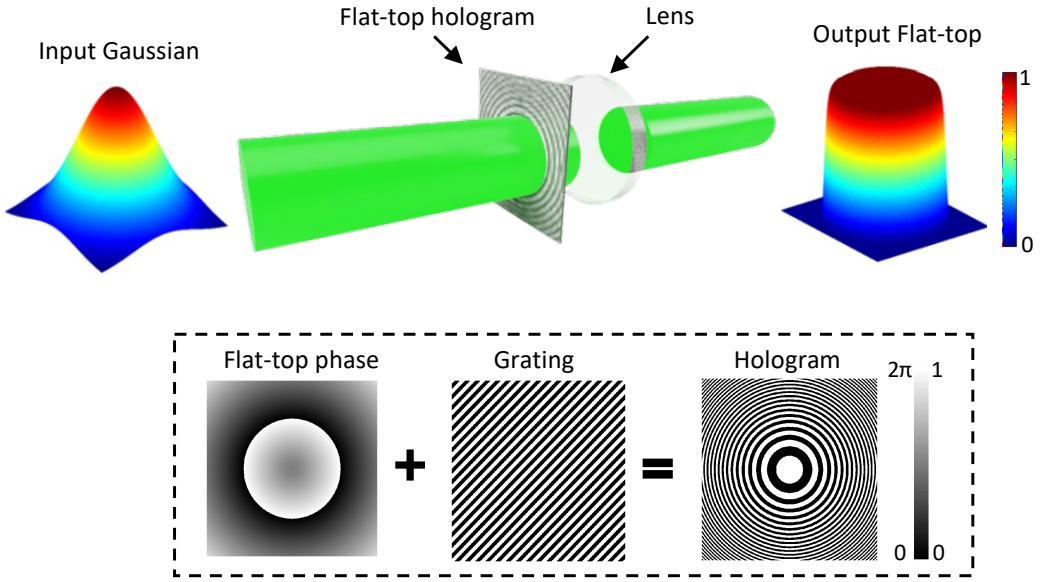


FIGURE 3.14: A Gaussian beam is modulated in phase and passed through a lens, with the desired output flat-top beam observed in the focal plane of the lens. The flat-top hologram consists of a flat-top phase (following the theory) and a grating, which are then binarised for display on the DMD. Aberration correction is not shown (but always applied) for pedagogical reasons.

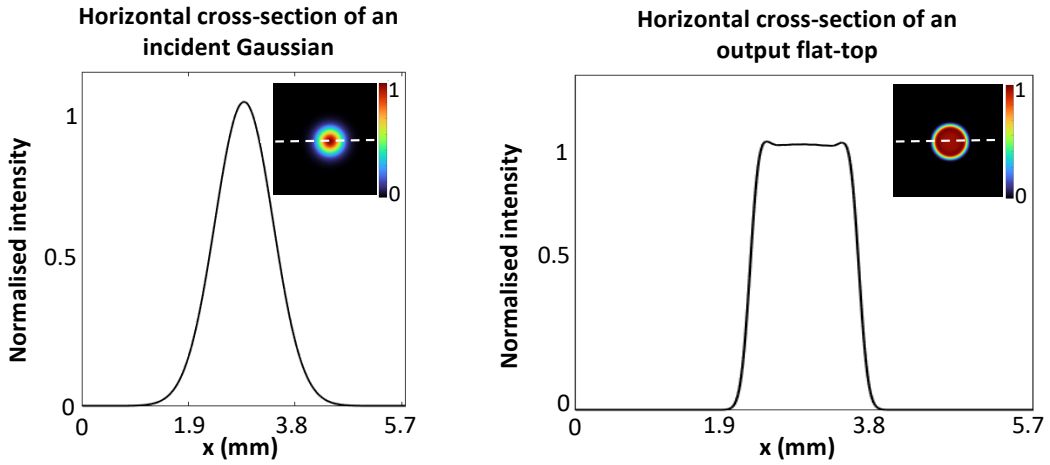


FIGURE 3.15: The simulated results of converting an incident Gaussian (left) through phase-only modulation to an output flat-top beam (right) using a hologram that would be encoded on a DMD. The cross sections of the individual modes are shown with their respective intensity profiles depicted as insets.

the 'noise' from unwanted orders, however because the scalar flat-top beam is only formed in the Fourier plane the charge-couple device (CCD) camera must occupy this position to allow us to observe the desired flat-top.

Figure 3.17 a) depicts the simulated and experimental flat-top beam's intensity profiles while Figure 3.17 b) depicts the corresponding cross-sections. The beam size of the incident Gaussian and desired flat-top was 0.48 mm and 0.50 mm, respectively which corresponds to a $\beta = 12$. The experimental flat-top was measured to be 0.515 mm ± 0.0068 mm and has a correlation value of 96.9% to simulation. Ideally one

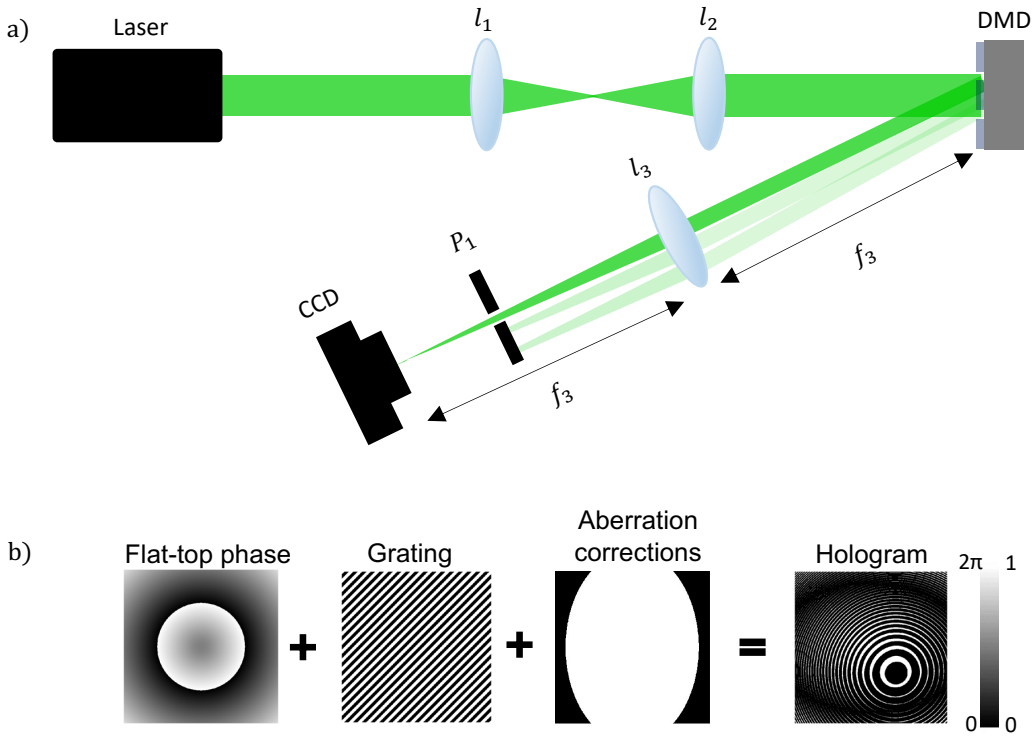


FIGURE 3.16: The experimental process of making a flat-top beam. a) The experimental setup: a monochromatic beam (λ = 514 nm) was imaged onto the DMD using lenses l_1 (f = 100 mm), l_2 (f = 100 mm). The DMD was encoded with b) a hologram comprising of a flat-top phase mask, grating and aberration correction phase mask. The incident beam was then modulated and diffracted into its various orders. A lens, l_3 (f = 200 mm) was placed a focal length away from the DMD and Fourier transforms the modes. Slightly before the Fourier plane, an aperture P_1 was inserted to single out the +1st order. A CCD camera was placed in the Fourier plane, allowing us to observe the desired flat-top.

would encode a flat-top with a larger β value. However, for the diffracted beams to separate from each other so one can select the +1st order, propagation is needed. Therefore, a lens with a longer focal length is preferred after the DMD. This unfortunately reduces the value of β. One could increase the beam size of the input Gaussian beam to compensate for this, however due to space limitations we were unable to do so in this instance.

3.4.2 Creating LG beams

In the second example, we want to create vortex beams in the manner illustrated in Figure 3.18. In this case the incoming beam is expanded to be a near plane wave, that is, constant phase (collimated) and amplitude normalised to $A_{\text{in}} = 1$. The desired beam is to be created by modulating both the amplitude and phase in proportion to a vortex beam of $l = 1$, therefore the transmittance function is $t(r,\phi) = |\text{LG}_0^1(r,\phi,0)|\exp(i\phi)$, normalised so that the peak value is 1, to match the incoming amplitude. The amplitude modulation carves out the desired function from the incoming field, similar to a cookie cutter, while the phase term imparts the azimuthal variation. Noting that the azimuthal angle is $\phi = \arctan(y/x)$, the desired hologram for the DMD for this second case is

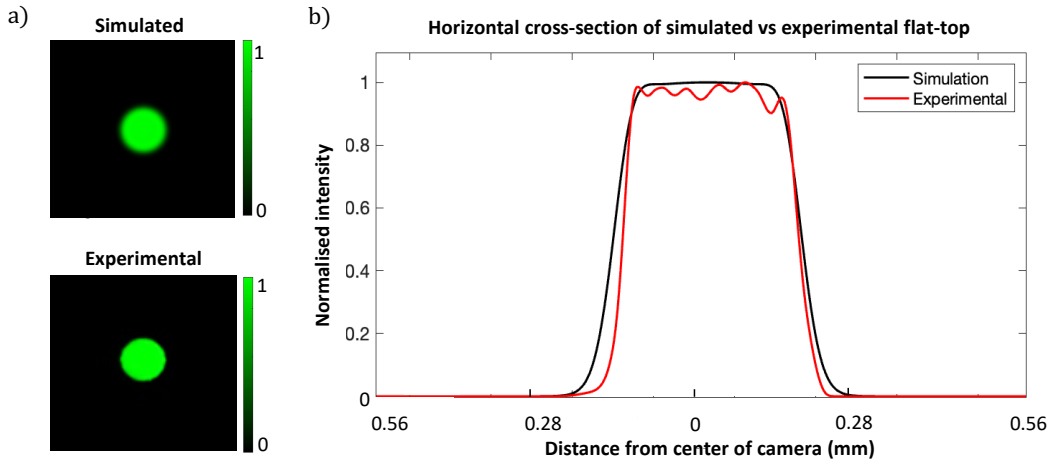


FIGURE 3.17: Experimental results of a created flat-top ($\lambda = 514$ nm). a) The intensity profiles of a simulated (top) and experimental (bottom) flat-top beam. b) Horizontal cross-sectional comparison of the simulated and experimental beams, which have a correlation value of 96.9%.

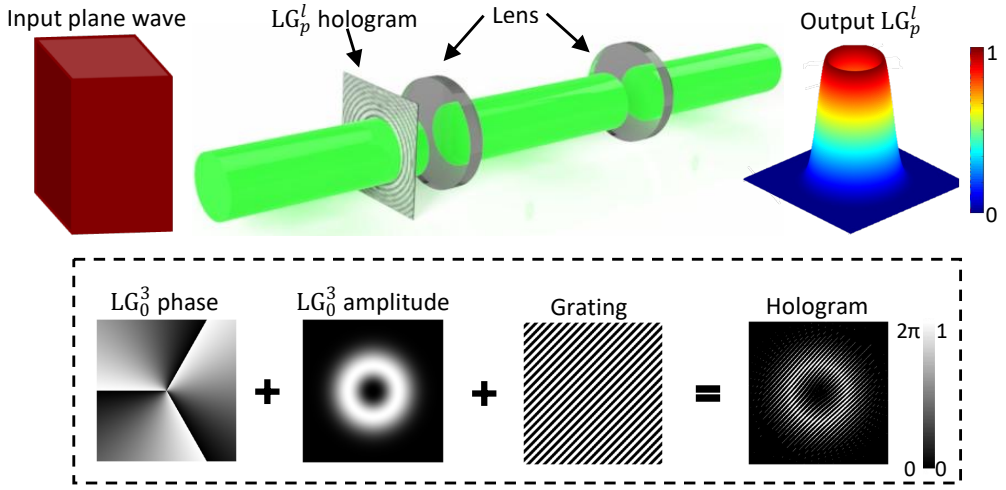


FIGURE 3.18: The process of making an LG beam: an expanded and collimated beam (plane wave) is incident on a beam shaping element which structures the incident light through complex-amplitude modulation. The beam then passes through a telescope that translates the generated mode to the image plane. In an ideal case, such as a simulation the LG_0^3 mode can be generated by (inset) a hologram that comprises of the desired amplitude, phase and lens masks as well as a grating. Using this hologram we are able to structure the incident beam through complex-amplitude modulation. c) The simulated intensity profiles and cross sections of the incident Gaussian and output LG_0^3 beams are given.

$$H_2(x,y) = \frac{1}{2} + \frac{1}{2}\text{sign}\left\{\cos[2\pi\left(\frac{x}{\lambda_x} + \frac{y}{\lambda_y}\right) + \arctan(y/x)] - \cos\left(\arcsin[|\text{LG}_0^1(r,\phi,0)|]\right)\right\}. \tag{3.21}$$

and can be visualised as depicted in the inset of Figure 3.18. By using this hologram we are able to manipulate both the phase and amplitude of the incident beam and generate the desired $LG_{p=0}^{l=3}$ mode. In this case the vortex beam is created at the plane of the DMD. One could simply allow it to propagate away, slowly separating from

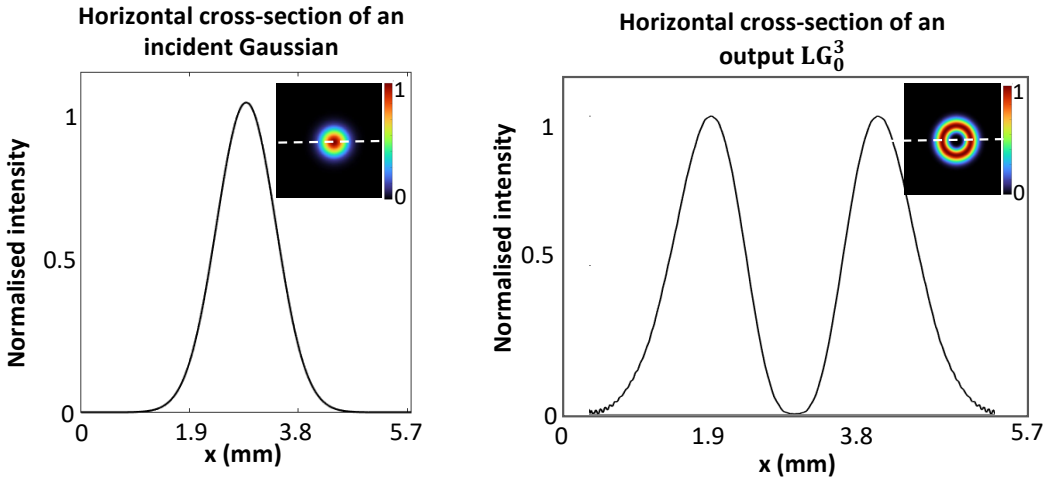


FIGURE 3.19: The simulated results of converting an incident Gaussian (left) through complex-amplitude modulation to an output LG_0^3 beam (right) using a hologram that would be encoded on a DMD. The cross-sections of the individual modes are shown with their respective intensity profiles depicted as insets.

the other diffraction orders, but this will introduce additional phases via the z dependent terms in the LG function. Instead, one can image the DMD plane with a telescope, relaying the desired mode away from the DMD to a more manageable optical plane. By encoding the telescope digitally we are able to simulate the process of manipulating the input Gaussian beam (left panel of Figure 3.19) through complex-amplitude modulation into the desired LG mode (right panel of Figure 3.19).

To demonstrate this experimentally we setup the system as depicted in Figure 3.20 a). In this experiment a coherent beam (λ = 514 nm) was expanded and collimated by l_1 (f = 100 mm) and l_2 (f = 300 mm). Aperture, P_1 controls the size of the incident beam. The DMD was encoded with the above mentioned hologram, however an additional phase mask was added to correct for inherent aberrations in the system, as seen in the Figure 3.20 b). When the collimated beam was incident on the DMD, it was then diffracted and modulated. The diffracted beams then passed through l_3 (f = 200 mm) where the +1st order was singled out by aperture P_2, located in the Fourier plane of l_3. The +1st order then passed through l_4 (f = 200 mm) which images the beam. Using a CCD camera, the LG_0^3 beam was observed in the image plane of the DMD.

Figure 3.21 shows the experimental results for a LG_0^3 mode. Figure 3.21 a) shows the simulated and experimental intensity profiles and Figure 3.21 b) depicts their corresponding cross sections. The experimental mode has a correlation value of 92.6% when compared to simulation. Using the cross-section one is able to measure the distance between the peak intensities and thus determine the beam size. Since one observes the mode in the image plane of the DMD, the size of the encoded LG mode and the size of the experimental mode should be similar. In this case the encoded LG beam's size was set to 0.500 mm, and the experimental beam had a beam size of 0.495 mm $\pm$ 0.004 mm. Hence, DMDs can indeed be used for monochromatic complex-amplitude modulation.

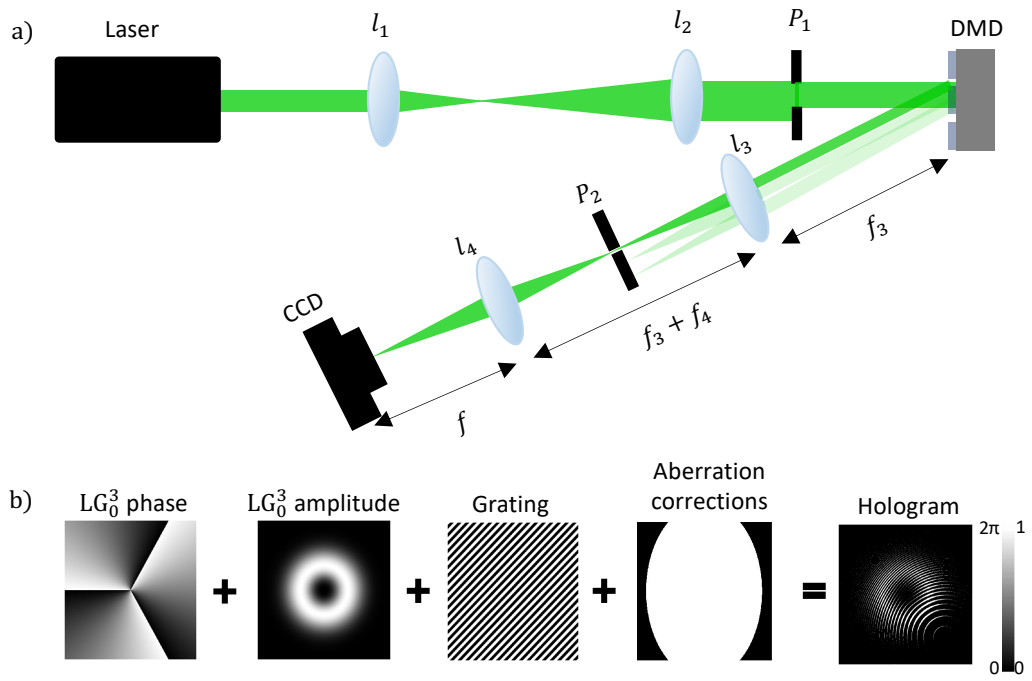


FIGURE 3.20: a) The experimental setup: a monochromatic beam (λ = 514 nm) is expanded and collimated using lenses l_1 (f = 100 mm), l_2 (f = 300 mm) with aperture P_1 controlling the beam size. The beam is then incident on the DMD that has been encoded with b) a hologram comprising the LG phase and amplitude, a grating and aberration correction. A telescope made of lens l_3 (f = 200 mm) and l_4 (f = 200 mm) images the DMD plane to that of the CCD camera, with an aperture P_2 is inserted to single out the desired diffraction order. c) The experimental output beam is shown with its intensity cross-section

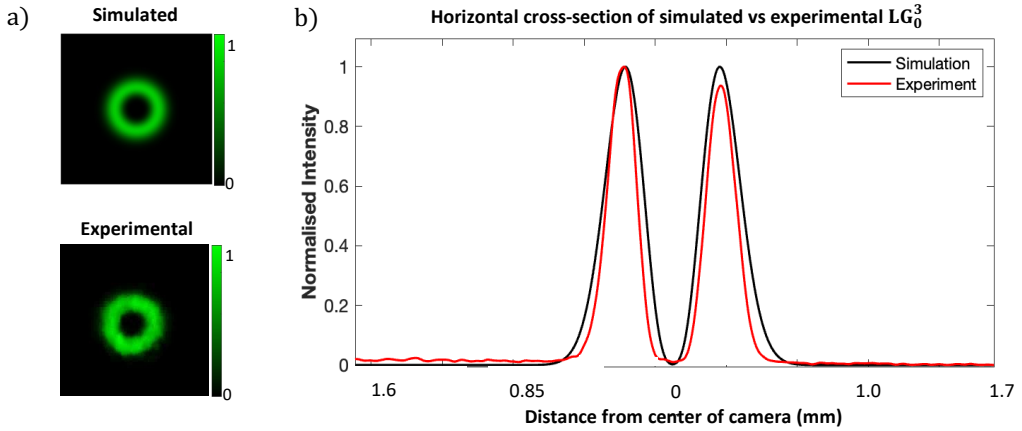


FIGURE 3.21: Experimental results of a created LG_0^3 (λ= 514 nm). a) The intensity profiles of a simulated (top) and experimental (bottom) LG beam. b) Horizontal cross-sectional comparison of the simulated and experimental beams, which have a correlation value of 92.6%.

3.5 Broadband beam shaping

In this section we extend the same tools and techniques to shape multiple wavelengths of light with a DMD. To do this we must remove or compensate for any

wavelength-dependency in the theory, optics and system as a whole. We have already shown theoretically that a simple grating will remove any wavelength dependency of the hologram, at the expense of a small efficiency drop and dispersion of the grating itself. In this section we first demonstrate that indeed the shaping can be wavelength independent, and then address the issue of dispersion compensation of the grating.

3.5.1 Wavelength independent beam shaping

We first simulate the beam shaping problem, with an example an LG_0^3 mode shown in Figure 3.22. In this simulation the phase mask is created for a design wavelength λ_0 = 488 nm. The wavelength of the incident beam is then set to λ_0 = 488 nm, followed by two additional off-design wavelengths of λ = 457 nm and λ = 514 nm. As expected, the results shown in Figure 3.22 a) show that all three modes have identical amplitude and phase structure. For enhanced visualisation, we then converted each image into its true colour using the 'spectrumRGB' function (available on MatLab's open source [126]) which takes an input wavelength value and outputs an RGB value that corresponds to the wavelength's true colour, as seen in Figure 3.22 b). The individual beams' images were then imported as matrices in MatLab, added together and normalised. The result was a digital broadband beam with the correct amplitude and phase structure, depicted in its true colour, as seen in Figure 3.22 c).

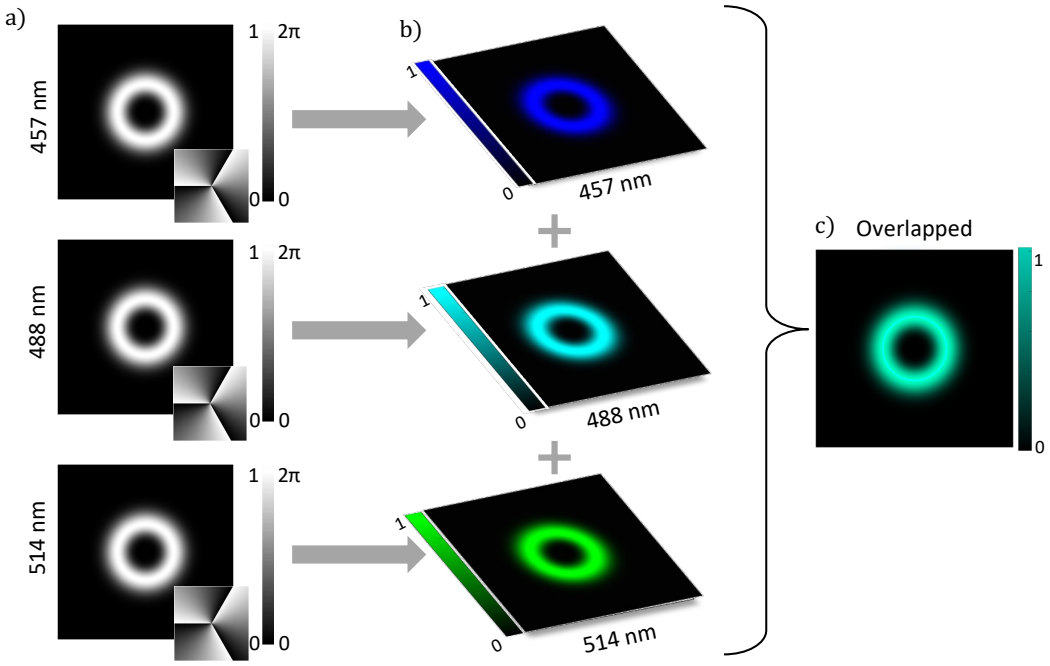


FIGURE 3.22: a) Simulated multi-wavelength LG_0^3 modes, all created with a hologram designed for λ_0 = 488 nm. The intensity is shown in grayscale with the phase shown in the insets. b) True colour visualisation of each mode using the 'spectrumRBG' function on MatLab. c) The individually coloured simulation matrices are then added together and normalised for an overlapped multi-wavelength beam.

To verify this process we used the setup seen in Figure 3.23 a), where this time the desired mode was a broadband flat-top. In this section, and subsequent chapters

where broadband beam shaping is done experimentally, we will use an argon-ion laser which emits three discrete wavelengths λ = 457 nm, 488 nm, 514 nm and a multiline where all three wavelengths are emitted and propagate co-linearly. We will also use achromatic lenses which are designed to compensate for chromatic aberrations.

The experiment was conducted as follows: a broadband beam composed of three wavelengths (λ = 457 nm, 488 nm, 514 nm) was emitted from an Argon-ion laser. Using two achromatic lenses, l_1 (f = 200 mm), l_2 (f = 200 mm) this beam was imaged onto the DMD which was encoded with the same experimental flat-top hologram as seen in the inset of Figure 3.23 a), where λ_0 = 488 nm. All alignment and aberration correction procedures were performed using λ_0. The broadband beam was then Fourier transformed using achromatic lens l_3 (f = 200 mm) and aperture P_1 was used to select the +1st order of each wavelength. It is worth noting that the grating frequencies in the encoded hologram had to be adjusted in an iterative manner until all beams were adequately separated. In the Fourier plane a CCD camera was used to view and capture an image of each beam independently, with the results shown in Figure 3.23 b). Using MatLab, these three individual images were imported as matrices and converted to their true colours using the 'spectrumRGB' function [126]. The matrices were then added together and normalised. The result is a digitally overlapped broadband flat-top as seen in Figure 3.23 c).

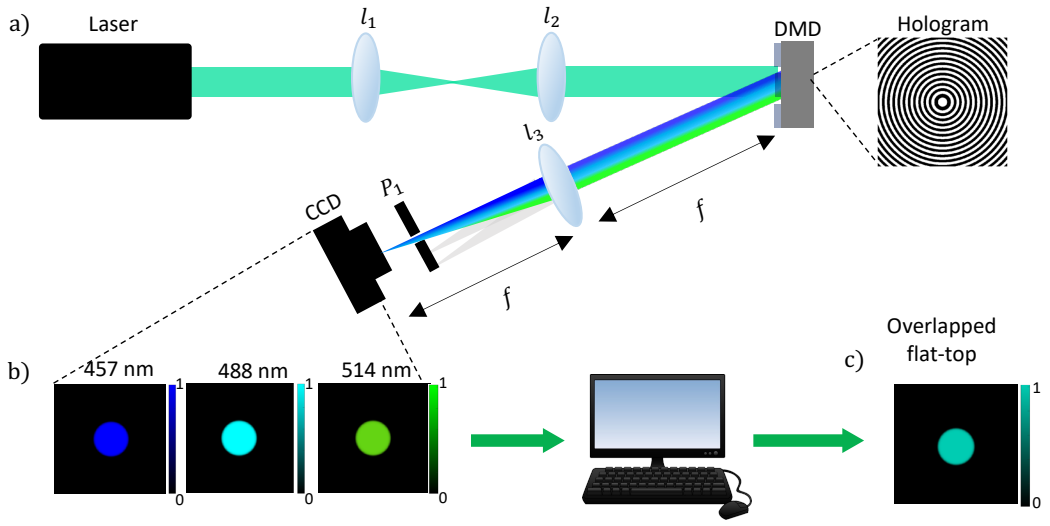


FIGURE 3.23: Experimental setup and process to generate flat-top beams for various wavelengths. a) An Argon-ion laser emitted a broadband beam (consisting of λ = 457 nm, 488 nm, 514 nm) and was imaged onto the DMD a telescope with achromatic lenses l_1 (f = 200 mm) and l_2 (f = 200 mm). The DMD was encoded with a hologram (inset) and Fourier transformed by achromatic lens l_3 (f = 200 mm). Before the focal plane, the +1st orders of each wavelength were selected using aperture, P_1. b) CCD camera intensities for each wavelength. c) The images were then imported as matrices into MatLab where they were converted into their true colour, added together and normalised, for the final digitally overlapped broadband flat-top.

A zoom in of the experimental results are shown in Figure 3.24. Figure 3.24 a) shows the camera images at each wavelength (λ = 457 nm, 488 nm, 514 nm) where the design wavelength was λ_0 = 488 nm. Figure 3.24 b) shows the intensity profile of the

broadband flat-top beam generated through digital overlap of the individual flat-tops for each wavelength. Figure 3.24 c) shows the cross-sectional comparison of the individual flat-tops as well as the digitally recombined broadband (multiline) flat-top beam. Apart from some noise, we see that the desired mode was produced correctly for all wavelengths with the digitally recombined flat-top having a correlation value of 89.2% with simulation.

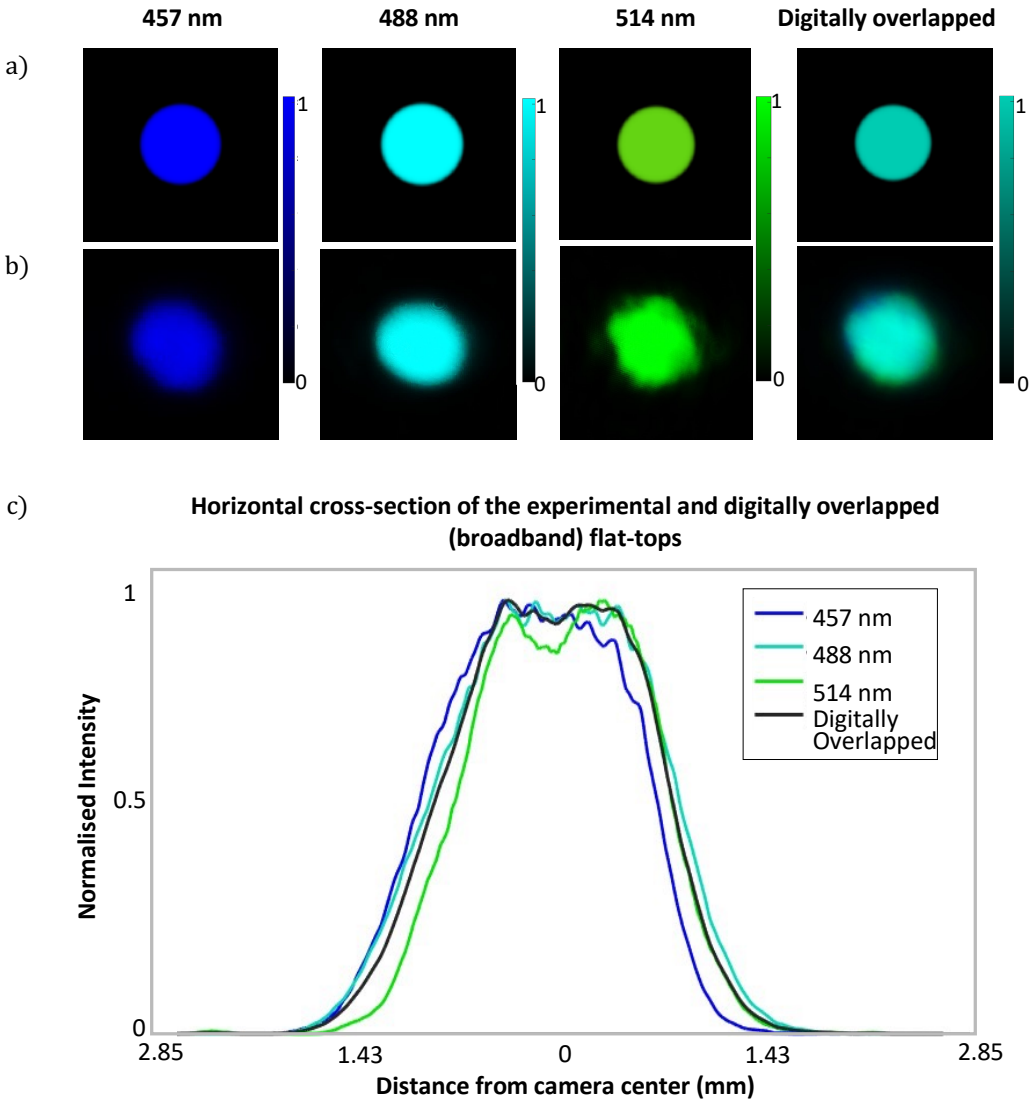


FIGURE 3.24: Experimental results of flat-top beams that have been generated for various wavelengths. a) The simulated and b) experimentally generated flat-top beams for each wavelength and the digitally overlapped broadband beam. c) A cross-sectional comparison of the experimentally generated flat-tops for each discrete wavelength and the digitally overlapped broadband beam.

3.5.2 Experimental compensation of dispersion

In the previous section we demonstrated that by digitally overlapping each structured beam per wavelength we could achieve a structured broadband beam. The task that now lies before us is to achieve this spatial overlap action experimentally.

In an experimental setting we can recombine the individual structured beams by adding an achromatic lens or achromatic telescope which can be used for single plane recombination as seen in Figure 3.25 a), or we can add a compensating dispersive element, such as a corrective grating (this can be digital or physical) for true collinear beam recombination as seen in Figure 3.25 b). We combine these notions in a typical system as illustrated in Figure 3.25 c), showing the DMD grating as a dispersive element, a telescope that first maps angles to position before recombining them back at an image plane, and an optional second dispersive element (complementary element) to recombine the many wavelengths into a single multi-wavelength outgoing structured beam. This type of configuration is very common in ultrafast laser beam shaping [127, 128]. The options are therefore: (1) if the multi-wavelength beam is needed only at a single plane with full amplitude and phase control, then a simple telescope will work, (2) if only intensity is needed at a single plane then this can be reduced to just one lens, and (3) if the multi-wavelength beam must be collinear and shaped then a telescope and grating pair is needed.

The outcome of this is shown in Figure 3.25 d) for cases (1) and (2): before the image plane the beams disperse, recombine at the image plane, and then separate again after the telescope. Case (3) is illustrated in Figure 3.25 e). By adding a compensating element such as a grating (either a digitally encoded grating or a physical) with the same grating frequency as that grating encoded on the DMD, the dispersion will be exactly counterbalanced, resulting in the individually structured beams travelling co-linearly. Hence what we observe after in the image plane and thereafter is a single structured broadband beam with the correct phase and intensity profile as seen in the right image of Figure 3.25 e). Using a second grating allows for a collinear beam, and has been done extensively with physical gratings [127, 128] and even more recently in the context of complex-amplitude and phase-only modulation using a DMD [64].

However, let's assume that for a particular application it is only important for the broadband beam to have the desired intensity profile (not the correct phase) in a single-plane. We can then use the simpler recombination method as illustrated in Figure 3.26. The reason why this single lens imaging system recombines the individually structured beams be understood by referring to basic ray-tracing theory. Although the broadband beam will have the correct structure, it will not have the correct phase because a second element has not been added to correct for the additional phase gained during propagation. After the image plane, the individual beams per wavelength will propagate separately as seen in the right inset of Figure 3.26.

We demonstrate this method experimentally, with the setup shown in Figure 3.27 a). In this experiment an argon-ion laser emmited a broadband beam (comprised of λ = 457 nm, 488 nm, and 514 nm) and was expanded and collimated by l_1 (f = 100 mm) and l_2 (f = 300 mm). Aperture, P_1 controls the size of the incident beam, as previously discussed. The DMD was encoded with a hologram generated for λ_0 = 488 nm (shown in Figure 3.27 b)) which was comprised of phase, amplitude and aberration correction masks as well as a grating. When the collimated beam was incident on the DMD, it was then modulated and diffracted into various orders per wavelength. The diffracted beams then passed through an achromatic lens l_3 (f = 200 mm) which was located a distance twice the focal length ($2f$) away from the DMD. In the Fourier plane of lens l_3, the +1st order per wavelength. The +1st orders

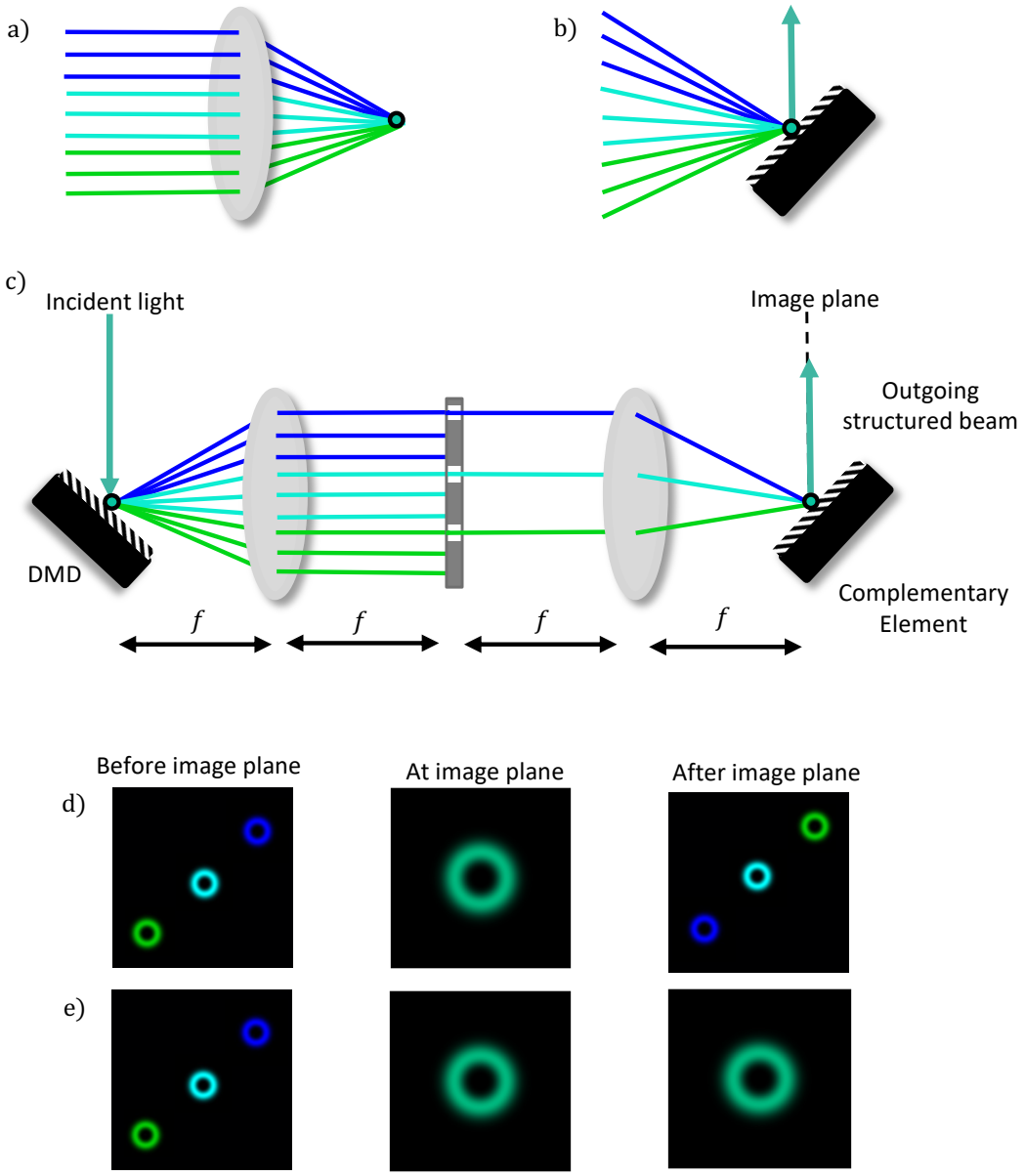


FIGURE 3.25: Experimental optical tools and techniques to compensate for the dispersion of the broadband beam. a) A simple lens or telescope can recombine wavelengths at one plane. b) A grating can combine wavelengths into a single collinear beam. c) A combination of both, where an incident broadband beam is wavelength separated by a grating on the DMD. The dispersed beam is then incident on an achromatic lens placed a focal length distance away from the DMD that maps the angles to positions, with a second achromatic lens recombining the beams at a single plane, the image plane of the DMD. An optional second dispersive element (complementary element) could be used to create a collinear shaped beam. Examples of the outcome are shown using LG_0^3 beams for d) just a telescope and e) telescope and complementary element with an identical grating (physical or digital).

were then observed in the image plane of the DMD using a CCD camera. To ensure that the CCD camera was placed in the correct plane it was shifted back-and-forth until a single beam was observed.

The results for a LG_0^3 mode (as an example) are shown in Figure 3.28 a) as camera

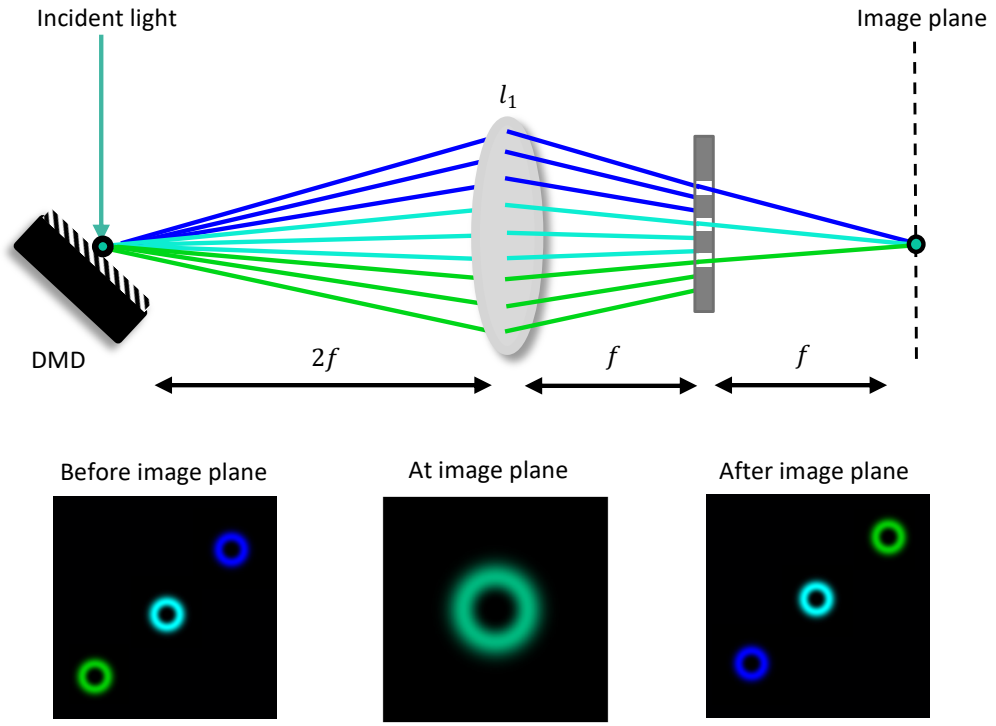


FIGURE 3.26: An experimental method for structuring a broadband beam using a DMD and a single lens so that it has the correct intensity at a single plane only. The panels below show the beams at achromatic lens l_1 (with focal length f), at the image plane, and after the image plane when the light separates due to propagation.

images, and in Figure 3.28 b) as beam intensity cross-sections for each discrete wavelength, as well as the broadband 'multiline'. In c) the cross-sectional comparison of the experimental multiline beam and the simulated result is shown and was found to have a correlation value of 95.3%.

The noise in the recorded beams is worth discussing as it highlights a challenge in these experiments. The noise in the system was as a result of the high grating frequencies used to adequately separate the +1st orders for each wavelength. This was necessary due to: (1) the space limitation, i.e, a large propagation distance to allow the modes to naturally separate was not feasible; (2) the wavelengths are quite close in value, hence when diffracted they are do not have a large initial spatial separation; (3) the individual wavelengths and their respective orders were not evenly spaced nor grouped together, for example, the +1st order of one wavelength could be overlapped with the 0th order of the another wavelength. Due to this effect a make-shift aperture had to be used which was not as efficient at blocking out unwanted modes or stray light as a traditional spatial filter, also contributing to the noise seen in the intensity images. Longer focal lengths and thus longer distances would solve these issues.

In Figure 3.28 we demonstrated broadband beam shaping and in-plane recombination for a specific case when the encoded mode was an LG_0^3 mode. However, it is important to note that any mode can be encoded and the same effect would be observed. To demonstrate this we encoded an array of various LG modes with varying azimuthal and radial indices. The experimental results for each discrete wavelength and for the broadband multiline are shown in Figure 3.29.

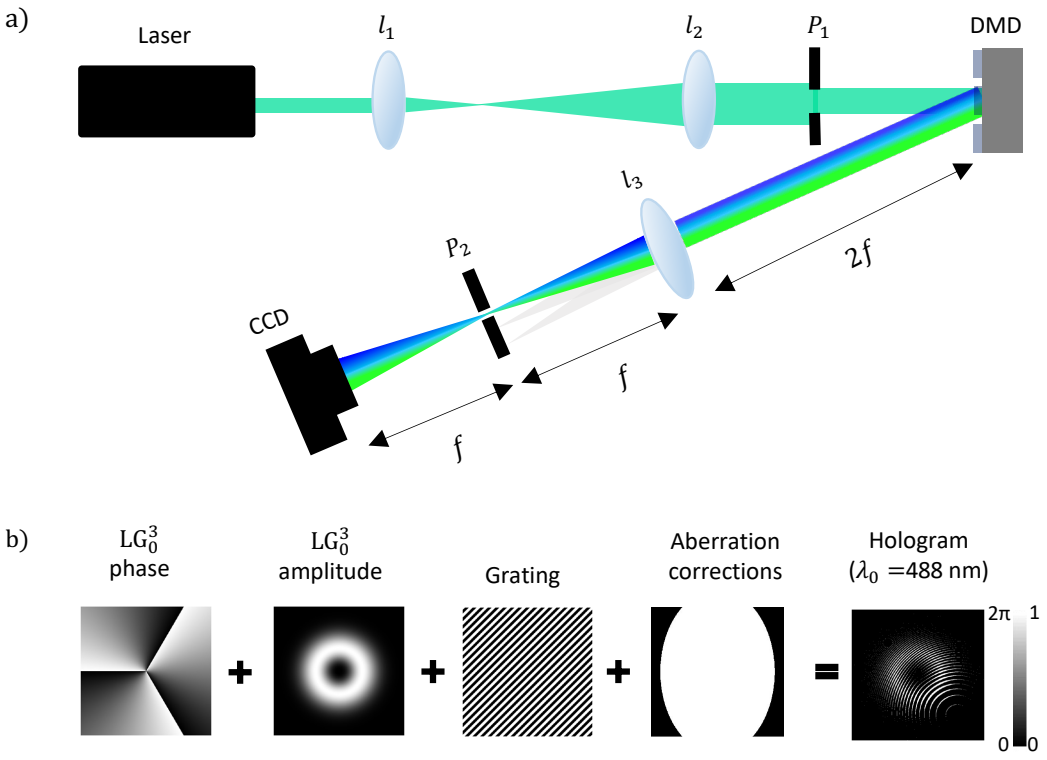


FIGURE 3.27: Experimental setup for demonstrating single-plane recombination. a) The experimental setup consists of a monochromatic broadband beam that has been expanded and collimated by two achromatic lenses l_1 (f = 100 mm), l_2 (f = 300mm), where the beam size is controlled by aperture, P_1. The beam is then incident on a DMD which has been encoded with a hologram to generate an LG_0^3 mode. The dispersed beam then propagates to achromatic lens l_3 (f = 200 mm) that is located twice the focal length after the DMD. A focal length after the lens a make-shift aperture is placed to select the +1st orders of each wavelength. The beams then propagate a focal length away to the image plane where a CCD camera is placed to observe the single-plane recombined, structured broadband beam.

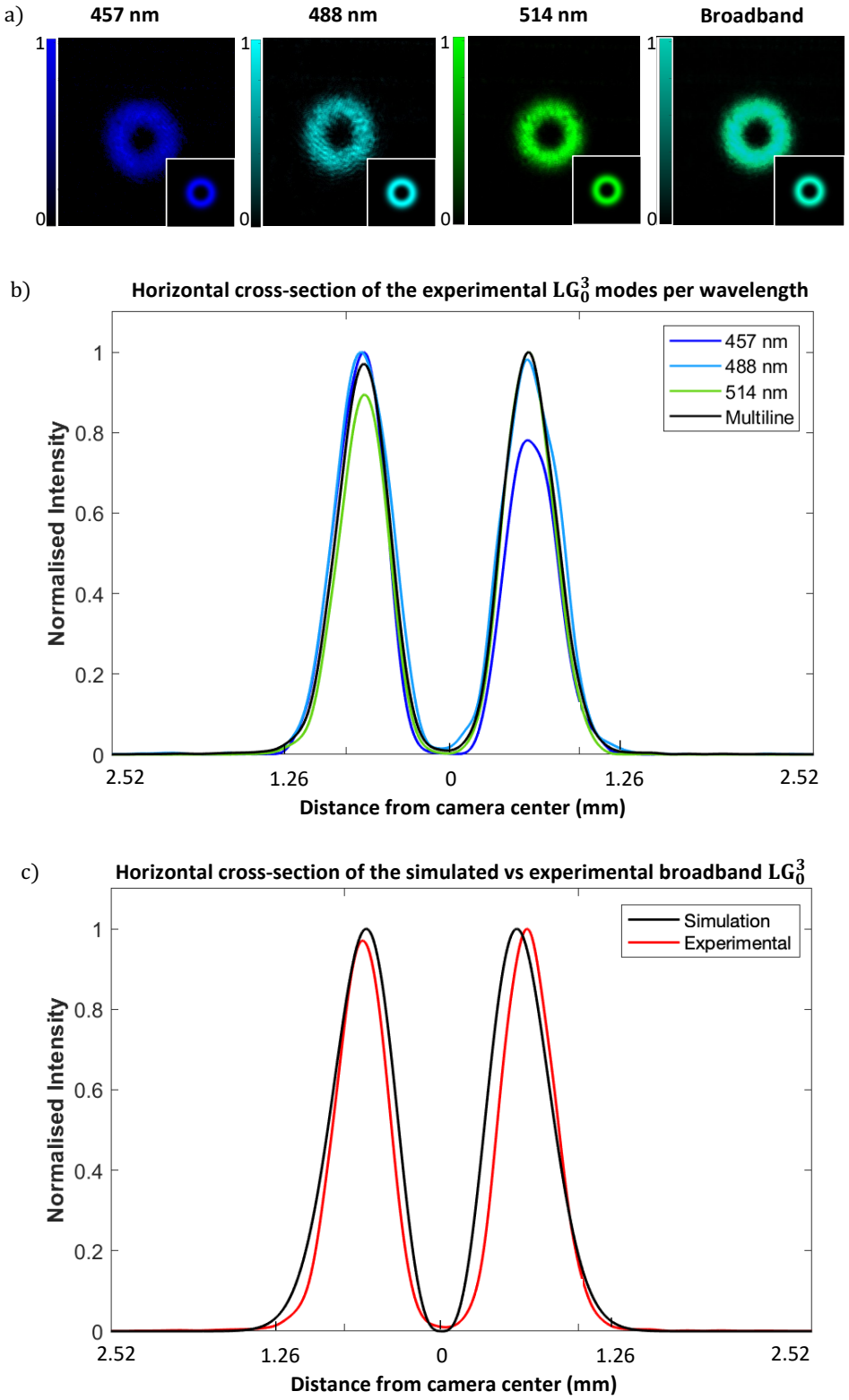


FIGURE 3.28: Experimental results demonstrating single-plane recombination. a) The intensity profiles of each structured LG_0^3 per wavelength, as well as the single-plane broadband beam with the simulated case shown as inserts; b) the cross-sectional comparison of each structured LG_0^3 mode per wavelength with the broadband beam; c) a cross-sectional comparison of the experimentally generated broadband beam and the simulated case (shown as insert), which correlate to each other by a factor of 95.3%.

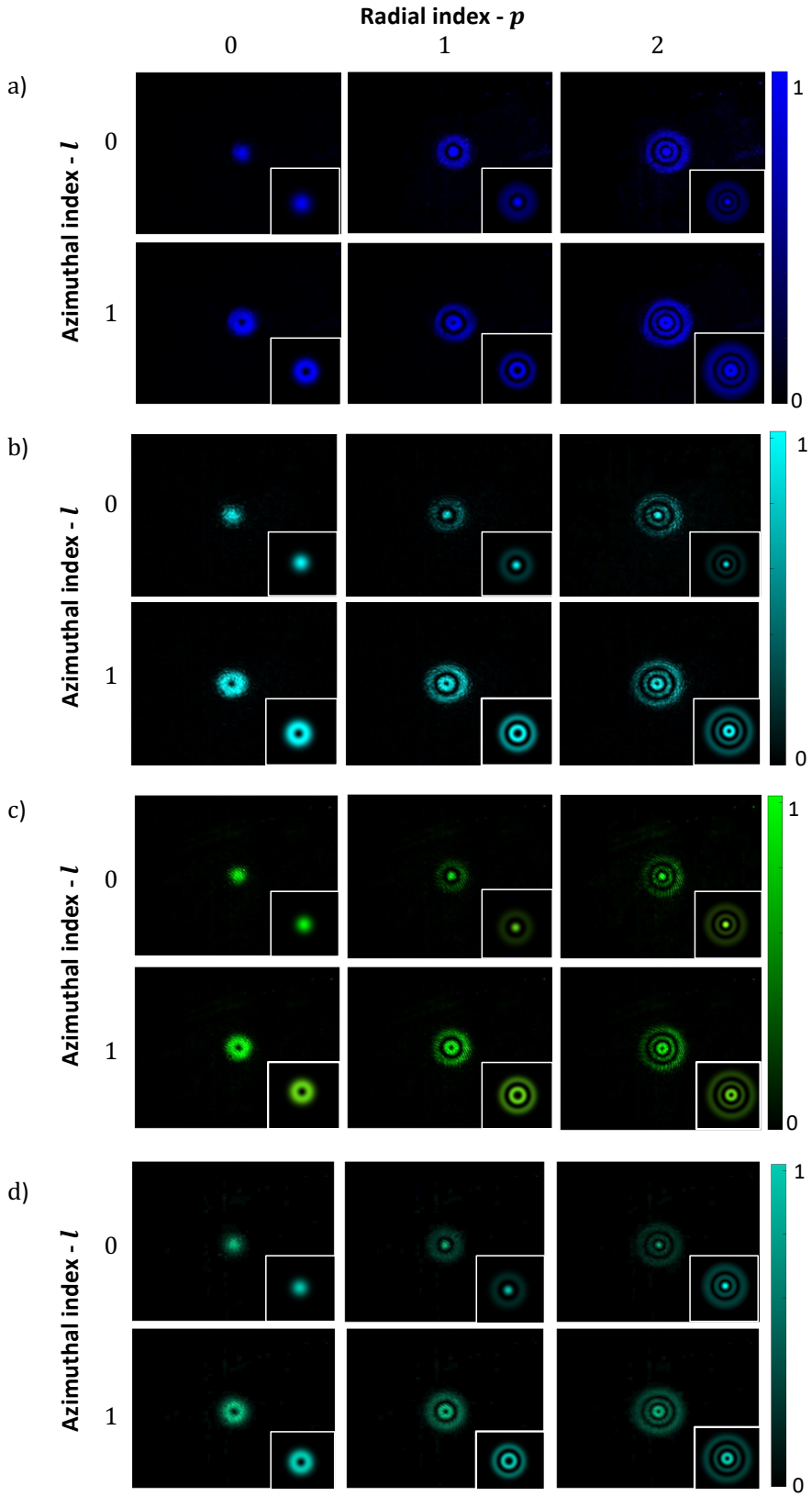


FIGURE 3.29: Experimental results demonstrating broadband beam shaping and single-plane recombination for various LG modes with varying azimuthal (l) and radial (p) indices for a) 457 nm; b) 488 nm; c) 514 nm; d) Multiline. Inserts depict the simulated case for each mode.

Chapter 4

3-D printing optics for broadband beam shaping

In this chapter we look at how to shape broadband light using a physical optic which we shall fabricate using the Quantum-X Nanoscribe - the world's first greyscale lithography 3-D printer. The printing material used to create the optic refracts visible light, hence the optic must be designed in a phase-only manner where portions of light are given a proportional phase delay where needed. The trick comes with trying to design the optic so that it can manipulate both the phase and amplitude of the incident beam. Fortunately this was already addressed by Arrizon [129]. Although this encoding scheme is typically used to create CGHs which are written to digital devices like SLMs, the holograms can be used as design template for a printed optic. This chapter begins with an introduction to the Quantum-X and a discussion of its operating principles followed by a step-by-step outline of how to design and print the optics. The printed optics are then analysed and optically tested to see if they do shape broadband light.

4.1 The Quantum-X Nanoscribe

The Quantum-X was debuted in 2022 by Nanoscribe [130]. It leverages the power of two-photon polymerisation (2PP) to produce high-resolution, complex structures on a nanoscale level thus making it an invaluable tool for applications in micro-fabrication, nanotechnology, and scientific research. The Quantum-X can therefore be used to craft micro-devices, optical components, and biomimetic structures with a level of detail and accuracy that was previously unattainable.

4.1.1 How it works

To create these intricate structures, the Quantum-X relies on a process which entails exciting photo-reactive molecules with a pulsed laser beam so that the printing material, a viscous liquid called 'resin', is converted into a polymer in a particular region of interest. For the polymerisation process [131] to be initiated, the photo-reactive molecules in the resin need to absorb enough energy to overcome the energy band gap and thus occupy the excited state. In the Quantum-X a femtosecond pulsed laser (λ = 780 nm) is used. If we consider the energy of a single emitted photon, it is insufficient to fully excite a resin molecule from the ground state to the excited state. However, due to the high photon flux density in the focal point of the beam, as well as the frequency of the laser pulses, the molecule is able to simultaneously absorb the energy of two photons. The total energy from both photons provides the molecule with sufficient energy so that the molecule can now transition from the

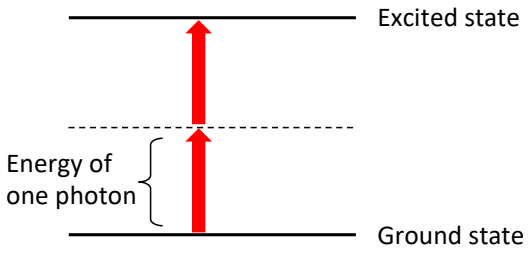


FIGURE 4.1: The process of 2 photon absorption for lithography. When absorbed, a single photon is insufficient to excite the molecule from the ground state to the excited state. However, due to the high photon flux density in the focal point of the beam, the molecule can absorb two photons simultaneously. The total energy provided by the two photons is sufficient to excite the molecule from the ground state to the excited state.

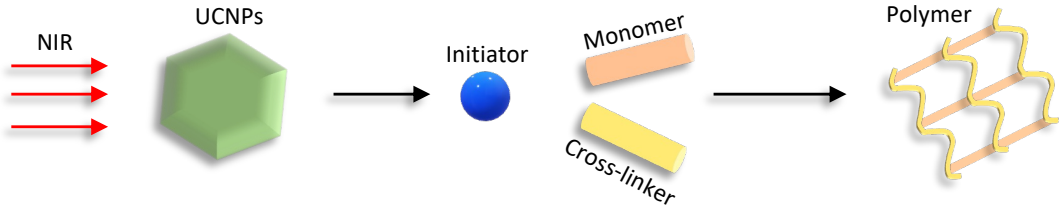


FIGURE 4.2: The process of how polymerisation occurs in two-photon lithography. A pulsed laser beam with a wavelength in the near-infrared (NIR) regime will excite up-conversion nanoparticles (UNCPs), i.e., photo-reactive molecules, which activates photo-initiators. These initiators lead to the creation of monomers which link together, with the help of cross-linkers, until the process is terminated and the desired polymer is created.

ground state to the excited state, thus initiating the polymerisation process. Hence, this process is commonly referred to as two-photon-polymerisation (2PP), and is depicted in Figure 4.1.

The excited state acts a minimum polymerisation threshold needed to activate molecules in the resin called "photo-initiators". When the photo-reactive molecules are excited and these photo-initiators are activated, they will in turn cause the production of free radicals (a highly reactive molecule that contains at least one unpaired electron). These free radicals now combine with monomers to form monomeric radicals (a larger molecule that also has an unpaired electron), which act as repeating building blocks that link together, with the help of cross-linkers, to form long chains. This generation and linking process continues until the long monomeric radical chains combine with free radicals or photo-initiators, leading to the termination of the process and the production of the final desired polymer.

If the intensity of the incident laser beam is too low, there will not be enough photons present in the region of interest to excite the molecules and overcome the minimum energy threshold. However, as the laser intensity is increased so does the concentration of photons that exceed the minimum polymerisation threshold, as depicted in the left panel of Figure 4.3. Therefore, a larger volume of the resin molecules will be excited and polymerised, leading to a thicker printed polymer. It is important to note that there is a maximum energy amount of energy that the resin molecules can absorb before they become ionised i.e., there is a maximum laser intensity that

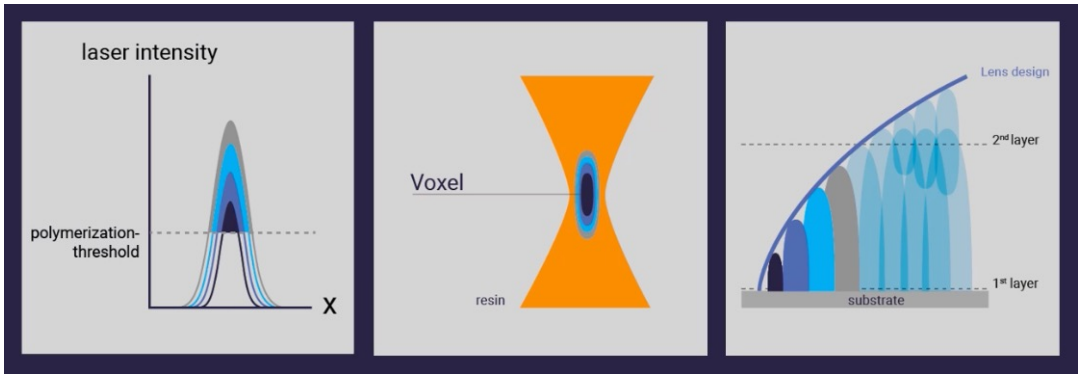


FIGURE 4.3: Different laser intensities lead to different volumes of resin molecules having sufficient energy to surpass the polymerisation threshold (left), which leads to different voxel sizes (middle) and eventually different sizes and heights of the polymer that is printed (right). Image taken from [130, 132]

can be used. Beyond this point, the resin will heat up and eventually burn, resulting in what is referred to as "explosions" which damage and distort the sample. Therefore, between the minimum and maximum thresholds, by adjusting the laser intensity one is able to freely change the volume of molecules that are excited and polymerised within the resin and thus vary the thickness of the printed structure.

Due to the Gaussian distribution of the laser beam's intensity, there will be a gradual decrease of photon density towards the edges of the beam. Therefore, for a given laser intensity there is a specific volume of resin molecules we can excite, which is not necessarily identical to the area covered by the entire beam. The smallest possible volume of resin molecules that could be excited and polymerised for a specific laser power is commonly referred to as the "voxel" as shown in the middle panel of Figure 4.3, and can be considered as a volume pixel in 3-D printing. The voxel size is dependent on additional printing parameters such as the scanning speed, for example, which shall be discussed further on.

It is clear to see that by adjusting the laser intensity one is able to change the voxel size and thus the size of the printed polymer. This can be compared to changing the thickness of a pen. Once the polymer has been created in a particular position with the desired shape and thickness, this is repeated over the region of interest on the substrate until the entire desired structure has been printed, as seen in the right panel of Figure 4.3.

4.1.2 Structure

The structure of the Quantum-X can be subdivided into its internal and external parts, as seen in Figures 4.4 a), b) respectively. Internally, the Quantum-X houses an optical system composed of a femtosecond pulsed laser (λ = 780 nm) which emits a beam that is expanded and collimated by two lenses l_1, l_2. Mirrors m_1, m_2 then redirect the beam in the x, y planes, respectively. The beam is then focused by an objective lens onto the substrate which has photo-reactive resin on it. The substrate is securely placed on a substrate holder that sits on a motorised translation stage.

Externally, the Quantum-X has the following: a hatch where the sample and substrate holder can be loaded (insert); a touch screen which allows one to adjust the

translation stage (shown in the insert) to move the substrate to the correct position, select printing jobs, and observe the printing live from various camera angles; the computer with the relevant GrayScribe-X and DeScribe-X softwares that are used for setting the printing parameters and uploading designs onto the printer.

4.1.3 The general printing process

To create any desired structure using this printer, the general process, as illustrated in Figure 4.5, is as follows: (1) prepare the substrate and design the desired object and upload it to the software interfaces; (2) print the object; (3) develop and clean the sample to expose the printed structure. If further analysis of the construction and quality of the printed structure is required, then: (4) metallise the sample which can now be characterised using microscopic imaging methods. In this section we will discuss each step of this process in detail.

Substrate preparation and design upload. Typical 3-D printers require one to input the design of the desired structure as a stereolithography (STL) file or computer aided (CAD) model. However, the Quantum-X is the first 3-D lithography printer that goes beyond these boundaries and is capable of interpreting a 2-D greyscale image as a 3-D structural design. This is possible with the aid of Nanoscribe's GrayScribe-X software which identifies and assigns the greyscale value of each pixel in the 2-D image as a value in the z plane (height). To accurately do this, the system has to be well calibrated, which will be discussed further on. Once a full 3-D structure has been realised the software will then partition the model, either through manual or automated actions, into printable portions. When the model is subdivided in the x and y planes, as seen in Figure 4.6 a), this is referred to as "hatching", and when the model is subdivide into printable sections in the z plane, as seen in Figure 4.6 b), this is referred to as "slicing". Together the hatching and slicing distances dictate the size of the voxel.

The extent that the desired structure is partitioned can have a noticeable effect on the quality of the final printed structure. By reducing the slicing and hatching distance, i.e. subdividing the desired structure into smaller parts, the printer is able to replicate finer structures and details of the desired object. Although, this will increase the overall structural quality of the printed structure, this is at the cost of an increase in the printing time. According to Nanoscribe, the print time scales according to x^{-1} if the slicing distance is decreased, while the printing time scales according to x^{-2} if the ratio between the slice and hatching distances are kept constant and are decreased. For this reason, Nanoscribe suggests simultaneously adjusting other parameters such as laser intensity and scanning speed to improve the overall printing quality without the hassle of a prolonged printing time.

Once the model has been correctly partitioned, there are additional parameters that must be set, for example, the printing speed. A slower printing speed allows for a larger volume of resin molecules to be excited, resulting in a larger voxel size and printed polymer, whereas, a faster scanning speed results in a smaller volume of resin molecules being excited, leading to a smaller voxel and printed area. This implies that a faster printing speed will result in a structure that was printed in a shorter period of time, but is less detailed and or accurate. On the other hand, a slower printing speed will lead to a longer printing duration, with a detailed and

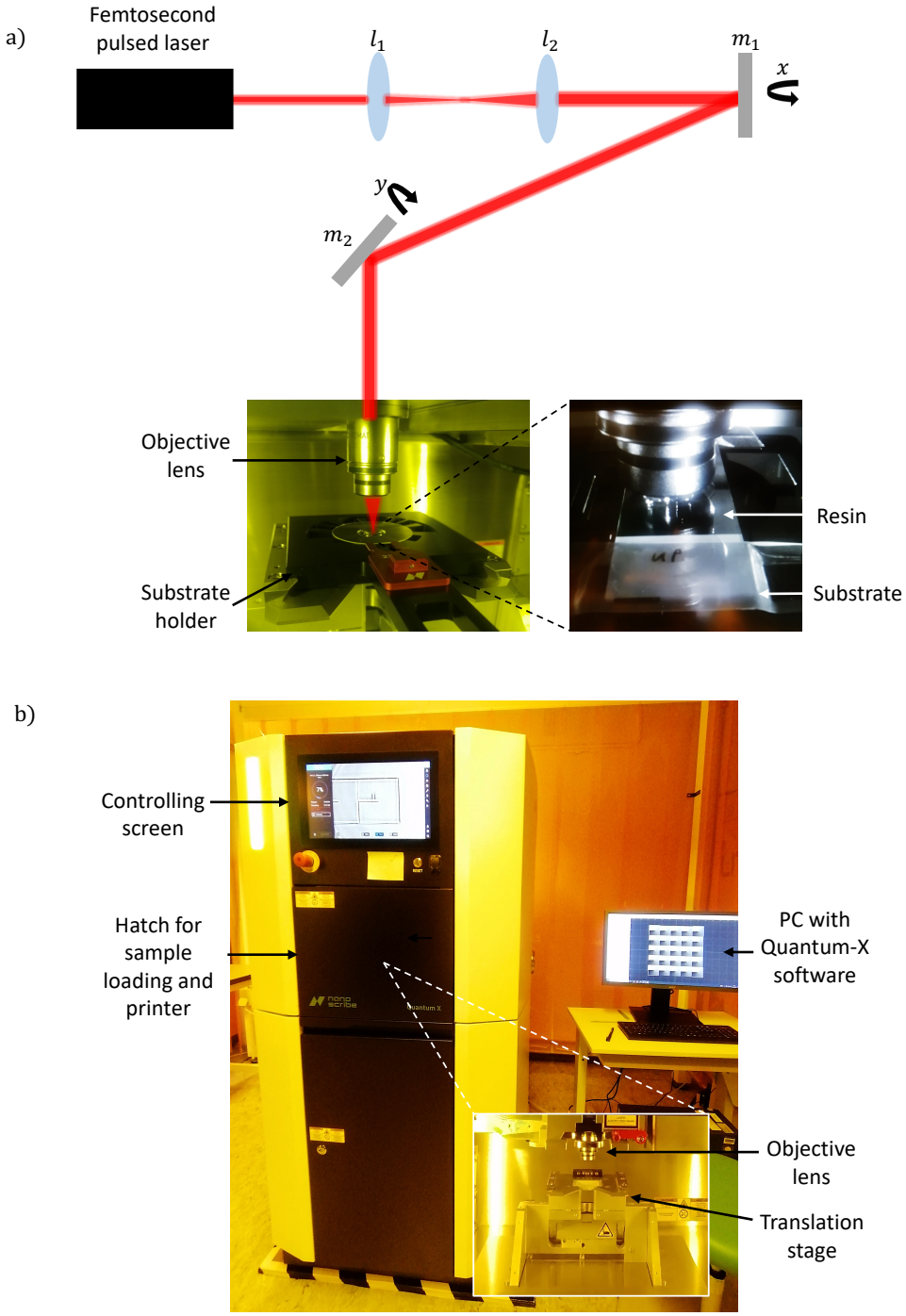


FIGURE 4.4: The structure of the Quantum-X Nanoscribe. a) Internally the printer has a femtosecond pulsed laser (λ = 780 nm). The emitted beam is then expanded and collimated by two lenses l_1, l_2. Mirrors m_1 , m_2 then redirect the beam in the x, y planes, respectively. The beam is then focused by an objective lens onto the substrate which is placed on a substrate holder. With the aid of (insert) a photo-reactive viscous liquid called "resin", which it is placed on the substrate, the desired structure will be printed. b) The external structure is composed of: a hatch where the sample and substrate holder can be loaded (insert); a touch screen which allows one to adjust the translation stage (shown in the insert) to move the substrate to the correct position, select printing jobs, and observe the printing live from various camera angles; the computer with the relevant GrayScribe-X and DeScribe-X softwares that are used for setting the printing parameters and uploading designs onto the printer.

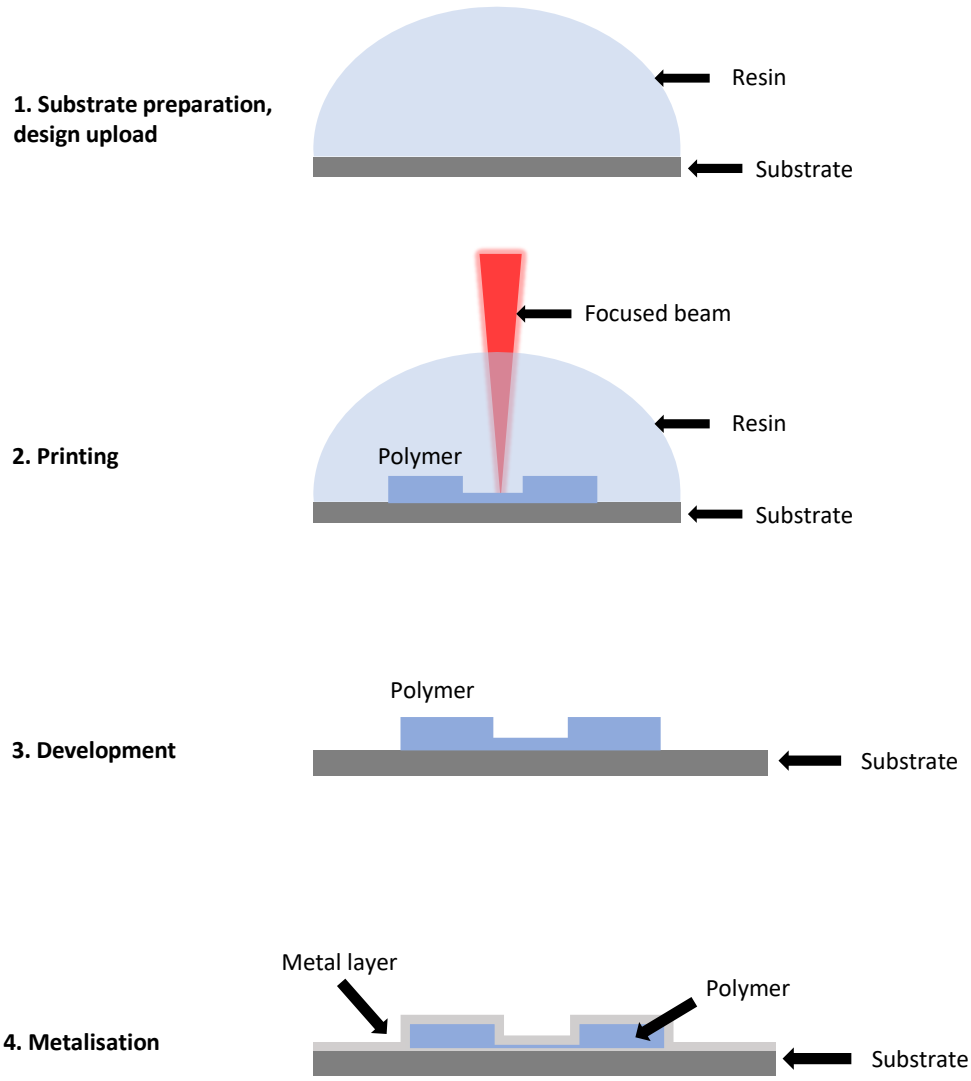


FIGURE 4.5: A summary of the general 3D-printing process. 1) prepare the substrate and design the desired object and upload it to the software interfaces; 2) print the object; 3) develop and clean the sample to expose the printed structure. If further analysis of the structure and quality of the printed structure is required, then: 4) metallise the sample which can now be characterised using microscopic imaging methods.

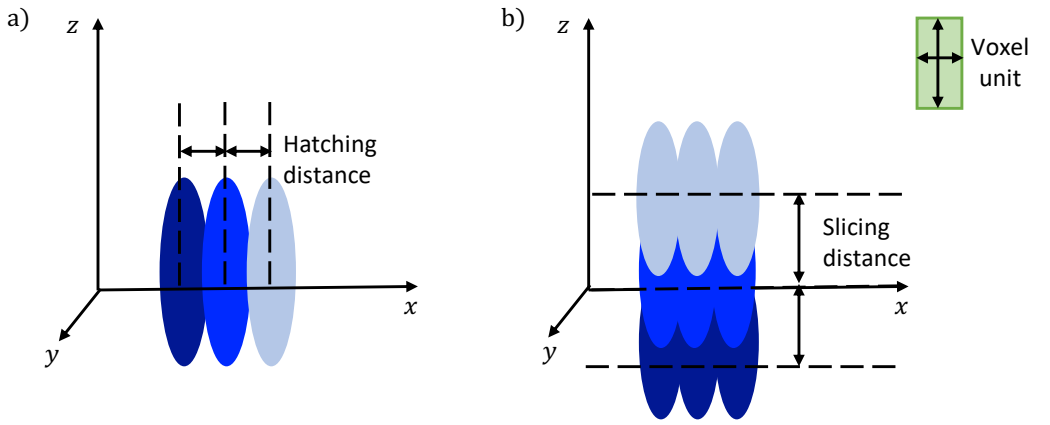


FIGURE 4.6: The two methods for partitioning a model into printable sections. a) when the model is subdivided in the x, y planes at a constant height in the z plane, this is referred to as 'hatching'; b) when the model is subdivided in the z plane for a given region in the x, y planes, this is referred to as 'stitching'. Together the hatching and slicing distances dictate the size of the voxel.

accurate structure. However, with a slower printing speed one also runs the risk of ionising the resin which causes overheating and explosions, as previously mentioned.

Other parameters that must be set are the size and position of the desired structure on the substrate. This can be manually adjusted using the GrayScribe-X software. Depending on the objective lens used, the laser beam has a maximum area that it is able to print within , i.e. a field of view (FOV) before the substrate must be shifted. If the desired structure is larger than this FOV, the model will be partitioned into printable areas that are equal in size to the FOV. Hence, when the model is printed it will be composed of many printed areas that appear to be 'stitched' together. Depending on the size of the designed structure and the objective lens used, the discontinuity between each adjacent printed area, i.e. the stitching lines, may be noticeable and have a significant effect on the structure.

Printing. Once the design has been uploaded, the next step of the process is printing. Before the printing begins all the necessary components must be prepared. First, an objective lens must be chosen from the list of available options which are mentioned in Table 4.1 and shown in Figure 4.7. Assuming that it is clean, the lens holder is then slid into a groove in the opening hatch and secured in place with a clamp.

Next, the substrate is prepared. The Quantum-X is able to print on various transparent and opaque substrates such as silica and fused silica wafers, and microscope slides, as seen in Figure 4.8. Depending on the type and size of the chosen substrate, the correct holder must be chosen so that the substrate fits exactly in the groove. Then, by pulling on the attached lever, the substrate is clamped, ensuring that the substrate remains stable throughout printing. These substrates are usually sufficiently clean when used directly from their packaging. However, in some cases it may be necessary that they are cleaned before use. This can be done by rinsing the substrate with isopropanol and drying it with nitrogen gas.

TABLE 4.1: A list of the possible objective lenses that can be inserted into the Quantum-X Nanoscribe, with their respective field of views and the type of resin they require [130, 133].

Objective lens	Field of view (μm)	Resin type
x 63	200	IP-Dip, IP-Dip 2
$\times$25	800	IP-S
$\times$10	2300	IPX-S, IPX-Q
$\times$5	5000	IPX-M, IPX-Q

Once the substrate is secure, a drop of resin is added. Depending on the objective lens used, the correct resin must be used as shown in Table 4.1. It is important that only one small drop is added to the substrate, as seen in Figure 4.9, to minimise the presence of air bubbles in the resin as it may lead to distortions in the printed structure.

The substrate holder is then slid into a groove within the hatch which is designed to position the holder on top of a translation stage. This makes it possible to automatically move the holder to any position in the x, y, z planes. Using the control buttons on the screen, as shown in Figure 4.10, the door of the hatch is locked. The substrate is then loaded. Once the printer registers this it will require information about the type of substrate and resin that is used. While viewing the live camera feed, one then re-positions the substrate until the objective lens is submerged in the resin, as seen in Figure 4.10. Finally the design is uploaded and the printing is started.

Development. When printing, only a portion of the resin is polymerised in a particular region of interest, while the rest of the resin is left unused. In this way the printer is able to "carve" out the desired structure from the resin. Hence, to fully expose the printed structure one must remove all excess resin present on the substrate. This process is referred to as 'development' and is done by submerging the sample in a solvent called PGMEA (propylene glycol methyl ether acetate), as seen in Figure 4.11 for approximately 10 minutes. The solvent will react with and dissolve the remaining un-polymerised resin while leaving the polymerised resin unaffected, thus exposing the printed structure. If the sample is removed too soon from the solvent, it is likely that all excess resin will not be adequately removed and the printed structure will not be properly exposed and therefore appear misshaped or warped. However, if the sample is left in the PGMEA solution for extended periods of time the solvent could weaken the polymer structure and thus compromise the quality and distort the shape of printed structure.

Further cleaning of the substrate surface of other impurities, such as dust or fingerprints, is done by submerging the substrate with solvents such as isopropanol, as seen in Figure 4.11, and or acetone for an additional 5-10 minutes. The sample is then partially dried using a gentle stream of nitrogen gas, and left to completely dry out in a fumehood for 5 minutes.

Metallisation. If further analysis of the sample is needed (to determine its quality, for example) additional steps in the printing process are necessary, beginning with the metallisation of the sample. In this process the sample is coated with a thin layer

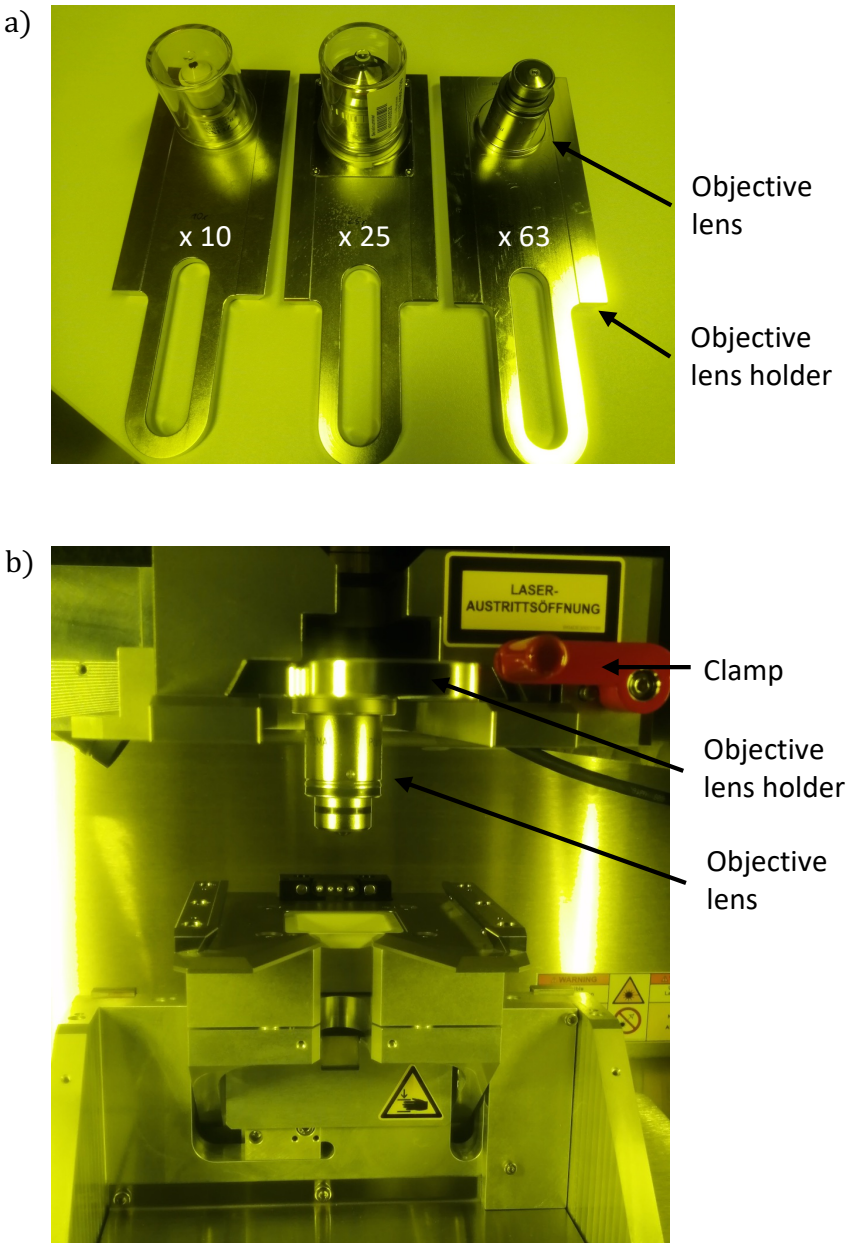


FIGURE 4.7: The objective lenses that can be used in the Quantum-X. a) There are a selection of a various objective lenses as summarised in Table 4.1. Shown here are the $\times 10$, $\times 25$ and $\times 63$ objective lenses which are attached to a lens holder. b) The lens holder is slotted into a groove in the hatch of the Quantum-X, and clamped into place using a lever.

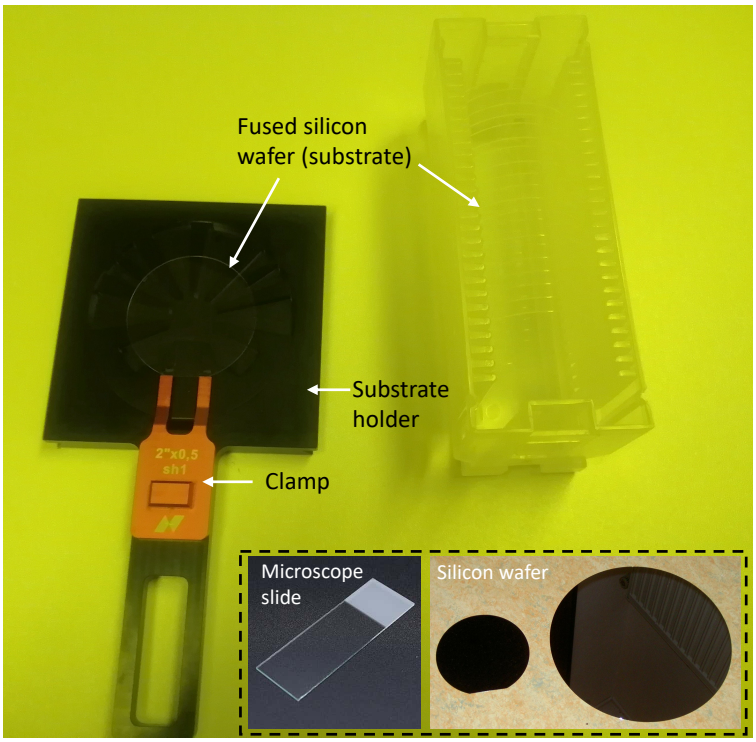


FIGURE 4.8: Printing can be done on various transparent or opaque substrates that can vary in size. The substrates used for printing when using the Quantum-X are usually fused silica wafers, (insert) microscope slides or silicon wafers. Depending on the type and size of these substrates the correct holder must be used so that the substrate is secure during printing.



FIGURE 4.9: Before printing a small drop of resin (insert) must be added to the chosen substrate. It is important that the correct resin is used for the chosen objective lens.

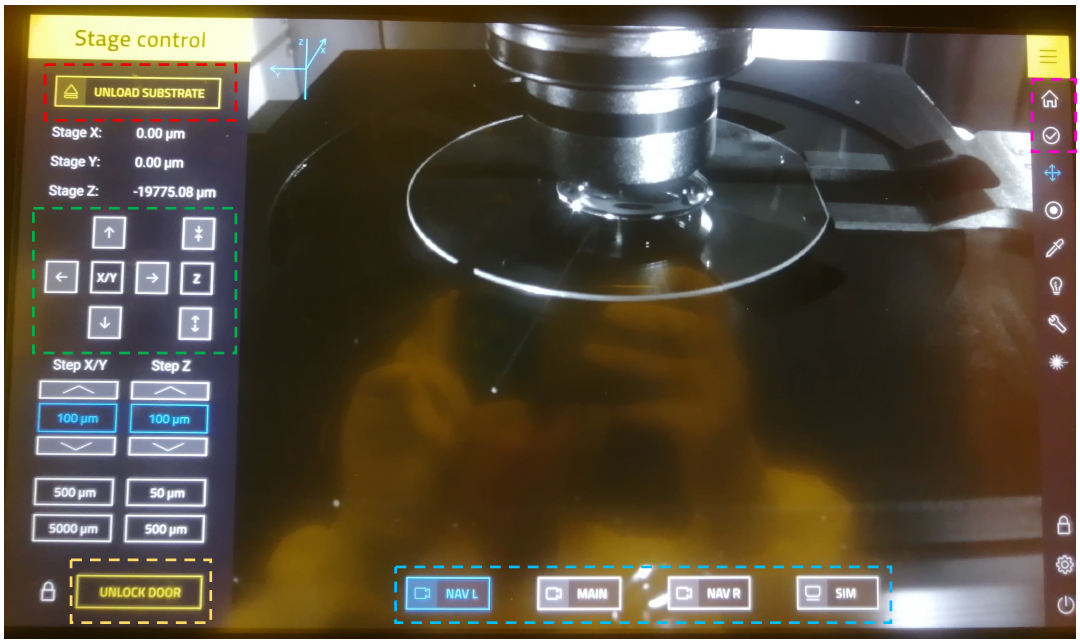


FIGURE 4.10: Once the substrate is prepared, it is placed in the hatch of the printer where it lies on an automated translation stage. The control buttons on the screen are then used to prepare and begin the printing as follows: the door of the hatch is closed (yellow), then the substrate is loaded (red). The printer will then require information about the substrate and resin that is being used. While viewing the live camera feed (the camera angle can be changed using the (blue) buttons), the substrate is re-positioned using the (green) buttons until the objective lens is submerged in the resin. The design is then uploaded and the printing started using the (pink) buttons.



FIGURE 4.11: To fully expose the printed structure one must remove all unused excess resin present on the substrate. This process is referred to as 'development' and is done by submerging the sample in PGMEA (propylene glycol methyl ether acetate) (left) for approximately 10 minutes. It is then cleaned of any further impurities by submerging the sample in isopropanol (right) and or acetone for an additional 5-10 minutes.

of a heavy metal such as aluminium or gold, making the sample opaque and even slightly reflective. Due to the high conductivity of the coated metal, when imaging the sample it will now have an improved signal-to-noise ratio and enhanced contrast with an overall better image quality.

To metallise the sample we used a technique called physical vapour deposition (PVD) [134] using a plasma sputtering high vaccuum metallising (PSHVM) spin coating machine, as seen in Figure 4.12 a). The sputtering machine is made up of the following parts: the chamber where the sample is placed; the vacuum pump that removes all air within the chamber; the gas lines that feed some inert gas like argon (Ar) into the chamber; the control buttons that allow one to change the parameters of the system and start the process; the display screen.

The PVD process is illustrated in Figure 4.12 b), which can be summarised as follows. The process begins with a metal target, which is typically composed of the material you want to deposit as a thin film. This target is placed inside a chamber. The sample you wish to metallise is also placed on a stage in the chamber, which is directly opposite the metal target. The chamber is then sealed to maintain a low pressure and pumped to create a vacuum. This is done to prevent contamination and control the deposition process more precisely. An inert gas such as argon (Ar) is then introduced into the vacuum chamber. By applying an electric field to the gas, the gas becomes ionised (Ar+) and a plasma is created. The high energy plasma consists of ions and electrons. A voltage is applied both to the target metal and the stage that the sample rests on, with the target metal acting as a cathode (-), and the stage as an anode (+). The positively charged ions in the plasma are attracted to and thus accelerate toward the target metal. When these ions collide with the target surface, they transfer their energy to the atoms within the target metal. This energy causes some of the target atoms to be dislodged or sputtered from the target surface. The target atoms then condense on the substrate and forms a thin film on the substrate. The process can be precisely controlled by adjusting parameters such as the gas pressure, the material of the target metal, power applied to the plasma, and the distance between the target and substrate.

The target material and the applied current directly influence the thickness of the sputtered material which coats the sample. Figure 4.13 is a plot of the thickness of the sputtered material (Au or Ag) versus time for various applied currents (30 mA or 45 mA), when the chamber is maintained at a pressure of 0.05 mbar and the inert gas used is Ar. From Figure 4.13 we see that when the current is higher, the time needed to achieve a thicker sputtered material is shorter. This is because the higher the current, the more ions present in the chamber to dislodge metal atoms from the target material. If we compare the trends for both gold (Au) and silver (Ag), we see that when using a gold target more time is needed to achieve a thicker sputtered material. Gold and silver have an atomic weight of 196.97 and 107.86 atomic mass unit (amu), respectively. This is implies that gold is heavier than silver. Hence, it requires more energy to dislodge gold atoms from the target surface than it does to dislodge silver atoms. In this thesis when metallising samples we used a Ag target with the applied current set to 30 mA and the sputtering time set to 120 seconds. This implies that our samples are coated with a metal layer that is ≈ 5 nm.

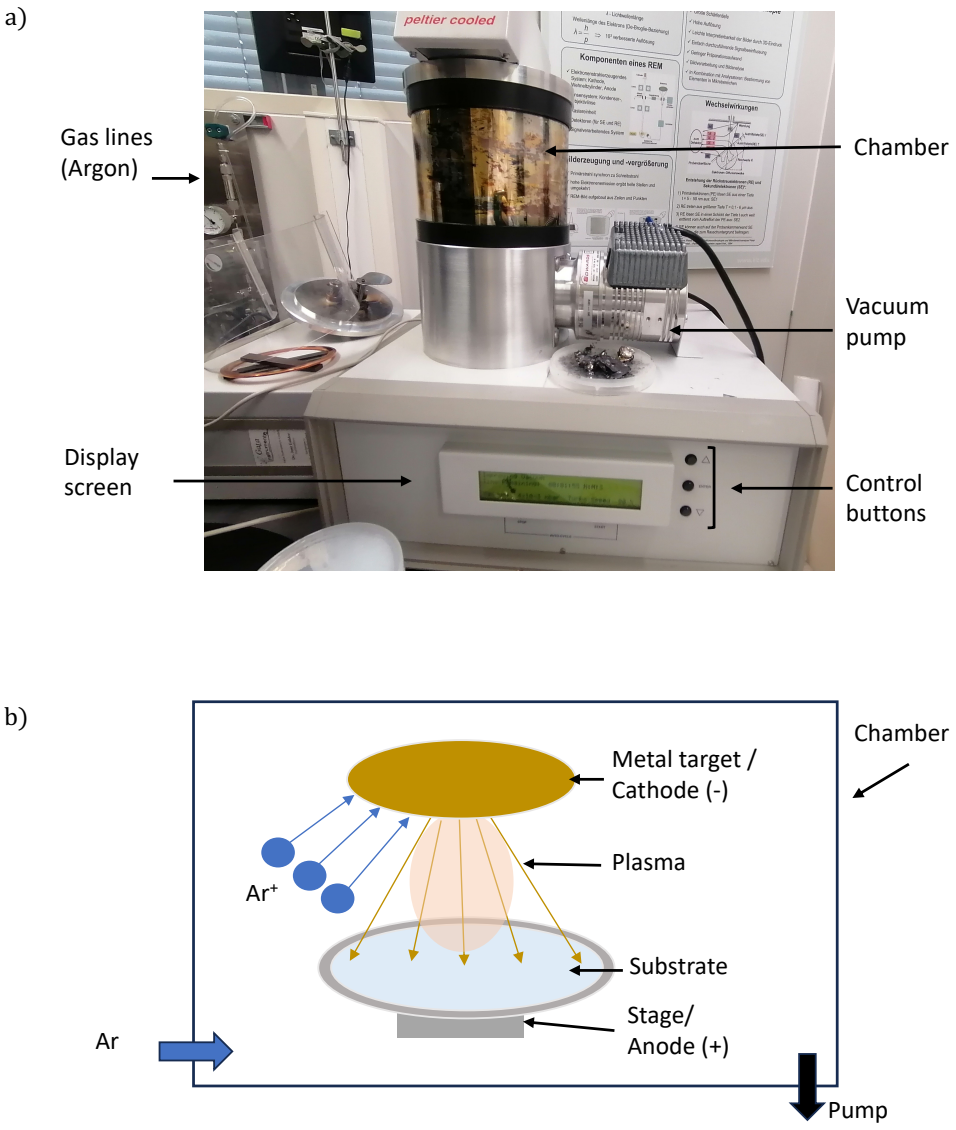


FIGURE 4.12: Diagrams of the plasma sputtering high vacuum metallising (PSHVM) spin coating machine and the physical vapour deposition (PVD) process which are needed to metallise a sample. a) The sputtering machine is composed of the following parts: the chamber, the vacuum pump, the gas lines that feed some inert gas like argon (Ar) into the chamber, the control buttons and the display screen. b) The PVD process relies on a sample and a target metal being placed in a chamber. Once the system is pumped and a vacuum created, argon gas (Ar) is introduced. The gas is ionised (Ar+) and a plasma is created. The ions accelerate toward the target metal and dislodge the atoms in its surface. These atoms are sputtered on the sample which lies across the target metal.

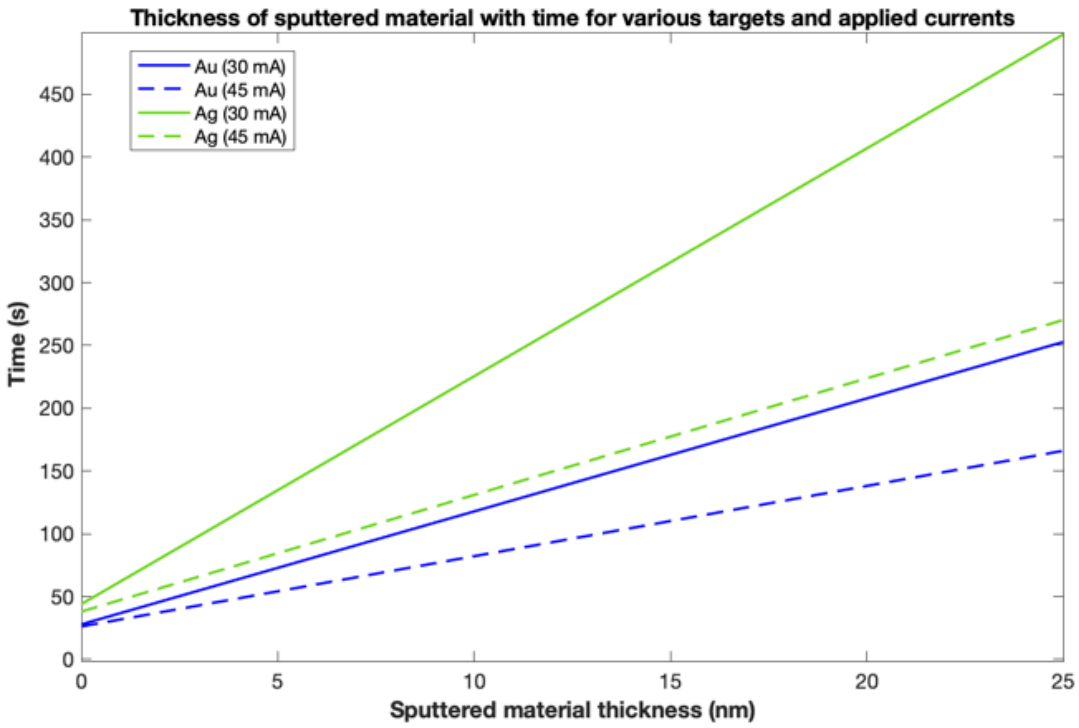


FIGURE 4.13: The thickness of the sputtered material (Au or Ag) versus time for various applied currents (30 mA or 45 mA), when the chamber is maintained at a pressure of 0.05 mbar and the inert gas used is Ar. Results provided were courtesy of IMT, Karlsruhe Institute of Technology.

4.1.4 Calibration

As shown in Figure 4.3, a given laser power corresponds to a voxel of a certain size. As the laser power is increased, so does the size of the voxel. This implies that various printing heights and thickness can be achieved within a single layer. However, there is a maximum laser power that can be used before the resin is burnt. This implies that there is a maximum height that can be achieved in a single printing layer. To create higher structures, these layers must be stacked upon each other. The laser power range between when the polymerisation threshold is overcome and the burning of the sample is referred to as the 'dynamic range' and varies between resins.

When a 2D greyscale image (the design of the desired structure) is uploaded to the GrayScribe-X printing software, each pixel's greyscale value is interpreted as a certain height value. When the system is calibrated the generated file serves as a mapping of input height values to output applied laser powers. If the desired height surpasses the maximum voxel size, then multiple layers must be printed. Hence, a calibration file serves as the translation of greyscale values to laser power, only for a set of given parameters such as the resin, scan speed and slicing and hatching distance. If any of these parameters are changed, the system must be re-calibrated.

To calibrate the system, one begins by uploading a prescribed printing design from Nanoscribe composed of a 3 x 3 array of convex lenses, to the GrayScribe-X software, as seen in Figure 4.14 a). The uploaded design is in the form of a 16-bit greyscale image with 65 000 shades of grey. The size of each lens is set so that the entire array lies within the field of view of the objective lens. In this case we performed a calibration using a $\times 63$ objective lens, so each lens was set to a size of 40 μm with a spacing of 15

μm between. One then sets the printing parameters such as the resin, substrate, scanning speed, hatching and slicing distances, and the maximum laser power. The resin used was IP-Dip, and a fused silica wafer was used as the substrate. The parameters were then set as follows: the scan speed was 60 000 μs, the hatching distance was 0.3 μm, the slicing distance was 0.5 μm and the maximum laser power was 75 mW.

A pre-loaded reference calibration file is then selected and the design is uploaded to the printer with the above mentioned parameters. The design is then printed as usual and once completed, the sample is developed and metallised. Using a 3-D measuring laser microscope (any other topography measuring system could be used instead) a model of the printed structure is created as seen Figure 4.14 b), and a height map (insert) of the printed structure is generated. The file is then uploaded to the GrayScribe-X software which converts it into a greyscale image and compares this greyscale image to the pre-loaded design lens-by-lens, as seen in Figure 4.14 c). In so doing the software is able to determine the relationship between the greyscale value in the initial design to the applied laser power and the resulting height of the structure that was printed. This relationship is visualised as a plotted curve of the print height versus the applied laser power per lens, as seen in Figure 4.15 a). An average of all the plotted curves is then created, which serves as the final calibration curve, as seen in Figure 4.15 b).

4.2 Fabrication of beam shaping optics

The various resins used by Quantum-X exhibits refractive properties across the entire visible spectrum. By exploiting this property of the material we can strategically deposit the resin so portions of the incident light are imparted with the relevant phase shift and thus produce the desired mode in some observation plane. This implies that should we want to manipulate both the phase and amplitude of the incident beam, it must be done using a phase-only approach.

Fortunately this problem was already solved by Arrizon [129] and has been used extensively since then to create computer generated holograms, for example, which can be written to phase-only devices such as SLMs. Because the Quantum-X is able to interpret greyscale images as a printable design, one can generate the hologram in a similar manner and directly upload these holograms to the printer. Once printed, the optic should shape the incident beam in the same manner that a phase-only digital device would.

4.2.1 Hologram encoding scheme

To generate the hologram we shall use Arrizon's encoding scheme which can be summarised as follows:

Consider an arbitrary amplitude, $A(x,y) \in [0,1]$ and phase, $\phi(x,y) \in [-\pi,\pi]$ to be imparted into an incident beam of light. The entire field can be expressed in the following form:

$$U_{des} = A(x,y)\phi(x,y) \tag{4.1}$$

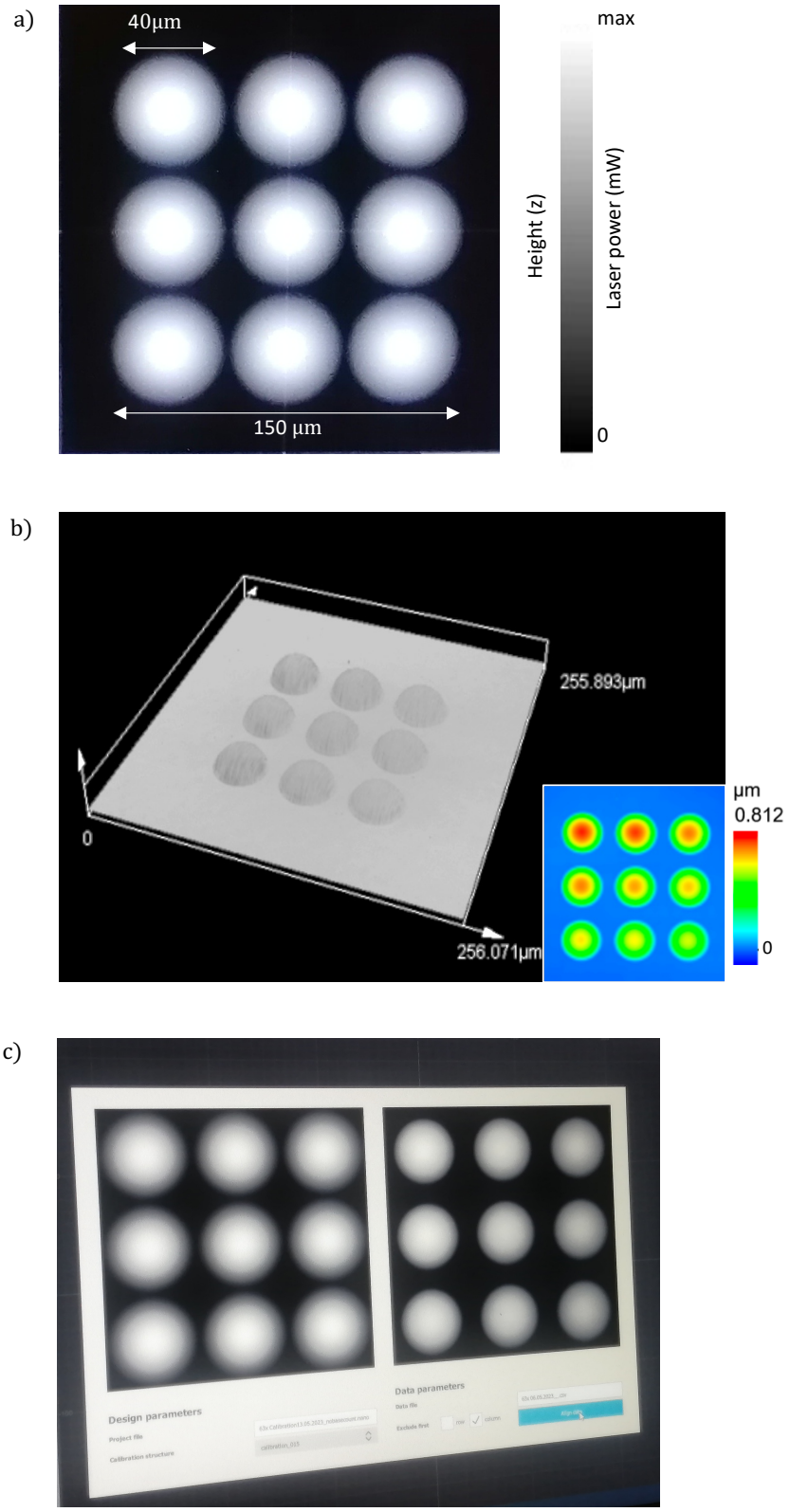
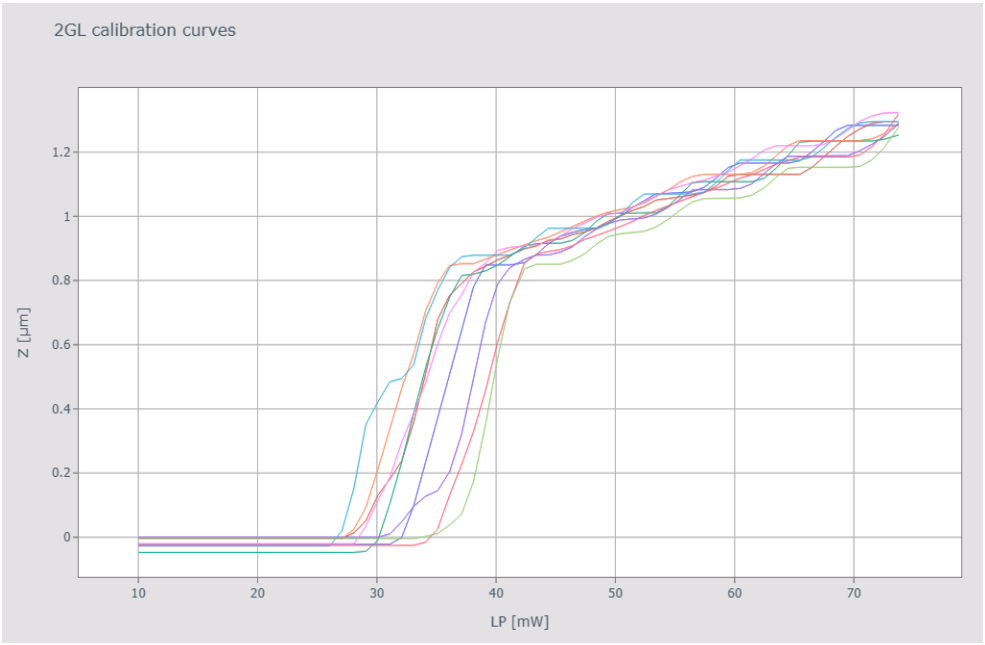


FIGURE 4.14: A summary of the calibration process of the Quantum-X Nanoscribe. a) A greyscale reference design composed of a 3 x 3 lens array is uploaded to the printer and resized. Each greyscale value per pixel in the picture corresponds to a certain laser power to be applied to achieve the desired height. The design is then printed. b) Using a 3-D measuring laser microscope a model of the printed structure is created as seen and a height map (insert) of the printed structure is generated. c) The file is then uploaded to the GrayScribe-X software which converts it into a greyscale image and compares this greyscale image to the preloaded design lens-by-lens. In so doing the software is able to determine the relationship between the greyscale value in the initial design to the applied laser power and the resulting height of the structure that was printed, resulting in a final calibration curve.

a)



b)

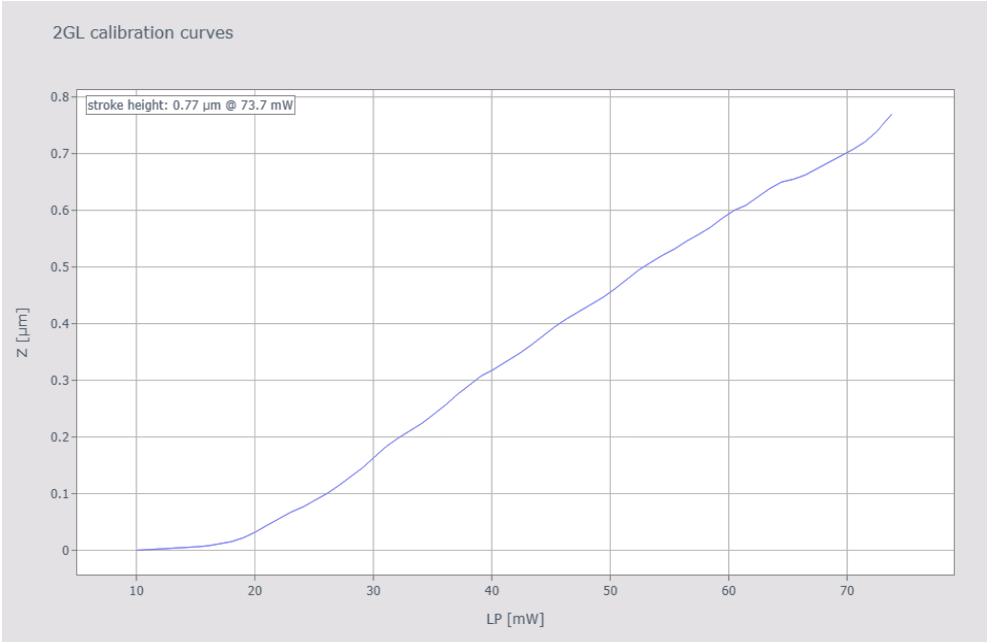


FIGURE 4.15: Generated calibration curves for the Quantum-X. a) A plot depicting the relationship between the applied laser power (LP) in milliwatts (mW) and effective printed height, z (μm) per lens structure and, b) a plot of the average laser power applied vs the printed height, which serves as the final calibration curve and is uploaded to the printer.

However, since it is only possible to impart a phase change to the incident beam, this implies that the effective amplitude change must become the input of some function that will map the desired amplitude profile to an appropriate phase effect. In other words, the hologram can be expressed as

$$H(x,y) = e^{(i\psi(A,\phi_H))} \tag{4.2}$$

where the encoded phase is dependent on $\phi = \phi(x,y)$ and $A = A(x,y)$. This implies that by finding equations that have the same form as Equation 4.2, we will be able to produce the desired complex field by using a phase-only approach. Since the hologram is defined by some periodic function, it can be expanded as a Fourier series of the desired phase ϕ

$$H(x,y) = \sum_{-\infty}^{\infty} C_q^a e^{iq\phi} \tag{4.3}$$

which now expresses the same periodic function as a sum of trigonometric functions with various weightings, C_q^a. These coefficients have a dependence on the desired amplitude and can be determined numerically using the following equation

$$C_q^a = \frac{1}{2\pi}\int_{-\pi}^{\pi} e^{i\psi(A,\phi)} e^{-iq\phi} d\phi \tag{4.4}$$

Assuming that it is desirable for the modulated field to be in the +1st-order i.e., $q = 1$, then $C_1^a = Aa$ where a>0 is a constant. This enforces two restrictions on the encoded hologram phase, namely:

$$\int_{-\pi}^{\pi} \sin(\psi(A,\phi) - \phi) d\phi = 0 \tag{4.5}$$

$$\int_{-\pi}^{\pi} \cos(\psi(A,\phi) - \phi) d\phi = 2\pi Aa \tag{4.6}$$

In totality, all functions that obey these restrictions will satisfy the transmission function and correctly modulate the incident field. However, now consider a subset of these functions which have an odd symmetry

$$\psi(A,\phi) = f(A)\sin(\phi(x,y)) \tag{4.7}$$

where $f()$ is an unknown function. When the encoded phase is written in this form, it is possible to expand the hologram function using the Jacobi-Anger identity (a method for expanding exponents of trigonometric functions)

$$H(x,y) = \sum_{m=-\infty}^{\infty} J_m(f(A)) e^{im\phi} \tag{4.8}$$

where $J_m()$ is the m-th Bessel function of the 1st kind. By comparing Equations 4.3, 4.8 we notice that

$$C_q^a = J_m(f(A)) \tag{4.9}$$

Since the desired field will be found in the +1st-order i.e., $q = 1$ we can apply the condition that $C_1^a = Aa$, such that

$$J_1(f(A)) = Aa \tag{4.10}$$

Therefore, by numerically inverting the function we are able to determine $f(A)$ and thus determine the amplitude structure to be imparted which has been correctly mapped to a phase-only effect. In this way, the hologram now has the following form:

$$H_{SLM}(x,y) = J_1^{-1}(U_{des}(x,y))sin(\phi) \tag{4.11}$$

where $U_{des}(x,y)$ is the desired field defined in Eq 4.1. This technique is true for values up until a maximum where $a = 0.58$. This corresponds to the maximum of the 1st-order Bessel function and thus restricts the value of $f(A)$ to a range that lies between [0, 1.8]. This therefore limits the optic to only implement phase changes that lies between the [-1.17π, 1.17π] which can be helpful for imparting phase changes that are not a whole multiple of 2π.

It is important to note that due to the possible manufacturing flaws or damage, the optic will not be entirely efficient at converting the incident light into the desired mode. For this reason one must separate the light that has been modulated from the light that has not. One method for achieving this is to shift the modulated light off-axis by encoding a grating. The grating also provides a way to spatially separate the various diffraction orders and thus single out the +1st-order which will have the desired phase and structure, which is especially important when doing broadband beam shaping (refer to Chapter 1). In other words, to generate the hologram for practical purposes $\phi \rightarrow \phi + 2\pi(g_x x + g_y y)$ where g_x, g_y are the grating frequencies in the x and y, respectively. By adjusting these relative values, one can adjust the spatial separation between the various diffraction orders.

4.2.2 Design considerations

Dimensions. To generate the hologram, we must know what the resolution and pixel size is. When generating a hologram to be encoded on a digital modulating device, the resolution and pixel size is set to match the dimensions of the device's screen, so that it has a one-to-one mapping with each pixel in the screen. However, to generate a hologram that is going to be printed, the resolution must be chosen to match the exact size of the desired optic. The pixel size, on the other hand, is equal to the smallest printable volume that can be printed and is therefore dictated by the printer's smallest voxel size which is 200 nm.

Using the Arrizon encoding scheme mentioned earlier, we are now able to generate the holograms needed for printing beam shaping optics. Figure 4.16 illustrates how to generate holograms for a phase-only vortex ($l = 1$) and HG_2^1. To create optics that shape the incident beam through phase-only modulation, as in the case of the vortex mode, the hologram must comprise of a phase mask and grating as seen in Figure 4.16 a). We add a grating to ensure that should the printed optic have an imperfections, the desired mode is shifted off-axis and can be easily isolated without any noise. To create modes through complex-amplitude modulation as in the case of HG modes, the hologram is composed of an amplitude mask, a phase mask and a grating as seen in Figures 4.16 b). In both cases the holograms were generated for an optic where λ_0 = 514 nm and its size was 1500 μm $\times$ 1500 μm in the x, y - directions

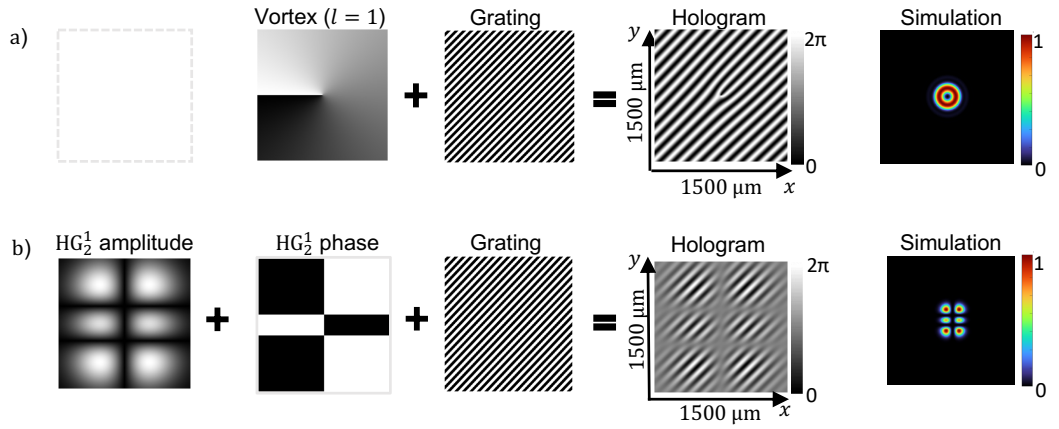


FIGURE 4.16: Examples of how to generate holograms, that when printed, generate modes through phase-only and complex-amplitude modulation. a) A hologram to generate a vortex ($l = 1$) through phase-only modulation comprises of a phase mask and grating. b) A hologram to generate a HG_2^1 through complex-amplitude modulation comprises of an amplitude mask, a phase mask and grating. All the holograms were generated for an optic where λ_0 = 514 nm and is 1500 μm $\times$ 1500 μm in size in the x, y - directions, respectively.

to ensure that it can be easily located on the substrate when performing experiments.

Thickness. When using a digital device for beam shaping, the hologram is a 2-D image that is displayed on the device's screen. However, if we print the hologram to create a physical optic it must take on a 3-D nature. This implies that we must consider additional factors, such as the dimension of the optic in the z - direction, i.e., its thickness.

To determine the correct thickness each spatial position must experience a relative phase shift that is described by the continuous phase function. To ensure that the optic has the correct thickness, t we can use Equation 2.10:

$$t = \frac{\lambda_0 \Delta\phi}{2\pi(n - n_i)} \tag{4.12}$$

Where t is the thickness of the optic, λ_0 is the design wavelength, $\Delta\phi$ is the desired phase shift to be imparted, n is the refractive index of the printing material (the resin), n_i is the refractive index of the surrounding material. The surrounding medium is air, hence $n_i = 1$. If we assume that the maximum phase shift to be imparted is a multiple of 2π, due to the periodicity of the continuous phase function, then $\Delta\phi = 2\pi m$ where $m \in \mathbb{N}$. This implies that the optic will have a maximum thickness, t_{max} and can be determined using Equation 4.12:

$$t_{max} = \frac{\lambda_0 m}{n - 1}. \tag{4.13}$$

If we assume that λ_0 = 514 nm, we can determine the refractive index of the resin for λ_0. The resins that are used for printing with the Quantum-X are specially engineered and have a unique chemical composition. Information regarding its properties such as the refractive index cannot be assumed or compared to any other material, and must therefore be provided directly by Nanoscribe. The results provided

TABLE 4.2: A list of printing resins (when in solid state) and their refractive indices for various wavelengths at 20°C. Experimental results provided by Nanoscribe[133].

Wavelength (nm)	**Refractive Index**		
	IP-Dip	**IP-S**	**IPX-S**
405	1.579	1.535	-
479.3	1.564	1.522	1.519
546.1	1.556	1.517	1.513
589.3	1.552	1.514	1.510
643	1.548	1.511	1.508
780	1.543	1.507	1.504
950	1.539	1.504	1.501

were as follows for the various resins when they are in a solid state at 20° C.

Using the experimental results from Table 4.2 and Matlab's data fitting tools we can fit a curve to the data provided, as seen in Figure 4.9. The fitted curves match the data trend with R-squared values between 0.98 - 0.99. Although there are more accurate approaches to determining the refractive index such as using the Sellmeier coefficients, due to the limited information available for this material, this approach should be sufficient to approximate the refractive index for a certain wavelength that lies within the range of the data.

To print the optics we opted to use the $\times 63$ objective lens and IP-Dip resin because this objective lens prints with the highest precision (200 nm) possible with the Quantum-X Nanoscribe. Using Figure 4.17, we approximate the refractive index, $n \approx 1.556$ for $\lambda_0 = 514$ nm. We set the printing parameters so that the printed optic will have a maximum thickness t_{max}= 25 μm (m = 27). Setting the m value to >10 ensures that the printed optic is structurally stable and produces the desired phase shift despite possible structural flaws that may arise from fabrication imperfections. However, m values >30 significantly increases the printing time. Hence, we arbitrarily chose a value within the range $m \in [10, 30]$.

4.2.3 Printing the optics

To print the optics, the generated holograms were uploaded to the GrayScribe-X software to prepare the print job. Depending on the dimensions of the substrate chosen and the size of the desired optic, one can upload and prepare many designs on a single substrate as seen in Figure 4.18 a). Once the design has been uploaded, it must be appropriately scaled and positioned. If the size of the optic spans multiple fields of view, it will require many printed areas to be stitched together. Because we required the finest precision possible when printing these structures, we opted to use the $\times 63$ objective lens. This implies that the field of view is limited to between 150 - 200 μm, hence the optic which was designed to be 1500 μm $\times$ 1500 μm must be subdivided into a 10 $\times$ 10 printable areas, as seen in (insert) of Figure 4.18 a). Other parameters such as the hatching and slicing distances, printing speed and laser power were then set and are summarised in Table 4.3.

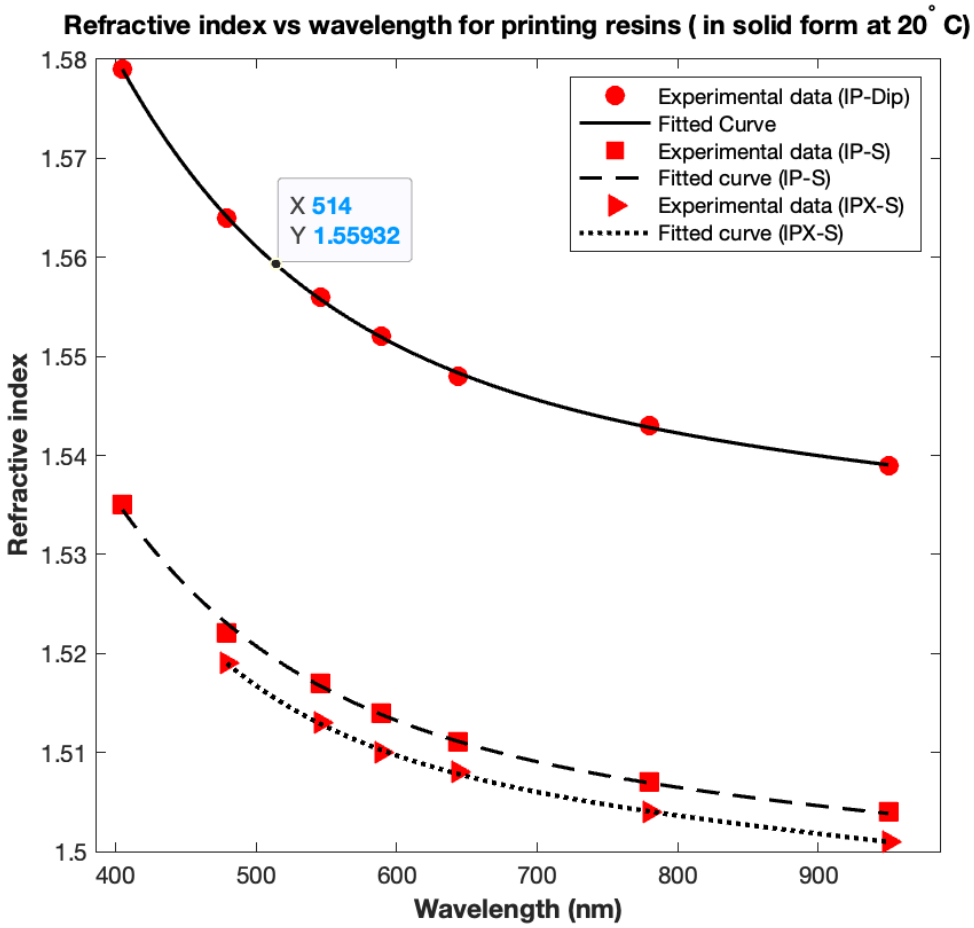


FIGURE 4.17: Refractive indices for various wavelengths for different printing resins when in solid state at 20° C. The experimentally measured refractive index values are in (red) [133], and curves fitted to the data with an R-squared value > 0.98 are in (black).

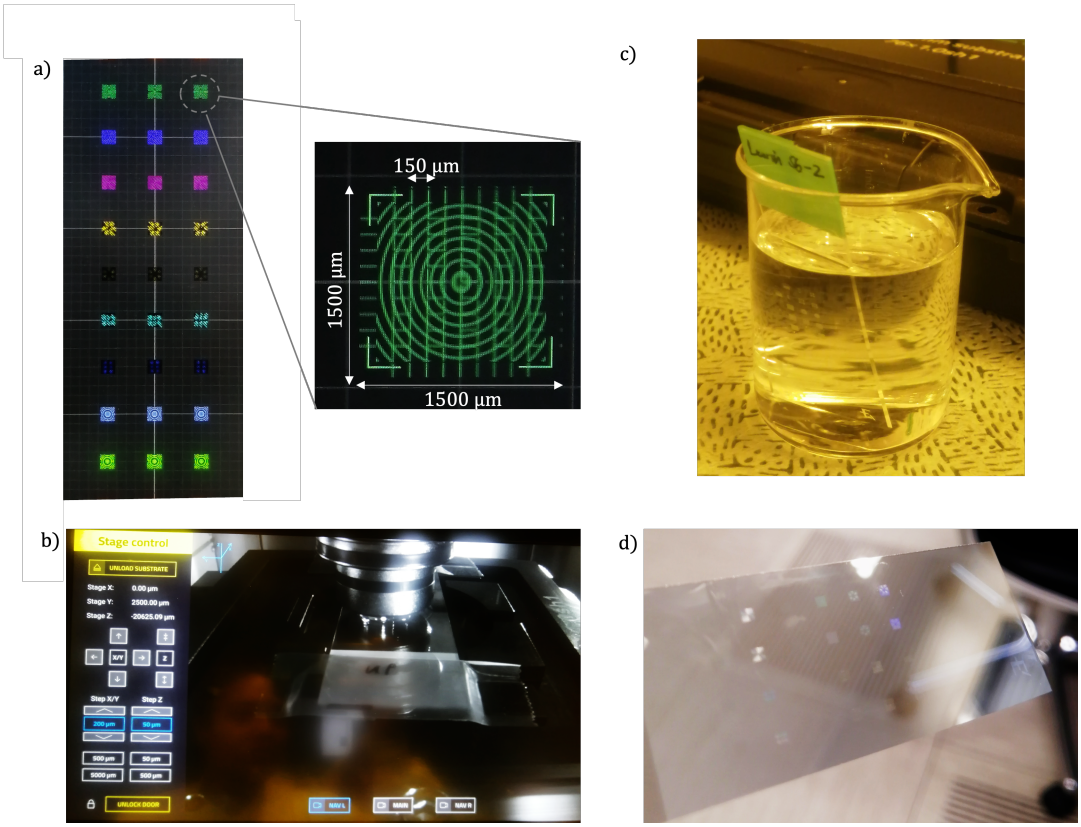


FIGURE 4.18: A summary of the printing process to make the desired beam shaping optics. a) The design is uploaded to the GrayScribe-X software to be scaled, hatched and sliced. Many optical elements can be uploaded, allowing for an array of optical elements to be printed on a single substrate. Here 9 unique optics are printed (each optic has its own colour), and x3 copies of each are made, leading to a total of 27 optics. Each optic was set to be 1500 μm × 1500 μm. Because the ×63 objective lens was used, (insert) the optic was subdivided into a 10 x 10 array of (150 μm x 150 μm) printable areas that are stitched together. b) After setting the printing parameters, uploading the design to the printer and preparing the substrate, the printing is done. 2 sample sets were printed- one for analysis, and the other for practical use. c) The samples were then developed in PGMEA followed by isopropyl. d) One sample was then metallised so it can be imaged and analysed.

After setting the parameters and uploading the design to the printer, the substrate had to be prepared as previously discussed. Here, we chose to use a microscope slide because its rough surface when compared to the silicon or fused silica wafers, offers a better surface adhesion for the printed structure thus improving overall structural stability. For optical testing, microscope slides are also easier to mount into a setup.

Once prepared and placed in the printer, as seen in Figure 4.18, the printing began and lasted for approximately 26.5 hours, i.e., approximately an hour per optic. Thereafter a second set of optics was printed, for analysis purposes. Both samples were then developed and one sample was metallised as seen in Figures 4.18 c), d).

4.2.4 Analysis

In this section the aim is to determine the quality of the printed optics. To do this the metallised sample was imaged and examined using a laser microscope (LM), scanning electron microscope (SEM) and various microscopy and analysis techniques.

TABLE 4.3: A summary of the printing parameters and their chosen/set values. These values were used for printing of any and all beam shaping optics in this chapter.

Parameter	Set value
Objective lens	x 63
Resin	IP-dip
Substrate	Microscope slide
Length per optical element (x -direction)	1500 μm
Width per optical element (y -direction)	1500 μm
Height per optical element	25 μm
Hatching distance	0.3 μm
Slicing distance	0.5 μm
Laser power	78 mW
Printing speed	60 000 $\mu m/s$

For example, using a LM one can view the printed optic and adjust the illumination settings to view it in the darkfield (where the background is dark and structures are light) or in the brightfield (where the background is light and the structures are dark), as seen in Figure 4.19 for vortex ($l = 3$) and HG_2^1 modes. Further on we will show how the LM, by illuminating the sample with various intensities and imaging it layer-by-layer, can be used to construct a 3-D digital model while one can image structures down to a nanometer level using a SEM. In this way we are able to view the optic from various perspectives and determine important information such as the dimensions and surface roughness of the printed optics. For the rest of this section we will focus solely on and analyse the vortex (l = 1) optic to avoid redundancy.

Length (x) and width (y). When using the LM, the software used to control the microscope also has analysis tools that can be used to determine the size of the sample, in this case the printed optic, in the x, y - directions. To do this one simply select two points of interest and the software will output the distance between those two points. The printed optic's dimensions were 1499 μm and 1500 μm in the x- and y-directions, respectively as seen in Figure 4.20. The slight difference in value is due to how the points of interest were selected on the software, and can be considered as negligible error ($\pm$ 1 μm). Hence, the optic's size exactly matches that of the design hologram which was encoded to have a length and width of 1500 μm in the x- and y- directions, respectively.

Next, to determine other properties of the printed optic, such as its thickness, we used the LM. By changing the intensity of the incident laser beam, the software is able to image the optic layer-by-layer and reconstruct a digital 3-D model of it as seen in Figure 4.21 a).

Thickness. All optics were designed to have a maximum thickness, t =25 μm in the z- direction. To verify this, using the digital 3-D model, a height map can be generated as seen in Figure 4.21 b). The minimum colour in the colourmap is set to the minimum thickness of the sample and is related to the base of the optic, i.e the substrate. The maximum colour represents the overall maximum printed thickness, which was measured to be $t_{max} = 24.653$ μm. By taking a horizontal cross-section in the x-direction (red) and a vertical cross-section in the y- direction (green) of the height map, we end up with the following profiles as seen in Figure 4.21 c).

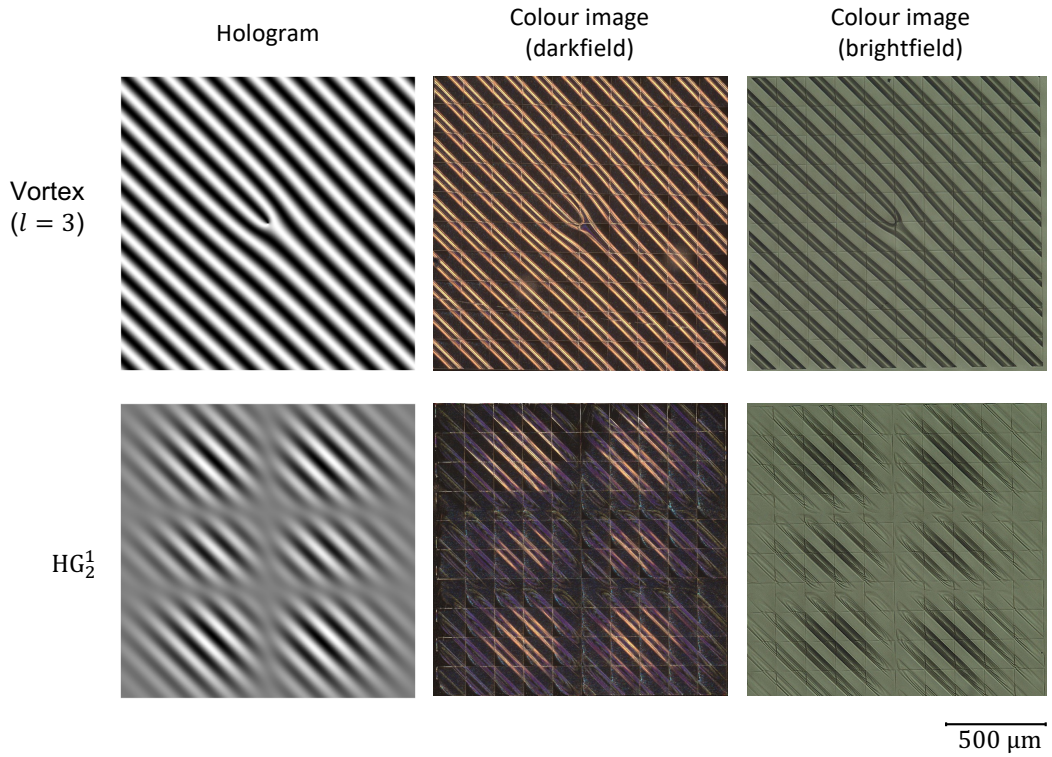


FIGURE 4.19: A comparison of the holograms that were previously generated for a vortex ($l = 3$) and HG_2^1 mode (left), and the microscopic images of the respective printed optics. Images of the printed optic were taken both the darkfield (middle) and brightfield (right). In all cases the scale is 500 μm.

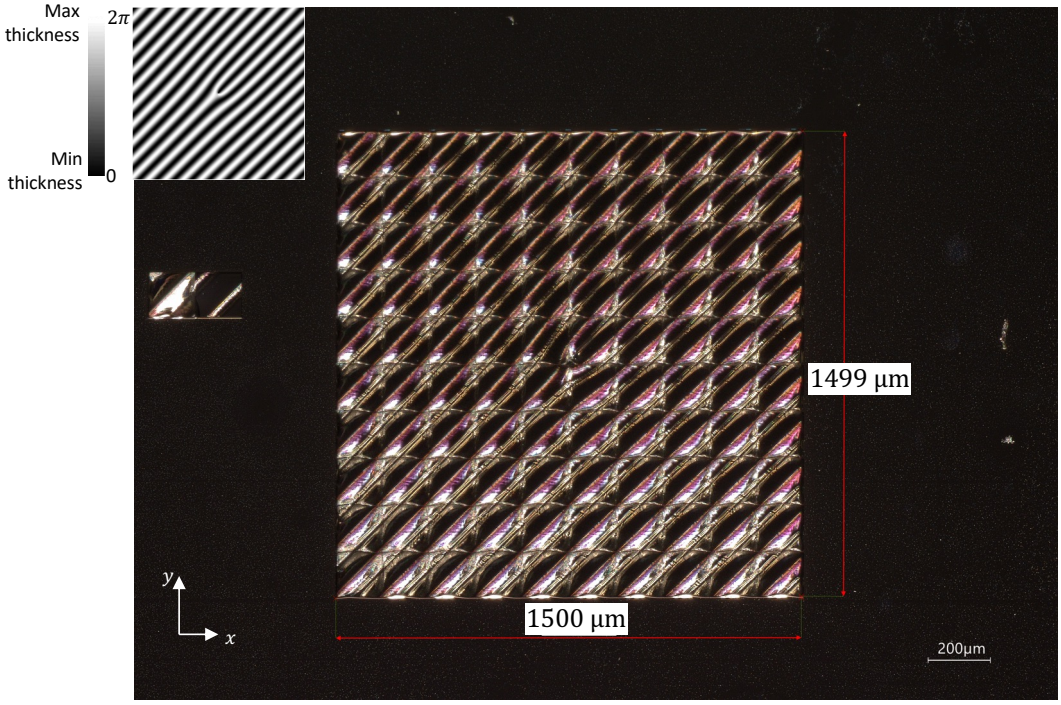


FIGURE 4.20: Determining the dimensions of the printed optic which was designed to produce a vortex ($l = 1$) mode. The hologram, seen in the (insert), was designed to have a length (x-direction) and width (y-direction) of 1500 μm. The printed optic's size in the x-direction (length) and y-direction (width), were measured to be 1499 μm and 1500 μm, respectively. The slight difference in value is due to how the points of interest were selected on the software, and can be considered as negligible error ($\pm$ 1 μm). The scale bar in the image is 200 μm.

By measuring the difference between the peak and base of arbitrary points (labelled [1] and [2]) in the respective cross-sections, we determined the average maximum thickness of the optic to be $t_{max,ave}$ = 23.154 μm. This difference from the design value is likely as a result of how the sample was developed. During development, the sample remained in the PGMEA solvent for too long which degraded and disintegrated the surface. This is not usually a problem for larger samples whose surfaces are not as exposed nor delicate. However, due to the intricate design of the optic, this effect is noticeable. It is important to note that these samples were metallised, but the thickness of the sputtered material is only 5 nm and can be considered negligible to these results.

One could always reduce the time that the sample is kept in the PGMEA solvent during development to ensure that the structure is not severely degraded. However, the more intricate the structure, the more gaps or openings for excess un-polymerised resin to fill. If this resin is not entirely dissolved and removed during the development process, resin deposits will disfigure the structure in a randomised pattern, as seen in Figure 4.22.

Spacing between structures. When generating the hologram that was used as a design for the vortex ($l = 1$) optic, a grating was encoded with a period λ_x= 10 grooves/m. Since the optic was designed to have a length of 1500 μm, this corresponds to a grating spacing, d_x= 150 μm in the $x-$ direction. Hence, another way to characterise the optic and verify the printing quality would be to measure the spacing between adjacent structures in a region of interest where the structures are linear, evenly spaced and thus mimics the encoded grating as seen in Figures 4.21 b), c) (labelled [3]). The distance between adjacent structures was measured to be 147.810 μm, as seen in Figure 4.21 c). The optic was designed in an identical manner in the $y-$direction, hence a similar result was measured. The difference between the measured and encoded grating spacing is because the encoded phase mask, which is included in the hologram, distorts the grating spacing. Hence to truly verify the grating spacing, one must use these results in conjunction with optical tests.

Surface roughness. The roughness of an optical surface is important because rough surfaces cause light to scatter and may lead to noise and or cause aberrations to the generated mode. To determine the roughness of the same vortex ($l = 1$) optic, we examined it using a SEM as seen in Figure 4.23. When magnified $\times$1700 the printing steps within the structure became visible and the structure no longer had a smooth appearance, as seen in Figure 4.23 a).

To determine the surface roughness of the optic (without taking into account the stitching lines), we magnified the area on the structure marked in green, as seen in Figure 4.23 b). The printing steps were then visible enough to be measured and was found to be approximately 231 nm. The size of the printing steps, i.e., the surface roughness lies on the order of 200 nm, which is to be expected as the smallest voxel i.e., the volume "pixel" size for the $\times$63 objective lens is 200 nm. This proves that the printing resolution of the Quantum-X is indeed within range of 200 nm .

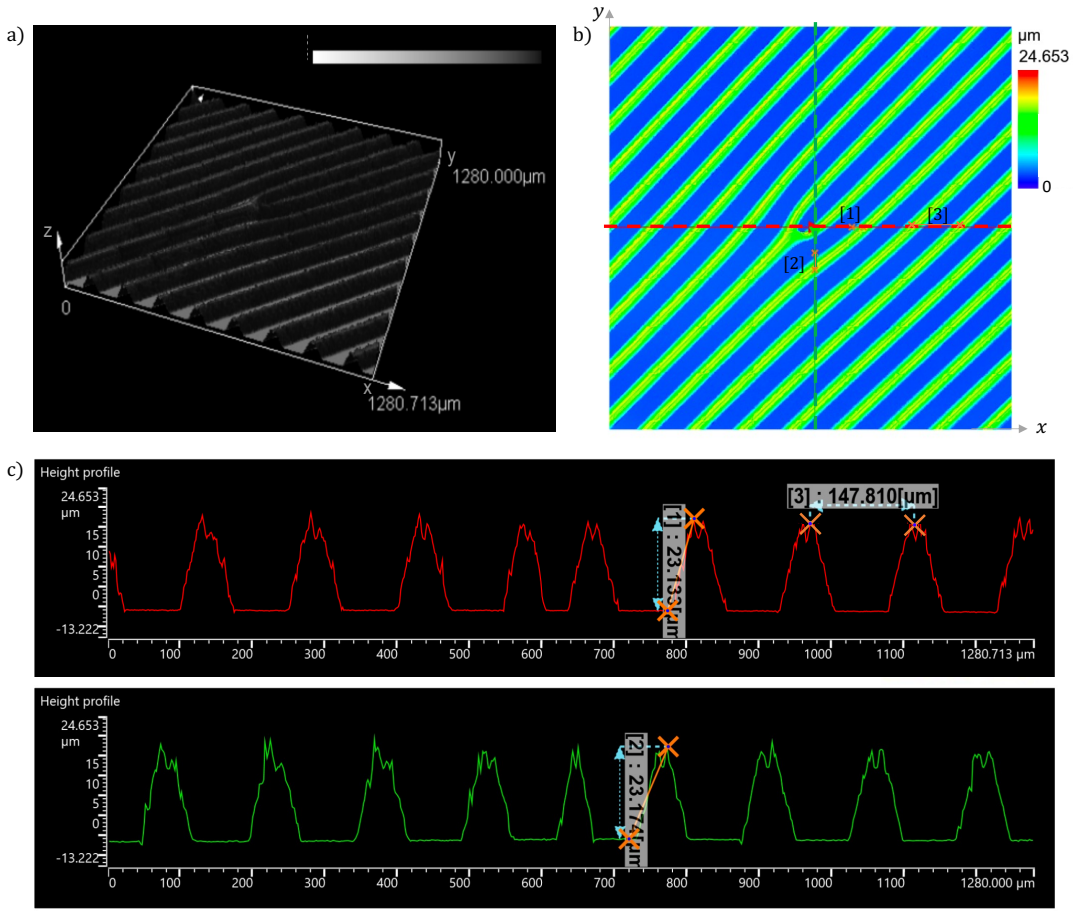
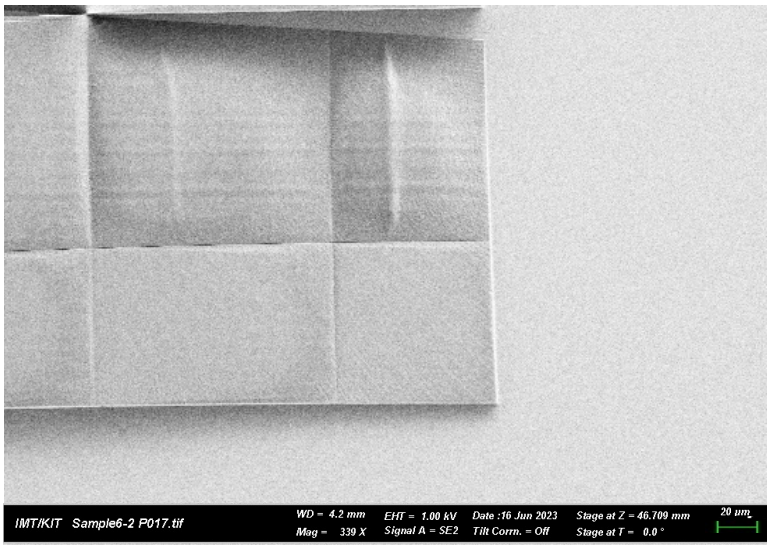
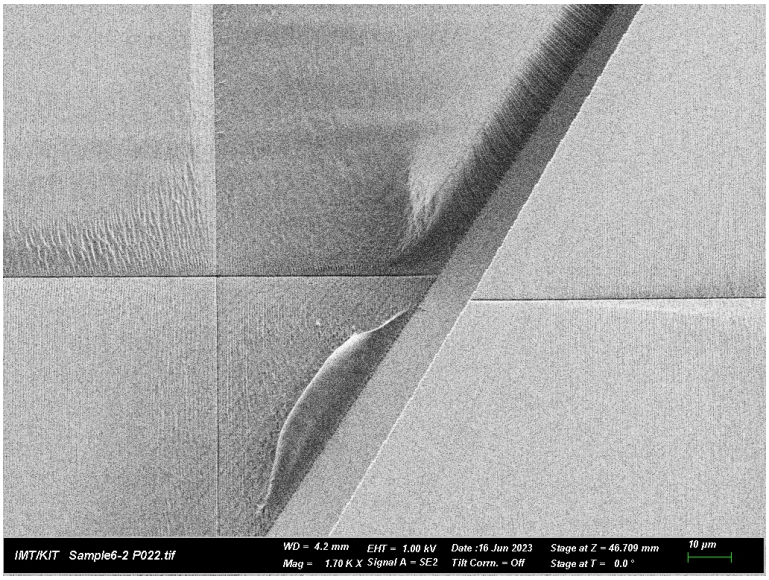


FIGURE 4.21: Analysing a vortex ($l = 1$) printed optic using a laser microscope (LM) to determine the thickness, and spacing between structures. a) By illuminating the optic with different laser intensities, the optic was imaged layer-by-layer and a digital 3-D model was constructed. b) Using the digital 3-D model a height map can be generated, where the minimum and maximum colours represents the minimum and maximum thickness of the optic, respectively. c) By taking a cross section of the height map in the (red) horizontal, x- and (green) vertical, y -directions, we determined the average maximum printed thickness across the optic to be 23.154 μm by measuring and taking the average of the distance between arbitrary peaks and the base (labelled [1] and [2]). By measuring the distance between the two adjacent peaks (labelled [3]), which was determined as 147.810 μm, we verify that the optic does have a grating period λ_x = 10 grooves/m which corresponds to a grating spacing d = 150 μm.





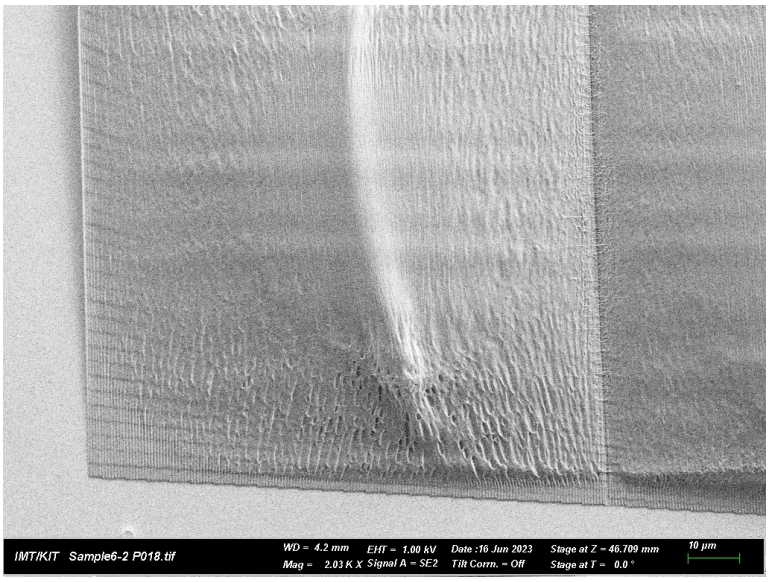
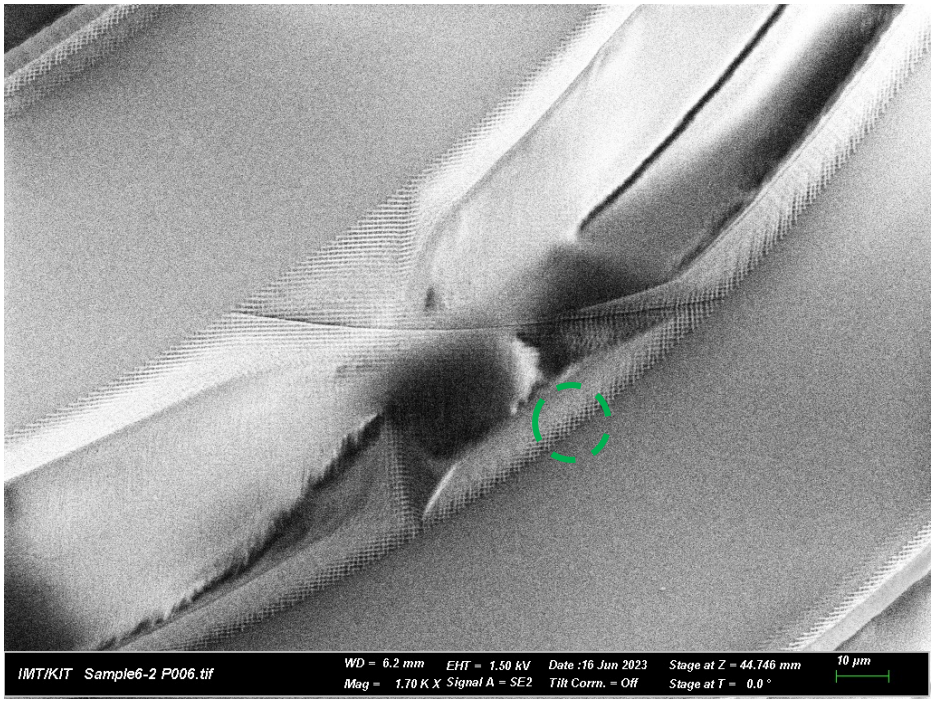


FIGURE 4.22: A visual depiction of the effect of undissolved resin on the surface of the optic. Resin deposits disfigure and distort the surface of the optic in a random manner. The scale bar for the first image is 20 μm, while the scale bar for the second and third are 10 μm.

a)



b)

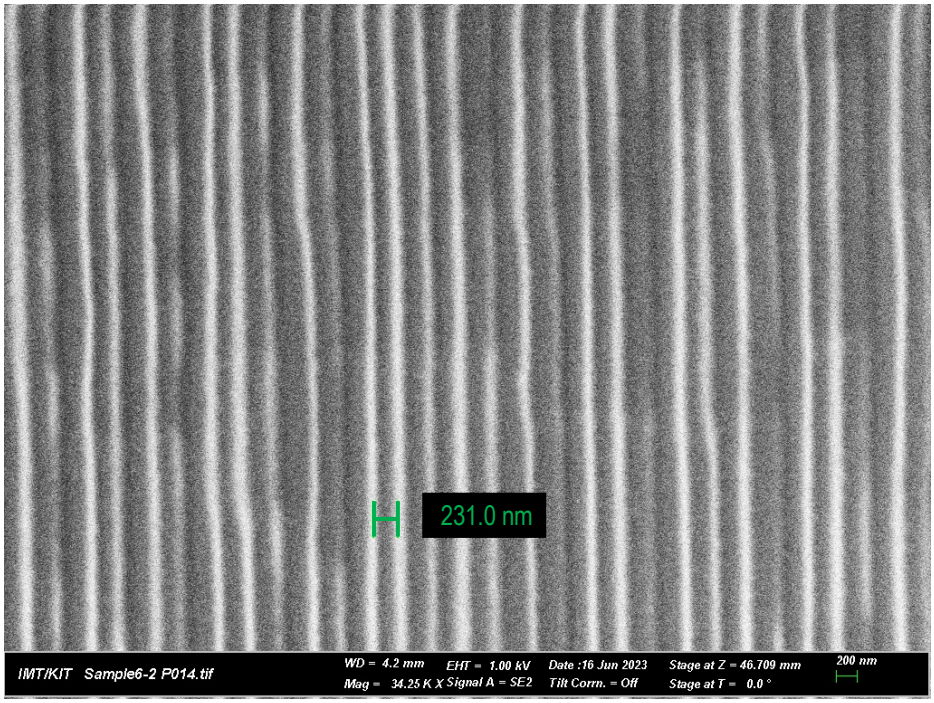


FIGURE 4.23: SEM images depicting how to determine the true printing resolution of the Quantum-X when a $\times 63$ objective lens is used. a) A printed optic to create a vortex ($l = 1$) was magnified $\times 1700$ where the scale bar is 10 nm. Looking at the structure, it no longer appears continuous as the grid or 'steps' lines are visible. By studying the area marked in green, b) at a magnification of $\times 34250$, where the scale bar is 200 nm, the distance between these steps, i.e., the surface roughness is measured to be 231 nm. This proves that the printing resolution of the Quantum-X is indeed within range of 200 nm .

4.3 Optical testing

In the previous section we analysed the printed optics from a printing/manufacturing perspective and determined that the holograms were correctly printed and have the properties, such as the size, that was desired. Now, in this section we will analyse the optics from an optical perspective to determine if it can indeed shape many wavelengths of light and produce the desired modes. To do this we select two optics: the vortex ($l = 1$) and HG_1^2 to serve as examples of where phase-only modulation and complex-amplitude modulation have been used.

4.3.1 Mounting and aligning the sample

Mounting. To test the sample, it must be added in the optical setup in a manner where it can be shifted in the x, y planes as well as tipped and tilted for alignment purposes. The mount that we used is shown in Figure 4.24, and was assembled in the following manner: the sample was slid into a microscope slide holder and secured by turning screw 1. This holder sat on a stage that could be tipped and tilted using screw 2. The stage was mounted on a translation stage that could be turned using screw 3. As the screw is turned the translation stage moves up and down in the y-axis. This can be used to adjust the height of the sample. This translation stage is mounted to another which lies in the x, z-plane. By turning screw 4 this translation stage will move back and forth in x-direction. This can be used to adjust the position of the sample relative to the incident beam.

Alignment. If the incident beam and sample are misaligned, the beam will appear to have an uneven distribution of the intensity, as seen in Figure 4.25 a). To align the sample to the incident beam, it can be shifted in the $x-$ and y- directions using the translation stages until the intensity of the mode is evenly distributed, as seen in Figure 4.25 b). If many optics are printed on the microscope slide, as in our case, then one can swap to a different structured mode by simply shifting the microscope slide using the translation stages.

Astigmatism. If the observed mode appears to have astigmatism it is likely because the substrate is tilted with respect to the optical axis. This can be corrected for by using tip-and-tilt screws (labelled 3 in Figure 4.24) until the back reflection of the sample is aligned to the optical axis. The beam will then appear symmetric.

4.3.2 Experimental setup

To test the optics we set up an experiment as seen in Figure 4.26. All the printed optics were designed for $\lambda_0 = 514$ nm, hence the setup was created and aligned using λ_0. The setup was as follows: a beam of light ($\lambda_0 = 514$ nm) was expanded and collimated (when testing optics that rely on complex-amplitude modulation) or imaged (when testing optics that rely on phase-only modulation) using lens l_1 with focal length $f_1 = 100$ mm, and lens l_2 with focal length $f_2 = 300$ mm.

The beam was then incident on the microscope slide which was composed of an array of 3-D printed optical elements. It is important to note that the beam was magnified so that it was large enough to cover the entire area of a single optic, but

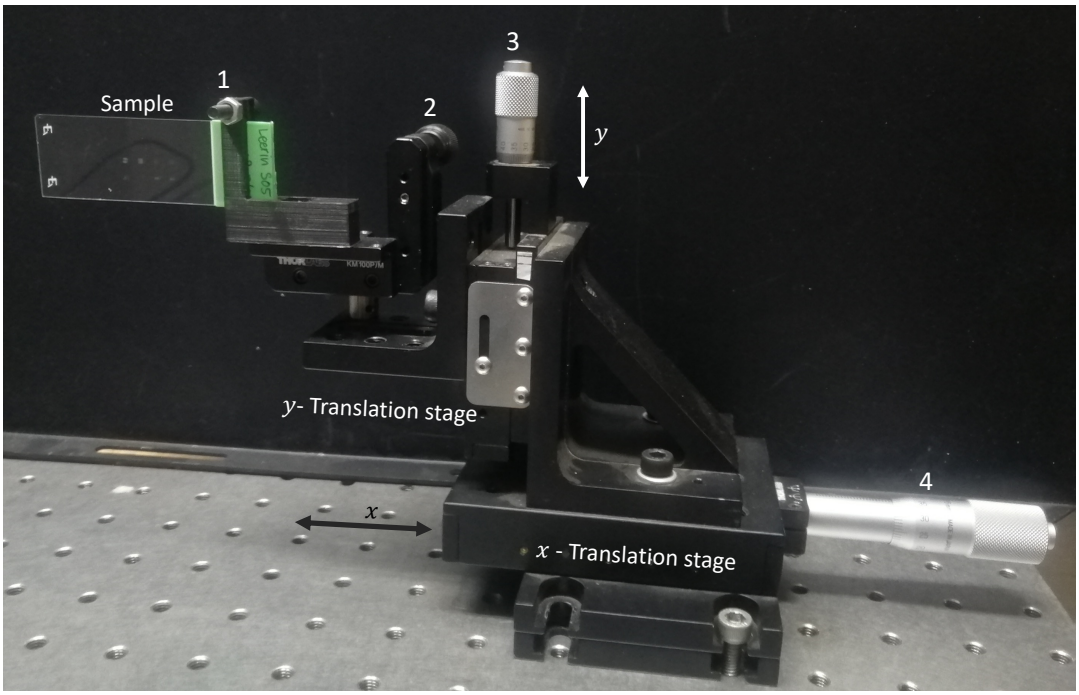


FIGURE 4.24: The ideal manner to mount the 3D- printed sample.The sample is placed in a holder and kept in position by fastening screw 1. This holder sits on a stage that can be tip and tilted using the screw 2. The stage is mounted to a translation stage that can be turned using screw 3. As the screw is turned the translation stage moves up and down in the y-axis. This can be used to adjust the height of the sample. This translation stage is mounted to another which lies in the x, z-plane. By turning screw 4 this translation stage will move back and forth in x-direction. In this way, when added to the optical setup, one is able to adjust the position of the sample as needed — making alignment easier.

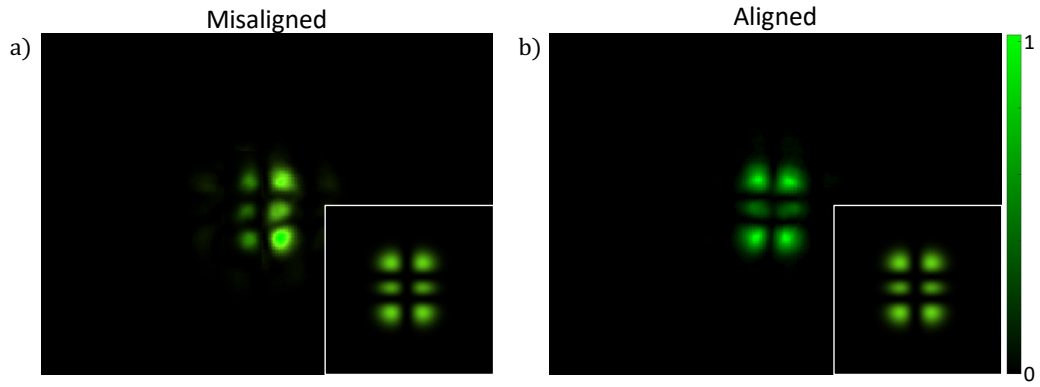


FIGURE 4.25: The effect of misalignment of the sample to the produced mode. a) When the sample is misaligned and or tilted with respect to the optical axis, the produced mode may appear to have astigmatism with an uneven intensity distribution. b) This can be corrected for by adjusting the alignment of the sample, and will result in a mode with an evenly distributed intensity and symmetric shape. In both cases the simulated desired HG mode is shown in the inserts.

not so large that it illuminated neighbouring optics, as seen in Figure 4.26 a). This ensured that the desired mode experienced no interference from modes produced from neighbouring optics.

Once incident on the hologram, the beam was diffracted into multiple orders, as seen in Figure 4.26 b). In this case, the beam was aligned to an optical element that produces an HG_1^2 mode. A lens l_3 with a focal length f_3 = 200 mm was then placed a distance f_3 away and aligned to the +1st-order. Since all the printed optics were designed to have a grating with the same grating frequency, we can maintain the same alignment as we shift the sample to swap between different optics and generated modes.

When using an optical element that relies on phase-only modulation to produce the desired mode, for example a vortex ($l = 1$) mode, the rest of the setup was as follows: close to the Fourier plane a pinhole was placed to select the +1st order with the minimum amount of noise. Ideally the pinhole would be placed in the Fourier plane, but this position was occupied by the CCD. By placing the CCD here, we were able to view the mode in far-field. The intensity image of the beam was then captured.

When using an optical element that relies on complex-amplitude modulation to produce the desired mode, for example a HG_1^2 mode, the setup after the l_3 was swapped to the configuration seen in Figure 4.26 c). In this case the pinhole was shifted to the Fourier plane. A mirror, m_1 was then added to redirect the beam to lens l_4 with focal length f_4 = 200 mm. The beam was then imaged and viewed using a CCD camera which was placed a distance f_4 away after l_4. As seen in Chapter 3, in the image plane, the dispersed broadband beam will be recombined. Therefore, to ensure that the CCD is placed in the correct plane, it was shifted until all the beams appeared as a single mode. Images were taken for each printed element in the sample per discrete wavelength whilst still maintaining the alignment for λ_0 = 514 nm.

4.3.3 Experimental results

The experimental results for an optic created to generate a vortex ($l = 1$) mode through phase-only modulation are shown in Figure 4.27. In Figure 4.27 a) the camera images (intensity profiles) are shown for each discrete wavelength. Because one observes the modes in the Fourier plane, to achieve a 'broadband' beam, we must digitally overlap each mode. In Figure 4.27 b) the intensity profile of the digitally overlapped mode is shown. In Figure 4.27 c) the intensity cross-sections for each discrete wavelength and the digitally overlapped mode are shown. In Figure 4.27 d) the cross-section of the the experimental 'broadband' mode (which is achieved by digitally overlapping the experimental modes) is compared to the simulated 'broadband' mode (which is achieved by digitally overlapping the simulated modes) and was found to have a correlation value of 96.9%.

Figure 4.28, on the other hand, shows the experimental results for an optic that generates an HG_1^2 mode, and serves as an example of an optic that uses complex-amplitude modulation. In Figure 4.28 a) the camera images (intensity profiles) are shown for each discrete wavelength and the broadband 'multiline'. Figure 4.28 b) the intensity cross-sections for each discrete wavelength and the multiline are shown,

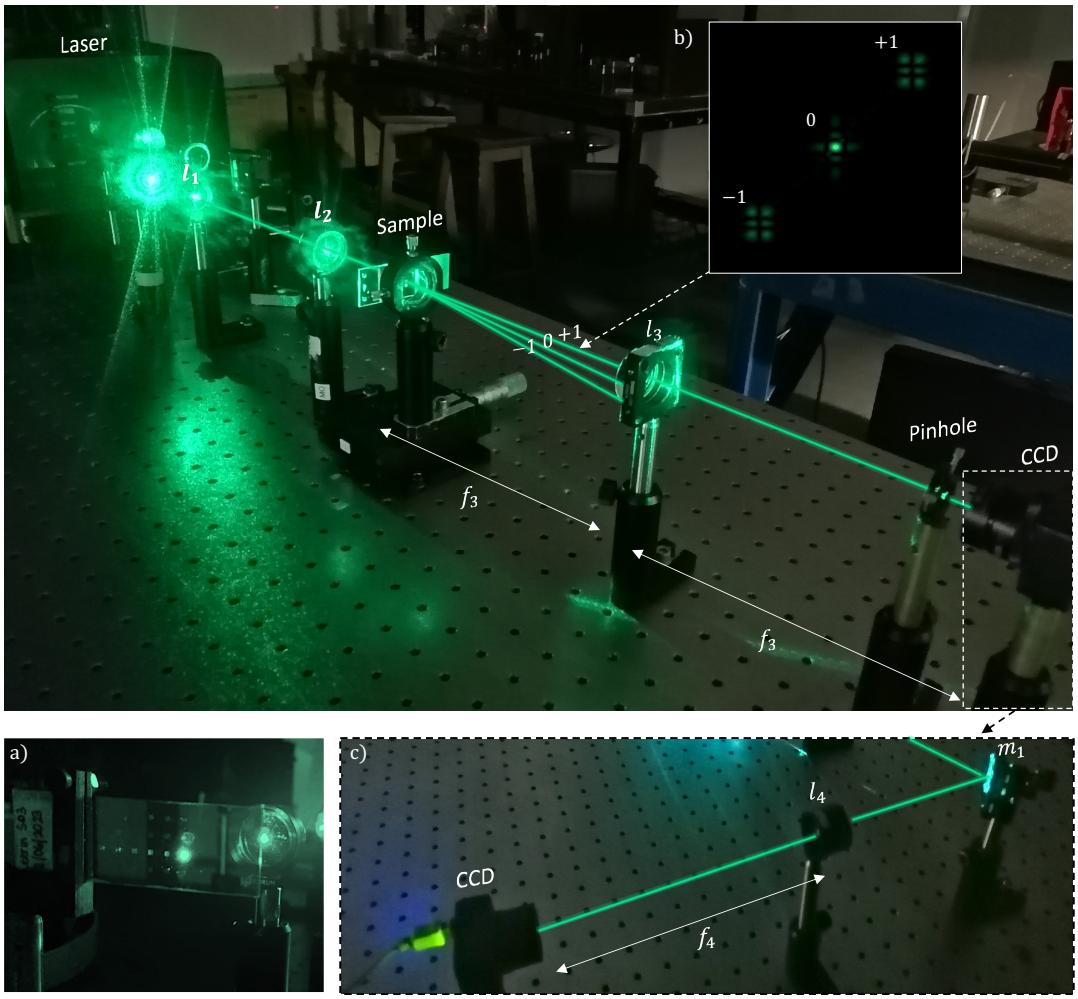


FIGURE 4.26: The experimental setup used to optically test the beam shaping ability of the 3-D printed optics (sample). Lenses l_1 (f_1 = 100 mm), l_2 (f_2= 300 mm) expand and collimate (for complex-amplitude modulation) or image (for phase-only modulation) the beam, which is incident on the sample. The size of the beam must be large enough to cover the entire area of the optic, but not illuminate neighbouring optics, as seen in a). The grating encoded in the optic causes the beam to diffract into various orders, as seen in b). Lens l_3 (f_3 = 200 mm), located a distance f_3, is aligned to the +1st-order, and Fourier transforms the beam. If doing phase-only modulation, slightly before the Fourier plane a pinhole is added to filter out noise. The beam is the then viewed in the Fourier plane using a CCD which is located f_3 after from l_3. If doing complex-amplitude modulation, the pinhole is placed in the Fourier plane. As seen in c), a mirror m_1 then redirects the light towards a lens l_4 (f_4 = 200 mm) which images the beam. The CCD is placed a distance f_4 after l_4 to observe the mode in the image plane.

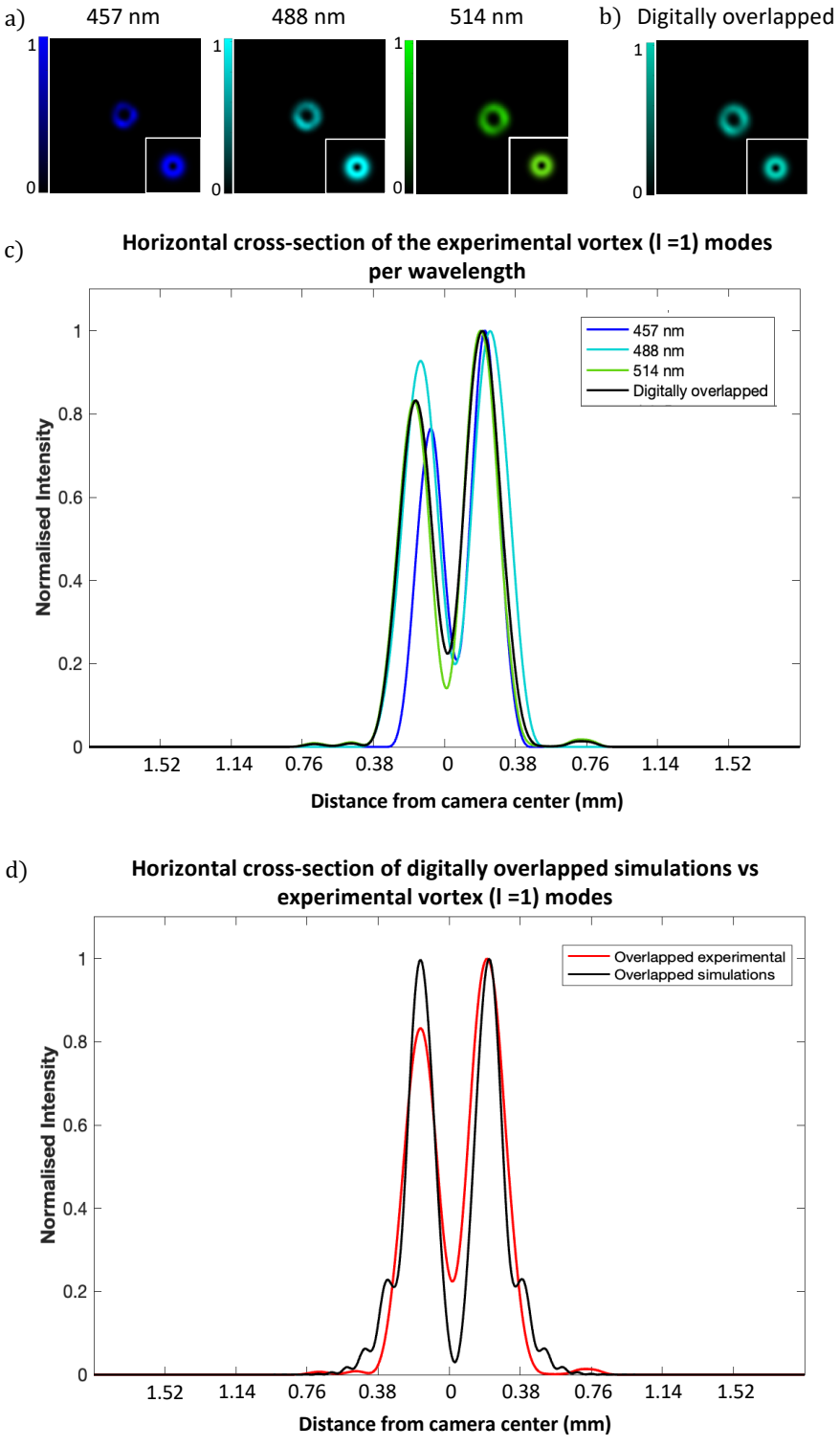


FIGURE 4.27: The experimental results for an optic that generates a vortex ($l = 1$) mode through phase-only modulation. a) The camera images (intensity profiles) are shown for each discrete wavelength. Because one observes the modes in the Fourier plane, to achieve a 'broadband' beam, we must digitally overlap each mode. b) The intensity profile of the digitally overlapped mode is shown. c) The intensity cross-sections for each discrete wavelength and the digitally overlapped mode are shown. d) The cross-section of the experimental 'broadband' mode (which is achieved by digitally overlapping the experimental modes) is compared to the simulated 'broadband' mode (which is achieved by digitally overlapping the simulated modes) and was found to have a correlation value of 96.9%

TABLE 4.4: Measured beam sizes per wavelength of HG_1^2 modes produced by a 3-D printed optic

Wavelength	**Beam size (mm) $\pm$ 0.008 mm**
457 nm	0.319
488 nm	0.441
514 nm	0.426
Multiline	0.410

while Figure 4.28 c) shows the cross-section of the experimental and simulated broadband mode which was found to have a correlation value of 94.8%.

When creating the HG optic the design wavelength, λ_0 = 514 nm and the desired beam size was set to 0.4 mm. In the image plane we expect the modes to have the same size as the desired/encoded beam size. Using Figure 4.28 b), the beam sizes of the experimental modes can be determined by measuring the peak-to-peak distance between the maximum intensity values. The results are summarised in Table 4.4. Although the beam sizes for wavelengths other than λ_0 differs slightly from the desired beam size, the broadband beam had a beam size that matched the encoded beam size quite well.

The noise in the recorded beams is worth discussing as it highlights a challenge in these experiments. Due to the limitations when making the optic, one cannot encode a grating with a very high frequency, as the fine structures would easily break-off or require a very long printing time. Hence, a grating with a small grating period was encoded. However due to the space limitation, a large propagation distance was not feasible to allow the modes to naturally separate. Because the wavelengths are quite close in value, when diffracted, they do not have a large initial spatial separation and their respective orders are not evenly spaced nor grouped together, for example, the +1st order of one wavelength could be overlapped with the 0th order of the another wavelength. Due to this effect a make-shift aperture had to be used which was not as efficient at blocking out unwanted modes or stray light as a traditional spatial filter, which contributed to the noise seen in the intensity images. Longer focal lengths and thus longer distances would solve these issues.

In Figures 4.27, 4.28 we demonstrated broadband beam shaping specific cases when the printed optics produced a vortex ($l = 1$) and HG_1^2 mode. However, it is important to note that any mode can be printed and the same effects would be observed, hence we printed many optics on the same microscope slide. In Figure 4.29 we consider 3 additional modes, namely a vortex ($l = 3$), LG_1^2 and HG_1^1. Microscopic images of 3 additional optics are show where the images were taken in the light-field, hence all printed structures will appear dark and the substrate will appear light, the inverse of the holograms shown in the insert. The simulated and experimental results per discrete wavelength are also shown.

In summary, when a computer generated hologram, which is typically used for digital modulating devices (like SLMs), is uploaded and 3-D printed (taking into account other factors such as thickness and size) the resultant physical optic will have a structure that resembles the 2-D generated hologram. When tested, the optic behaves in the same way that the encoded hologram does, and is therefore able to shape multiple wavelengths. In this way a simple, compact optic capable of broadband beam

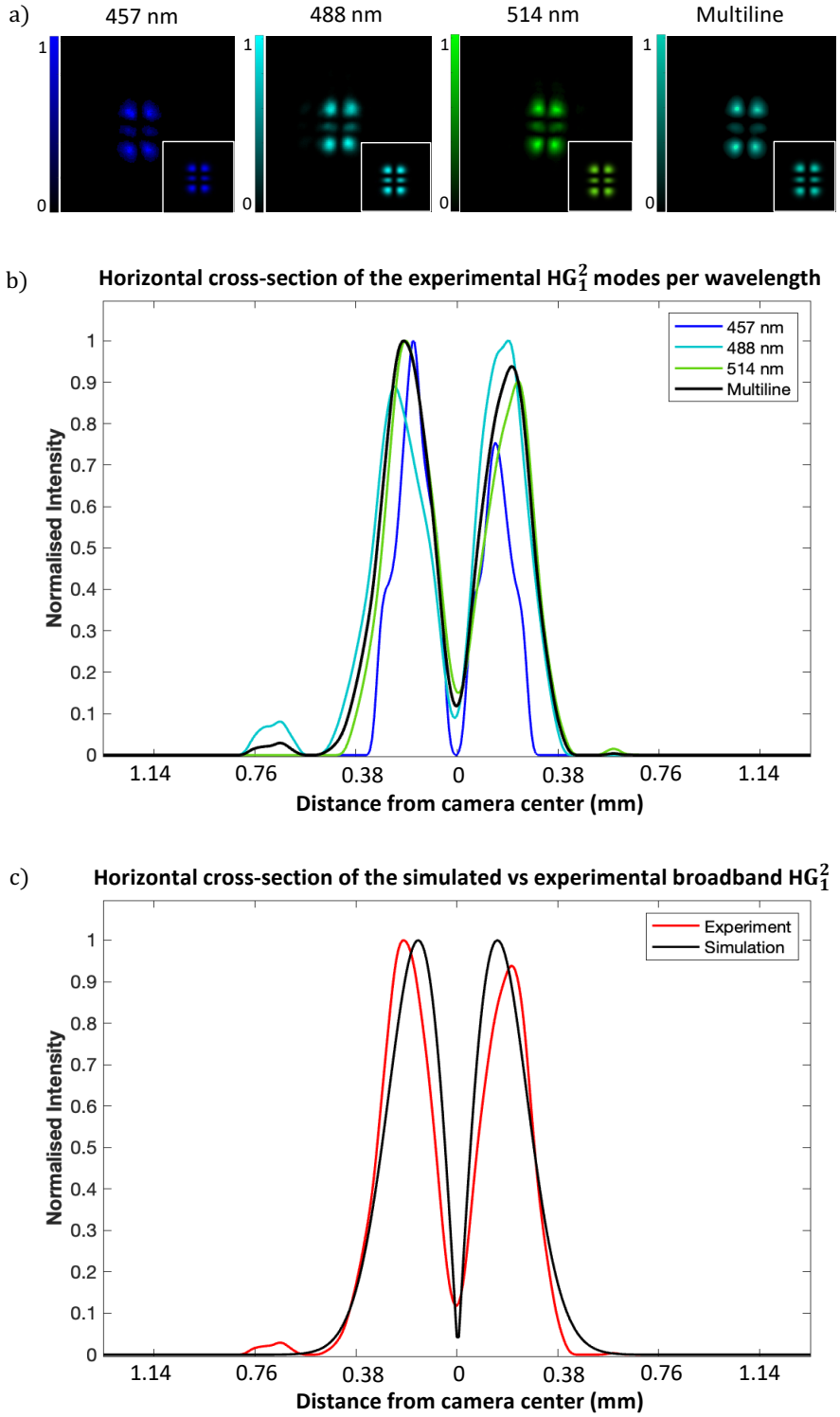


FIGURE 4.28: Experimental results for an optic that generates an HG_1^2 mode through complex-amplitude modulation. a) Camera images (intensity profiles) are shown for each discrete wavelength and the broadband 'multiline' with simulations given as inserts. b) The intensity cross-sections for each discrete wavelength and the multiline are shown, while in c) the cross-section of the experimental and simulated broadband mode which was found to have a correlation value of 94.8%.

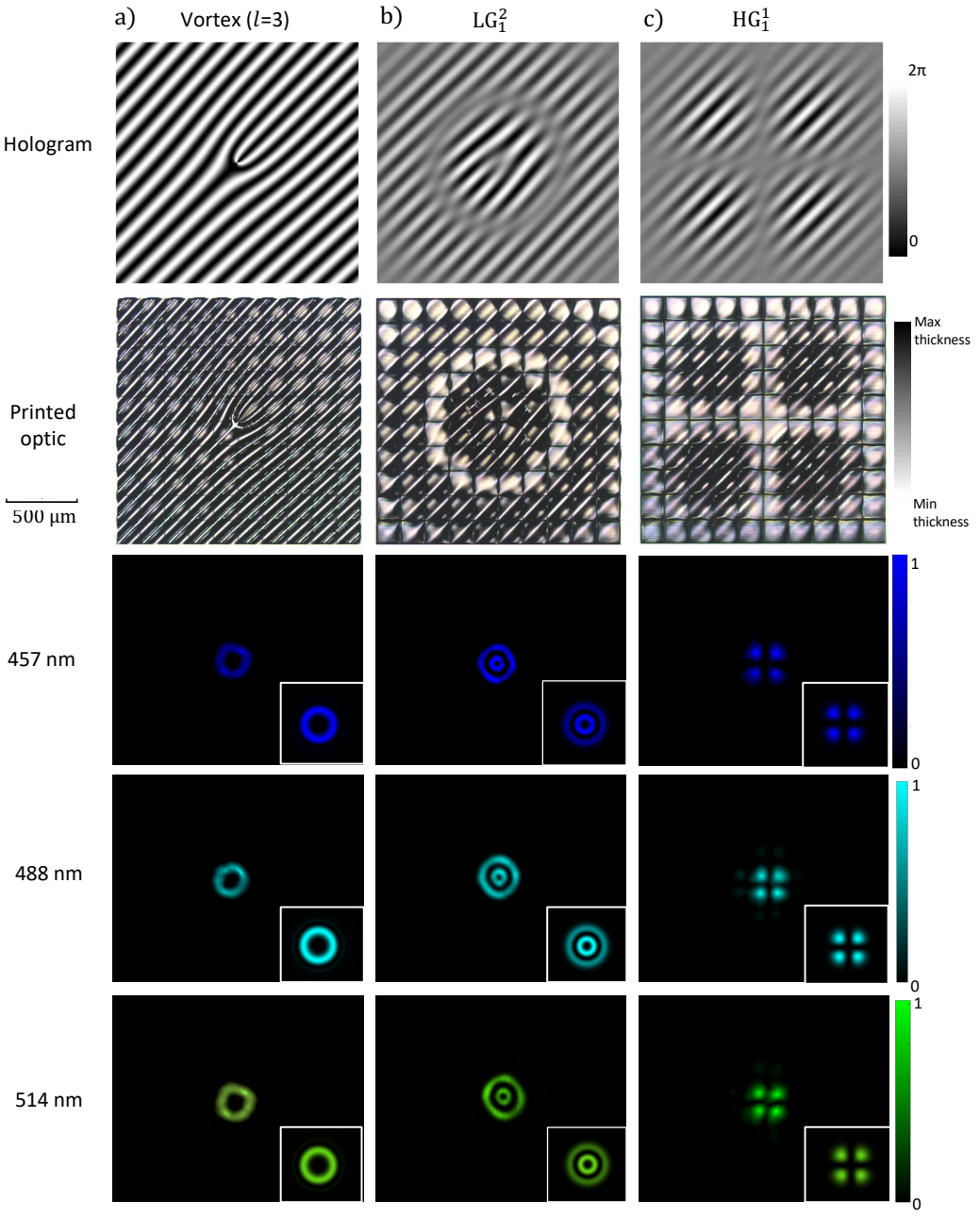


FIGURE 4.29: Broadband beam shaping can be achieved for various modes with 3-D printed optics. Here we showcase additional examples in the following columns: a) vortex ($l = 3$), b) LG_1^2 and c) HG_1^1. The holograms used as a design template are shown for the various modes. Microscopic images of 3 optics are shown where the images were taken in the light-field, hence all printed structures will appear dark and the substrate will appear light- the inverse of the holograms (insert). The scale bar is 500 μm. The simulated mode and experimental results per discrete wavelength are also shown.

shaping is realised.

Chapter 5

Conclusion and prospectives

5.1 Conclusion

The focus of this work was to create a system that could shape multiple wavelengths of light either discretely or simultaneously and thus generate broadband structured light. To do this, the task was broken up into 3 objectives: (1) establish how a system should operate and what it should consist of to generate the desired structured beams then, (2) create a system that uses a digital beam shaping element and (3) a physical beam shaping element.

In Chapter 1 we considered *how* beam shaping systems could operate through CAM and phase-only modulation, and then established general expressions to determine the transmission function of the necessary broadband beam shaping element.

In Chapter 2 we considered the experimental tools and techniques needed to practically implement broadband beam shaping. The chapter began by first characterising the broadband laser source as well as lenses, which are instrumental in any optical experiment. The chapter then continued with a discussion and introduction of physical beam shaping optics (refractive and diffractive) and digital beam shaping devices, such as the SLM and DMD. With the foundation laid, all that was left to do is practically demonstrate broadband beam shaping.

In Chapter 3 we looked at using digital devices, specifically DMDs for broadband beam shaping. Because the DMD is an amplitude-only device, we began by first establishing how to create holograms, when encoded on the DMD, that are capable of CAM despite the binary manner of the DMD. The chapter then continued with first demonstrating how to setup and shape monochromatic light through phase-only and CAM modulation, which resulted in the generation of flat-top and LG beams for each case respectively. This concept was then extended to broadband beam shaping where additional considerations such as dispersion effects needed to be addressed. We offered solutions to compensate these effects and demonstrated it for a specific case.

In Chapter 4 the objective was to demonstrate broadband beam shaping with a physical optic. To do this, we resorted to 3-D lithography printing as a fabrication method. Due to the properties of the printing material, the printed optic was only able to impart phase changes into an incident beam. We can therefore used the same encoding technique used to create CGHs intended for the SLM to create a design for the optic. The chapter began therefore with a brief summary of the encoding scheme, followed by a discussion of how the optics were fabricated. Next, an analysis was done to determine the quality of the printed optics. Finally the chapter

concluded with a demonstration of how the optics could be used to shape broadband light through phase-only modulation and CAM and thus generate vortex and HG modes, respectively.

To conclude, we successfully demonstrated broadband beam shaping through two techniques namely phase-only and complex amplitude modulation which was implemented using both physical optics and digital modulating devices. In this way we have explored and now offer a way to introduce broadband beam shaping into various applications that may benefit from the compact size of the physical beam shaping optic or the dynamic ability of the digital, which will hopefully act as a basis for new and exciting developments.

5.2 Future work

In this work we looked into tools and techniques for broadband beam shaping coherent light in the visible regime (400 nm - 700 nm). One of the first extensions of this work would be to shape broadband incoherent light. When using spatially coherent light from lasers for beam shaping one often observes speckles which arises from the destructive interference between adjacent sampling points and acts as noise. This can be problematic especially for a particular application where high precision is needed. However, incoherent light does not have this same issue and is in fact more resilient against obstacles in its path. Incoherent light sources are also easily accessed and more economical. Hence, beam shaping broadband incoherent light has become quite topical lately and has in fact been already demonstrated by Wang [62, 63] using 3-D printed optics. Although there has been some progress made in the field using physical optics true demonstrations using digital modulating devices such as DMDs or SLMs remains to be explored. One particular application where such an approach may be beneficial is in optical communication systems.

Another avenue which deserves exploration is extending this work to wavelengths beyond visible light, specifically towards the X-ray regime. Many imaging systems rely on the use of spatially incoherent X-ray sources that emit a range of wavelengths (energies). To maximise the imaging resolution, the beam is allowed to propagate quite far to improve the coherence, and a single wavelength is usually filtered. Most of the incident light is discarded, making it a highly inefficient process. If an optic which shapes incoherent broadband X-ray waves could be created and added to the system this would significantly improve the efficiency. This concept is of high interest at the moment as it holds much potential.

Recently broadband X-ray optics (achromatic and apochromatic X-ray lenses) and monochromatic beam shaping optics for coherent X-rays have been demonstrated, but none have combined the two methods, nor extended it to incoherent sources yet. Building upon this work we would like create optics that can shape incoherent broadband X-rays. To do this, we must first create optics that can shape monochromatic X-ray waves. We have recently begun investigating the fabrication of such optics and have considered using the Quantum-X Nanoscribe.

Although the properties of printing resin are quite well known in the visible regime, this is not the case in the X-ray regime. Nevertheless, recent work has proven that the resin can indeed be used for the fabrication of X-ray optics, even though it has

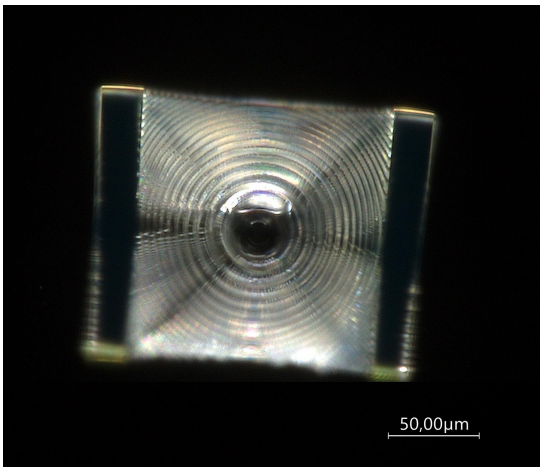


FIGURE 5.1: A microscopic image of a printed converging lens designed to focus x-rays (λ_0 = 0.52 nm)

weak refractive properties. To overcome this multiple optics are used so that when combined they effectively produce the desired beam. Using this concept as a guide, we designed our first X-ray optic — a set of $\times 10$ converging lenses (λ_0 = 0.52 nm) with a combined effective focal length of 0.5 m. Figure 5.1 shows a microscopic image of one of the printed lenses present in the set.

From this brief overview, it should be clear that the techniques used to shape broadband light can be used beyond the coherent, visible regime to explore unimaginable avenues. Broadband beam shaping is therefore an invaluable tool that holds the potential to make a significant impact on current and future applications.

Appendix A

Supplementary information on the calibration of a Spatial Light Modulator (SLM)

This appendix discusses the experimental procedure used to calibrate the spatial light modulator (SLM) to a specific wavelength, λ. Before using the SLM for beam shaping it is imperative that it is well calibrated as the phase shift, $\Delta\phi$ imparted into the incident beam is dependent on the wavelength λ. The calibration process thus generates a mapping to ensure that the 256 greyscale values used in holograms correctly corresponds to the voltage needed for proper liquid crystal (LC) orientation, resulting in the desired phase change between $[0, 2\pi]$ (or a multiple of 2π). For example, a hologram with greyscale value = 0 corresponds to no imparted phase shift. If the greyscale value = 128, $\Delta\phi = \pi$ while a greyscale value = 255 corresponds to $\Delta\phi = 2\pi$.

The calibration process is conducted experimentally, as illustrated in Figure A.1. To achieve calibration, two lenses, denoted as l_1 and l_2, with focal lengths f_1 and f_2 (where $f_1 < f_2$), are positioned to expand and collimate the incident beam. The central intensity of the resultant plane wave is directed onto a physical mask featuring double pinholes, generating two identical plane waves that are incident upon two halves of the SLM screen.

Each half of the SLM screen is encoded with its specific constant phase screen, essentially a hologram comprising a single greyscale value. Subsequently, the modulated light reflected from each half of the SLM screen passes through a lens, l_3 (with focal length f_3), inducing interference between the two beams in the Fourier/focal plane, located a distance f_3 away. Given that the interference pattern in the Fourier plane tends to be relatively small, an objective lens is introduced to magnify the beam, allowing for thorough observation using a webcam, as shown in the insert.
One half of the screen displays a constant phase mask that is black (greyscale value = 0) that corresponds to no induced phase shift i.e., $\Delta\phi = 0$ while the other half of the SLM screen cycles through the various greyscale values.

The phase difference between the modulated beams influences the position of the interference pattern. Therefore, as the hologram on one half of the screen cycles through the different greyscale values, the phase difference between the two beams varies and the interference pattern shifts laterally along the plane, as depicted in the inserts of Figure A.2. The shift in the interference pattern, ΔInt is related to the relative phase shift $\Delta\phi$ as follows:

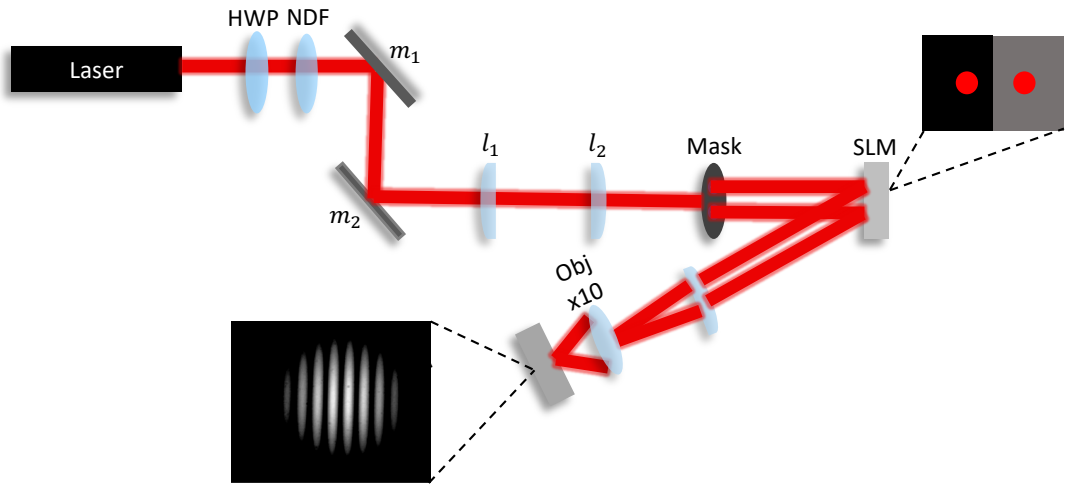


FIGURE A.1: Experimental setup of the calibration procedure for an SLM. A beam (λ = 633 nm) is polarised and attenuated using a half wave plate (HWP) and neutral density filter (NDF). The beam is then redirected using mirrors M_1, M_2 towards an expansion-collimation setup composed of lenses L_1, L_2. The resultant plane wave is incident on a physical mask with 2 pin holes. This leads to two beams being produced which are each incident on one half of the SLM screen. One half of the screen is encoded with a constant phase mask / greylevel, while the other cycles through various shades. These beams are then Fourier transformed using lens L_3 to observe them in the far-field where they overlap. An objective lens is added in the Fourier plane to magnify the interference pattern that is viewed with a webcam.

$$\Delta\phi = \frac{\Delta \text{Int}}{0.5\,T} \tag{A.1}$$

where T is the period of the interference fringes.

Using the Holoeye phasecam software and a webcam, this lateral shift of the interference pattern is recorded by identifying a minimum in the interference pattern and then tracking it as the holograms are changed. Figure A.3 shows the shift in the interference pattern before and after calibration. The plot (shown in red) has 256 rows which correspond to the intensity of the interference pattern for that particular grey value.

Using Equation A.1 one can determine the phase change induced by the default voltages as a function of the greyscale values. The mapping between the voltages and greyscale values are contained in a "gamma file", which are applicable for a specific wavelength (usually in the NIR spectrum). Using this gamma file, a correction response is calculated and applied manually or automatically - which is possible with some models. Once this correction response has been applied, a new gamma curve and its corresponding phase shift curve is measured. If the phase shift curve adequately matches the desired/reference pre-loaded phase shift curve, then the new experimentally measured phase shift curve is set as the default for the SLM. However, if this is not the case the calibration process is repeated. In our calibration process the desired phase shift was 2π. Before calibration the measured phase shift was 4.59π and after calibration the measured phase shift was 1.96π. The plots are shown in Figure A.4

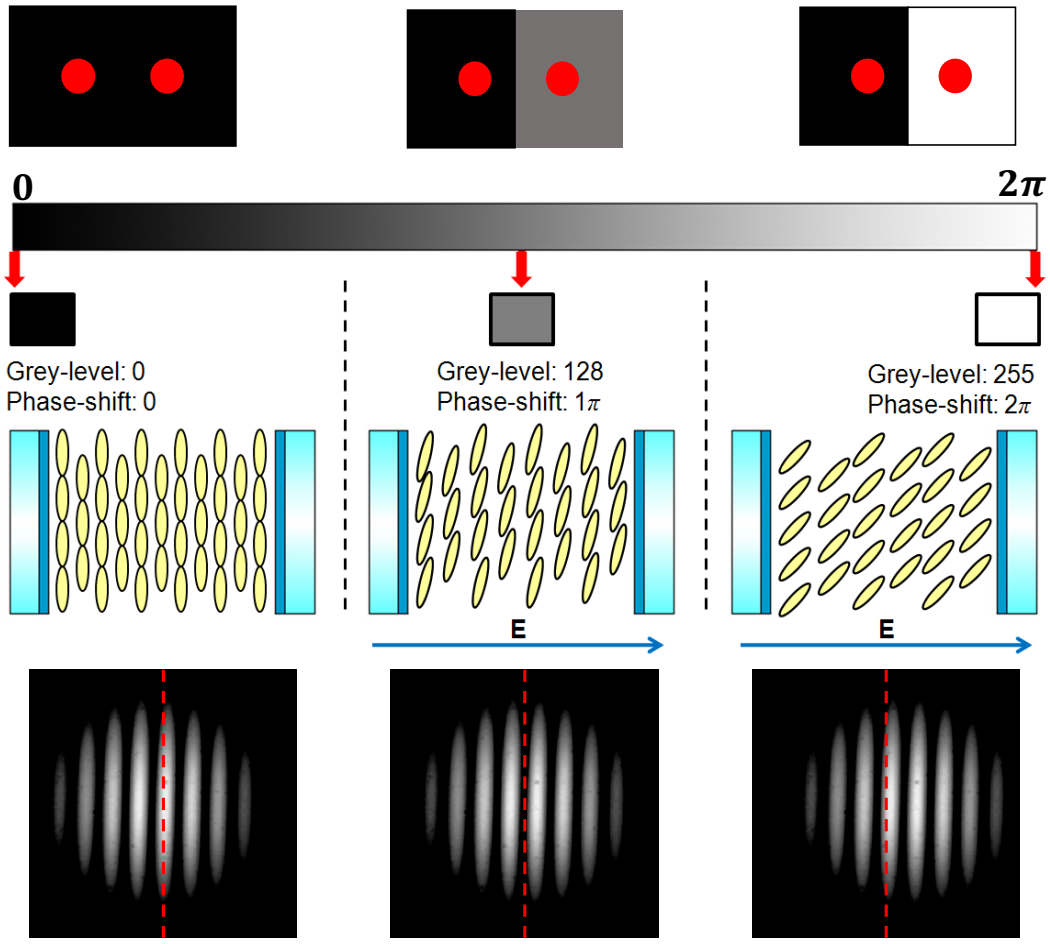


FIGURE A.2: To calibrate the SLM, one half of the screen is encoded with a constant phase mask (black in this case, which refers to a phase shift of 0), while the other half of the screen cycles through various greyscale levels, and thus different phase shift values. This results in a difference in the phase between the two reflected beams, leading to a lateral shift of the interference pattern in the Fourier plane.

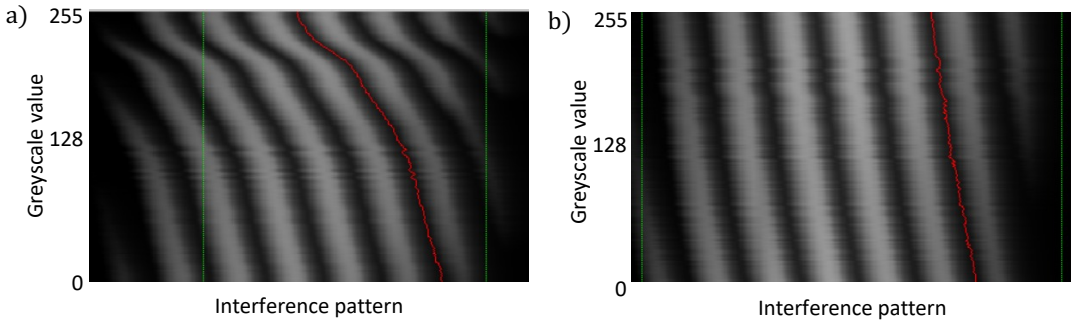


FIGURE A.3: Interference pattern shifts a) before and b) after the SLM was calibrated.

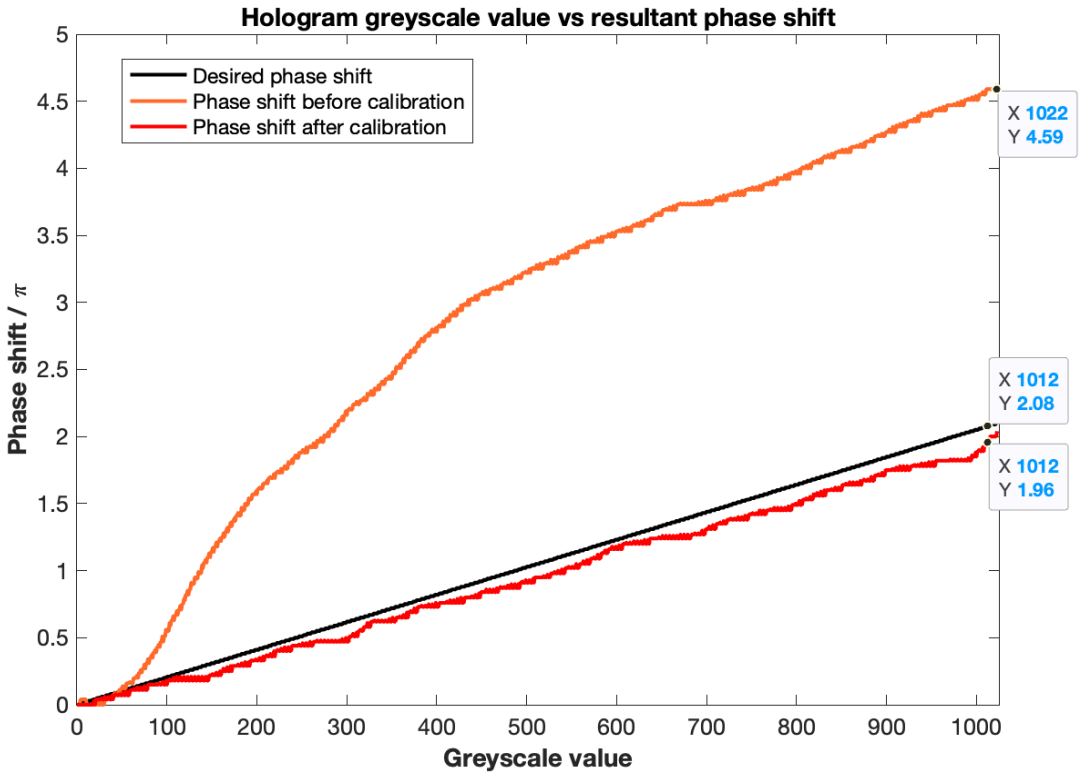


FIGURE A.4: Comparison of the reference (black) vs measured phase shift before (orange) and after (red) calibration.

Assuming that the SLM has been correctly calibrated, it can now impart any desired phase change, and thus modulate an entire complex field (amplitude and phase) of an incident beam to create a desired structured mode. Figure 2.16 illustrates the effect of using an un-calibrated and calibrated SLM when doing beam shaping.

Bibliography

1. Dickey, F. M. Laser beam shaping. *Optics and photonics news* **14,** 30–35 (2003).
2. Goodman, J. W. *Introduction to Fourier optics* (Roberts and Company publishers, 2005).
3. Claus, A. C. On Archimedes' burning glass. *Applied optics* **12,** A14–A14 (1973).
4. Aničin, B., Babović, V. & Davidović, D. Fresnel lenses. *American Journal of Physics* **57,** 312–316 (1989).
5. Caley, A. J., Thomson, M. J., Liu, J., Waddie, A. J. & Taghizadeh, M. R. Diffractive optical elements for high gain lasers with arbitrary output beam profiles. *Optics express* **15,** 10699–10704 (2007).
6. Soifer, V. A. *Methods for computer design of diffractive optical elements* (John Wiley & Sons, Inc., 2001).
7. Turunen, J. & Wyrowski, F. Diffractive optics for industrial and commercial applications. *Diffractive Optics for Industrial and Commercial Applications, by Jari Turunen (Editor), Frank Wyrowski (Editor), pp. 440. ISBN 3-527-40100-8. Wiley-VCH, March 1998.,* 440 (1998).
8. Ma, H. *et al.* Generation of flat-top beam with phase-only liquid crystal spatial light modulators. *Journal of Optics* **12,** 045704 (2010).
9. Frieden, B. R. Lossless conversion of a plane laser wave to a plane wave of uniform irradiance. *Applied Optics* **4,** 1400–1403 (1965).
10. Hecht, J. Short history of laser development. *Optical engineering* **49,** 091002–091002 (2010).
11. Forbes, A. Structured Light: Tailored for Purpose. *Optics and Photonics News* **31,** 24–31 (2020).
12. Forbes, A., de Oliveira, M. & Dennis, M. R. Structured light. *Nature Photonics* **15,** 253–262 (2021).
13. Forbes, A. *Laser beam propagation: generation and propagation of customized light* (CRC Press, 2014).
14. Forbes, A. Structured Light from Lasers. *Laser & Photonics Reviews* **13,** 1900140 (2019).
15. Shen, Y. Rays, waves, SU (2) symmetry and geometry: toolkits for structured light. *Journal of Optics* **23,** 124004 (2021).
16. Hoffnagle, J. A. & Jefferson, C. M. Design and performance of a refractive optical system that converts a Gaussian to a flattop beam. *Applied optics* **39,** 5488–5499 (2000).
17. Thompson, K. P. & Rolland, J. P. Freeform optical surfaces: a revolution in imaging optical design. *Optics and Photonics News* **23,** 30–35 (2012).
18. Nassiri, M. G. & Brasselet, E. Multispectral Management of the Photon Orbital Angular Momentum. *Physical Review Letters* **121,** 213901 (2018).

19. Rubano, A., Cardano, F., Piccirillo, B. & Marrucci, L. Q-plate technology: a progress review. *JOSA B* **36,** D70–D87 (2019).
20. Brasselet, E., Murazawa, N., Misawa, H. & Juodkazis, S. Optical vortices from liquid crystal droplets. *Physical review letters* **103,** 103903 (2009).
21. Bomzon, Z., Kleiner, V. & Hasman, E. Pancharatnam–Berry phase in space-variant polarization-state manipulations with subwavelength gratings. *Optics Letters* **26,** 1424–1426 (2001).
22. Devlin, R. C., Ambrosio, A., Rubin, N. A., Mueller, J. B. & Capasso, F. Arbitrary spin-to–orbital angular momentum conversion of light. *Science* **358,** 896–901 (2017).
23. Wang, J. Metasurfaces enabling structured light manipulation: advances and perspectives. *Chinese Optics Letters* **16,** 050006 (2018).
24. Forbes, A., Dudley, A. & McLaren, M. Creation and detection of optical modes with spatial light modulators. *Advances in Optics and Photonics* **8,** 200–227 (2016).
25. Rosales-Guzmán, C. & Forbes, A. *How to shape light with spatial light modulators* 57. ISBN: 9781510613027 (SPIE Press, 2017).
26. Lazarev, G., Chen, P.-J., Strauss, J., Fontaine, N. & Forbes, A. Beyond the display: Phase-only liquid crystal on Silicon devices and their applications in photonics. *Optics express* **27,** 16206–16249 (2019).
27. Scholes, S., Kara, R., Pinnell, J., Rodríguez-Fajardo, V. & Forbes, A. Structured light with digital micromirror devices: a guide to best practice. *Optical Engineering* **59,** 041202 (2019).
28. Ren, Y.-X., Lu, R.-D. & Gong, L. Tailoring light with a digital micromirror device. *Annalen der physik* **527,** 447–470 (2015).
29. Andrews, D. L. *Structured light and its applications* (Academic Press, 2008).
30. Maurer, C., Jesacher, A., Bernet, S. & Ritsch-Marte, M. What spatial light modulators can do for optical microscopy. *Laser & Photonics Reviews* **5,** 81–101 (2011).
31. Yu, W. *et al.* Super-resolution deep imaging with hollow Bessel beam STED microscopy. *Laser & Photonics Reviews* **10,** 147–152 (2016).
32. Török, P. & Munro, P. The use of Gauss-Laguerre vector beams in STED microscopy. *Optics Express* **12,** 3605–3617 (2004).
33. Segawa, S., Kozawa, Y. & Sato, S. Resolution enhancement of confocal microscopy by subtraction method with vector beams. *Optics Letters* **39,** 3118–21 (2014).
34. Chen, R., Agarwal, K., Sheppard, C. J. R. & Chen, X. Imaging using cylindrical vector beams in a high-numerical-aperture microscopy system. *Optics Letters* **38,** 3111–3114 (2013).
35. Wang, N. & Kobayashi, T. Polarization modulation for fluorescence emission difference microscopy. *Optics Express* **23,** 13704 (2015).
36. Wang, J. *et al.* Terabit free-space data transmission employing orbital angular momentum multiplexing. *Nature Photonics* **6,** 488 (2012).
37. Wang, Z., Zhang, N. & Yuan, X.-C. High-volume optical vortex multiplexing and de-multiplexing for free-space optical communication. *Opt. Express* **19,** 482–492 (2011).

38. Gibson, G. & Courtial J. and. Padgett, M. J. Free-space information transfer using light beams carrying orbital angular momentum. *Opt. Express* **12,** 5448–5456 (2004).

39. Mphuthi, N. *et al.* Free-space optical communication link with shape-invariant orbital angular momentum Bessel beams. *Applied Optics* **58,** 4258–4264 (2019).

40. Cox, M. A. *et al.* The resilience of Hermite–and Laguerre–Gaussian modes in turbulence. *Journal of Lightwave Technology* **37,** 3911–3917 (2019).

41. Zhao, S. M., Leach, J., Gong, L. Y., Ding, J. & Zheng, B. Y. Aberration corrections for free-space optical communications in atmosphere turbulence using orbital angular momentum states. *Opt. Express* **20,** 452 (2012).

42. Nape, I. *et al.* Revealing the invariance of vectorial structured light in complex media. *Nature Photonics* **16,** 538–546 (2022).

43. Račiukaitis, G. *et al.* Laser Processing by Using Diffractive Optical Laser Beam Shaping Technique. *Journal of laser micro/nanoengineering* **6** (2011).

44. Olson, R. W. & Swope, W. C. Laser drilling with focused Gaussian beams. *Journal of applied physics* **72,** 3686–3696 (1992).

45. Duocastella, M. & Arnold, C. B. Bessel and annular beams for materials processing. *Laser & Photonics Reviews* **6,** 607–621 (2012).

46. Chen, M.-F., Lin, K.-m. & Ho, Y.-S. Laser annealing process of ITO thin films using beam shaping technology. *Optics and Lasers in Engineering* **50,** 491–495 (2012).

47. Roberts, C. *Biomechanics of the cornea and wavefront-guided laser refractive surgery* 2002.

48. Matthias, B. *et al. Concept for image-guided vitreo-retinal fs-laser surgery: adaptive optics and optical coherence tomography for laser beam shaping and positioning* in *Ophthalmic Technologies XXV* **9307** (2015), 55–62.

49. Keus, R., Noach, P., De Boer, R. & Lebesque, J. The effect of customized beam shaping on normal tissue complications in radiation therapy of parotid gland tumors. *Radiotherapy and Oncology* **21,** 211–217 (1991).

50. Alster, T. S. & Lupton, J. R. Treatment of complications of laser skin resurfacing. *Archives of facial plastic surgery* **2,** 279–284 (2000).

51. Lizotte, T. E. & Tuttle, T. *Beam shaping for cosmetic hair removal* in *Laser Beam Shaping VIII* **6663** (2007), 172–179.

52. Tahiliani, S. T. & Tahiliani, H. S. Prospective Evaluation of the Safety and Efficacy of a 1060-nm Large Spot Size, Vacuum-Assisted Hair Removal Diode Laser System in Asian/Pacific Fitzpatrick's Skin Types IV-V Patients. *Journal of drugs in dermatology: JDD* **15,** 1427–1434 (2016).

53. Zhang, Y. *et al.* Identification and separation of chiral particles by focused circularly polarized vortex beams. *JOSA A* **39,** 1371–1377 (2022).

54. Forbes, A. & Nape, I. Quantum mechanics with patterns of light: Progress in high dimensional and multidimensional entanglement with structured light. *AVS Quantum Science* **1,** 011701 (2019).

55. Ndagano, B., Nape, I., Cox, M. A., Rosales-Guzman, C. & Forbes, A. Creation and Characterization of Vector Vortex Modes for Classical and Quantum Communication. *arXiv. org.-2017.*

56. Simpson, S. H. & Hanna, S. Optical trapping of spheroidal particles in Gaussian beams. *JOSA A* **24,** 430–443 (2007).
57. Schut, T. B., Schipper, E., De Grooth, B. & Greve, J. Optical-trapping micromanipulation using 780-nm diode lasers. *Optics letters* **18,** 447–449 (1993).
58. Lee, W., Yuan, X.-C. & Cheong, W. Optical vortex beam shaping by use of highly efficient irregular spiral phase plates for optical micromanipulation. *Optics letters* **29,** 1796–1798 (2004).
59. Cizmar, T., Garces-Chavez, V., Dholakia, K. & Zemanek, P. *Optical trapping in counter-propagating Bessel beams* in *Optical Trapping and Optical Micromanipulation* **5514** (2004), 643–651.
60. Ren, H. *et al.* An achromatic metafiber for focusing and imaging across the entire telecommunication range. *nature communications* **13,** 4183 (2022).
61. Laskin, A. *Achromatic refractive beam shaping optics for broad spectrum laser applications* in *Laser Beam Shaping X* **7430** (2009), 19–29.
62. Wang, H. *et al.* Coloured vortex beams with incoherent white light illumination. *Nature Nanotechnology* **18,** 264–272 (2023).
63. Forbes, A. & Perumal, L. Twisted light gets a splash of colour. *Nature Nanotechnology* **18,** 221–222 (2023).
64. Cheng, J., Gu, C., Zhang, D. & Chen, S.-C. High-speed femtosecond laser beam shaping based on binary holography using a digital micromirror device. *Opt. Lett.* **40,** 4875–4878 (Nov. 2015).
65. Spangenberg, D., Dudley, A., Neethling, P. H., Rohwer, E. G. & Forbes, A. White light wavefront control with a spatial light modulator. *Opt. Express* **22,** 13870–13879 (2014).
66. Forbes, A., Dickey, F., DeGama, M. & Du Plessis, A. Wavelength tunable laser beam shaping. *Optics letters* **37,** 49–51 (2012).
67. Leach, J. *et al.* Generation of achromatic Bessel beams using a compensated spatial light modulator. *Optics express* **14,** 5581–5587 (2006).
68. Huang, H. *et al.* 100 Tbit/s free-space data link enabled by three-dimensional multiplexing of orbital angular momentum, polarization, and wavelength. *Opt. Lett.* **39,** 197–200 (2014).
69. Padgett, M. J. Orbital angular momentum 25 years on. *Optics Express* **25,** 11265–11274 (2017).
70. Shen, Y. *et al.* Optical vortices 30 years on: OAM manipulation from topological charge to multiple singularities. *Light: Science & Applications* **8,** 1–29 (2019).
71. Sephton, B., Dudley, A. & Forbes, A. Revealing the radial modes in vortex beams. *Applied optics* **55,** 7830–7835 (2016).
72. Kreuzer, J. L. *Coherent light optical system yielding an output beam of desired intensity distribution at a desired equiphase surface* US Patent 3,476,463. 1969.
73. Kreuzer, J. L. Laser light redistribution in illuminating optical signal processing systems. *Optical and Electro-Optical Information Processing,* 365 (1965).
74. Dickey, F. M. & Holswade, S. C. Gaussian laser beam profile shaping. *Optical Engineering* **35,** 3285–3296 (1996).
75. Bryngdahl, O. Geometrical transformations in optics. *JOSA* **64,** 1092–1099 (1974).

76. Rhodes, P. W. & Shealy, D. L. Refractive optical systems for irradiance redistribution of collimated radiation: their design and analysis. *Applied optics* **19,** 3545–3553 (1980).
77. Dickey, F. M. *Laser beam shaping: theory and techniques* (CRC press, 2018).
78. Karimi, E., Zito, G., Piccirillo, B., Marrucci, L. & Santamato, E. Hypergeometric-gaussian modes. *Optics letters* **32,** 3053–3055 (2007).
79. Rafayelyan, M. & Brasselet, E. Laguerre–Gaussian modal q-plates. *Optics letters* **42,** 1966–1969 (2017).
80. Shafer, D. Gaussian to flat-top intensity distributing lens. *Optics & Laser Technology* **14,** 159–160 (1982).
81. Han, C.-Y., Ishii, Y. & Murata, K. Reshaping collimated laser beams with Gaussian profile to uniform profiles. *Applied optics* **22,** 3644–3647 (1983).
82. Kawamura, Y., Itagaki, Y., Toyoda, K. & Namba, S. A simple optical device for generating square flat-top intensity irradiation from a Gaussian laser beam. *Optics Communications* **48,** 44–46 (1983).
83. Jahan, S. & Karim, M. Refracting systems for Gaussian-to-uniform beam transformations. *Optics & Laser Technology* **21,** 27–30 (1989).
84. Dickey, F. M. & Holswade, S. C. in *Laser Beam Shaping Applications* 269–305 (CRC Press, 2018).
85. Perumal, L. M. & Forbes, A. Broadband structured light using digital micromirror devices (DMDs): a tutorial. *Journal of Optics* (2023).
86. Scholes, S., Rodríguez-Fajardo, V. & Forbes, A. Lossless reshaping of structured light. *JOSA A* **37,** C80–C85. http://josaa.osa.org/abstract.cfm?URI=josaa-37-11-C80 (2020).
87. Scholes, S., Sroor, H., Ait-Ameur, K., Zhan, Q. & Forbes, A. General design principle for structured light lasers. *Optics Express* **28,** 35006–35017 (2020).
88. Physics, L. url https://www.laserphysics.co.uk/store/lasers/stellar-series-argon-lasers/stellar-pro-l. accessed 18 November 2023.
89. ThorLabs. *N-BK7 Plano-Convex Lenses (Uncoated)* https://www.thorlabs.com/newgrouppage9.cfm?objectgroup_id=112. accessed 18 November 2023.
90. ThorLabs. *N-BK7 Plano-Convex Lenses (Uncoated)* https://www.thorlabs.com/newgrouppage9.cfm?objectgroup_id=120. accessed 18 November 2023.
91. Umhofer, U., Jäger, E. & Bischoff, C. *Refractive and diffractive laser beam shaping optics: High end components for material processing* 2011.
92. Sueda, K., Miyaji, G., Miyanaga, N. & Nakatsuka, M. Laguerre-Gaussian beam generated with a multilevel spiral phase plate for high intensity laser pulses. *Optics express* **12,** 3548–3553 (2004).
93. Mawardi, A., Hild, S., Widera, A. & Meschede, D. ABCD-treatment of a propagating doughnut beam generated by a spiral phase plate. *Optics express* **19,** 21205–21210 (2011).
94. Gorelick, S. *et al.* High-efficiency Fresnel zone plates for hard X-rays by 100 keV e-beam lithography and electroplating. *Journal of Synchrotron Radiation* **18,** 442–446 (2011).
95. Baez, A. V. Fresnel zone plate for optical image formation using extreme ultraviolet and soft x radiation. *JOSA* **51,** 405–412 (1961).

96. Chen, Z. *et al.* Design and fabrication of Fresnel zone plates with large numbers of zones. *Journal of Vacuum Science & Technology B: Microelectronics and Nanometer Structures Processing, Measurement, and Phenomena* **15,** 2522–2527 (1997).
97. Turunen, J. & Wyrowski, F. *Diffractive Optics for Industrial and Commercial Applications* ISBN: 9783055017339. https://books.google.co.za/books?id=XBuSQgAACAAJ (John Wiley & Sons, Limited, 1997).
98. Dresel, T., Beyerlein, M. & Schwider, J. Design and fabrication of computer-generated beam-shaping holograms. *Applied Optics* **35,** 4615–4621 (1996).
99. Holoeye. *Pluto 2.1 Spatial Light Modulator* https://holoeye.com/slm-pluto-phase-only/. accessed 27 August 2023.
100. Hornbeck, L. J. *Deformable mirror light modulator* US Patent 4,441,791. Apr. 1984.
101. Hornbeck, L. J. *Digital light processing and MEMS: An overview* in *Digest IEEE/Leos 1996 Summer Topical Meeting. Advanced Applications of Lasers in Materials and Processing* (1996), 7–8.
102. Hornbeck, L. J. *Digital light processing: a new MEMS-based display technology* in *Technical digest of the sensor symposium* **14** (1996), 297–304.
103. Hornbeck, L. J., Howell, T. R., Knipe, R. L. & Mignardi, M. A. *Digital Micromirror Device™: Commercialization of a Massively Parallel MEMS Technology* in *ASME International Mechanical Engineering Congress and Exposition* **18435** (1997), 3–8.
104. Tew, C. *et al. Electronic control of a digital micromirror device for projection displays* in *Proceedings of IEEE International Solid-State Circuits Conference-ISSCC'94* (1994), 130–131.
105. Hornbeck, L. J. *Digital light processing for high-brightness high-resolution applications* in *Projection Displays III* **3013** (1997), 27–40.
106. Hornbeck, L. J. *Current status of the digital micromirror device (DMD) for projection television applications* in *Proceedings of IEEE International Electron Devices Meeting* (1993), 381–384.
107. Sampsell, J. B. Digital micromirror device and its application to projection displays. *Journal of Vacuum Science & Technology B: Microelectronics and Nanometer Structures Processing, Measurement, and Phenomena* **12,** 3242–3246 (1994).
108. Hornbeck, L. J. *Combining digital optical MEMS, CMOS and algorithms for unique display solutions* in *2007 IEEE International Electron Devices Meeting* (2007), 17–24.
109. Sheng, Z., Zhou, X. & Shaw, S. *Compact digital micromirror device (DMD)-based optical architecture for augmented reality (AR) glasses* in *Emerging Digital Micromirror Device Based Systems and Applications XV* **12435** (2023), 51–61.
110. Hung, C.-C. *et al.* Optical design of automotive headlight system incorporating digital micromirror device. *Applied optics* **49,** 4182–4187 (2010).
111. Dudley, D., Duncan, W. M. & Slaughter, J. *Emerging digital micromirror device (DMD) applications* in *MOEMS display and imaging systems* **4985** (2003), 14–25.
112. Liang, J., Kohn Jr, R. N., Becker, M. F. & Heinzen, D. J. High-precision laser beam shaping using a binary-amplitude spatial light modulator. *Applied optics* **49,** 1323–1330 (2010).

113. Liang, J., Kohn Jr, R. N., Becker, M. F. & Heinzen, D. J. *High-precision beam shaper for coherent and incoherent light using a DLP spatial light modulator* in *Emerging Digital Micromirror Device Based Systems and Applications III* **7932** (2011), 67–75.

114. Goorden, S. A., Bertolotti, J. & Mosk, A. P. Superpixel-based spatial amplitude and phase modulation using a digital micromirror device. *Opt. Express* **22,** 17999–18009 (July 2014).

115. Lee, W.-H. Binary computer-generated holograms. *Applied Optics* **18,** 3661–3669 (1979).

116. Gong, L. *et al.* Generation of cylindrically polarized vector vortex beams with digital micromirror device. *Journal of Applied Physics* **116** (2014).

117. Peters, E. *et al.* Real-time acquisition of complex optical fields by binary amplitude modulation. *Optics letters* **42,** 2030–2033 (2017).

118. Singh, K. & Dudley, A. Digital toolbox for vector field characterization. *Nanophotonics* **11,** 753–761 (2021).

119. Vohnsen, B., Martins, A. C., Qaysi, S. & Sharmin, N. Hartmann–Shack wavefront sensing without a lenslet array using a digital micromirror device. *Applied optics* **57,** E199–E204 (2018).

120. Singh, K., Dudley, A. & Forbes, A. Versatile all-digital transport-of-intensity based wavefront sensor and adaptive optics using a DMD. *Optics Express* **31,** 8987–8997 (2023).

121. Texas Instruments. *DLP0.3 WVGA chipset data manual* Available at: https://www.ti.com/lit/an/dlpz005a/dlpz005a.pdf?ts=1680645005296&ref_url=https%253A%252F%252Fwww.google.com%252F.

122. Texas Instruments. *DLP0.65 WVGA chipset data manual* Available at: https://www.ti.com/product/DLP6500FLQ.

123. Texas Instruments. *DLP660TE ACTIVE 0.66-inch 4K UHD 2XLVDS DLP® digital micromirror device (DMD)* Available at: https://www.ti.com/product/DLP660TE#features.

124. Mirhosseini, M. *et al.* Rapid generation of light beams carrying orbital angular momentum. *Optics Express* **21,** 30196–30203 (2013).

125. Lakshminarayanan, V. & Fleck, A. Zernike polynomials: a guide. *Journal of Modern Optics* **58,** 545–561 (2011).

126. https://www.mathworks.com/matlabcentral/fileexchange/7021-spectral-and-xyz-color-functions.

127. Weiner, A. M. Ultrafast optical pulse shaping: A tutorial review. *Optics Communications* **284,** 3669–3692 (2011).

128. Weiner, A. M. Femtosecond pulse shaping using spatial light modulators. *Review of scientific instruments* **71,** 1929–1960 (2000).

129. Arrizon, V., Ruiz, U., Carrada, R. & González, L. a. Pixelated phase computer holograms for the accurate encoding of scalar complex fields. *Journal of the Optical Society of America. A, Optics, image science, and vision* **24,** 3500–7. ISSN: 1084-7529. http://www.ncbi.nlm.nih.gov/pubmed/17975577 (Nov. 2007).

130. Nanoscribe. *Quantum-X Nanoscribe information* https://www.nanoscribe.com/en/products/quantum-x/. accessed 03 January 2024.

131. Odian, G. *Principles of polymerization* (John Wiley & Sons, 2004).

132. Hahn, V. *et al.* Rapid assembly of small materials building blocks (voxels) into large functional 3D metamaterials. *Advanced Functional Materials* **30,** 1907795 (2020).

133. Nanoscribe. *Quantum-X Nanoscribe resins* https://support.nanoscribe.com/hc/en-gb/articles/360002486493-Resins-Overview. accessed 03 January 2024.

134. Mattox, D. M. in *Handbook of Physical Vapor Deposition (PVD) Processing (Second Edition)* (ed Mattox, D. M.) Second Edition, 1–24 (William Andrew Publishing, Boston, 2010). ISBN: 978-0-8155-2037-5. https://www.sciencedirect.com/science/article/pii/B9780815520375000010.